VOLUME 13 NUMBER 1-2 2026 ISSN 2409-6121; eISSN 2522-1361

Physical Sciences and Technology

National Nanotechnological Laboratory of Open Type
Institute of Experimental and Theoretical Physics

Physical Sciences and Technology is publishing two number in a year by al-Farabi Kazakh National University, al-Farabi ave., 71, 050040, Almaty, the Republic of Kazakhstan
website: http://phst.kaznu.kz/

Any inquiry for subscriptions should be send to:
Dr. Gauhar Mussabek, al-Farabi Kazakh National University
al-Farabi ave., 71, 050040, Almaty, the Republic of Kazakhstan
e-mail: phst@kaznu.edu.kz

SCOPE AND AIM

Physical Sciences and Technology provides an original paperback for the publication of peerreviewed research and review articles in all fields of Physics and related Technology. The topics, included in the scope, especially emphasize understanding of the physics underlying modern technology.

Subject areas may include, but are not limited to the following fields: Astronomy and Space Research, Theoretical Physics and Astrophysics, Plasma Physics and Related Technology, Chemical Physics and Related Technology, Condensed Matter Physics and Related Technology, Thermal physics and Related Technology, Nuclear Physics and Related Technology, Nanomaterials and Nanotechnology, Applied Atomic and Molecular Physics, Material Sciences and Related Technology, Electronics and Related Technology, Instrumentation, Photonics and Quantum Electronics, Signal processing.

The Journal is issued under the auspices of the National Nanotechnological Laboratory of Open Type and Institute of Experimental and Theoretical Physics and is published two times a year by the «Kazakh University» Publishing House. The International Editorial Board of the Journal consists of leading researchers from different countries of the world. The Journal is wide open for contributions that both lie at the far frontiers of contemporary physics and are particularly aimed at applications of the scientific principles of physics to modern technological problems.

IRSTI 58.81.91 https://doi.org/10.26577/phst20261311

Radiation safety justification of spent nuclear fuel management technology for a reactor facility

I.V. Prozorova*, A.K. Mukhamediev, I.N. Bogomolova, A.A. Prozorov, Yu.A. Popov, Yu.Yu. Baklanova and V.A. Pospelov

Branch "Institute of Atomic Energy" of RSE National Nuclear Center of the Republic of Kazakhstan, Kurchatov, Kazakhstan,
*e-mail: prozorova@nnc.kz

(Received February 11, 2026; received in revised form May 25, 2026; accepted May 31, 2026)

Research at the Institute of Atomic Energy of the National Nuclear Center of the Republic of Kazakhstan (IAE NNC RK) is focused on developing effective technologies for the management of spent nuclear fuel (SNF) from the BN-350 fast reactor. Among the approaches under consideration is a dilution and immobilization technology developed for irradiated uranium–graphite fuel from the Impulse Graphite Reactor (IGR). The process involves dry mixing of highly enriched uranium (HEU) fuel with depleted uranium dioxide, followed by immobilization through cementation. This study presents a comprehensive assessment of radiation conditions throughout the technological cycle of HEU fuel processing. Radiation field analysis at each processing stage is essential for establishing design requirements, optimizing facility operation, and ensuring personnel protection. Monte Carlo simulations performed using the MCNP code were employed to evaluate dose distributions and support radiation safety justification of the facility design. Based on the simulation results, several design modifications were implemented to improve shielding effectiveness and reduce occupational exposure. The proposed approach introduces a systematic methodology for radiation field assessment under conditions of incomplete information on fuel distribution, providing a conservative framework for safety analysis. Given the absence of direct international analogues for the management of irradiated HEU graphite fuel, the developed methodology offers both practical value for the IGR fuel immobilization project and potential applicability to future SNF management technologies for the BN-350 reactor.

Keywords: spent nuclear fuel, management, measured effective dose, radiation situation.

1. Introduction

Currently, the IAE NNC RK is designing a fuel dilution and immobilization facility (hereinafter referred to as the facility) for the IGR research reactor [13]. This facility is planned to process the IGR reactor fuel, which was unloaded in 1966. The main facility areas include temporary storage for daily fuel batches, the immobilization area (fuel and "dilutant" grinding and cementation process), and the barrel drying area (matrix solution hardening process).

According to international recommendations for the design and operation of processing facilities [14], all processes must comply with the basic safety principles: protection of people, prevention of nuclear materials criticality, control of emissions, and environmental protection. The facility operation requires a multi-level system of protective barriers (defense in depth), with emphasis on the ALARA principle: keeping radiation doses to personnel and the public "as low as reasonably achievable." The assessment of radiological impact associated with different fuel management options (e.g., reprocessing versus direct disposal) is well presented in [15]. The article [16] describes a spent nuclear fuel reprocessing plant divided into four production areas and presents methods for assessing the risks associated with the reprocessing process. These methods make it possible to predict which areas pose the greatest hazards and therefore require enhanced control and protection. Fuzzy comprehensive assessment and probabilistic statistical analysis methods are used to calculate the risk level for each assessment unit and each production area.

For the monitoring and control of operating nuclear reactors, various detection modules are being developed [5]. In study [6], the relationship between radon accumulation in indoor environments and the concentration of its decay products in soil is investigated in order to provide a comprehensive assessment of public health impacts. The article [7] is devoted to the development of a low-cost alpha and gamma spectrometric system for experimental physics and field applications, such as radiation detection and environmental monitoring of nuclear facilities.

The article [8] presents a method and a framework for optimizing the allocation of radiation monitoring resources based on an analysis of nuclear incident risks and the relative importance of facilities at a spent nuclear fuel (SNF) reprocessing plant. The study provides a theoretical and technical basis for safety management and operational decision-making at SNF reprocessing plants.

In recent years, significant progress has been achieved in the development of nanostructured materials within the framework of modern physical research. In particular, carbon-containing nanomaterials synthesized via electric arc discharge exhibit a high degree of graphitization and a nanoscale structure (on the order of tens of nanometers), leading to enhanced thermal stability and electrical conductivity [9]. Such properties make them promising candidates for application in radiation-resistant systems and functional components operating under extreme conditions.

Moreover, studies on carbon nanowalls have shown that their morphology and surface structure can be precisely controlled, which directly affects their physicochemical properties. This tunability is particularly important for processes involving interaction with radionuclides, including sorption, surface binding, and barrier functions [10]. The high specific surface area of such nanostructures further expands their potential applicability in nuclear technologies.

The article [11] presents calculation approaches for estimating personnel radiation doses during the following technological stages: unloading, dismantling, and processing. The calculations accounted for neutron and photon sources SNF, photon sources in control rods, and photon sources in structural materials, including the reactor vessel and fuel assemblies. When calculating dose rates from neutrons and secondary gamma photons, direct calculations using MCNP-4B produced acceptable results in most cases, with an acceptable level of methodological uncertainty. However, for problems involving photon sources, direct MCNP-4B calculations yielded unsatisfactory results due to strong radiation attenuation. To reduce statistical dispersion, several variance-reduction techniques were applied, including the assignment of different importance values to cells and the use of the weighted window iteration method.

When assessing the safety of a reprocessing facility, it is also necessary to take into account the national context: what standards and legislative features are in place in the country. Article [12] examines issues of state regulation of safety, as well as the policy and practice of handling accumulated and generated radioactive waste in the Republic of Kazakhstan. The Republic of Kazakhstan does not have industrial facilities for reprocessing SNF, and the main focus is on the safe storage, conditioning, and accounting of nuclear materials. The developed infrastructure of the NNC RK and international cooperation provide support for the radiation monitoring system and the improvement of the regulatory and technical framework. The national approach is based on the principles of multi-level protection and risk assessment to ensure long-term nuclear and radiation safety.

The present study is based on Monte Carlo simulations performed to assess radiation conditions in various areas of the facility and to establish requirements for the design, construction, and operation of process equipment, as well as to ensure adequate radiation protection of personnel. A particular challenge of the considered system is the uncertainty associated with the spatial distribution of irradiated fuel within the technological equipment. To address this issue, a set of conservative fuel distribution scenarios was developed and analyzed.

The calculations made it possible to identify the most unfavorable operating conditions, determine the factors having the greatest influence on dose formation, and evaluate the effectiveness of the proposed shielding solutions. The results were subsequently used to support design decisions and optimize the radiation protection measures incorporated into the facility project. The proposed approach may also be useful for radiation safety assessments of other facilities involved in the handling and processing of spent nuclear fuel under conditions where the exact distribution of radioactive materials cannot be determined with sufficient accuracy.

2. Methodology

The irradiated graphite fuel from the IGR reactor has an enrichment of up to 90% in ^{235}U, which is classified as highly enriched uranium (HEU), and in order to remove the material from IAEA safeguards,

it is planned to reduce the fuel enrichment in ^{235}U to 5%. The dry mixing method was chosen as the design solution for the HEU fuel dilution stage. This method involves the joint grinding of the fuel and depleted uranium dioxide to a fraction of ≈200 μm in specified ratios. Next, the diluted fuel is immobilized by cementation. Cementation of irradiated, now low-enriched uranium (LEU) fuel is carried out in a type "A" barrel (55 gallons) with a built-in mixer, in accordance with the developed technological regulations and using the established matrix recipe [13]. The concentration of fuel in the cement matrix does not exceed 50 ppm of ^{235}U [14,15].

During operation (from 1962 to 1966), the fuel received a dose of 4×10^{18} n/cm². The maximum temperature during reactor operation was approximately 2000 K, and the fuel burnup was less than 1%. Irradiated elements are expected to be handled in the form of blocks (Figure 1) and rods, as well as fragments thereof.

The estimated radionuclide composition and activity of the fuel are presented in Table 1.

Table 1. Number and activity of nuclides in irradiated graphite HEU fuel from the IGR reactor.

№	Nuclide	N (number of nuclei)	Main radiation type	Q (activity), sec^{-1}
1	^{137}Cs	$9.65 \cdot 10^{20}$	β, γ	$7.03 \cdot 10^{11}$
2	^{90}Sr	$8.00 \cdot 10^{20}$	B	$6.15 \cdot 10^{11}$
3	^{151}Sm	$9.03 \cdot 10^{19}$	B	$2.20 \cdot 10^{10}$
4	^{99}Tc	$2.71 \cdot 10^{21}$	B	$2.21 \cdot 10^{8}$
5	^{155}Eu	$1.36 \cdot 10^{16}$	β, γ	$6.04 \cdot 10^{7}$
6	^{93}Zr	$3.11 \cdot 10^{21}$	B	$4.38 \cdot 10^{7}$
7	^{135}Cs	$3.00 \cdot 10^{21}$	B	$2.86 \cdot 10^{7}$
8	^{129}I	$5.93 \cdot 10^{20}$	β, γ	$8.30 \cdot 10^{5}$
9	^{107}Pd	$1.30 \cdot 10^{20}$	B	$4.20 \cdot 10^{5}$

Among the radionuclides listed in the table, only ^{137}Cs exhibits both a high gamma-ray emission yield and significant activity, making it the dominant source of gamma radiation. Its activity is 7.03×10^{11} s^{-1}, which is the highest among the radionuclides considered. During the decay of ^{137}Cs, metastable ^{137m}Ba is produced, emitting gamma photons with an energy of approximately 662 keV. The remaining radionuclides are predominantly beta emitters or possess insufficient gamma activity to make a significant contribution to the radiation field.

The measured effective dose (MED) of gamma radiation on the surface of uranium-graphite blocks stored in the storage is approximately 2 - 2.5 μSv/h, and at a distance of 10 cm from a single block of irradiated fuel, it is approximately 0.33 μSv/h. The nuclide ^{137}Cs contributes most significantly to the gamma radiation level. The activity of ^{137}Cs in a single graphite block weighing 2 kg was assumed to be 10^8 Bq.

To carry out the immobilization and dilution process, preliminary work was performed to repackage the spent fuel into daily containers. A total of 640 blocks were extracted and repackaged.

The technological scheme for diluting HEU fuel: first, uranium-graphite blocks are pre-crushed and ground. For this purpose, a jaw crusher will be used, which allows the entire irradiated block to be loaded and ensures grinding to fractions of 25–5 mm. Further grinding of the fuel is carried out together with depleted uranium dioxide in a ball mill or rotary fine grinding mill. The next stage involves cementing, in which the proportion of solid radioactive waste introduced must not exceed 20%. The final stage involves pouring and mixing the cement mixture into containers – 200-liter barrels – and then transporting them to specialized storage facilities.

Figure 1 shows the design of the facility. The rooms in the planned building are divided into zones with different levels of radiation safety, each with corresponding access restrictions. The building design have been developed taking into account radiation protection requirements, including the use of protective barriers and structural elements to minimize radiation exposure. HEU fuel will be stored in special containers and equipment at all stages of operation; open handling is not permitted. The technological equipment is designed to be reliable and convenient to operate, made of corrosion-resistant and radiation-resistant materials that can be decontaminated, has the necessary tightness, and provides the possibility of using remote methods for equipment operation and monitoring. Figure 1 shows rather the technological chains in the process of processing blocks.

According to the project, personnel are restricted to spending only limited amounts of time in rooms with high radiation levels in order to ensure that permissible exposure levels are not exceeded.

This paper considers a radiation scenario describing the full processing cycle: from loading the graphite block into the crusher to placing the cemented LEU fuel into a container. At all stages of the cycle: grinding, mixing, cementation will be conducted on grinding installation (Fig. 2).

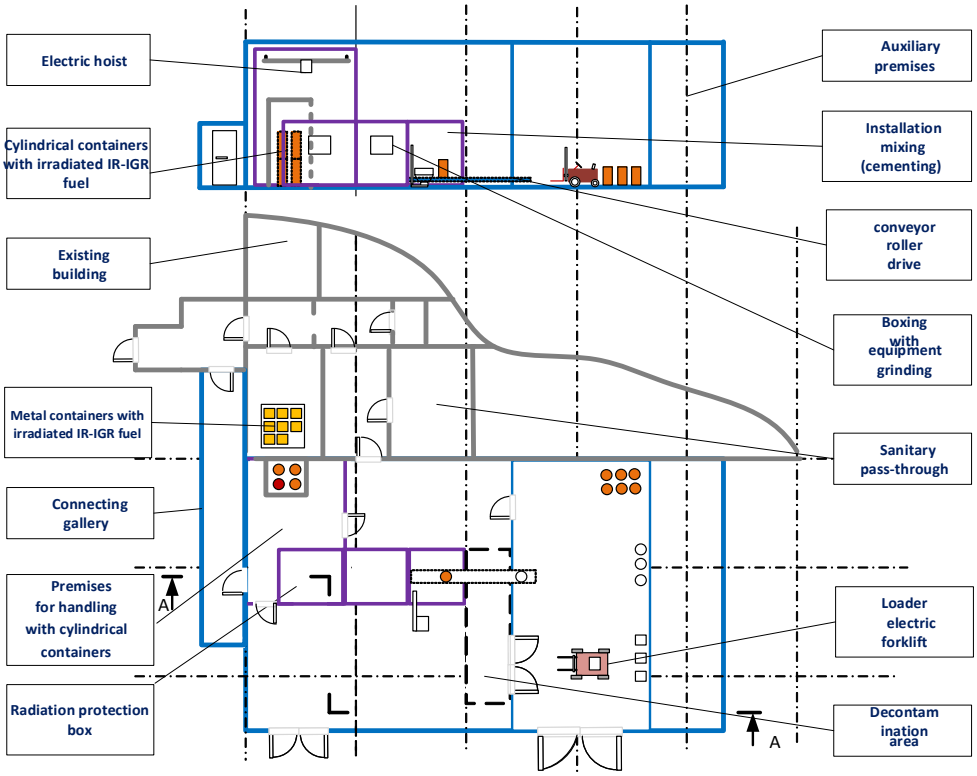

Figure 1. Design of HEU fuel dilution and immobilization facility.

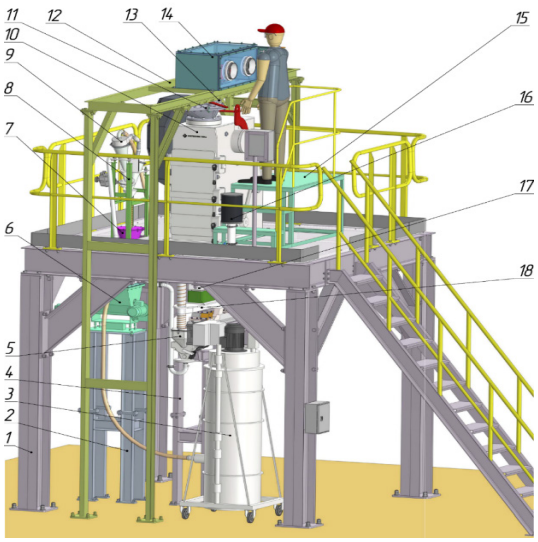

1 – service area; 2 – weight dispenser stand; 3 – turbine vacuum cleaner; 4 – feeder and mill support; 5 – universal mill (point 3) (A4); 6 – weight dispenser (point 4) (A8); 7 – storage hopper (A6); 8 – cyclone support; 9 – double cyclone (A5); 10 – jaw crusher (A2); 11 – rotary valve; 12 – loading chamber support; 13 – adapter; 14 – feed chamber (point 1) (A1); 15 – pedestal; 16 – air filter; 17 – chute; 18 – electromagnetic dosing feeder (point 2) (A3).

Figure 2. Grinding installation.

According to the technology, only two graphite blocks will be processed per cycle, due to activity and permissible dose limits. However, the most complex scenario takes into account the potential for graphite dust to remain in various parts of the equipment.

This discretization is not arbitrary, but reflects the actual dynamics of fuel transport and accumulation in the system. This demonstrates the reliability of the model's conservatism and the representativeness of the results.

During the calculations, the radiation sources were specified in volumetric form as entire blocks on the production line and as volumetric cylindrical sources in the storage warehouse (barrels). This has been corrected in the article.

Systematic uncertainties were taken into account when defining the geometry. The fuel position was selected at five points, corresponding to the maximum amount of fuel transported within the facility. It was conservatively assumed that two fuel blocks remain in the facility at all times as dust deposited on the internal equipment. Therefore, it was assumed that 0.5 blocks were always present at each calculation point.

The facility was not modeled; the calculation geometry included only radiation shielding elements (glass and screens) and building structures, specifically the room walls and metal barrels, which significantly impact dose distribution.

Uncertainties in the fuel composition were also considered when developing the scenario (graphite was specified without additional impurities that have an absorbing effect), and the activity of a single graphite block was chosen to be maximum. Various scenarios were considered, taking into account the uncertainty in the geometry, shielding, and fuel distribution within the facility.

When conducting calculations, the facility was not modeled in detail as having complex industrial geometry. This is due to conservatism; all the facility components are made of stainless steel, which serves as an additional absorbing element. However, when constructing the models, we took into account that this could affect scattering, shielding, and the overall formation of dose fields.

The adopted approach represents a generalized methodology for handling incomplete source term information, where discrete conservative scenarios are used to approximate the envelope of possible fuel distributions.

Such an approach allows the identification of bounding radiation conditions without requiring detailed real-time material tracking, which is often unavailable at early design stages.

3. Calculation methodology

The calculations were performed in 3D geometry using the MCNP6 code. Conservative approaches and assumptions were applied in setting up the tasks and modeling. The Visual Editor and Excel were used for visualization.

Due to the lack of detailed data on fuel distribution at each point of the grinding installation, the following assumptions were made to simplify the calculation. The fuel distribution was evaluated at five key locations corresponding to the maximum amount of fuel during its movement through the facility: point 1 – the loading throat of the jaw crusher; point 2 – the electromagnetic metering feeder; point 3 – the mill; point 4 – the receiving hopper of the weigh feeder; point 0 – the bottom of the barrel.

A conservative assumption was made that two fuel blocks that two fuel blocks, in the form of dust settled on the internal equipment, remain in the installation at all times. Thus, it is assumed that 0.5 blocks are constantly present at each calculation point. Table 2 presents five scenarios for fuel placement at the service area and site.

Table 2. HEU fuel location in the installation of fuel dilution and immobilization.

Scenario	Option				
	Point 1	Point 2	Point 3	Point 4	Point 0 (Barrel)
1	2.5 block	0.5 block	0.5 block	0.5 block	-
2	1.5 block	1.5 block	0.5 block	0.5 block	-
3	0.5 block	1.5 block	1.5 block	0.5 block	-
4	0.5 block	0.5 block	0.5 block	2.5 block	-
5	0.5 block	0.5 block	0.5 block	0.5 block	2 blocks evenly distributed in the cement matrix

For dose field calculations in MCNP, the F4 tally was employed, followed by dose conversion from particle flux to effective dose. The conversion was performed using photon fluence-to-effective dose coefficients for air corresponding to the anterior–posterior irradiation geometry (AP, eng). The adopted effective dose conversion coefficients were taken from *On the Approval of Hygienic Standards for Radiation Safety Requirements* (02/08/2022).

Photon libraries *mcplib84,* included in MCNP6 and based on the ENDF/B-VI.8 nuclear data files, were used in the calculations. The selection of this library was motivated by its status as a standard and validated dataset, ensuring reproducibility and comparability of the simulation results.

Dose calculations were performed using the MCNP code (Monte Carlo method) [16, 17]. The models were constructed considering the area where

the equipment is located and the facility as a whole. For a conservative assessment, the installation itself was not explicitly modeled was not modeled, but radiation protection elements and building structures that have a significant impact on dose distribution were included in the calculated geometry.

During the modeling, a minimal number of objects was specified – only walls, blocks, and, in the second version of the project, radiation protection screens.

The radiation sources were specified as volume sources with constant energy characteristics. Five scenarios were considered, differing in the position of the sources and the configuration of the protective elements. For each scenario, the dose fields at the service area and the site as a whole were calculated. For each scenario, at least 10^{12} particles were simulated, which ensured a statistical error of no more than 10^{-3} near the sources.

The first version of the project assumed the absence of radiation-protective screens near the grinding unit equipment, and the absence of mobile radiation-protective screens when the barrel is full at the mixing unit and in the holding area.

4. Results and discussion

Nuclear safety at the fuel dilution and immobilization facility is ensured by limiting the number of fissile materials based on its isotopic composition. In accordance with [18], the designed building is not classified as a nuclear hazard area, since the total mass of ^{235}U present at any given time in the production facilities where nuclear materials are handled does not exceed 300 g.

To analyze the radiation situation within the facility, two volumetric dose fields were constructed: one at floor level “0” and the other at service area level “+3” (1.5 m above floor level). The calculation results made it possible to identify areas with increased radiation and formed the basis for the design of a multilayer radiation protection system located in the most vulnerable areas of radiation propagation.

The results are presented in figures 3a – 8a in the form of effective dose distribution maps constructed on the basis of dose function data [19] in planes corresponding to working levels. As a result of calculations for areas where work with HEU fuel is carried out, it was proposed to strengthen radiation protection measures and use the following to protect personnel:

- from the grinding equipment - RZM Abris-1, RZM Abris-2, RZM Abris-3 radiation protection mats;
- from the filled barrel at the mixing unit - ZS-311A mobile radiation protection screens;
- for filled barrels at the filled barrel storage area - ZS-321A mobile radiation protection screens.

The project also provides for the organization of dosimetric control. The effective dose distribution maps after strengthening protective measures are shown in Figures 3 and 8 with index b. In Figures 3-8, a darker shade of color corresponds to a higher dose value.

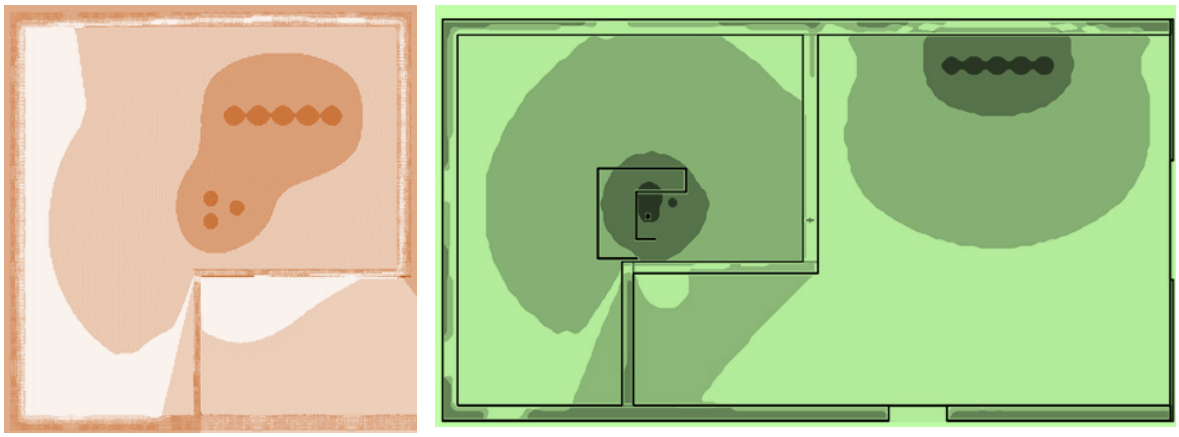

a) b)

Figure 3. Scenario 1: a) initial version; b) final version.

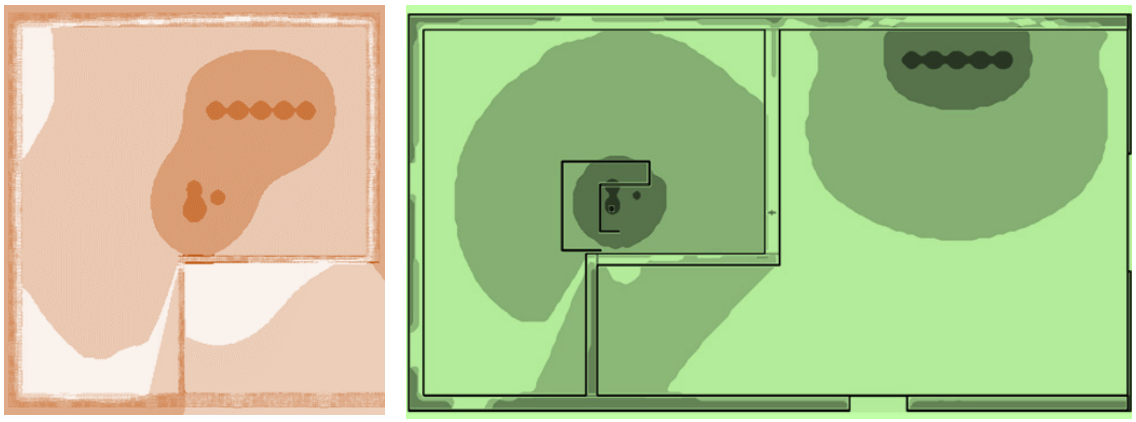

a) b)

Figure 4. Scenario 2: a) initial version; b) final version.

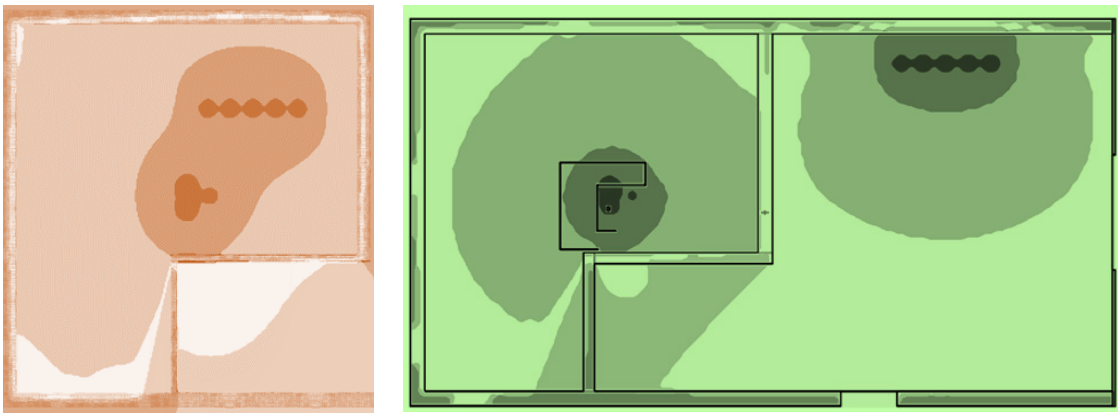

a) b)

Figure 5. Scenario 3: a) initial version; b) final version.

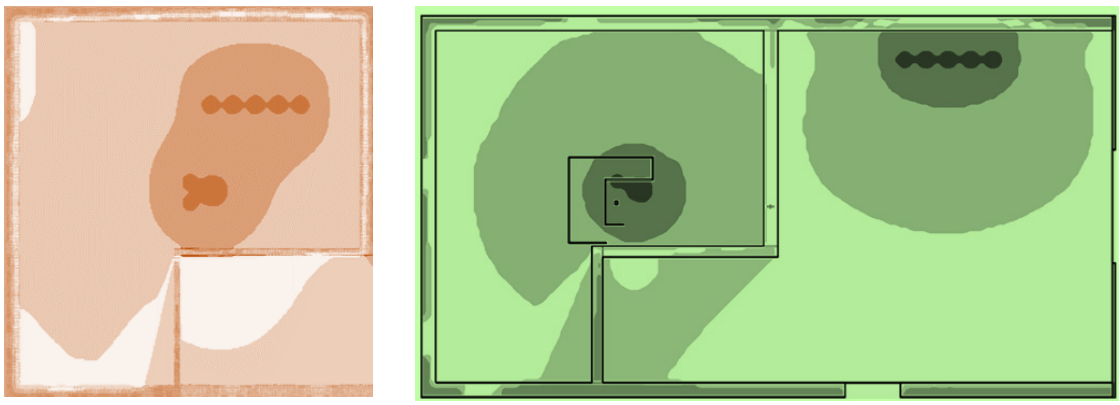

a) b)

Figure 6. Scenario 4: a) initial version; b) final version.

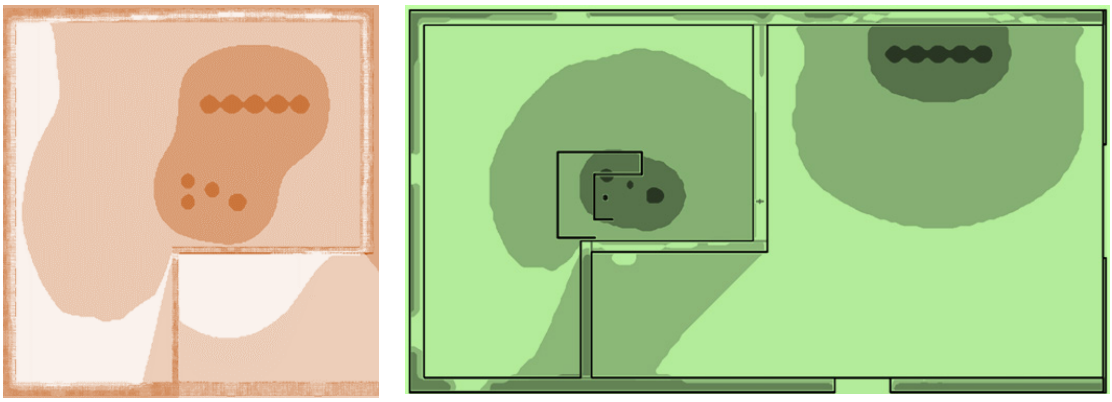

a) b)

Figure 7. Scenario 5: a) initial version; b) final version.

The initial version of the project provided the placement of a total of 15 barrels containing cemented LEU fuel. After the calculations, the number of barrels was reduced to 5, and they were relocated to a separate room with additional lead plate shielding. Figure 8 shows the arrangement of barrels with cemented LEU fuel in the initial design.

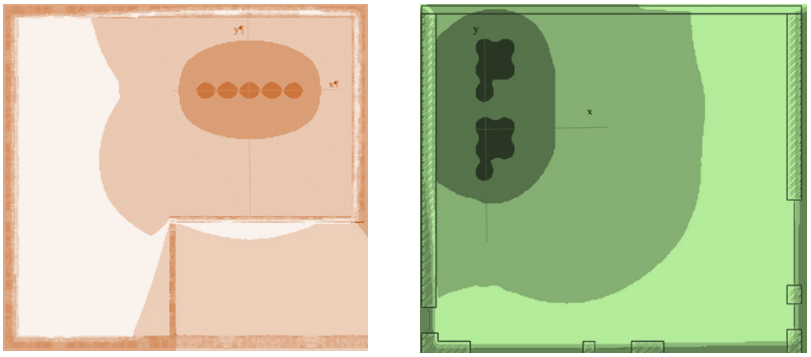

a) b)

Figure 8. Initial placement of barrels containing cemented LEU fuel: a) central hall; b) barrel storage room.

Table 3. Maximum MED value in key positions, μSv/h.

Distance, m	Scenarios for the simultaneous presence of spent nuclear fuel at points				
	1	2	3	4	5
Mixing barrel					
0,02 (close to the barrel)	7.14	8.62	10.10	18.49	122.00
0,5 (from the barrel)	4.55	5.38	6.20	9.69	17.64
1 (from the barrel)	3.28	3.78	4.27	6.07	7.64
2 (from the barrel)	2.04	2.26	2.47	3.15	3.01
3 (from the barrel)	1.48	1.60	1.71	2.06	1.79
4 (from the barrel)	0.81	0.81	0.81	0.81	0.81
Service area for the grinding plant					
0,02 (inside the loading chamber)	5137.56	3102.08	1056.90	1049.10	1038.55

Continuation of the table

Distance, m		Scenarios for the simultaneous presence of spent nuclear fuel at points				
		1	2	3	4	5
0,02 (close to the loading chamber)		194.94	134.55	65.73	56.26	48.73
0,5 (from the loading chamber)		31.16	27.91	21.47	16.51	11.95
1 (from the loading chamber)		13.26	13.16	11.97	8.90	6.29
2 (from the loading chamber)		4.73	4.95	4.90	3.90	2.65
Boundary of the site						
In front of the wall (along the perimeter of the room 32)		0.98	1.02	1.12	1.13	0.82
Behind the wall (along the perimeter of room 32)		0.0028	0.0032	0.004	0.0039	0.0025
Behind the leaded windows		0.66	1.20	1.46	1.99	1.13
Behind the partition wall		0.05	0.09	0.12	0.05	0.05
Center of the site						
Zone A		1041.69	1057.63	3106.78	**5136.69**	1045.22
Zone B	On the border of the first RPM	835.22	846.67	**2489.22**	854.43	835.90
	After the first RPM	407.83	417.94	**1210.07**	424.01	408.87
Zone C	Before the second RPM	11.05	13.40	**23.69**	19.99	11.34
	After the second RPM	9.67	11.83	**20.78**	17.72	9.91

* *RPM – On the border of the first radiation protection mats*

The first shielding layer significantly reduces the radiation level, by more than a factor of two compared to the initial values. The second layer further decreases the dose. However, its effectiveness is lower, which is attributed to the fact that irradiation in this region occurs from all directions rather than predominantly from a single side.

The initial design called for 15 drums of immobilized spent nuclear fuel to be placed in the reprocessing room. Following radiation safety calculations, the number of drums was reduced to five, and they were moved to a separate room with additional shielding in the form of lead plates.

The effective dose rate from a group of five drums of the mixer containing the spent nuclear fuel matrix solution was calculated, taking into account the installation of lead plate shields. The results are presented in Table 4.

Table 4. MED values near a group of 5 barrels.

Distance, m	MED value μSv/h
0.02 (close to the barrels)	151.06
0.02 (close to the RPM)	81.22
0.5 (from the RPM)	30.11
1 (from the RPM)	15.88
2 (from the RPM)	6.34

The maximum values of the MED along the OX axis are presented in the form of graphs in Figure 9. The numerical values of the MED are presented in logarithmic form at the site and service area.

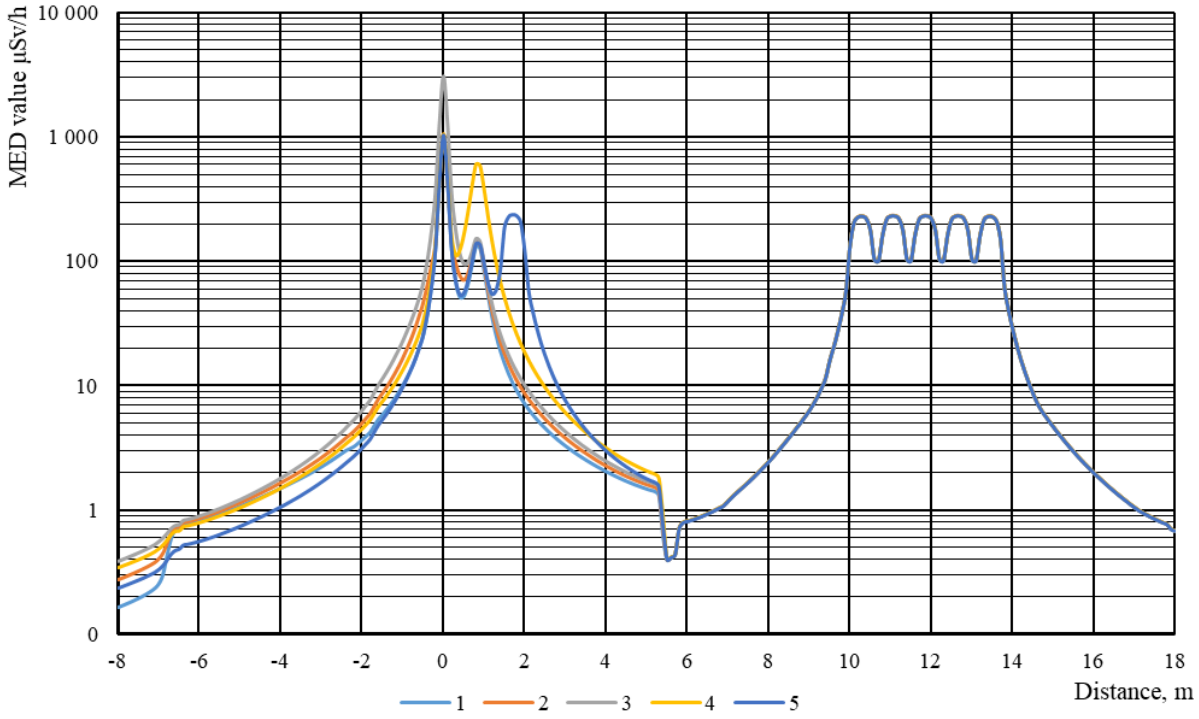

(a) facility

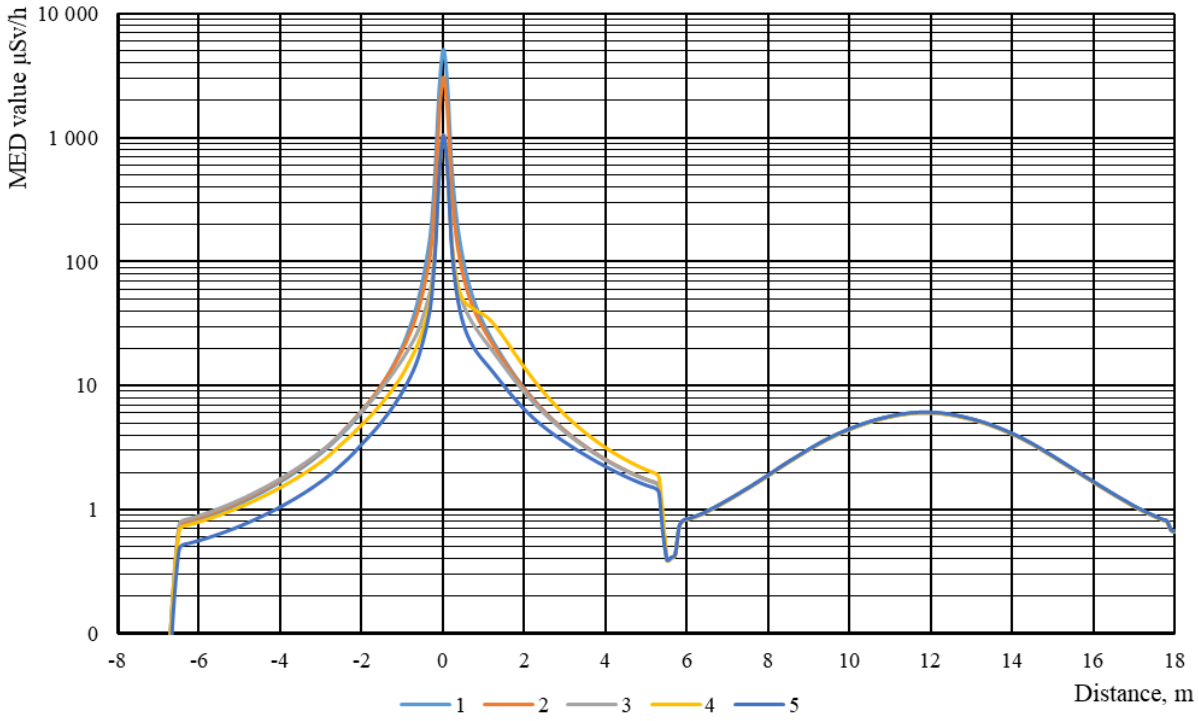

(b) separate room (service area)
1) Scenario №1; 2) Scenario № 2; 3) Scenario № 3; 4) Scenario №4; 5) Scenario №5

Figure 9. Maximum values MED.

Analysis of the causes of maximum dose generation

An analysis of the distribution of the maximum effective dose rate (EDR) shows that the nature of the radiation field is determined not only by the total activity of the sources, but primarily by their spatial location relative to the working areas and the effectiveness of their shielding.

The highest DER values are observed in the immediate vicinity of the grinding unit loading chamber and in the central part of the section, where the arrangement of the graphite blocks creates the most intense local gamma field. Thus, the maximum DER inside the loading chamber reaches 5137.56 μSv/h (scenario 1), while at a distance of 0.5–1 m, the level decreases by more than an order of magnitude. This indicates the dominant influence of the geometric factor and the law of radiation attenuation with distance, as well as the high sensitivity of dose loads to the local concentration of radioactive material.

A different mechanism for dose field generation is observed for the mixing drum. The maximum value (122 μSv/h) is achieved only in scenario 5 when located close to the barrel; however, at a distance of 1–2 meters, the difference between the scenarios decreases significantly. This indicates that the effect of fuel redistribution is localized, and the dose increase is due to the formation of a limited area of increased activity located in close proximity to the work position.

Additional analysis demonstrates the high effectiveness of engineered barriers. Despite significant radiation levels inside the central hall, the dose rate decreases by several orders of magnitude behind protective walls and shields. For example, behind the perimeter wall of the central hall, the values are only $(2.5–4.0)\times10^{-3}$ μSv/h, confirming the sufficient effectiveness of biological shielding and the localization of radiation exposure within the process zone.

Thus, the determining factor in the formation of maximum doses is the localized accumulation of the source in an unfavorable geometric configuration, and not solely the total mass or activity of the fuel. This confirms the need to analyze material redistribution scenarios as a key element of a conservative radiation safety assessment.

A comparison of the scenarios shows that the most conservative (worst-case) scenario depends on the control zone under consideration, as the maximum doses occur in different HEU configurations.

For the loading chamber of the milling facility, the worst-case scenario is Scenario 1, in which the DER inside the chamber reaches 5137.56 μSv/h, and close to the chamber, 194.94 μSv/h. This is likely due to the configuration in which the source is located as close as possible to the loading area, ensuring minimal geometric attenuation and the absence of intermediate shielding elements.

In the central part of the section, the highest values are observed for Scenario 4, where the DER in Zone A is 5136.69 μSv/h, significantly exceeding alternative configurations. Similarly, at the boundary of the first radiation shield, the maximum is realized in scenario 3 (2489.22 μSv/h), and after the first shield, also in scenario 3 (1210.07 μSv/h). This indicates a pronounced dependence of the dose field on the spatial redistribution of the source and the relative position of the protective shields.

Scenario 5 for the mixing barrel requires special attention, as it leads to a sharp local maximum (122 μSv/h) in the immediate vicinity of the equipment, despite the absence of extreme values at other control points. Therefore, this scenario should be considered a local worst-case scenario for equipment maintenance operations, although it is not the most radiation-intensive on a site-wide scale.

Overall, the results show that there is no single worst-case scenario for the entire facility. The most conservative estimate is achieved by analyzing a set of scenarios, since different fuel configurations lead to maxima in different critical zones. This approach is more physically sound than choosing a single limiting case and provides a conservative assessment of radiation safety with incomplete information on the fuel distribution.

The obtained results demonstrate a pronounced dependence of dose fields on the spatial distribution of radiation sources and the configuration of technological equipment. The highest dose rate values are observed near regions with localized material accumulation, confirming the key role of geometry and non-uniform radionuclide distribution in shaping the radiation environment. In this context, the total source activity appears to be a less decisive factor than its spatial localization.

The installation of additional radiation shielding reduced dose rates by approximately a factor of two in the most highly loaded working area (Zone B), whereas in the less loaded area (Zone C), the shielding effect was limited to approximately 10–15%. These values are consistent with findings reported in previously published studies, where Monte Carlo simulations demonstrated that local shielding configurations in spent nuclear fuel handling systems can reduce dose fields from several tens of percent up to multiple-fold decreases, depending on system geometry and shield placement [20].

An important factor determining radiation shielding effectiveness is the spatial configuration of sources and shielding structures. As reported in the literature, even when identical shielding materials are used, variations in their arrangement and relative geometry with respect to the source can result in significant redistribution of dose fields and changes in local dose maxima [21]. In this regard, the observed difference in shielding effectiveness among various facility zones can be explained by a combination of geometric factors, shielding by structural components, and heterogeneous source distribution.

It should be noted that the computational model is based on a number of conservative assumptions related to the simplified representation of equipment geometry and the absence of a detailed description of internal structural elements. In addition, the source distribution was defined through scenario-based assumptions due to insufficient initial information regarding the actual fuel configuration during reprocessing. Such an approach enables the derivation of upper-bound dose estimates sufficient for radiation safety justification and engineering decision-making.

Thus, the calculation results confirm the applicability of the scenario-based Monte Carlo approach for radiation environment assessment under conditions of incomplete input data and demonstrate the importance of accounting for geometric factors in the design of radiation protection systems.

The results obtained in this work show that the distribution of radioactive material within the process equipment has a significant influence on the radiation conditions at the facility. In particular, local accumulations of fuel may lead to substantially higher dose rates than those predicted from the total fuel inventory alone. This observation should be taken into account when developing shielding systems and selecting equipment layouts.

The performed calculations demonstrate that the use of several conservative fuel distribution scenarios makes it possible to assess radiation conditions under limited information about the actual location of radioactive materials. Such an approach can be applied at the design stage to identify potentially unfavorable operating conditions and to evaluate the effectiveness of proposed radiation protection measures.

The obtained results were used to support engineering decisions related to shielding design and personnel protection. The methodology developed in this study may also be useful for radiation safety assessments of other spent fuel handling and processing facilities where uncertainties in material distribution are present.

5. Conclusion

This section should summarize the main findings of the study in a concise and clear manner, directly reflecting the stated objectives. It should highlight the scientific novelty and key contributions without repeating detailed results. Authors should indicate the practical significance and potential applications of the work, as well as its limitations. Where appropriate, brief recommendations for future research may be included.

An assessment of the radiation situation during the dilution process of HEU graphite fuel from the IGR reactor was performed based on the layout of the grinding and immobilization equipment in the designed facility. Due to the lack of quantitative information on the fuel distribution at each point of the installation, five scenarios representing different simultaneous distributions of HEU fuel blocks were considered:

Scenario 2: The maximum number of HEU fuel blocks (1.5 blocks) is located in the feed hopper of the jaw crusher and in the electromagnetic dosing feeder. At the remaining two positions – the mill and the receiving hopper of the weigh feeder – 0.5 HEU fuel blocks are assumed at each location.

Scenario 3: The maximum number of HEU fuel blocks (1.5 blocks) is located in the mill and in the electromagnetic dosing feeder. At the other two positions – the loading throat of the jaw crusher and the receiving hopper of the weigh feeder – 0.5 HEU fuel blocks are assumed at each location.

Scenario 4: The maximum number of HEU fuel blocks (2.5 blocks) is located in the receiving hopper of the weigh feeder. At the remaining positions – the feed inlet of the jaw crusher, the mill, and the electromagnetic dosing feeder – 0.5 HEU fuel blocks are assumed at each location.

Scenario 5: The maximum number of HEU fuel blocks (2 blocks) is uniformly distributed within the cement matrix inside the barrel, while 0.5 HEU fuel blocks are assumed at each of the other positions. The research results were used to revise the facility design and justify the use of additional equipment to ensure normal operation of the technological process.

Based on the calculation results, the following modifications were implemented:

1. Three SRZ-6 lead glass windows (lead equivalent of 12 mm) were added for monitoring the technological process.

2. Radiation protection screens made of

- SRZ-Z lead glass (lead equivalent of 2.5 mm) were installed in the loading chamber;

- RZM Abris mats were added in the service area.

3.With regard to the barrels containing cemented LEU fuel:

- The number of barrels with spent nuclear fuel was reduced, and the barrels were relocated to a separate room.

- In the barrel storage room, 10 mm thick lead plate shields were installed on three sides of the barrel storage area.

In conclusion, this study extends beyond a conventional engineering assessment by proposing a systematic methodology for evaluating radiation fields under conditions of incomplete information on fuel distribution.

The work introduces a conservative, scenario-based modeling framework that enables the representation of uncertain fuel configurations in complex technological systems. It demonstrates that peak dose formation is governed primarily by localized fuel accumulation rather than by the total fuel mass, thereby refining the understanding of key radiological drivers. In addition, the study provides a quantitative assessment of shielding effectiveness, directly linking Monte Carlo simulation results with design optimization decisions.

Importantly, the proposed approach is transferable and can be applied to a wide range of spent nuclear fuel management systems. Overall, the methodology offers not only site-specific insights but also a generalized framework for radiation safety analysis in fuel processing facilities.

The facility design was subjected to expert review. It was concluded that the designed dilution facility complies with the safety requirements specified in the technical documentation, as well as with the applicable rules and regulations of the Republic of Kazakhstan governing the use of nuclear energy.

Funding

This research was funded by the Committee of Science of the Ministry of Science and Higher Education of the Republic of Kazakhstan (Grant No. BR24993104).

Conflicts of interest

The authors declare no conflict of interest.

Author contributions

“Conceptualization, I.P. and A.M.; Methodology, I.B.; Software, A.M.; Validation, A.M., I.P. and A.P.; Formal Analysis, V.P.; Investigation, Y.B.; Resources, Y.B.; Data Curation, I.B.; Writing – Original Draft Preparation, I.P.; Writing – Review & Editing, A.P.; Visualization, A.M.; Supervision, I.P.; Project Administration, V.P.; Funding Acquisition, Y.B.”

References

1. E. G. Batyrbekov, V. V. Baklanov, E. T. Koyanbayev, et al., “Method for dilution and immobilization of irradiated highly enriched uranium-graphite fuel by dry mixing and cementation,” Kazakhstan Patent No. 37124, Jan. 10, 2025.

2. International Atomic Energy Agency, “Safety of nuclear fuel reprocessing facilities: IAEA safety standards series No. SSG-42,” IAEA, Vienna, Austria, 2018.

3. OECD Nuclear Energy Agency, “Radiological impacts of spent nuclear fuel management options: A comparative study,” OECD Publishing, Paris, France, 2000. https://doi.org/10.1787/9789264182028-en

4. C. Wei, S. Xu, S. Zou, et al., “Risk analysis and evaluation of nuclear security radiation events in spent fuel reprocessing plants,” *Sustainability*, vol. 15, no. 1, Art. no. 781, 2023. https://doi.org/10.3390/su15010781

5. A. S. Kussainov, P. Arnqvist, N. Pya Arnqvist, et al., “3He neutron detector with Android smartphone integration,” *Physical Sciences and Technology*, vol. 12, no. 3–4, pp. 80–88, 2025. https://doi.org/10.26577/phst20251228

6. Y. Zaripova, A. Yushkov, N. Amangeldiyeva, et al., “Monitoring the distribution of radon isotopes and their decay products in Almaty,” *Physical Sciences and Technology*, vol. 11, no. 3–4, pp. 4–13, 2024. https://doi.org/10.26577/phst2024v11i2b01

7. A. Temirzhanov, B. Sadykov, T. Zholdybayev, et al., “STM32F407 microcontroller based multichannel analyzer for spectroscopy,” *Physical Sciences and Technology,* vol. 11, no. 3–4, pp. 21–28, 2024. https://doi.org/10.26577/phst2024v11i2b03

8. M. Sun, Q. Li, C. Wei, et al., “Research on radiation monitoring strategy for spent fuel reprocessing plant based on coordination of nuclear security risk and facility importance evaluation,” *Sustainability*, vol. 16, no. 4, Art. no. 1495, 2024. https://doi.org/10.3390/su16041495

9. A. Malgazhdarova, M. Kazankapova, B. Yermagambet, et al., “Synthesis and characterization of carbon nanomaterials obtained using electric discharge,” *Physical Sciences and Technology,* vol. 12, no. 1–2, pp. 68–83, 2025. https://doi.org/10.26577/phst20251217

10. Y. Yerlanuly, “Investigation of the effect of short-pulsed ion irradiation on the stability of carbon nanowalls,” *Recent Contributions to Physics*, vol. 96, no. 1, pp. 67–76, 2025. https://doi.org/10.26577/RCPh96120268

11. E. V. Devkina, I. R. Suslov, and V. A. Chernov, “Carrying out calculations of radiation safety during unloading and disassembly of cores of spent removable parts of reactors with liquid metal coolant of submarines,” (in Russian), *Izvestiya vuzov. Yadernaya Energetika,*, no. 2, pp. 73–80, 2022. https://doi.org/10.26583/npe.2022.2.07

12. I. L. Tazhibayeva, A. K. Klepikov, O. G. Romanenko, et al., "Regulatory aspects and practice of radioactive waste management in the Republic of Kazakhstan," *At. Energy*, vol. 137, pp. 121–128, 2024. https://doi.org/10.1007/s10512-025-01185-0

13. O. S. Bukina, Y. Yu. Baklanova, K. K. Samarkhanova, et al., "Development of the technological process for the IGR reactor's highly-enriched irradiated uranium-graphite fuel immobilization," *Journal of Nuclear Materials*, vol. 610, Art. no. 155801, 2025.

14. M. K. Skakov, V. V. Baklanov, E. T. Koyanbayev, et al., "Composition of the matrix for immobilization of spent uranium-graphite fuel," *Application for Patent of the Republic of Kazakhstan* No. 2025/0239.1, Mar. 13, 2025.

15. O. S. Bukina, Y. Yu. Baklanova, M. N. Azbergenov, et al., "Methodology of selecting cement matrix composition for immobilization of irradiated uranium-graphite fuel" (in Russian), *NNC RK Bulletin*, vol. 100, no. 4, pp. 43–53, 2024. https://doi.org/10.52676/1729-7885-2024-4-43-53

16. R. S. Detwiler, R. J. McConn Jr., T. F. Grimes, et al., "Compendium of material composition data for radiation transport modeling," Pacific Northwest National Laboratory, Technical Report PNNL-15870, Rev. 2, Richland, WA, USA, 2021.

17. J. A. Kulesza, T. R. Adams, J. C. Armstrong, et al., "MCNP® Code Version 6.3.1 Theory & User Manual," Los Alamos National Laboratory, Technical Report LA-UR-24-24602, Rev. 1, Los Alamos, NM, USA, 2024.

18. "Nuclear safety rules for nuclear fuel cycle facilities: NP-063-05," Resolution of the Federal service for environmental, technological and nuclear supervision, Moscow, Russia, 2006 (adopted Dec. 20, 2005).

19. "Sanitary and epidemiological requirements for ensuring radiation safety," Hygienic Standards, approved by order of the Minister of National Economy of the Republic of Kazakhstan, No. 155, Feb. 27, 2015.

20. N. Xoubi, "Neutrons and gamma-ray dose calculations in subcritical reactor facility using MCNP," *Atoms*, vol. 4, no. 3, Art. no. 20, 2016

21. B. Gultekin, E. Ozturk, T.R. Torun. "Monte Carlo analysis of radiation shielding and damage in multi-layer HDPE shields"*Positive Science International*, no. 1(2), pp. 57–73, 2025. https://izlik.org/JA27UB44WM

Information about the authors:

Irina Prozorova (corresponding author) – MS in Physics, Head of the laboratory of neutronic physics at the Institute of Atomic Energy of the National Nuclear Center of the Republic of Kazakhstan (Kurchatov, Kazakhstan, e-mail: Prozorova@nnc.kz).

Askhat Mukhamediyev – 2nd category engineer of the laboratory of neutronic physics at the Institute of Atomic Energy of the National Nuclear Center of the Republic of Kazakhstan (Kurchatov, Kazakhstan, e-mail: Mukhamediyev @nnc.kz);

Inga Bogomolova – Head of the design bureau at the Institute of Atomic Energy of the National Nuclear Center of the Republic of Kazakhstan (Kurchatov, Kazakhstan, e-mail: Dep402@nnc.kz).

Andrii Prozorov – Head of the group of the laboratory of neutronic physics at the Institute of Atomic Energy of the National Nuclear Center of the Republic of Kazakhstan (Kurchatov, Kazakhstan, e-mail: Paa@nnc.kz).

Yuriy Popov – Deputy head of the laboratory of neutronic physics at the Institute of Atomic Energy of the National Nuclear Center of the Republic of Kazakhstan (Kurchatov, Kazakhstan, e-mail: Popov@nnc.kz).

Yuliya Baklanova – MS in Physics, Head of the materials testing department at the Institute of Atomic Energy of the National Nuclear Center of the Republic of Kazakhstan (Kurchatov, Kazakhstan, e-mail: Basalai@nnc.kz).

Vitaliy Pospelov – Head of the nuclear safety and nuclear energy development at the Institute of Atomic Energy of the National Nuclear Center of the Republic of Kazakhstan (Kurchatov, Kazakhstan, e-mail: Pospelov@nnc.kz).

IRSTI 29.33.51 https://doi.org/10.26577/phst20261312

Nonlinear ultrafast laser processing of diamond surfaces for precision microfabrication

Y. White[1,2,*]

[1]University of Tennessee Space Institute, Tullahoma, USA
[2]Georgia Southern University, Swainsboro, USA
*e-mail: ywhite@georgiasouthern.edu

(*Received March 9, 2026; received in revised form April 8, 2026; accepted April 29, 2026)*

Ultrafast femtosecond laser processing provides a versatile platform for precision micro- and nanoscale modification of wide-bandgap materials such as diamond. In this work, the formation of microscale and submicron surface features on high-pressure high-temperature (HPHT) single-crystal diamond and chemical vapor deposition (CVD) diamond films is investigated using high-repetition-rate femtosecond laser pulses. Systematic experiments examined the influence of laser fluence, pulse energy, and spatial pulse overlap on ablation morphology, feature dimensions, and material response. Arrays of craters, microchannels, and reservoir structures were fabricated through localized ablation, demonstrating the capability of femtosecond laser processing for flexible surface microstructuring of diamond. Differences in ablation behavior between HPHT single-crystal and polycrystalline CVD diamond were analyzed in terms of structural and electronic properties. The depth of laser-machined features was determined using an acetate replication technique followed by scanning electron microscopy. Results show a strong dependence of feature geometry and ablation efficiency on processing conditions, with single-crystal diamond exhibiting deeper ablation and sharper features at comparable fluence. These findings highlight the role of nonlinear absorption and defect-mediated carrier dynamics in ultrafast laser–diamond interactions and suggest applications in diamond-based microfluidic devices, field-emission structures, and advanced electronic and photonic systems.

Keywords: femtosecond laser, laser ablation, diamond micromachining, laser nanomachining, ultrafast laser processing.

1. Introduction

Femtosecond laser micro- and nanomachining has emerged as a powerful technique for precision material processing due to its ability to deposit energy on timescales shorter than thermal diffusion within the lattice. As a result, energy confinement within the focal volume enables highly localized structural modification and material removal with minimal heat-affected zones and excellent spatial precision [1-4]. These characteristics make ultrafast laser processing particularly attractive for the fabrication of microscale and nanoscale structures in materials that are otherwise difficult to machine using conventional techniques. Recent studies have also investigated nanostructured materials and their optical properties in related contexts [5]. Wide range of materials including silicon nanostructures and carbon-based coating have been explored for technological applications [6].

Laser–matter interaction in wide-bandgap materials under ultrafast excitation is governed by strong-field ionization processes including multiphoton ionization, tunneling ionization described by Keldysh theory, and avalanche ionization driven by impact excitation [7-9]. Under sufficiently high intensities, these processes generate a dense electron plasma within the focal volume. Subsequent energy transfer from the excited electron system to the lattice can lead to a variety of material removal mechanisms, including Coulomb explosion, phase explosion, and rapid melting followed by vaporization [10, 4]. The relative contribution of these mechanisms depends on laser parameters such as pulse duration, fluence, and repetition rate, as well as on the electronic and structural properties of the material.

Diamond is a particularly compelling platform for ultrafast laser processing due to its exceptional physical and electronic properties. The growth and structural properties of diamond films produced by

CVD methods have been widely investigated [11]. Diamond exhibits the highest known thermal conductivity among bulk materials, extreme mechanical hardness, chemical inertness, and a wide electronic bandgap of approximately 5.5 eV [12]. These properties make diamond attractive for a wide range of advanced technologies, including high-power electronics, quantum photonics, radiation detectors, field-emission devices, and microfluidic systems [13-17].

In this work, we investigate femtosecond laser microstructuring of high-pressure high-temperature (HPHT) single-crystal diamond and plasma-enhanced chemical vapor deposition (PE-CVD) diamond films using high-repetition-rate femtosecond laser pulses. The influence of laser pulse energy, spatial overlap, and material structure on ablation morphology and feature formation is examined. Particular attention is given to the role of nonlinear absorption, incubation effects, and defect-mediated carrier dynamics in determining ablation efficiency and feature geometry.

2. Materials and methods

All surface features in this study were fabricated using a customized femtosecond laser ablation system. The system consisted of a diode-pumped, frequency-doubled Neodymium-doped Yttrium Orthovanadate ($Nd:YVO_4$) pump laser operating at 532 nm (Verdi V18, Coherent, Inc.), which pumped a Ti:Sapphire laser oscillator (Tsunami, Spectra-Physics, Inc.) and a regenerative amplifier (RegA 9000, Coherent, Inc.). The system produced ultrafast laser pulses at a central wavelength of 800 nm with a pulse duration of approximately 200 fs, pulse energies up to 4 μJ, and repetition rates as high as 250 kHz. The repetition rates could be controlled by an external transistor-transistor logic (TTL) pulse generator, directly connected to the amplifier.

The ablation time during experiments was controlled using an externally triggered mechanical shutter. Laser power was controlled by a neutral density filter placed into the beam path. The laser beam was focused onto the front surface of the samples using microscope objectives with numerical apertures (NA) of 0.85 and 0.90. Under these focusing conditions, the resulting focal spot diameter was approximately 0.55 μm. The objective was mounted on a stage with adjustable Z-positioning to allow precise focusing on the sample surface. The optical delivery system also enabled direct observation of the ablation region through a 10× eyepiece and a high-resolution digital camera.

Precise sample positioning was achieved using a piezoelectric nanopositioning stage (Mad City Labs, Inc.) that provided nanometer-scale resolution with a travel range of 200 μm in the X–Y directions and 100 μm in the Z direction. This stage was mounted on a larger-range X–Y microstage (McBain, Inc. precision stages equipped with Compumotor, Inc. stepper motors and National Instruments motor drivers). During the ablation process, the microstage remained fixed while the piezoelectric stage translated the sample at a scanning speed of approximately 11 μm/s to generate the desired micropatterns. Both positioning stages, as well as the mechanical shutter, were controlled through LabVIEW™ software. In addition to enabling the fabrication of individual features on a variety of materials, this configuration allowed precise alignment and placement of microstructures through software-controlled positioning with nanometer-scale accuracy. A He:Ne laser was introduced to the system for precise positioning purposes [18].

Figure 1 shows the experimental setup used for femtosecond laser ablation of diamond film surfaces [19]. Several corrective lenses were placed in the beam path to compensate for beam divergence and to match the beam size with the entrance aperture of the objective lens. The placement and optical configuration of these lenses were optimized using Zemax software in order to minimize spherical aberrations and preserve beam quality at the focus. This optical arrangement enabled high precision during laser ablation process and provided a flexible platform for performing parametric studies of laser ablation and micromachining across a broad range of operating conditions.

All experiments were performed in a controlled environment of a Class-1000 Clean Room. The samples were cleaned with acetone, methanol, and deionized water in an ultrasonic bath prior to laser ablation.

While the width of features, such as small holes, machined by femtosecond laser can be estimated from the numerical aperture of the focusing objective lens, the depth cannot be directly measured during laser machining. After ablation, sample surfaces were cleaned again, and replicated with cellulose-based acetate films. The acetate replication technique provides a cost-efficient, reliable, and nondestructive method for depth estimation. However, its fidelity depends on the aspect ratio of the replicated features. The reported depth values for high-aspect-ratio features should be considered as approximate lower bounds. Extended acetate film application and drying times were used to maximize filling, and the consistency of replica morphology in SEM images

supports adequate, though potentially not complete, penetration of the acetate material into these features This technique and the validity of depth estimation are described in detail in our previous work [18]. The replicas and diamond samples were then sputter-coated with carbon, platinum, or gold for conductivity and imaged with the Scanning Electron Microscope (SEM).

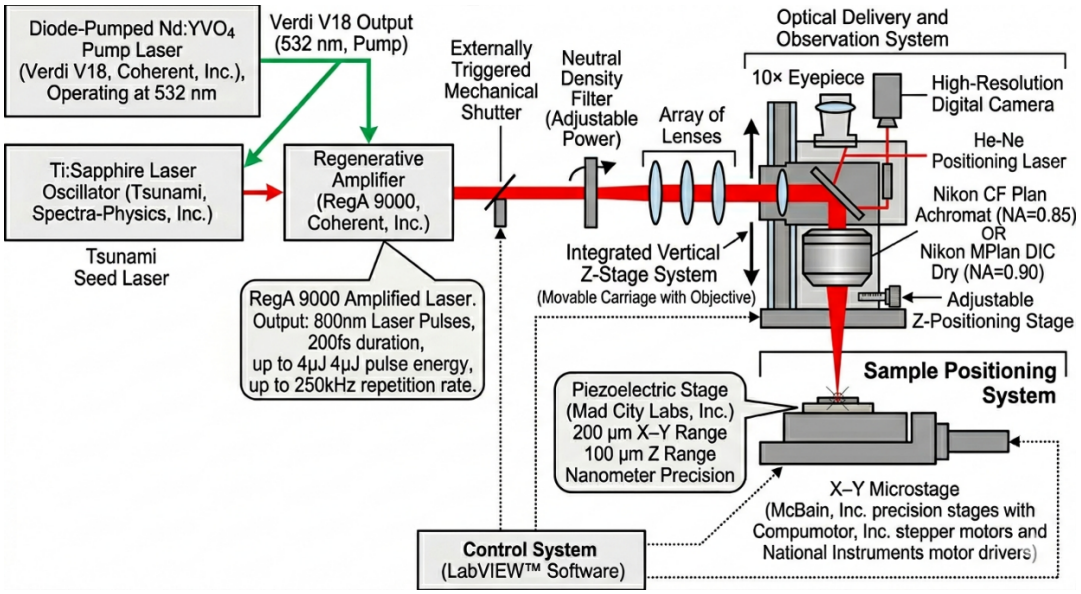

Figure 1. Schematic diagram of experimental setup for laser micro- and nanomachining.

In our experiments, we investigated two types of diamond materials: single-crystal diamond synthesized by the high-pressure high-temperature (HPHT) process, and polycrystalline diamond films produced by plasma-enhanced chemical vapor deposition (PECVD) [20, 21], a technique widely used for the fabrication of diamond-based and diamond-like carbon films for technological applications [22]. Ideal single-crystal diamond is largely transparent at the laser wavelength of 800 nm due to its wide electronic bandgap (~5.5 eV). Consequently, energy deposition under ultrafast irradiation occurs primarily through nonlinear absorption mechanisms such as multiphoton ionization and avalanche ionization [23]. In contrast, polycrystalline CVD diamond films often contain grain boundaries, defect states, and regions of sp^2-bonded carbon, which introduce sub-bandgap electronic states that can enhance linear and defect-assisted absorption at near-infrared wavelengths. These structural differences significantly influence carrier generation dynamics and energy coupling during femtosecond laser irradiation, thereby affecting the resulting ablation morphology and material removal efficiency [24-26].

At a repetition rate of 250 kHz, the interval between pulses is 4 μs. With the pulse width of 200 fs, the pulses are well-separated. Given the high thermal diffusivity of single-crystal diamond (~1200 mm^2/s), the thermal diffusion length within this interval far exceeds the sub-micron focal spot, ensuring that heat dissipates between successive pulses and that ablation proceeds in a predominantly non-thermal regime. In polycrystalline CVD diamond, grain boundaries and sp^2-bonded intergranular phases reduce the effective thermal conductivity; however, the thermal diffusion length during the 4 μs interpulse interval still substantially exceeds the focal volume dimensions. The clean feature morphology and minimal heat-affected zones observed in our SEM images (Figures 5, 6, 7 below) confirm that non-thermal ablation conditions are maintained for both materials at this repetition rate, consistent with recent studies of femtosecond laser structuring of diamond at comparable repetition rates [27, 28].

Although sp^2-bonded intergranular phases in CVD diamond enhance sub-bandgap optical absorption, these regions simultaneously function as carrier recombination centers and electron scattering sites that attenuate avalanche ionization buildup, thereby reducing the effective ablation efficiency relative to single-crystal diamond at comparable laser fluence [29, 30].

3. Results and discussion

In this work, diamond surface micropatterning is performed by localized material removal through femtosecond laser ablation at a precisely defined position on the surface. When an ultrafast pulse is tightly focused on the target material, the extremely high peak intensity within the focal volume initiates nonlinear absorption processes, including multiphoton ionization and avalanche ionization. These processes generate a population of free electrons that rapidly evolve into a dense microplasma near the surface. The subsequent expansion of this plasma results in the ejection of material from a highly confined region of the target. Because the energy deposition occurs on a timescale shorter than thermal diffusion in the lattice, the interaction proceeds largely in a nonthermal regime, often referred to as "cold ablation," which enables the fabrication of micron- and submicron-scale structures with minimal heat-affected zones and high edge fidelity [31-33].

A single ablation event typically produces an isolated crater or hole at the location of the laser focus. By translating the sample relative to the focal spot or by sequentially triggering pulses at predefined coordinates, multiple ablation sites can be arranged in desired patterns or arrays. Such arrays provide a convenient platform for evaluating the spatial precision and repeatability of the ablation process, as well as parametric studies of feature morphology, laser pulse energy, fluence, and repetition rate.

Figure 2(a) shows an array of ablation sites fabricated on the surface of a chemical vapor deposition (CVD) diamond film using a laser pulse energy of 0.8 μJ. Under these conditions, the resulting craters exhibit diameters of approximately 750 nm with a center-to-center spacing of about 3.5 μm. Increasing the pulse energy to 1.2 μJ produces the array shown in Figure 2(b). At this higher energy, the ablation sites expand significantly; to accommodate the expansion, the approximate spacing between adjacent features was kept at 4.5 μm. The resulting craters showed diameters of approximately approaching 2 μm. Surface structure between craters is notably different from the original, indicating potential graphitization.

The altered surface texture between craters observed in Figure 2(b) is attributed to partial sp^3-to-sp^2 phase transformation, commonly referred to as laser-induced graphitization. Recent studies indicate that under femtosecond irradiation near the ablation threshold, this conversion is confined to a nanoscale surface layer-typically tens to approximately 100 nm in depth—and retains predominantly sp^3 character with localized sp^2 domains [34, 35]. At the fluences employed in the present work, the graphitized layer is expected to be superficial and should not significantly affect the mechanical or chemical properties relevant to microfluidic or field-emission applications. However, for electronic or photonic applications that depend on pristine diamond surface properties, post-processing steps such as oxidative etching may be employed to selectively remove the sp^2 phase without damaging the underlying sp^3 lattice [36].

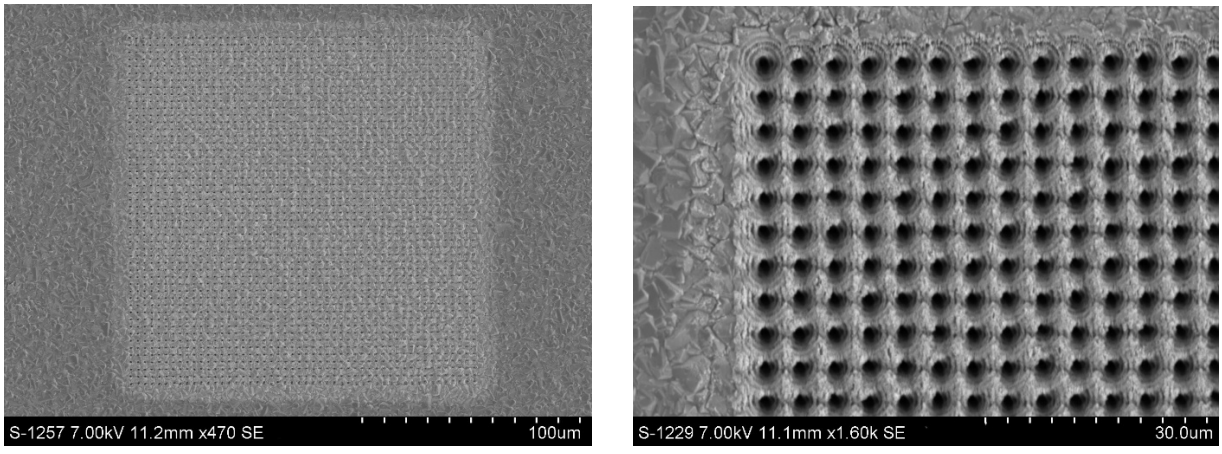

(a) (b)

Figure 2. SEM scans of laser-machined CVD diamond surface at laser pulse repetition rate of 250 kHz: (a) Laser Pulse Energy = 0.8 μJ; (b) Laser Pulse Energy = 1.2 μJ.

We next examine the effects of crater spacing on CVD diamond surface. In Figure 3, two patterns were machined a laser pulse energy of 1.2 μJ. The spacing between consecutive sites is approximately 3 μm for Figure 3(a) and 2.5 μm for Figure 3(b). The resulting patterns indicate that higher laser pulse energies and smaller hole spacing lead to feature overlap and form a continuous pattern.

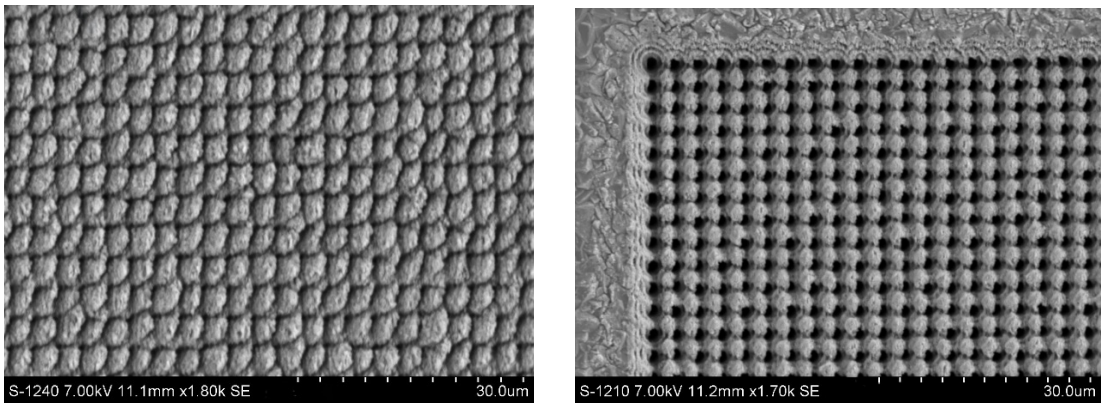

(a) (b)

Figure 3. SEM scans of laser-machined CVD diamond surface at laser pulse repetition rate of 250 kHz and Laser Pulse Energy of 1.2 μJ: (a) Pattern spacing = 3 μm; (b) Pattern spacing = 2.5 μm.

The observed increase in feature diameter and overlap with increasing pulse energy reflects the strong dependence of femtosecond laser ablation on deposited fluence. As the laser fluence exceeds the material ablation threshold, the radial region within the focal spot where the deposited energy surpasses the threshold expands, resulting in a corresponding increase in crater diameter. This behavior is consistent with the logarithmic scaling of ablation diameter with laser fluence observed in ultrafast micromachining of dielectric materials [2, 4]. In addition, higher pulse energies generate denser plasma within the focal volume, leading to enhanced energy coupling and increased material removal. These effects collectively contribute to the expansion and eventual overlap of adjacent ablation sites, enabling the formation of continuous surface structures.

Following the laser patterning, the surface features were replicated to investigate the depth and structure of machined features. Figure 4 shows an array of nanowires replicated from a corresponding array of craters ablated on CVD diamond surface. The original array was produced using a laser pulse energy of 2.2 μJ with a spatial separation of 10 μm between ablation sites. The SEM images of replicated arrays were taken at 45 degree tilt for a better estimate of feature depth. The height of acetate replica nanowires indicates that the craters in the original array reached a depth of approximately 6 μm.

The features of desired configurations can be fabricated by translating the sample through the focused laser beam incident on the surface. As mentioned above, arrays of holes or continuous patterns are produced through the controlled overlap of individual ablation sites. It is also possible to create other types of surface such as microchannels or reservoir. Channels are formed by delivering multiple consecutive laser pulses along a single path, resulting in continuous, well-defined structures. Figure 5 shows a microchannel fabricated on the surface of the CVD diamond at laser pulse energy of 0.8 μJ (a), and 2.2 μJ (b). The edges of the channel are well-defined, with minimal debris, and its width ranges between 1-2 μm.

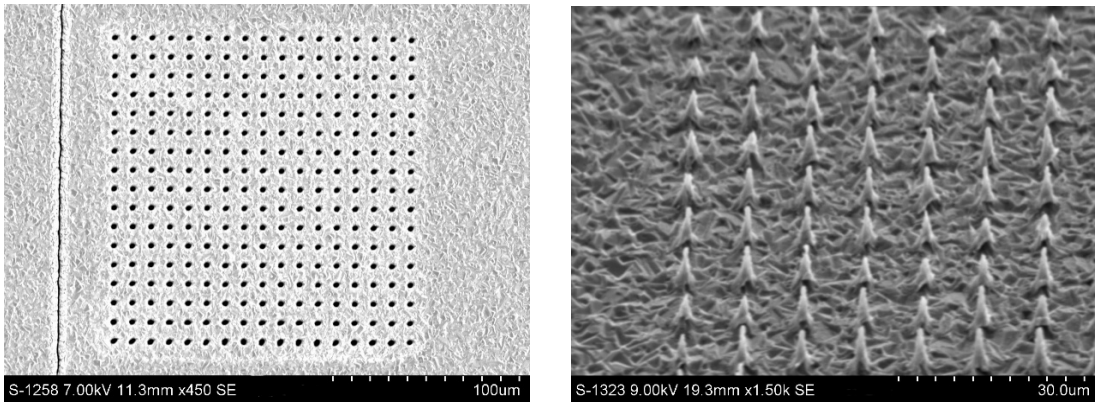

(a) (b)

Figure 4. CVD Diamond. (a) Surface machined at E=2.2 μJ, and (b) Replica of the surface (45 degree tilt).

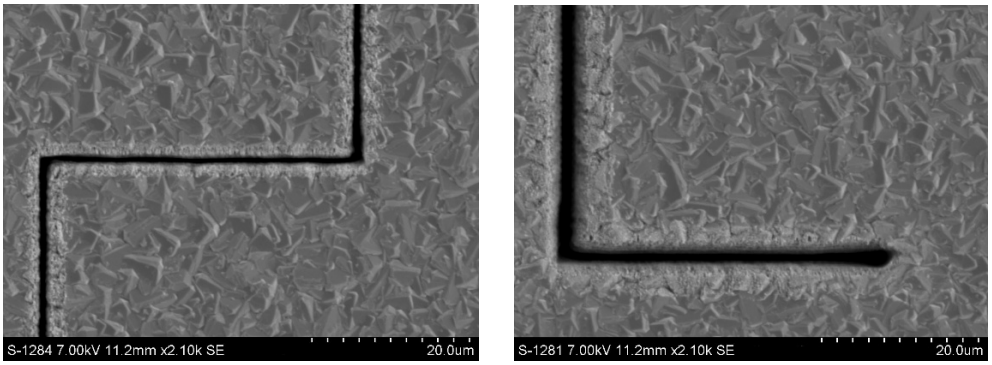

(a) (b)

Figure 5. Microchannel machined on CVD diamond surface at (a) E=0.8 μJ, and (b) E=2.2 μJ, with pulse repetition rate of 250 kHz.

Figure 6 shows a pattern of multiple vertical lines ablated on CVD diamond with a horizontal line spacing of approximately 4 μm and a feature width ranging from 0.8 to 1 μm. These structures were fabricated using a laser pulse energy of 1.8 μJ.

The observed feature widths of 0.8–1 μm exceed the diffraction-limited focal spot diameter of approximately 0.55 μm. This broadening is attributable to the extreme spatial pulse overlap achieved at the scanning speed of 11 μm/s and repetition rate of 250 kHz, corresponding to a pulse-to-pulse displacement of approximately 0.044 nm and an effective pulse overlap count on the order of ~12,500 pulses per spot diameter. Under these conditions, incubation effects progressively reduce the effective ablation threshold, allowing material removal to occur across a wider region of the Gaussian beam profile where the fluence exceeds the modified threshold. Additionally, the above-threshold area of the beam naturally extends beyond the $1/e^2$ spot radius at the pulse energy of 1.8 μJ employed. The combined effects of incubation-enhanced peripheral ablation and above-threshold fluence widening are consistent with established models of multipulse femtosecond laser machining [37, 38].

The variation of laser processing parameters allows fabrication of a wide range of structural designs with specific properties on the surface or in the bulk of a diamond. Careful selection of laser machining parameters produces well-defined microstructures, and is directed towards micromachining of fully-integrated assemblies, such as diamond emitters and fluidic devices. Figure 7 shows a reservoir structure on the CVD diamond surface. The reservoir was formed by translating the sample through the focused laser beam in a pre-programmed square pattern at a laser pulse energy of 3 μJ. The length of the sides of the feature is about 40 μm and the depth is approximately 8.8 μm.

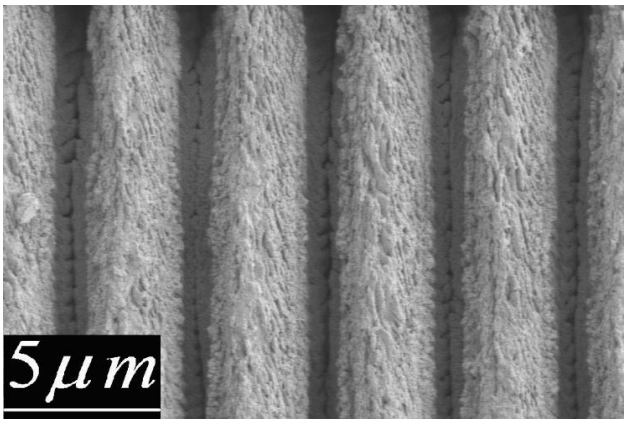

Figure 6. An array of microchannels on CVD diamond surface machined at E=1.8 μJ.

The formation of surface features on single-crystal diamond is examined next. Figure 8 shows an array of craters machined at the laser pulse energy of 0.8 μJ and repetition rate of 250 kHz on the surface of single-crystal diamond, and its acetate surface replica with the length of nanowires of approximately 5-7. This length is achieved at considerable lower laser pulse energies than in CVD diamond (Fig. 4).

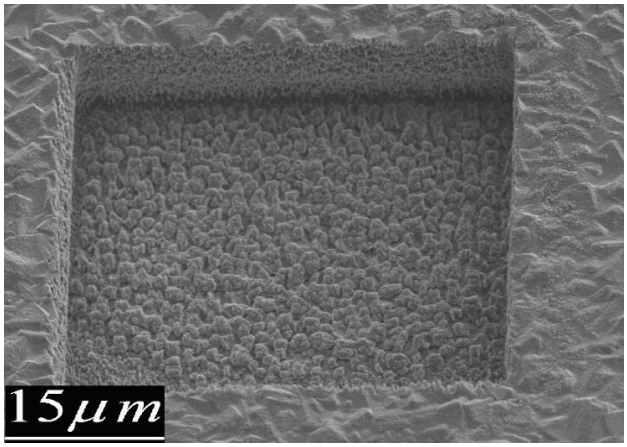

Figure 7. A reservoir structure on CVD diamond surface machined at E=3 μJ.

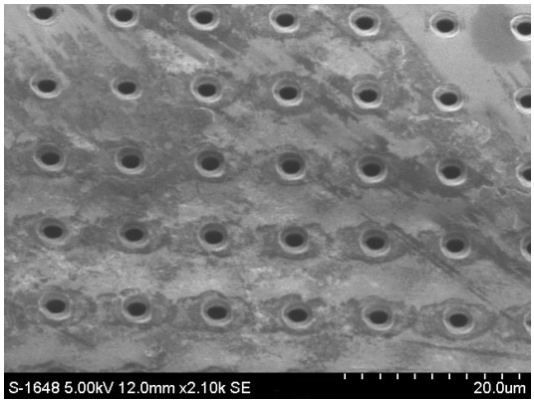

(a)

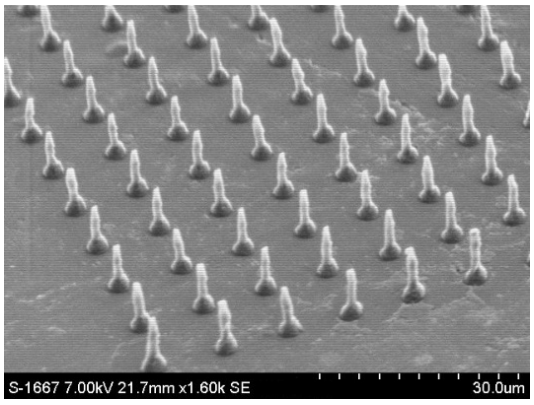

(b)

Figure 8. Single-Crystal Diamond surface. (a) Machined with incident energy of 0.8 μJ per pulse and repetition rate of 250 kHz, and (b) Array of nanowires from surface replication by acetate film.

Various surface features can be machined by translating a nanostage with a mounted sample through the focused laser beam. With the goal of device fabrication, we generated a curved pattern with sharp edges. The structure shown in Figure 9(a) was machined on HPHT single crystal diamond at laser pulse energy of 0.8 μJ, producing features with an estimated depth of 16-19 μm. This is considerably higher than the depth of features of 12-13 μm, observed for CVD diamond at similar laser pulse energies (Fig. 9(b)). The resulting structure exhibits well-defined morphology and shows that the process enables fabrication of curved features with high repeatability and spatial precision. SEM images were taken at 45-degree tilt for depth estimation.

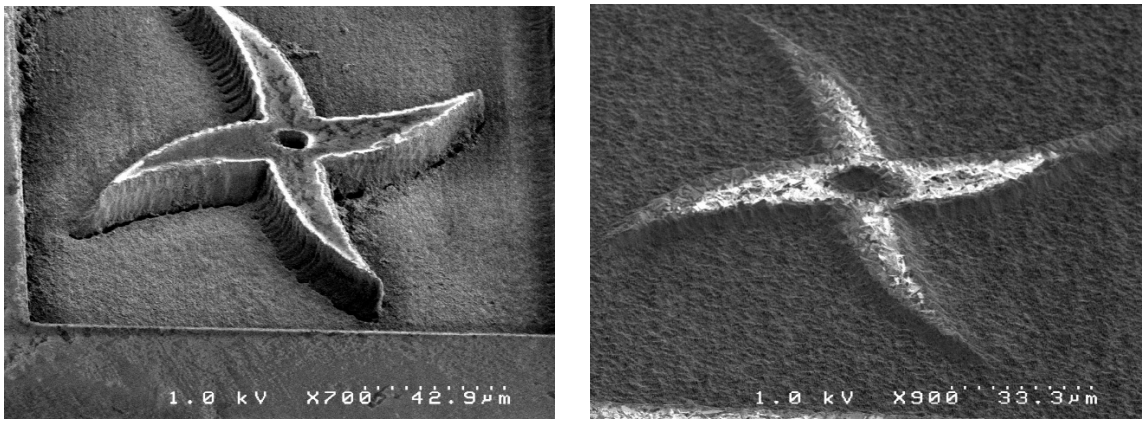

(a) (b)

Figure 9. A curved structure machined on the diamond surface at E= 0.8 µJ.
(a) HPHT Single Crystal Diamond, and (b) CVD Diamond.

The plasma dynamics underlying femtosecond laser ablation of wide-bandgap materials proceed through several distinct stages. During the laser pulse, nonlinear photoionization–including multiphoton ionization and tunneling ionization–generates seed free electrons in the conduction band. These electrons gain kinetic energy from the laser field through inverse bremsstrahlung absorption and, once they exceed the ionization energy of the lattice, trigger avalanche ionization that exponentially multiplies the free electron density. Within hundreds of femtoseconds, this process produces a dense, transient electron plasma confined to the focal volume. Following the termination of the laser pulse, the electron plasma transfers its energy to the lattice on a picosecond timescale through electron-phonon coupling. At fluences above the ablation threshold, two primary material removal mechanisms may contribute: Coulomb explosion, in which rapid electron ejection leaves behind a positively charged surface layer that undergoes electrostatic disintegration, and phase explosion, in which rapid lattice superheating drives explosive decomposition of the material into a mixture of vapor and nanoscale fragments [39, 40]. The subsequent expansion of the ablation plume carries ejected material away from the surface, leaving behind a well-defined crater. In single-crystal diamond, the highly ordered sp^3 lattice supports efficient avalanche ionization and dense plasma buildup, leading to strong energy confinement and rapid, directional plume expansion. In polycrystalline CVD diamond, grain boundaries and sp^2-rich intergranular regions act as carrier recombination centers and scattering sites, attenuating the buildup of the electron plasma and reducing the efficiency of energy coupling into the lattice. This results in lower ablation rates and less sharply defined features compared to single-crystal material [29, 41].

The features produced on single-crystal diamond are consistently deeper and exhibit sharper morphology than those generated on polycrystalline diamond under comparable irradiation conditions. This behavior arises from fundamental differences in the microstructure and electronic defect density of the two materials. Single-crystal diamond consists of a highly ordered sp^3-bonded lattice with minimal grain boundaries or impurity phases. In contrast, polycrystalline CVD diamond films typically contain grain boundaries, structural defects, and regions of graphitic or amorphous carbon. These features can act as carrier recombination centers and scattering sites that reduce the efficiency of avalanche ionization and limit the buildup of the electron plasma responsible for material removal. In single-crystal diamond, however, plasma expansion and reduced defect-mediated energy dissipation, as compared to polycrystalline material, contributes to increased ablation efficiency and improved feature quality. These findings further explain the deeper and more well-defined structures observed in single-crystal diamond [41].

The differences in bonding uniformity, defect density, and nonlinear ionization pathways lead to distinct ablation mechanisms in single-crystal and polycrystalline diamond. These material-dependent interaction processes directly influence feature morphology, depth, and reproducibility during femtosecond laser micromachining.

4. Conclusion

This work demonstrates that femtosecond laser ablation at 800 nm and 250 kHz repetition rate enables precise, non-thermal microstructuring of both HPHT single-crystal diamond and polycrystalline CVD diamond films, producing well-defined craters, microchannels, and reservoir structures. Both CVD and single-crystal diamond exhibit a strong dependence of ablation behavior on laser pulse energy; however, significant differences in feature size, depth, and morphology were observed between the two materials. Single-crystal diamond consistently produced deeper and more well-defined structures, reflecting differences in nonlinear absorption mechanisms, defect density, and plasma dynamics. These findings are consistent with recent reports demonstrating that ultrafast laser–diamond interactions are strongly influenced by crystal structure and impurity content.

Surface graphitization observed between ablation sites at higher pulse energies is confined to a nanoscale surface layer and does not compromise the structural integrity of the fabricated features for microfluidic or field-emission applications. Feature broadening beyond the diffraction-limited focal spot results from extreme pulse overlap and incubation-driven threshold reduction, offering a controllable mechanism for tuning channel width through scanning speed adjustment.

These results show that femtosecond laser micromachining is a viable single-step fabrication method for diamond-based microfluidic devices, field-emission structures, and photonic components, with material selection between single-crystal and polycrystalline diamond providing an additional degree of control over feature geometry and surface quality.

Acknowledgements

The authors acknowledge the support of the Center for Laser Applications at the University of Tennessee Space Institute.

Conflicts of interest

The authors declare no conflict of interest.

References

1. A. Zoubir et al., “Practical uses of femtosecond laser micro-materials processing,” *Appl. Phys. A*, vol. 77, pp. 311–315, 2003. https://doi.org/10.1007/s00339-003-2121-9

2. X. Liu, D. Du, and G. Mourou, “Laser ablation and micromachining with ultrashort laser pulses,” *IEEE J. Quantum Electron*., vol. 33, no. 10, pp. 1706–1716, 1997. https://doi.org/10.1109/3.631270

3. D. F. Farson et al., “Femtosecond laser micromachining of dielectric materials for biomedical applications,” *J. Micromech. Microeng*., vol. 18, no. 3, Art. no. 035020, 2008. https://doi.org/10.1088/0960-1317/18/3/035020

4. R. R. Gattass and E. Mazur, “Femtosecond laser micromachining in transparent materials,” *Nat. Photonics*, vol. 2, no. 4, pp. 219–225, 2008. https://doi.org/10.1038/nphoton.2008.47

5. A. Y. Kharin and V. Y. Timoshenko, “Optical properties of dextran-stabilized silicon nanoparticles in aqueous medium,” *Phys. Sci. Technol*., vol. 8, no. 3–4, pp. 22–27, 2021. https://doi.org/10.26577/phst.2021.v8.i2.03

6. A. Belarouci, R. Tkach, and D. Averin, “Engineering high aspect-ratio silicon nanostructures,” *Phys. Sci. Technol*., vol. 10, no. 3–4, pp. 87–94, 2023. https://doi.org/10.26577/phst.2023.v10.i2.011

7. A. M. Perelomov, V. S. Popov, and M. V. Terentev, “Ionization of atoms in an alternating electric field,” *Sov. Phys. JETP*, vol. 23, no. 5, pp. 924–934, 1966.

8. V. R. Bhardwaj, P. P. Rajeev, P. B. Corkum, and D. M. Rayner, “Strong field ionization inside transparent solids,” *J. Phys. B: At. Mol. Opt. Phys*., vol. 39, p. S397, 2006. https://doi.org/10.1088/0953-4075/39/13/S13

9. T. Abdulkareem Khalil Al-Aish and H. Amjed Kamil, “A new system to the spectroscopy analysis with multiple X-ray of free electron laser,” *Phys. Sci. Technol*., vol. 11, no. 3–4, pp. 86–91, 2024. https://doi.org/10.26577/phst2024v11i2b010

10. E. G. Gamaly, A. V. Rode, B. Luther-Davies, and V. T. Tikhonchuk, “Ablation of solids by femtosecond lasers: Ablation mechanism and ablation thresholds for metals and dielectrics,” *Phys. Plasmas*, vol. 9, no. 3, pp. 949–957, 2002. https://doi.org/10.1063/1.1447555

11. A. S. Saidov, S. N. Usmonov, and U. K. Rakhmonov, “Diamond films obtained on silicone substrates by the CVD method and properties of structures based on them,” *Phys. Sci. Technol*., vol. 10, no. 1–2, pp. 35–41, 2023. https://doi.org/10.26577/phst.2023.v10.i1.05

12. K. E. Spear and J. P. Dismukes, Eds., *Synthetic diamond: Emerging CVD science and technology*. New York, NY, USA: Wiley, 1994.

13. T. Kononenko, M. Meier, M. Komlenok, et al., “Microstructuring of diamond bulk by IR femtosecond laser pulses,” *Appl. Phys. A* 90, 645–651, 2008. https://doi.org/10.1007/s00339-007-4350-9

14. Y.-L. Liou et al., “Fabrication and field emission properties of ultra-nanocrystalline diamond lateral emitters,” *Diamond Relat. Mater*., vol. 17, no. 4–5, pp. 776–781, 2008. https://doi.org/10.1016/j.diamond.2008.01.024

15. K. Subramanian et al., “Nanodiamond lateral field emitter devices on thick insulator substrates for reliable high-power applications,” *Diamond Relat. Mater*., vol. 17, no. 4–5, pp. 786–789, 2008. https://doi.org/10.1016/j.diamond.2007.10.026

16. P. S. Salter and M. J. Booth, "Ultrafast laser processing of diamond," in *Proc. SPIE*, vol. 8974, 2014, Art. no. 89740T. https://doi.org/10.1117/12.2040384

17. A. Courvoisier, M. J. Booth, and P. S. Salter, "Inscription of 3D waveguides in diamond using an ultrafast laser," *Appl. Phys. Lett*., vol. 109, no. 3, 2016, Art. no. 031109. https://doi.org/10.1063/1.4959267

18. Y. V. White, X. Li, Z. Sikorski, L. M. Davis, and W. Hofmeister, "Single-pulse ultrafast-laser machining of high aspect nanoholes at the surface of SiO2," *Opt. Express*, vol. 16, no. 19, pp. 14411–14420, 2008. https://doi.org/10.1364/OE.16.014411

19. Y. V. White, M. Parrish, X. Li, L. M. Davis, and W. Hofmeister, "Femtosecond micro- and nano-machining of materials for microfluidic applications," in *Proc. SPIE*, vol. 7039, 2008, Art. no. 70390J. https://doi.org/10.1117/12.799855

20. W. P. Kang et al., "Diamond vacuum field emission devices," *Diamond Relat. Mater*., vol. 13, no. 11–12, pp. 1944–1948, 2004. https://doi.org/10.1016/j.diamond.2004.07.024

21. K. Subramanian et al., "Enhanced electron field emission from micropatterned pyramidal diamond tips incorporating CH4/H2/N2 plasma-deposited nanodiamond," *Diamond Relat. Mater*., vol. 15, no. 4–8, pp. 1126–1131, 2006. https://doi.org/10.1016/j.diamond.2005.12.047

22. Z. Rutkuniene, M. Balandyte, and G. Karbauskyte, "Formation of diamond-like carbon films on materials for medical application," *Phys. Sci. Technol*., vol. 8, no. 1–2, pp. 35–40, 2021. https://doi.org/10.26577/phst.2021.v8.i1.04

23. K. C. Phillips, H. H. Gandhi, E. Mazur, and S. K. Sundaram, "Ultrafast laser processing of materials: A review," *Adv. Opt. Photon*., vol. 7, pp. 684–712, 2015. https://doi.org/10.1364/AOP.7.000684

24. Y. Gurbuz et al., "PECVD diamond-based high performance power diodes," *IEEE Trans. Power Electron*., vol. 20, no. 1, pp. 1–10, 2005. https://doi.org/10.1109/TPEL.2004.839883

25. T. Apostolova, V. Kurylo, and G. Gnilitskyi, "Ultrafast laser processing of diamond materials: a review," *Front. Phys*., vol. 9, 2021, Art. no. 650280. https://doi.org/10.3389/fphy.2021.650280

26. V.V. Kononenko, "Modification of diamond surface by femtosecond laser pulses," *Photonics*, vol. 10, no. 10, 2023, Art. no. 1077. https://doi.org/10.3390/photonics10101077

27. A. Abdelmalek et al., "Morphological study of nanostructures induced by direct femtosecond laser ablation on diamond," *Micromachines*, vol. 12, p. 583, 2021. https://doi.org/10.3390/mi12050583

28. B. Khan, I. Litvinyuk, and M. Rybachuk, "Femtosecond laser micromachining of diamond: Current research status, applications and challenges," arXiv, 2021. https://doi.org/10.48550/arXiv.2103.00491

29. P. Calvani et al., "Absorptance enhancement in fs-laser-treated CVD diamond," *Phys. Status Solidi* A, vol. 212, pp. 2463–2467, 2015. https://doi.org/10.1002/pssa.201532189

30. O. Monteiro, "Structural defects and sp2 localization in CVD diamond," *J. Mater. Sci*., vol. 54, Art. no. 10, 2019. https://doi.org/10.1007/s10853-018-2949-1

31. M. Tulej et al., "Current progress in femtosecond laser ablation/ionisation time-of-flight mass spectrometry," *Appl. Sci*., vol. 11, no. 6, 2021, Art. no. 2562. https://doi.org/10.3390/app11062562

32. Y. Yao, H. Chen, and W. Zhang, "Time scale effects in laser material removal: A review," *Int. J. Adv. Manuf. Technol*., vol. 26, pp. 598–608, 2005. https://doi.org/10.1007/s00170-003-2026-y

33. X. Jing et al., "Modeling validity of femtosecond laser breakdown in wide bandgap dielectrics," *Appl. Surf. Sci*., vol. 258, no. 10, pp. 4741–4749, 2012. https://doi.org/10.1016/j.apsusc.2012.01.070

34. A. A. Khomich et al., "Raman study of the diamond to graphite transition induced by the single femtosecond laser pulse on the (111) face," *Nanomaterials*, vol. 13, no. 1, Art. no. 162, 2023. https://doi.org/10.3390/nano13010162

35. B. Ali et al., "Laser-induced graphitization of diamond under 30 fs laser pulse irradiation," J. *Phys. Chem. Lett*., vol. 13, pp. 2679–2685, 2022. https://doi.org/10.1021/acs.jpclett.2c00254

36. D. Zhang et al., "Structural evolution of polycrystalline diamond films under single-pulse femtosecond laser irradiation," *Appl. Surf. Sci*., vol. 702, 2025, Art. no. 163318. https://doi.org/10.1016/j.apsusc.2025.163318

37. G. Schnell, U. Duenow, and H. Seitz, "Effect of laser pulse overlap and scanning line overlap on femtosecond laser-structured Ti6Al4V surfaces," *Materials*, vol. 13, no. 4, p. 969, 2020. https://doi.org/10.3390/ma13040969

38. Z. Lin and M. Hong, "Femtosecond laser precision engineering: From micron, submicron, to nanoscale," *Ultrafast Sci*., vol. 2021, 2021, Art. no. 9783514. https://doi.org/10.34133/2021/9783514

39. S. A. Irimiciuc, P.-E. Nica, M. Agop, and C. Focsa, "Target properties – Plasma dynamics relationship in laser ablation of metals," *Appl. Surf. Sci*., vol. 506, 2020, Art. no. 144926. https://doi.org/10.1016/j.apsusc.2019.144926

40. J. Yao et al., "Exploring femtosecond laser ablation by snapshot ultrafast imaging and molecular dynamics simulation," *Ultrafast Sci*., vol. 2022, 2022, Art. no. 9754131. https://doi.org/10.34133/2022/9754131

41. J. Yin, G. Chen, Z. Zhu, M. Jin, and B. Hu, "Ablation mechanism investigation and ablation threshold prediction of single crystal diamond irradiated by femtosecond laser," *Diamond Relat. Mater*., vol. 111, 2021, Art. no. 108173. https://doi.org/10.1016/j.diamond.2020.108173

Information about the author:

Yelena V. White (corresponding author) – Doctor of Physics, Professor, Department of Biochemistry, Chemistry and Physics, Georgia Southern University (Swainsboro, USA, e-mail: ywhite@georgiasouthern.edu).

IRSTI 29.19.22 https://doi.org/10.26577/phst20261313

Electrophysical properties of diamond films deposited on silicon substrates by HFCVD method

A.S. Saidov, A. Kutlimratov, U.Kh. Rakhmonov*, O.Sh. Turgunov, D.V. Saparov and T.M. Saliev

S.A. Azimov Physical-Technical Institute of Academy of Sciences of Uzbekistan, Tashkent, Uzbekistan
*e-mail: fti_uz.@mail.ru

(*Received September 22, 2025; received in revised form May 7, 2026; accepted May 15, 2026)*

Electrically conductive diamond films were deposited on n-type Si(100) substrates by the hot filament chemical vapor deposition (HFCVD) method using a hydrogen–methanol gas mixture with ammonia addition. In contrast to conventional approaches, film growth was performed without preliminary hydrogen etching of the silicon surface, which simplified the technological process. The deposition conditions were optimized to suppress the formation of non-diamond carbon phases and improve film quality. Raman spectroscopy revealed a pronounced diamond-related peak at 1333 cm^{-1} with a relatively small contribution of sp^2-bonded carbon, indicating the predominance of the diamond phase in the deposited films. The films had thicknesses of 2.2–2.8 μm and were grown at a rate of 0.2–0.3 μm h^{-1}. The electrophysical properties were investigated in the temperature range of 300–500 K using Hall-effect measurements. The carrier concentration increased exponentially with temperature, while the carrier mobility decreased due to enhanced phonon scattering, confirming the semiconducting nature of the deposited films. The observed temperature dependences of carrier concentration, mobility, and resistivity were found to be consistent with the behavior expected for semiconductor materials. The results demonstrate that high-temperature HFCVD growth without preliminary hydrogen etching can produce diamond films with satisfactory structural quality and stable electrical characteristics, making them promising for potential electronic and optoelectronic applications.

Keywords: CVD technology, diamond film, silicon substrate, Raman spectra, charge carrier mobility, temperature dependence.

1. Introduction

Recently, there has been increasing interest in thin diamond films deposited on various substrates, particularly on silicon, due to their potential applications in micro- and optoelectronic devices [1–5]. Raman spectroscopy remains one of the most informative and widely used techniques for structural characterization of carbon-based and semiconductor nanostructures, providing information on crystallinity, defect formation, and phase composition [4, 8]. Diamond films on silicon are especially attractive because of the well-established silicon-based technology. In our previous studies [9–12], diamond films were successfully grown on silicon substrates using the HFCVD method. However, the obtained films were predominantly polycrystalline with grain sizes of 2–3 μm and contained noticeable amounts of graphite phases and a 15R-SiC interlayer, as revealed by Raman spectroscopy. In addition, the temperature dependence of electrophysical parameters such as carrier concentration, mobility, and resistivity were not investigated. Despite certain limitations related to filament degradation during operation, the HFCVD method remains attractive due to its simplicity and scalability. The film growth rate is typically about 1 μm/h and can be controlled by adjusting process parameters such as filament temperature and substrate distance [13]. In this work, diamond films were deposited on Si(100) substrates using the HFCVD method, and their electrophysical properties were investigated. The study of transport properties in nanostructured semiconductor materials remains important for understanding the relationship between synthesis conditions, structural quality, and functional characteristics [14]. Particular attention was paid to the temperature dependence of charge carrier concentration, mobility, and resistivity in order

to evaluate the suitability of this method for obtaining diamond films with properties close to those of single-crystal materials.

2. Materials and methods

Diamond films investigated in this study were deposited on Si(100) substrates using the hot filament chemical vapor deposition (HFCVD) method, as described in [1–3] and in our previous works [11, 12]. The substrates were n-type monocrystalline silicon wafers with a thickness of 300 μm and a resistivity of 0.1 Ω·cm. The gas phase consisted of a hydrogen–methanol (CH_3OH) mixture with the addition of ammonia (NH_3). In contrast to our previous studies, the deposition process was carried out without preliminary hydrogen etching of the silicon substrate, and the technological parameters were slightly modified. In the HFCVD process, a reduced pressure (typically 20–60 Torr) is maintained in the reaction chamber, and gas activation is achieved by a heated tungsten filament operating at temperatures of 2000–2200 °C. Before discussing the deposition process in detail, it is necessary to consider the key technological parameters influencing the properties of the diamond films. In HFCVD, diamond growth occurs in a hydrogen-rich atmosphere containing a carbon source (such as CH_4, CH_3OH, C_2H_6, or C_2H_5OH) and, in some cases, additional impurities such as NH_3. The addition of ammonia introduces nitrogen into the diamond lattice, which can affect both growth kinetics and film morphology. It is reported that nitrogen concentrations in the range of 0.1–0.6% can enhance the growth rate and stabilize the surface during deposition [15,16]. Nitrogen incorporation in diamond introduces deep donor levels (~1.7 eV below the conduction band), which influence the electrical properties of the films. In addition, nitrogen-related defects, such as NV centers, have been widely studied due to their potential applications in quantum technologies [17–20]. Diamond film growth on Si(100) substrates was carried out under the following conditions: filament temperature 2250–2300 °C, substrate temperature 870–900 °C, total gas flow rate ($CH_3OH + H_2 + NH_3$) of 65–70 cm³/min, and chamber pressure of 75–80 Torr. The methanol vapor concentration was maintained at 0.5–0.8% of the total gas mixture. The deposition time was 8–10 hours, resulting in film thicknesses of 2.2–2.8 μm and an average growth rate of 0.2–0.3 μm/h. It should be noted that, under identical growth conditions, approximately 50% of the samples exhibited a polycrystalline structure. This variability may be attributed to fluctuations in nucleation density, local temperature gradients, and variations in active hydrogen concentration during the deposition process. The selected growth conditions involve relatively high filament and substrate temperatures compared to those reported in [4, 5, 9]. These parameters were chosen to enhance the concentration and activity of atomic hydrogen, which preferentially etches sp^2-bonded carbon (graphite phase) more effectively than sp^3-bonded carbon (diamond). As a result, the graphite phase content is reduced, leading to improved film quality, although at the expense of a lower growth rate.

3. Results and discussion

The HFCVD method is based on complex gas-phase reactions leading to the deposition of synthetic diamond layers on a solid substrate [21]. In the present process, near the tungsten filament heated to 2250–2300 °C, methanol (CH_3OH) decomposes into carbon-containing species (primarily CO and H_2), while molecular hydrogen (H_2) dissociates into atomic hydrogen (H). Ammonia (NH_3) also undergoes thermal decomposition, forming reactive species such as NH radicals and hydrogen atoms. The decomposition of methanol can be described by the reaction: $CH_3OH \rightarrow CO + 2H_2$. According to [15], ammonia decomposition at temperatures above 1200–1300 °C may proceed via the formation of nitrogen and hydrogen ($2NH_3 \rightarrow N_2 + 3H_2$) or intermediate species. However, under typical HFCVD conditions, NH_3 predominantly decomposes into NH radicals and hydrogen ($2NH_3 \rightarrow N_2 + 3H_2$), where NH radicals play a key role in nitrogen incorporation into the diamond lattice. Diamond films are formed from carbon-containing radicals that reach the substrate surface. In this process, carbon atoms initially interact with silicon atoms at the substrate surface, forming a thin silicon carbide (SiC) interlayer. Subsequently, diamond nuclei are formed on the SiC surface, where both sp^2- and sp^3-bonded carbon species are deposited. The gas-phase reactions during HFCVD lead to the formation of both sp^2- and sp^3-hybridized carbon. However, sp^2-bonded carbon (graphite phase) is preferentially etched by atomic hydrogen due to its lower bond energy compared to sp^3-bonded carbon (diamond). This selective etching process plays a key role in promoting diamond growth. As a result, the growth conditions can be adjusted such that the etching rate of the non-diamond phase exceeds its formation rate. Under these conditions, the growth rate of the diamond film decreases, but the structural quality improves due to the reduc-

tion of graphite inclusions. Ideally, diamond consists entirely of sp^3-bonded carbon, which determines its unique mechanical and electrical properties. To confirm the formation and structural quality of the diamond films, Raman spectra were recorded at 300 K using a laser with a wavelength of 514 nm (Figure 1a). A pronounced peak near 1333 cm^{-1}, characteristic of sp^3-bonded carbon and typically associated with diamond, is observed, which is close to the reference value of 1332 cm^{-1} [10]. Similar approaches based on Raman spectroscopy have been successfully applied for structural characterization of nanostructured silicon and semiconductor materials, where peak position and linewidth were shown to be sensitive to crystal quality and defect concentration [6, 20]. The full width at half maximum (FWHM) of the diamond peak is estimated to be approximately 10–12 cm^{-1}, indicating relatively good crystalline quality. The slight broadening of the peak suggests the presence of minor structural defects and small amounts of sp^2-bonded carbon. A weaker peak at ~1561 cm^{-1} is also observed, corresponding to the graphite phase (sp^2-bonded carbon), indicating incomplete etching during the growth process. The relatively weak G-band intensity, compared to the sharp sp^3-related peak near 1332 cm^{-1}, indicates that the film is predominantly sp^3-bonded carbon [10, 23]. Thus, the Raman analysis demonstrates that the selected HFCVD conditions favor the formation of diamond with a relatively low content of non-diamond phases.

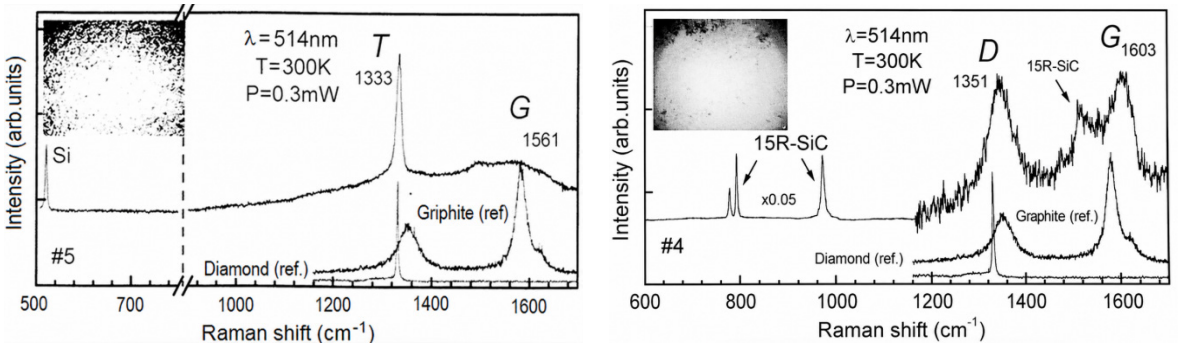

a) *b)*

Figure 1. Raman spectra of diamond films grown by HFCVD on silicon substrates with (100) (a) and (111) (b) orientations under different technological conditions.

Figure 1a suggests improved structural quality of the deposited carbon film with a predominance of sp^3-bonded carbon.

When the substrate was pre-etched with hydrogen before film deposition, diamond peaks were not detected in the Raman spectrum. Instead, peaks corresponding to a graphite-like phase were observed. The Raman spectrum of this film also contains an additional peak associated with the 15R-SiC polymorph, which is absent in Figure 1a. The formation of the 15R-SiC interlayer is likely related to the initial interaction between carbon species and the silicon substrate, resulting in a transition layer at the interface. As the film thickness increases, the contribution of this interlayer decreases, while graphite growth becomes dominant. The sharper peak in Figure 1a confirms the improved structural quality of the diamond film obtained under the present growth conditions. Figure 2 shows the temperature dependence of the charge carrier concentration in a diamond film in both normal (a) and semilogarithmic (b) scales. The Raman spectrum of this sample is shown in Figure 1a. As seen from the semi-logarithmic plot, the carrier concentration increases exponentially with temperature, indicating thermally activated conduction typical of semiconductors [23]. At temperatures up to approximately 480–485 K, the concentration increases gradually, corresponding to partial ionization of impurity centers. At higher temperatures (above ~490 K), a more pronounced increase is observed, which can be attributed to the activation of deeper impurity levels or defect-related states, possibly associated with residual sp^2-bonded carbon. The temperature dependences of carrier mobility (Fig. 4a) and resistivity (Fig. 4b) were also investigated. The increase in carrier concentration leads to a corresponding decrease in resistivity. A slight increase in resistivity observed in the low-temperature region

(300–320 K) may be associated with carrier localization or compensation effects. The mobility decreases with increasing temperature: at lower temperatures the change is weak, while at higher temperatures it becomes more pronounced due to enhanced phonon scattering and increased carrier–carrier interactions.

Overall, the observed temperature dependences of carrier concentration, mobility, and resistivity are generally consistent with the behavior expected for semiconducting materials.

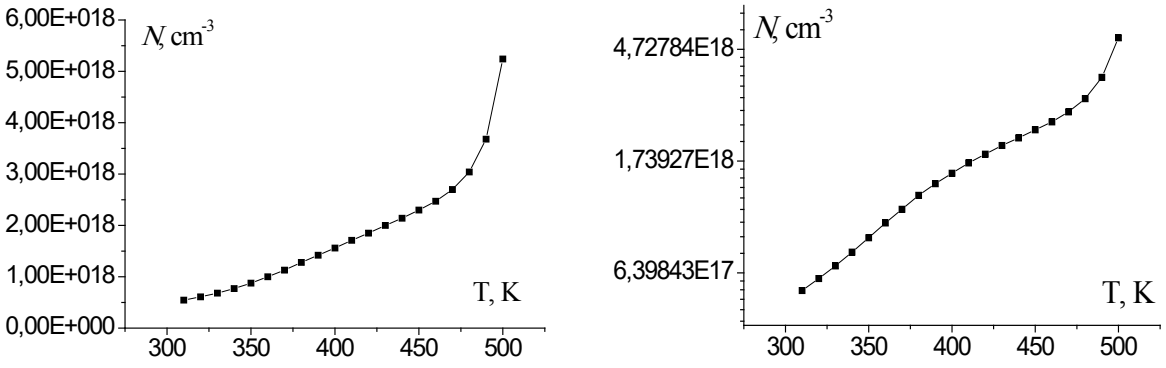

a) b)

Figure 2. Temperature dependence of the charge carrier concentration (N) in the diamond film in normal (a) and semi-logarithmic (b) scales.

The temperature dependence of the carrier concentration reflects impurity ionization processes and the activation of intrinsic defects. Analysis of the N(T) behavior allows estimation of the activation energy of impurity levels and the presence of deep defect states.

The resistivity of the semiconductor is related to the carrier concentration and mobility by the expression $\rho = 1/q(\mu_n n + \mu_p p)$, where n and p are the concentrations of electrons and holes, respectively [22]. Electrical measurements were performed using the Van der Pauw method with an HMS-7000 Hall measurement system, enabling simultaneous acquisition of temperature-dependent data. Ohmic contacts were formed by thermal evaporation of silver (Ag) in vacuum (~10^{-5} Torr) at a sample temperature of approximately 450 °C, followed by annealing for 10 minutes. Four contacts were placed at the sample edges, as shown in Figure 3a. The experimental sample mounted in the measurement holder used for Hall-effect characterization is shown in Figure 3b. The overall uncertainty of resistivity, Hall mobility, and carrier concentration measurements was approximately 2%.

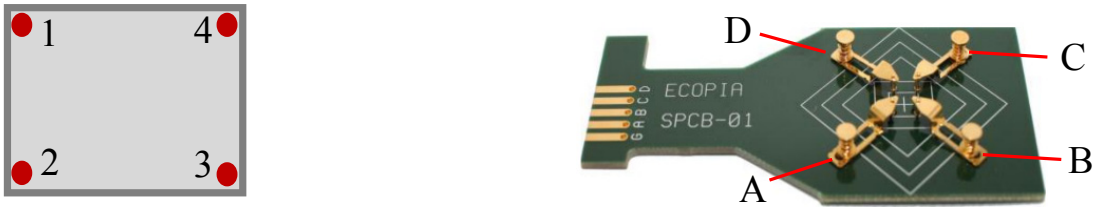

a) b)

Figure 3. Contact configuration for Van der Pauw measurements on the diamond film, showing four ohmic contacts placed at the sample edges (a), and the experimental sample holder (b).

The temperature dependence of charge carrier mobility μ(T) is governed by the competition between different scattering mechanisms. At low temperatures, mobility is mainly limited by scattering on ionized impurities, resulting in $\mu \propto T^{3/2}$. At higher temperatures, scattering by acoustic and optical phonons becomes dominant, leading to $\mu \propto T^{-3/2}$ [23]. In non-polar semiconductors such as Si, Ge, and diamond, the dominant scattering mechanisms are impurity scattering and phonon scattering. The overall mobility can be described by Matthiessen's rule, which combines the contributions of different scattering processes. The observed decrease in mobility with increasing temperature in this work indicates that phonon scattering plays a dominant role at elevated temperatures, while impurity scattering is more significant at lower temperatures.

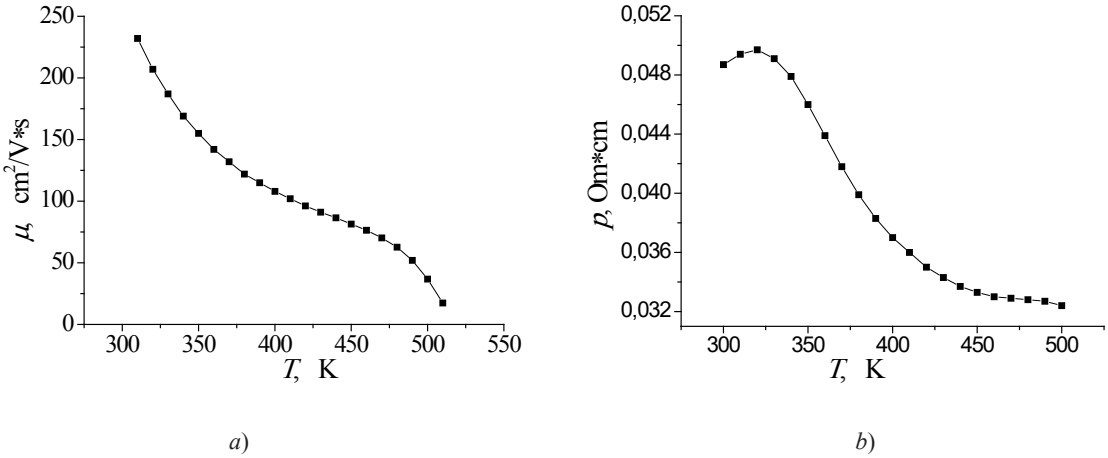

a) *b*)

Figure 4. Temperature dependence of charge carrier mobility μ (a) and resistivity ρ (b) of the diamond film.

Figure 4 shows the temperature dependence of charge carrier mobility and resistivity of the diamond film. As seen from Figure 4a, the mobility decreases with increasing temperature. This behavior is typical for semiconductors and is mainly attributed to enhanced phonon scattering at elevated temperatures. At lower temperatures, the decrease in mobility is relatively gradual, indicating a contribution of impurity scattering. However, at higher temperatures, the mobility decreases more rapidly due to the dominant role of lattice vibrations. Figure 4b demonstrates that the resistivity decreases with increasing temperature, which is consistent with the increase in carrier concentration observed in Figure 2. A slight increase in resistivity at low temperatures may be associated with carrier localization or compensation effects. Overall, the observed temperature dependences of mobility and resistivity confirm the semiconducting nature of the obtained diamond films. These results can be explained by the increase in thermal energy with temperature, which leads to higher electron velocities and enhanced scattering by acoustic and optical phonons. As a result, phonon scattering becomes the dominant mechanism at elevated temperatures, causing a decrease in charge carrier mobility [24, 25]. As shown in Figures 2 and 4, the temperature dependences of carrier concentration (N), mobility (μ), and resistivity (ρ) are generally consistent with the behavior expected for semiconducting materials.

4. Conclusions

Diamond films were successfully deposited on Si(100) substrates using the HFCVD method under the selected growth conditions. The obtained films had thicknesses of 2.2–2.5 μm and were formed at a growth rate of 0.2–0.3 μm/h. Raman analysis indicated the presence of predominantly sp^3-bonded carbon with a characteristic peak near 1333 cm^{-1}. The temperature dependences of charge carrier concentration, mobility, and resistivity were investigated. The results demonstrate typical semiconductor behavior: the carrier concentration increases with temperature, while mobility decreases due to enhanced phonon scattering. Overall, the obtained results indicate that the HFCVD method enables the

growth of diamond films on silicon substrates with stable structural and electrical properties, making them promising for potential electronic and optoelectronic applications.

Funding

This work was supported by the Fundamental Research Program of the Academy of Sciences of Uzbekistan.

Conflicts of interest

The authors declare no conflict of interest.

Author contributions

Conceptualization: A.S.S and A.K.; Methodology: A.K. and U.Kh.R.; Software: U.Kh.R.; Validation: A.S.S., A.K. and D.V.S.; Formal Analysis: A.S.S. and D.V.S.; Investigation: U.Kh.R. and O.Z.T.; Resources: A.K. and D.V.S.; Data Curation: U.Kh.R.; Writing – Original Draft Preparation: U.Kh.R.; Writing – Review & Editing: A.S.S and A.K.; Visualization: U.Kh.R.; Supervision: A.S.S.; Project Administration: A. K.; Funding Acquisition: A.S.S. All authors have read and agreed to the published version of the manuscript.

References

1. N. A. Feoktistov et al., "Evolution of the morphology of diamond particles and mechanism of their growth during the synthesis by chemical vapor deposition," *Phys. Solid State*, vol. 57, no. 11, pp. 2184–2190, Nov. 2015, https://doi.org/10.1134/S1063783415110104

2. M. V. Baidakova et al., "Obtaining diamond films on crystalline silicon by thermal gas-phase deposition," *Semiconductors*, vol. 36, no. 6, pp. 651–657, Jun. 2002 (in Russian).

3. I. B. Yanchuk et al., "Raman scattering, AFM and nanoindentation characterisation of diamond films obtained by hot filament CVD," *Diamond Relat. Mater.,* vol. 13, pp. 266–269, 2004, https://doi.org/10.1016/j.diamond.2003.11.001

4. A. K. Martyanov, "Formation of diamond films and composites containing optically active impurities Si, Ge, Eu in microwave plasma," Ph.D. dissertation, Moscow, Russia, 2019. (in Russian).

5. C. J. Tang et al., "A comparison study of hydrogen incorporation among nanocrystalline, microcrystalline and polycrystalline diamond films grown by chemical vapor deposition," *Thin Solid Films*, vol. 515, pp. 3539–3546, 2007, https://doi.org/10.1016/j.tsf.2006.10.132

6. A. Malgazhdarova et al. "Synthesis and characterization of carbon nanomaterials obtained using electric discharge", *Physical Sciences and Technology,* vol. 12, No. 1-2, pp. 68–83, 2025, https://doi.org/10.26577/phst2025121

7. R. Zhumadilov et al. "In-situ Raman analysis of carbon nanowalls during electrochemical measurement", *Physical Sciences and Technology*, vol. 12, No. 1-2, pp. 57–67, 2025, https://doi.org/10.26577/phst20251217

8. D.A. Mamichev D.A. et al. "Enhanced Raman scattering in multilayer structures of porous silicon." *Journal of Raman Spectroscopy*, vol.42, No.6, pp. 1392-1395, 2011. https://doi.org/10.1002/jrs.2865

9. W. Ahmed et al., "CVD diamond: controlling structure and morphology," *Vacuum*, vol. 56, pp. 153–158, 2000. https://doi.org/10.1016/S0042-207X(99)00147-5

10. A. C. Ferrari and J. Robertson, "Resonant Raman spectroscopy of disordered, amorphous, and diamondlike carbon," *Physical Review B*, vol. 64, no. 7, p. 075414, 2001, https://doi.org/10.1103/PhysRevB.64.075414

11. A. Kutlimratov et al., "Properties of diamond films obtained by chemical vapor deposition on silicon substrates," in Proc. 7th Int. Sci. Pract. Conf. "Problems and Scientific Solutions," Melbourne, Australia, Apr. 25–26, 2021, pp. 681–690.

12. A. Kutlimratov et al., "Properties of diamond films obtained on silicon substrates by the method of chemical vapor deposition," *Sci. Herit*., vol. 1, no. 77, pp. 37–41, 2021.

13. D. A. Romanov, "Features of the formation of the real structure of epitaxial CVD diamond films with natural and modified isotopic composition," Ph.D. dissertation, Moscow, Russia, 2021. (in Russian).

14. M. Isaiev, et al. *"*Application of photoacoustic approach for characterization of nanostructured materials*." Nanomaterials*, vol. 12(4). pp. 708, 2022. https://doi.org/10.3390/nano12040708

15. R. Schirhagl et al., "Nitrogen-vacancy centers in diamond: nanoscale sensors for physics and biology," *Annu. Rev. Phys. Chem.,* vol. 65, pp. 83–105, 2014, doi: 10.1146/annurev-physchem-040513-103659.

16. V. A. Sobyanin et al., "Decomposition of ammonia on tungsten at low pressure," *Kinet. Catal*., vol. 23, no. 1, pp. 89–93, 1982.

17. A. M. Gorbachev et al., "Formation of multilayered nanostructures of NV sites in single-crystal CVD diamond," *Tech. Phys. Lett.,* vol. 46, no. 7, pp. 641–645, 2020.

18. M. A. Lobaev et al., "NV-center formation in single crystal diamond at different CVD growth conditions," *Phys. Status Solidi A*, vol. 215, 2018, Art. no. 1800205, https://doi.org/10.1134/S1063785020070093

19. I. Aharonovich et al., "Diamond photonics," *Nat. Photonics*, vol. 5, pp. 397–405, 2011, doi: 10.1038/nphoton.2011.54.

20. D. D. Awschalom et al., "The diamond age of spintronics," *Sci. Am.,* vol. 297, no. 4, pp. 84–91, 2007, https://doi.org/10.1038/nphoton.2011.54.

21. W. Wuyi et al., "Gem-quality synthetic diamonds grown by a chemical vapor deposition (CVD) method," *Gems & Gemology,* vol. 39, no. 4, pp. 268–283, 2003, doi: 10.5741/GEMS.39.4.268.

22. K.A. Gonchar K.A. et al. "Enhancement of photoluminescence and Raman scattering in one-dimensional photonic crystals based on porous silicon" *Semiconductors*. vol. 45, No 5, pp. 614–617, 2011. https://doi.org/10.5741/GEMS.39.4.268.

23. V. L. Bonch-Bruevich and S. G. Kalashnikov, Physics of Semiconductors, 2nd ed. Moscow, Russia: Nauka, 1990, 685 p.

24. S. M. Sze and K. N. Ng, Physics of Semiconductor Devices, 3rd ed. Hoboken, NJ, USA: Wiley, 2006, doi: 10.1002/0470068329. https://doi.org/10.1002/0470068329

25. 25. S.A. Dyakov et al. "Resonance enhancement of Raman scattering from one-dimensional periodical structures of porous silicon" *J. Nanoel.Optoel*. vol. 7, No 6, pp. 591–595, 2012. https://doi.org/ 10.1166/jno.2012.1398

Information about the authors:

Amin Safarbaevich Saidov – Doctor of Science in Physics and Mathematics, Professor, Laboratory of the Semiconductor Crystals Grow, S.A. Azimov Physical-Technical Institute of the Academy of Sciences of Uzbekistan (Tashkent, Uzbekistan, e-mail: amin@uzsci.net).

Aleksandr Kutlimratov – Candidate of Science in Physics and Mathematics, Senior Scientific Researcher, Laboratory of the Semiconductor Crystals Grow, S.A. Azimov Physical-Technical Institute of the Academy of Sciences of Uzbekistan (Tashkent, Uzbekistan, e-mail: kutlimratov5401@mail.ru).

Utkurjon Khikmatalievich Rakhmonov (corresponding author) – PhD in Physics and Mathematics, Researcher, Laboratory of the Semiconductor Crystals Grow, S.A. Azimov Physical-Technical Institute of the Academy of Sciences of Uzbekistan (Tashkent, Uzbekistan, e-mail: utkurraxmonov@gmail.com);

Otabek Zokir o'g'li Turgunov – Researcher, Laboratory of the Semiconductor Crystals Grow, S.A. Azimov Physical-Technical Institute of the Academy of Sciences of Uzbekistan (Tashkent, Uzbekistan, e-mail: otabeksemicon@gmail.com).

Dadajon Saparov – PhD in Physics and Mathematics, Researcher, Laboratory of the Semiconductor Crystals Grow, S.A. Azimov Physical-Technical Institute of the Academy of Sciences of Uzbekistan (Tashkent, Uzbekistan, e-mail: dada@uzsci.net).

Tojiddin Saliev – Candidate of Science in Physics and Mathematics, Senior Scientific Researcher, Tashkent Institute of Accounting and Technology (Tashkent, Uzbekistan, deceased author).

IRSTI 41.51.31; 37.15.15 https://doi.org/10.26577/phst20261314

Near-infrared imaging of the twilight sky: enhanced detection of noctilucent and high-altitude clouds

A.A. Solodovnik, T.B. Kasenov, P.I. Leontyev, B.M. Useinov* and N.P. Solodovnik

Manash Kozybayev North Kazakhstan University, Petropavl, Kazakhstan
*e-mail: buseinov@gmail.com

(*Received March 31, 2026; received in revised form May 18, 2026; accepted May 28, 2026*)

As part of efforts to improve the methodology for detecting and monitoring noctilucent clouds (NLCs), observations of the twilight sky conducted during the summer season of 2025 were analyzed. The study examines existing approaches to NLC imaging and demonstrates that the information content of ground-based observations can be significantly enhanced through increased image contrast. To achieve this, observations were extended from the visible spectral range to the near-infrared (NIR) region using a modified CANON 1000D camera with enhanced NIR sensitivity and a set of interchangeable optical filters. For the first time, simultaneous monitoring of the twilight sky was performed using two cameras operating in different spectral ranges: a modified CANON 1000D in the near infrared and a CANON 2000D in visible light. Observations carried out from late May to early September 2025 revealed a substantial increase in image contrast in the NIR region compared with conventional visible-light imaging. The obtained results demonstrate the advantages of near-infrared observations for the detection and analysis of noctilucent clouds and other atmospheric phenomena under twilight conditions. The proposed approach expands the capabilities of ground-based optical monitoring and provides a basis for further development of observational techniques for upper-atmosphere studies.

Keywords: twilight segment, noctilucent clouds, image contrast, infrared camera, infrared imaging, cloud monitoring.

1. Introduction

In standard astronomical research practice, objects are observed in the dark night sky, with the notable exception of solar studies. However, there are phenomena and objects observed within the twilight (or auroral) segment of the celestial sphere. Besides bright celestial bodies such as Venus and Jupiter (which are the first to appear in the evening sky), these include, primarily, noctilucent and nacreous clouds. Occasionally, phenomena such as zodiacal light and the gegenschein are also attributed to this category [1-3].

In atmospheric optics and astronomy, twilight refers to strictly defined time intervals after sunset or before sunrise. During twilight, the solar disk is not visible above the horizon, yet the celestial sphere is illuminated by radiation scattered by the atmosphere. The level of illumination is determined by the altitude of the center of the solar disk, i.e., the angle at which the Sun has dipped below the horizon. Based on the depression angle, twilight is classified into civil (from 0° to -6°), nautical (from -6° to -12°), and astronomical (from -12° to -18°). When the Sun dips below -18°, "astronomical night" begins, at which point sunlight scattered by the upper atmospheric layers practically ceases to affect astronomical observations [4-6].

The part of the celestial sphere illuminated by solar radiation scattered by overlying atmospheric layers is called the twilight segment. It is clearly visible to the naked eye as an arc-shaped bright region stretched along the azimuth above the point where the Sun has set below the horizon. It is bounded at the top by the dark band of the Earth's shadow and at the bottom by the horizon line. The altitude of the upper boundary of the twilight segment changes continuously, descending in the evening and ascending in the morning. The formation of the twilight segment is associated with the scattering of solar rays in

the upper atmospheric layers (mainly in the stratosphere) [4-6]. The twilight segment is observed particularly distinctly under conditions of minimal dust and high tropospheric humidity, for example, after rainy weather. Conversely, its visibility is negatively affected by lunar illumination (near a full moon) or bright artificial light sources (urban environments). Latitudinal and seasonal factors also significantly influence the duration of twilight [4-6].

The first of the aforementioned objects that stand out specifically against the background of the twilight part of the sky are NLC. Photometric visibility conditions are exceptionally important for them. These clouds are completely invisible in the daytime sky due to their exceptionally low contrast against the sky background, which is caused by a low aerosol concentration within them, and consequently, weak scattering of solar radiation [7, 8]. An exception is total solar eclipses, during which the background sky brightness drops sharply so that stars become visible. It should be noted that the visibility of stars in the sky is a significant photometric marker of the background sky brightness required for the visual observation of NLC. Such conditions occur at the boundary between civil and nautical twilight; however, with the transition from nautical to astronomical twilight, the visibility of NLC sharply deteriorates due to a decrease in their illumination by solar rays.

As for zodiacal light, caused by the scattering of solar radiation on interplanetary dust particles, the conditions for its observation are generally similar to those characteristics of NLC. However, unlike the latter, this glow is observed only at a relatively small angular distance from the Sun, which is explained by the features of the spatial distribution of the scattering particles. A phenomenon such as the gegenschein, due to its extremely low brightness, is observed only under conditions of astronomical night, unlike zodiacal light [6].

Often, objects observed in the twilight segment are comets. Indeed, as comets approach the Sun, they rapidly increase their brightness, which reaches its maximum (in absolute magnitude) near the epoch of their perihelion passage.

Thus, observations of a variety of celestial objects and phenomena for which there is expressed scientific interest are highly relevant within the twilight segment region.

2. Features of ground-based registration of high-altitude clouds

To date, there are two comprehensive approaches to obtaining information about the state of NLC fields: studying them using orbital spacecraft and ground-based observations. Despite all the undeniable advantages of studying NLC from space (primarily due to the elimination of weather effects), ground-based methods for investigating them have not lost their relevance. The reason for this lies not only in the episodic nature of space missions but also in the variety of experimental approaches that can be utilized when studying NLC from the Earth's surface. Examples of the most significant scientific achievements associated with ground-based NLC observation methods include the development of a morphological classification of cloud forms, estimates of aerosol microphysical parameters, and conclusions regarding the relationship between the evolution of NLC fields and meteorological processes in the troposphere [2, 7-10].

In particular, one of the most important tasks in studying NLC and their connection to atmospheric processes is registering the very fact of the presence of mesospheric clouds at a given time and in a given location. Such observations are called synoptic, and they are currently conducted using digital cameras, often operating in automatic mode. Obtaining data on the presence (or absence) of NLC allows for a more precise understanding of the influence of various physical factors of terrestrial or cosmic origin on the state of the upper atmosphere [9-14].

As an example of the importance of obtaining such data, one can point to the operation (since 2004) in the Northern Hemisphere of a network of digital automatic cameras for registering NLC and studying their spatiotemporal dynamics [15]. This network, called Network of Automatic Photographic Survey of NLC, includes observation points located along a latitudinal circle (53–56° N), which allows for comparable NLC observations. This creates conditions of identical illumination of the twilight segment by the Sun and similar physical conditions in the mesopause (temperature and wind speed within it depend on geographic latitude). The first scientific results based on this network measurements were published in the work of Dalin et al. [16].

The obtained data made it possible to trace the propagation of atmospheric planetary waves with periods of two and five days. Propagating into the region where NLC can form, they affect the frequency and brightness of their appearance. Specifically, during the 2006 and 2007 seasons, two-day planetary waves influenced NLC activity to a greater extent than five-day waves [13]. Furthermore, it was found that the influence of planetary waves on NLC brightness variations is small, with their average contribution being 3–5%.

Naturally, the first and most serious obstacle to synoptic NLC observations is tropospheric cloudiness, the density of which increases toward the horizon. However, clouds are not the only hindrance to NLC registration. The season of NLC fields evolution covers the period from the end of May to the beginning of August, and in the summer period the dustiness of the ground layer of air increases noticeably. Scattering by atmospheric dust aerosols significantly reduces the visibility of NLC at low altitudes above the horizon. Additionally, the question logically arises of expanding the temporal window for NLC registration, for instance, making it accessible immediately after sunset. This requires reducing the background brightness of the twilight sky.

Solving this latter task would increase the efficiency of registering not only NLC but also nacreous (stratospheric) clouds, and raise the possibility of registering other poorly studied forms of high-altitude clouds.

3. Methodology of IR monitoring of the twilight segment

A typical program for synoptic NLC observations is fairly simple. It involves obtaining a series of images of the twilight segment with the widest possible azimuth viewing angle. The need for a wide field of view is dictated by the potential appearance of NLC, for example, in the evening from the west to the north. When using wide-angle optics in manual mode, a single camera is quite sufficient. For automated observations with stationary cameras throughout the night, two cameras will be required. Imaging is conducted from the end of civil twilight in the evening until its onset in the morning. Usually, these times are calculated in advance for each day of the season; however, there are situations when NLC are clearly visible in the mornings even under civil twilight conditions. The interval between shots can vary from 1 to several minutes.

Typically, digital cameras have a spectral sensitivity maximally approximated to that of the human eye. In this case, all the aforementioned limitations on NLC visibility remain valid. In some sources [2], there are recommendations regarding the use of optical filters selecting the blue-cyan wavelength region when taking NLC images. It can be assumed that these are based on the consideration that NLC aerosols most effectively scatter visible radiation specifically in these colors. Consequently, one might expect an increase in the contrast of NLC images in the photographs. However, one should not forget that air molecules also have maximum scattering efficiency at the same wavelengths (which, in particular, determines the color of the sky). For this reason, and due to the fact that conventional black-and-white photographic films had a sensitivity peak in blue-cyan rays, the application of such techniques did not see further development [2].

It is possible to increase the contrast of NLC images in twilight segment photographs using another method. Specifically, by significantly reducing the sky background brightness. To achieve this, it is sufficient to transition from imaging the sky in the visible range to photographing in the near-IR spectral region [17, 18].

Isolating the required wavelength range is not complicated due to the availability of a wide selection of good-quality optical light filters. Unfortunately, conventional cameras practically do not detect radiation with a wavelength longer than 750 nm. This is because camera manufacturers deliberately restrict the sensitivity range to the visible region to enhance image sharpness. This is achieved by installing a corresponding glass filter over the surface of the radiation receiver. Figure 1 presents the wavelength dependencies of the transmittance for the digital camera sensor, the glass light filter in front of it, and the camera lens.

As can be seen, the transmittance of the glass filter in front of the sensor excludes the entry of radiation with a wavelength longer than 740 nm, despite the sensor itself possessing good sensitivity in the region up to 1000 nm. The residual sensitivity of cameras in the near-IR spectral region requires exposures of several seconds under daylight conditions and no less than 5 minutes under twilight conditions [17, 18]. Such long exposures are unacceptable for implementing the NLC monitoring task.

The sensitivity of a digital camera to IR radiation can be significantly increased (by 2-3 orders of magnitude) by removing the aforementioned light filter. This was done for the CANON 1000D camera [17] in the in a specialized optical workshop. The general view of the camera and its schematic diagram are shown in Figure 2.

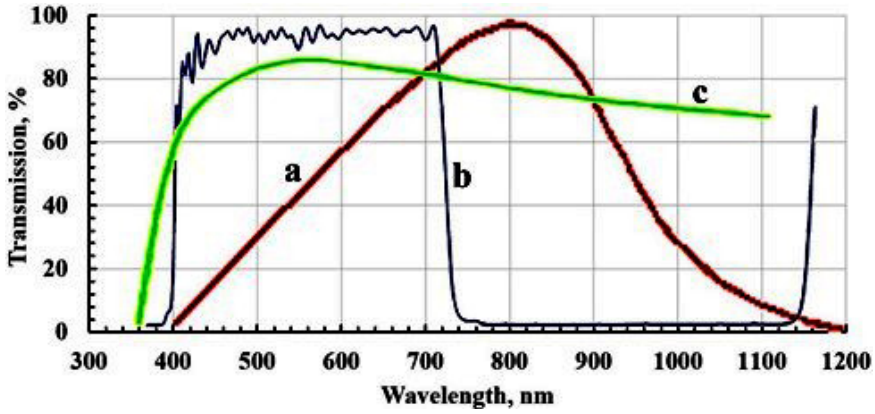

Figure 1. Wavelength dependence of the light transmittance for:
a) the digital camera sensor; b) the camera's glass light filter; c) the camera lens.

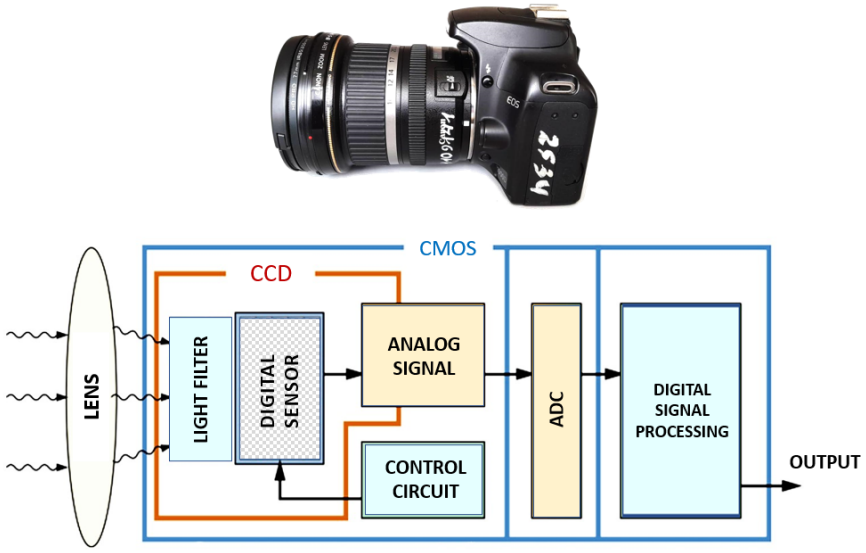

Figure 2. General view of the CANON 1000D camera and its schematic diagram [19]
The light filter is removed when the camera is modified.

Test shots using RG780, RG830, and RG850 IR filters (where the numbers indicate the start of the transmission band in nm) confirmed a hundredfold increase in camera sensitivity under identical aperture settings and specified sensor sensitivity.

The overall goal of monitoring the twilight segment was to compare the quality and information content of sky images in the visible and near-IR spectral regions (RG850 filter), as well as to conduct a general analysis of NLC registration efficiency in the IR spectral region. For the first time in the practice of studying NLC, filming was carried out using two cameras: CANON 2000D [21] in visible light and a modernized CANON 1000D in the near IR wavelength region. The cameras had identical CANON EF-S LENS wide-angle lenses. Photographing was carried out at the exact same moments in time (with an accuracy of up to 5 seconds). Camera sensitivities were set to ensure comparable exposure durations. It should be noted that obtaining an infrared image of the twilight segment at the end of nautical twilight at an ISO value of 1600 required an exposure of approximately 25-30 seconds at an aperture of 4.5. Observations were conducted in the evening from the beginning of June to September 2025 in the city of Petropavlovsk (54.87°N, 69.13°E) facing west with a virtually completely open horizon. The shooting was conducted manually with the cameras mounted

on tripods. The total number of observation nights was 41, with the number of images suitable for subsequent analysis being 474, of which 356 were in the IR range. Detailed monitoring information is provided in Table 1. Gaps in dates correspond to nights with overcast (rainy) weather.

Table 1. General information on NLC monitoring in the 2025 season.

№	Date	Time	Weather conditions	Presence and type of NLC
1	05.27	22:00 22:40	Clear	Bands parallel to the horizon from the west-northwest to the north. Five degrees below Capella.
2	05.28	-	Low clouds	None
3	05.30	-	Cloudy	None
4	05.31	-	Cloudy	None
5	06.02	22:15 22:45	Clear	Faint NLCs. Five degrees above Capella. From the west-northwest to the north. Veil and bands.
6	06.03	-	Cloudy	-
7	06.04	-	Cloudy	IR images taken.
8	06.06	-	Cloudiness	None
9	06.07	-	Cloudiness	None
10	06.08	-	Light cloudiness	None
11	06.09	-	Light cloudiness	None
12	06.10	-	Light cloudiness	None
13	06.11	-	Clear	None
14	06.14	22:10 22:55	Clear	Faint, low bands in the direction from the west initially, moving to the north by 23:20.
15	06.15	-	Clear	None. Images taken.
16	06.16	-	Clear	None. Images taken.
17	06.19	22:00 22:42	Clear	Clouds are not visible visually, but the IR camera records them as filaments in the northwest direction at an altitude of 10-15 degrees.
18	06.21	-	Partly cloudy	None
19	06.22	22:20 22:37	Cloudiness	Presence of NLCs is noticeable.
20	06.25	21:40 22:25	Clear	Unusual clouds. Recorded by the IR camera, but not by the conventional camera. Rapid movement. Possibly cirrus clouds.
21	06.26	-	Clear	None
22	06.27	-	Clear	None
23	06.28	-	Clear	No NLCs in the evening sky. NLCs observed in the morning in Poludino.
24	06.29	-	Cloudy	None
25	06.30	-	Clear 0%	None
26	07.01	-	Clear 0%	None
27	07.02	-	Cloudy	None
28	07.04	-	Cloudy	Photographs taken.

Continuation of the table

№	Date	Time	Weather conditions	Presence and type of NLC
29	07.05	-	Cloudy	Photographs taken.
30	07.07	21:50 22:57	Partly cloudy	Not recorded by the IR camera, but captured by the conventional camera. Lunar illumination?
31	07.08	-	Cloudy	Photographed with two cameras. No NLCs.
32	07.14	21:46 22:27	Cloudy	Photographed with two cameras. No NLCs.
33	07.15	21:25 22:39	Clear	Formations resembling NLCs. Images taken with two cameras.
34	07.16	-	Clear	None
35	07.17	-	Clear	None
36	07.19	-	Clear	None
37	07.20	-	Clear	None. Photographs taken.
38	07.28	-	Cloudy	No NLCs. Photographs taken.
39	07.29	-	Cloudy	Photographs taken.
40	07.30	-	Cloudy	Images of lightning.
41	08.01	-	Cloudy	Interesting vortex.

Unfortunately, the number of nights in which NLC appeared during the 2025 season was small. It should be noted that the comparative rarity of NLC occurrences this season was also documented by other observers in the Northern Hemisphere. This circumstance is associated not with unfavorable weather conditions, but most likely with the physical influence of solar activity factors. As is known, the intensity of NLC formation can anti-correlate with solar activity indices [21-23].

4. Analysis oof twilight segment data in two spectral regions

Figure 3 presents examples of fragments of paired twilight segment images obtained during the study. Here, the IR images are presented in black and white. The dates and times of image acquisition are indicated.

Upon general review of the images, their substantial difference is noticeable. For example, LED lamps on the building roof are practically invisible in the IR images, which, however, is not surprising. Much more important are the sharp differences in cloud structure. In the upper and lower rows, details of cirrus and stratiform clouds that are barely distinguishable in the visible range are drawn with high contrast down to fine structural details in the IR region. In the middle row images, cloudiness in the visible range is virtually absent in the upper and central parts of the image, but it is clearly distinguishable (as cirrus clouds) in the IR rays.

Of particular interest is the comparison of images in which NLC are present (typically identified visually in the sky). Figure 4 provides a comparison of one such pair.

At the time of imaging (nautical twilight), the Sun was located at an altitude of -9.5° below the horizon. A simple visual comparison of the images appears to be quite challenging. While faint NLC bands are quite distinctly visible in the visible-light image, they are not as clearly traced in the IR region image. At the same time, cloud details in the upper left part are displayed with prominent relief in the IR image, whereas they are completely absent in the visible light image. A certain degree of clarity in the qualitative comparison of the informational value of the two approaches can be provided by determining the contrast coefficients of these and other images.

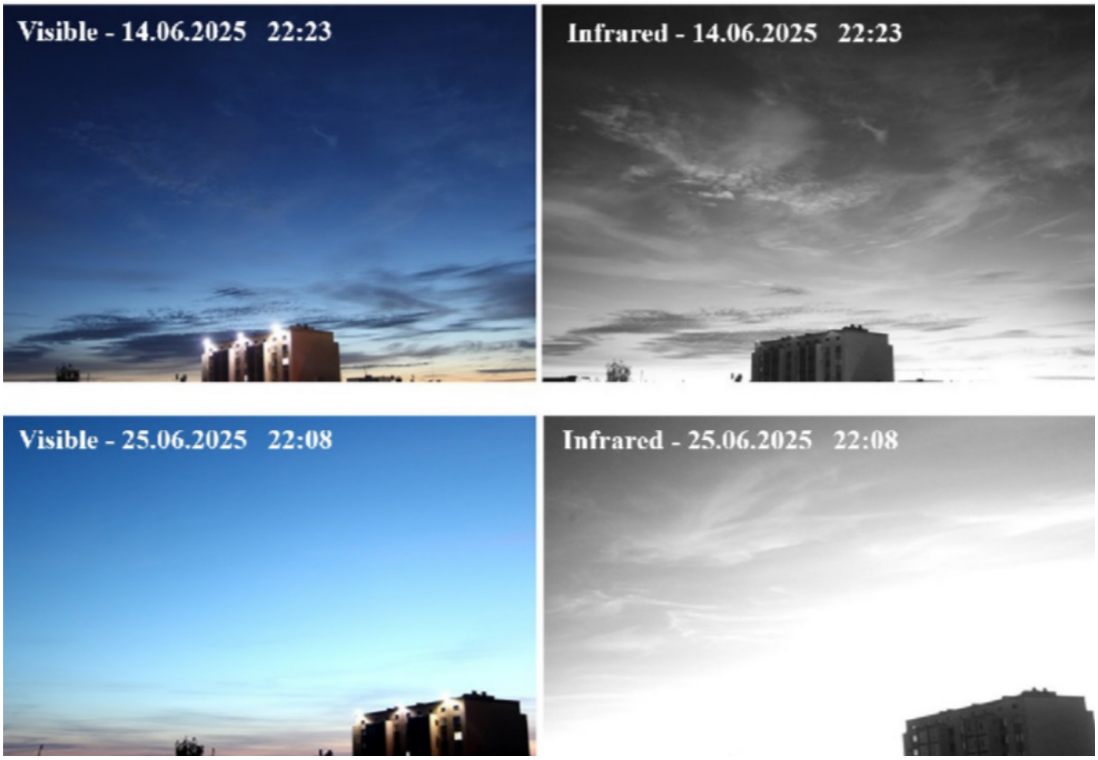

Figure 3. Examples of twilight segment images in the visible spectral region (left) and in the near-IR range ($\lambda \geq 850$ nm, right).

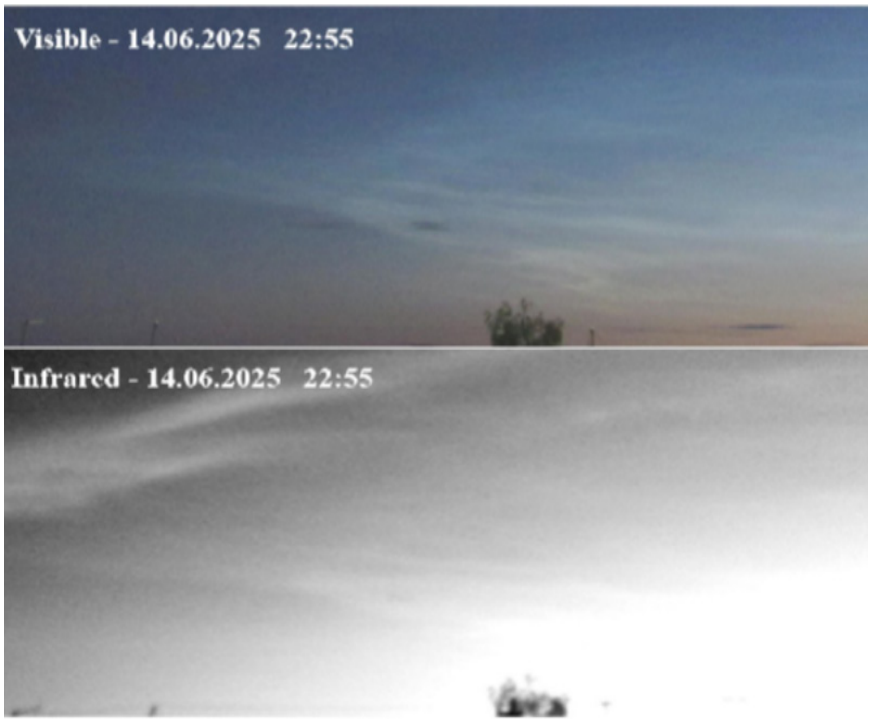

Figure 4. Twilight segment images where NLC are present.

5. Quantitative assessment of image information content

To assess the contrast of the twilight segment images, a method based on calculating the root-mean-square deviation (RMSD) of brightness was used. The method is implemented in available software programs [24-27]. Fundamental to this method is the principle that the greater the spread (variation) in pixel brightness values in an image, the higher the contrast. Here, the RMSD is precisely the mathematical measure of the spread of brightness values. In this procedure, the average brightness of all pixels is calculated for a given image area. Next, the difference between each pixel's brightness and the average value is determined. These values are squared, summed, divided by the number of pixels, and the square root is extracted from the result.

The result obtained is the standard deviation for the brightness of image pixels σ. The global contrast for the entire image was calculated using the formula:

$$K_{\Gamma} = \frac{2\sigma}{G-1}.$$

Processing of images to obtain a quantitative assessment of their quality (contrast) was performed using the ImageJ software package [29]. This program, in particular, allows one to obtain histograms of pixel brightness distribution across an image field and, if necessary, achieve local contrast enhancement. An example of processing and subsequent comparison of the results is shown in Figure 5.

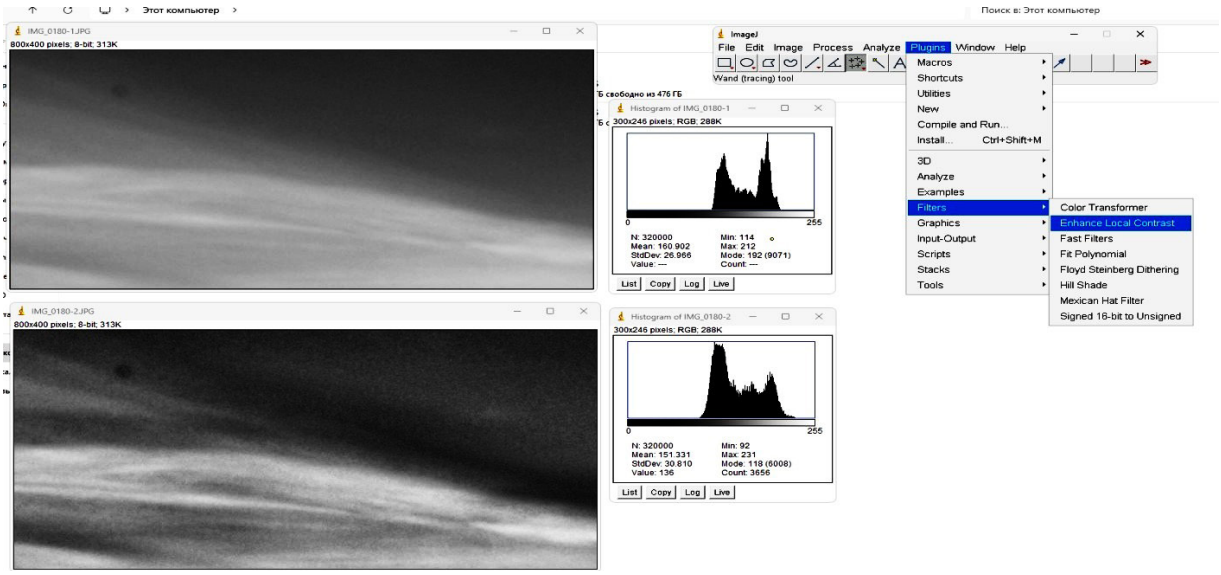

Figure 5. Example of image analysis and processing in ImageJ software.

When comparing the contrast of the photographs, the images were converted to a single 8-bit format. Using ImageJ software, identical objects were highlighted in both photographs, visible against the twilight sky. Exposure times for both cameras were selected to be as close as possible, with the difference in shooting times not exceeding 5 seconds. Table 2 provides examples of calculating the RMSD (σ) of pixel brightness for a series of twilight segment images in the visible range and in the near-IR spectral region.

As is easily observed, the change in cloud image contrast in the twilight segment upon transitioning from imaging in the visible spectral region to the near-IR region is positive throughout. At the same time, the spread of contrast change values is quite significant. A prime example of this is illustrated by the images from July 28, 2025 (Fig. 6).

Table 2. Comparison of image contrast in visible light and in the near-IR region.

Date of shooting	The visible region of the spectrum		The IR region of the spectrum		Changing the contrast, %
	Img_№	σ1	Img_№	σ2	(σ2-σ1)/ σ1
14.06	7008	23.5	0470	26.8	+ 14
	7011	19.5	0471	29.2	+ 50
	7014	15.7	0473	27.9	+ 78
25.06	0127	40.5	0534	49.3	+ 22
7.07	0168	46.0	0628	51.1	+ 11
14.07	0191	35.2	0655	51.4	+ 46
15.07	0201	31.0	0674	39.3	+ 27
28.07	0208	15.9	0700	35.7	+ 124
	0209	11.8	0705	13.3	+ 13
01.08	0210	35.6	0719	48.0	+ 35
	0213	28.2	0721	53.8	+ 91
	0215	22.2	0722	32.7	+ 47
	0216	13.1	0723	15.7	+ 20
Mean					+44

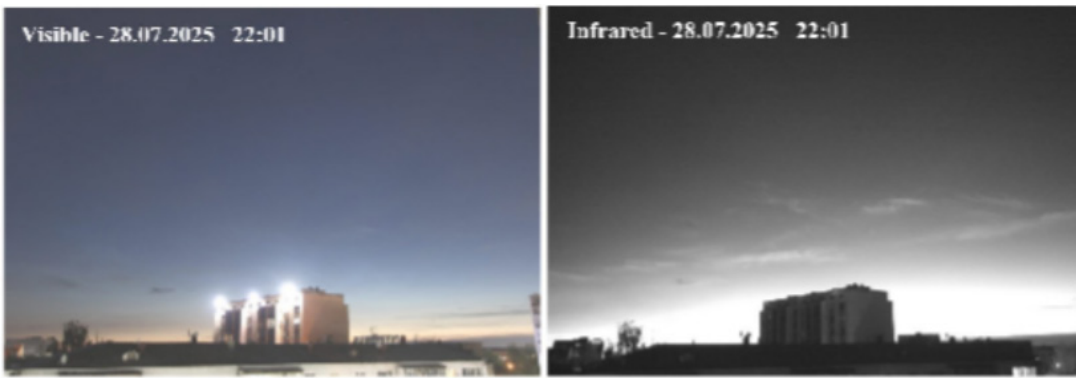

Figure 6. Twilight segment images with the greatest difference in contrast between the visible and IR ranges.

The cloudiness visible in the IR spectral region in Figure 4 may represent one of the high-altitude forms, including NLC. For now, one can only assume that the magnitude of the contrast change can be influenced by two external factors and one technical parameter. Firstly, the differences in the type of cloudiness in images taken on different dates, and secondly, differences in the altitude of the Sun below the horizon. Regarding the latter, this refers to the influence of the ratio between the camera sensitivity set during shooting and the exposure duration. As is known, high ISO values reduce image contrast, but it is difficult to avoid their use when imaging in the IR range due to the noticeably lower sensor sensitivity and much weaker radiation fluxes. In the perspective of further method refinement, these circumstances will need to be taken into account.

6. Examples of atmospheric objects and phenomena in the IR region

The abundance of material obtained during monitoring made it possible to identify interesting examples related to the specificities of operating in the IR range. Some of them warrant separate consideration.

For instance, on the night of July 29, a distant thunderstorm front was observed in the southwestern part of the twilight segment. Subsequently, analysis of the images revealed the presence of lightning discharges (Fig. 7).

In principle, this is not surprising. What is noteworthy is the fact that lightning is confidently discernible through the cloud medium on IR images, whereas on standard images or during visual observation, only an increase in the brightness of the cloud field is recorded.

Figure 7. Image fragment with a lightning discharge in the IR range.

In a number of cases, cloud formations that are completely inaccessible to the naked eye (whose contrast sensitivity is higher than that of conventional photography, making the sky look absolutely clear to the eye) are noticeable on IR images. An example is shown in Figure 8.

imilar situations were repeatedly recorded by the cameras. Thus, Figure 9 shows that in cases where images from a conventional camera (or visual observations) do not detect the presence of cloudiness in the sky, clouds may be present on images in the IR range. Identifying the cloud type in these cases can sometimes be quite difficult.

Figure 8. IR image of cloudiness in the form of filaments in the northwest direction at an altitude of 10-15 degrees, which are visually indistinguishable.

Structurally, the cloud field in the image obtained by the IR camera resembles one of the most transparent types of cirrus clouds (Ci fib or Cs fib). However, unlike the indicated cloud forms, they moved much faster, traveling in a southwestern direction. Such rapid movement is characteristic of high-altitude cloud types if they form in the uppermost layers of the troposphere or in the stratosphere at altitudes of 11–14 km [6, 29].

Figure 9. Cloudiness recorded only by the IR camera.

However, opposite situations were occasionally encountered, where a conventional camera recorded cloud details, while they were absent in the IR images. This occurred when there was an almost full Moon in the sky (Fig. 10).

Such situation can be explained by the attenuation of the IR component in the lunar spectrum compared to solar radiation. In this case the Moon lights cirrus clouds in the visible region of the spectrum even beyond the twilight segment. Inexperienced observers might mistake such view for NLC.

The high contrast of IR images sometimes completely alters the appearance of cloudiness compared to the picture in the visible spectral region. A striking example of this can be seen in Figure 11.

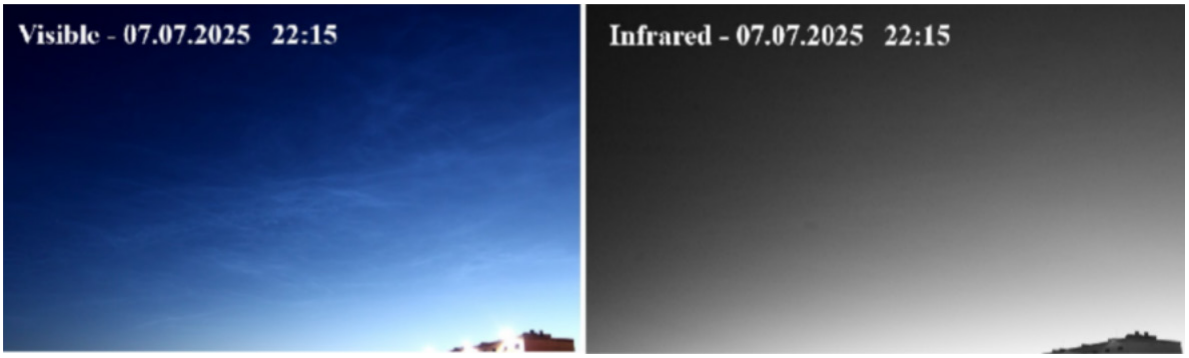

Figure 10. Illumination of cirrus clouds by a full Moon.

Figure 11. S-shaped cloud vortex on an IR image.

Here, in the IR range image, a vast cloud vortex in high-altitude stratiform clouds stands out. However, it is completely indistinguishable in visible light. Vortex structures in cloudiness are typically observed in satellite images. Thus, this example illustrates new possibilities for ground-based cloud study using IR cameras.

The image examples presented here do not exhaust the full scope of unusual objects or phenomena that were captured when imaging in the near-IR range. The most interesting cases are those when cloud formations are visible only in IR rays. Moreover, such objects often move very rapidly. Additionally, attention is drawn to the unusual morphology of cloud forms in such images. It is possible that, due to the increased contrast of the images, rather rare cloud forms have been captured on them. These could be, for example, finely dispersed dust clouds, the possible existence of which is pointed out by a number of researchers [30]. In particular, one might note the "ultracirrus" mentioned by Minnaert [6]. In this regard, it is obvious that observations of cloud forms in the near-IR region must be continued.

7. Discussion

Taking into account the fact that in the study of NLC obtaining images in the IR spectral region has not previously been practiced, it is not possible to compare the results of this work with the data of

other authors. Moreover, when conducting synoptic observations of NLC, researchers usually limited themselves to the fact of registering such cloudiness, without evaluating the information content (for example, contrast) of the images. And this is quite justified in the case of sufficiently bright cloud fields appearing in the sky. With this approach, the photographic method essentially refines visual observations, imparting to them such crucial qualities as documentation and objectivity.

Although the contrast sensitivity of the human eye is high, there are frequent cases where visual observations do not allow one to confidently judge the presence or absence of NLC in the twilight segment under favorable conditions of its illumination and clear weather. At the same time, discussing the possibility of registering NLC using traditional methods prior to the onset of nautical twilight generally makes no sense.

In this context, the results obtained during the present study provide grounds for an optimistic outlook on the prospects of using near-IR photography to expand capabilities in the study of NLC and other high-altitude cloud formations. This concerns the enhancement of image information content achieved through a significant increase in image contrast.

It should be considered that the potential of the proposed methodology at this stage is far from exhausted. A further increase in the contrast gain for cloud images in the twilight segment is achievable by applying identical ISO values on both the IR and conventional cameras. Naturally, this will require an increase in exposure times when shooting in the IR range, but they will nonetheless remain within acceptable limits. Alongside this, the implementation of cameras featuring sensors with higher sensitivity in the near-IR spectral region becomes a relevant prospect for the future.

8. Conclusion

In order to develop tools and methods for registering NLC during ground-based observations, this work substantiates the possibility of increasing image contrast in the twilight sky segment by transitioning to photographic observations in the near-IR spectral region. In doing so, the discriminability of the structure of low-contrast objects, which is difficult to distinguish when using traditional approaches, is enhanced. The increase in image contrast for diffuse cloud objects is achieved by reducing the background sky brightness.

To implement the new method for registering cloud forms, a Canon 1000D camera was modified by removing the built-in filter in front of the receiver that cuts off IR radiation. Concurrently, filters transmitting only IR radiation of specified wavelengths were mounted on the camera lens [17]. As a result, the sensitivity of the modified camera in the IR spectral region increased by approximately three orders of magnitude [17, 28]. During the summer season of 2025, using the Canon 1000DI camera, systematic observations of the twilight sky segment at wavelengths longer than 850 nm were conducted for the first time. Control images in the visible region were taken simultaneously using a Canon 2000D camera.

Visual matching and comparison of the numerical characteristics of the images in the IR and visible spectral regions revealed interesting results. In particular, in every randomly selected pair of images (IR and visible range), a higher contrast of cloud details was found specifically for the IR images. The relative contrast difference generally amounted to tens, and occasionally more than a hundred percent. Of course, looking ahead, it is interesting to investigate the factors influencing the magnitude of the contrast difference.

It is shown that upon visual comparison of the photographs, the higher image contrast allows for the identification of cloud structures on the IR images that are completely indistinguishable on the images in the visible spectral region [28]. Furthermore, the boundaries of cloud formations on IR images are much sharper, and the structural detailing is much higher than on visible light images. At the same time, the possibility emerges of expanding the temporal range for registering NLC by incorporating a portion of civil twilight into it.

Further refinement of the method for increasing the contrast and quality of cloud images in the twilight sky segment in the IR range is possible by equalizing the sensitivity (ISO) of the main and control cameras. It is possible that some of the cloud formations recorded exclusively in the IR region represent understudied forms of high-altitude clouds. Thus, one can speak of the prospect of applying IR cameras not only for NLC monitoring but also for studying other atmospheric formations whose registration in visible light is problematic [31-34].

Conflicts of interest

The authors declare no conflict of interest.

Author contributions

Conceptualization: A.S.S. and P.I.L.; Methodology: A.S.S., T.B.K. and B.M.U.; Software: T.B.K.; Validation: A.S.S, T.B.K., P.I.L. and B.M.U.; Formal Analysis: A.S.S., T.B.K., P.I.L. and B.M.U.; Investigation: A.S.S. and N.P. S.; Resources: N.P.S..; Data Curation: A.S.S., T.B.K., P.I.L. and B.M.U.; Writing – Original Draft Preparation: A.S.S. and P.I.L.; Writing – Review & Editing: A.S.S.; T.B.K and P.I.L.; Visualization: T.B.K.; Supervision: A.S.S.; Project Administration: B.M.U.; Funding Acquisition: N.P.S.. All authors have read and agreed to the published version of the manuscript.

References

1. M. Gadsden and W. Schröder, Noctilucent Clouds. New York, NY, USA: Springer, 1989.
2. V. A. Bronshten, Noctilucent Clouds and Their Observation: Observation Conditions, Heights and Velocities of Noctilucent Clouds, (in Russian). Moscow, Russia: Redaktsionnaya kollegiya, 1984.
3. P. A. Dalin, V. A. Romeiko, N. N. Pertsev, and V. I. Perminov, "Noctilucent clouds are already 130 years old," (in Russian), *Priroda*, no. 11(1203), pp. 18-26, 2015, EDN: VHXLIT.
4. S. V. Zvereva, *In a World of Sunshine*, (in Russian). Leningrad, USSR: Gidrometeoizdat, 1988.
5. G. V. Rozenberg, *Twilight*, (in Russian). Moscow, USSR: Fizmatgiz, 1963.
6. M. Minnaert, *Light and Color in the Outdoors*. Springer Science & Business Media, 1995.
7. O. S. Ugolnikov, I. A. Maslov, B. V. Kozelov, and J. M. Dlugach, "Noctilucent cloud polarimetry: Twilight measurements in a wide range of scattering angles," *Planet. Space Sci.*, vol. 125, pp. 105-113, 2016, https://doi.org/10.1016/j.pss.2016.03.010
8. O. S. Ugolnikov, A. A. Galkin, S. V. Pilgaev, and A. V. Roldugin, "Noctilucent cloud particle size determination based on multi-wavelength all-sky analysis," Planet. Space Sci., vol. 146, pp. 10-19, 2017. [Online]. Available: http://arxiv.org/abs/1611.00073
9. A. A. Solodovnik, P. I. Leontiev, and P. Dalin, "Studies of the influence of tropospheric factors on the formation of silvery clouds by cartographic method," *J. Atmos. Sol.-Terr. Phys.*, vol. 200, 2020, Art. no. 105224, https://doi.org/10.1016/j.jastp.2020.105224
10. A. Solodovnik, P. Leontiev, P. Dalin, B. Takenov, and D. Alyoshin, "Seasonal evolution and interseasonal changes in polar mesospheric clouds at high latitudes in the Southern Hemisphere," *J. Atmos. Sol.-Terr. Phys.*, vol. 226, 2021, Art. no. 105787, https://doi.org/10.1016/j.jastp.2021.105787
11. H. Gao, L. Li, L. Bu, Q. Zhang, Y. Tang, Z. Wang, "Effect of small-scale gravity waves on polar mesospheric clouds observed from CIPS/AIM," *J. Geophys. Res. Space Phys.,* vol. 123, pp. 4026-4045, 2018, https://doi.org/10.1029/2017JA024855
12. P. Dalin et al., "A case study of long gravity wave crests in noctilucent clouds and their origin in the upper tropospheric jet stream," *J. Geophys. Res. Atmos.*, vol. 121, no. 23, 2016, https://doi.org/10.1002/2016JD025422
13. N. Shevchuk, N. Pertsev, P. Dalin, V. Perminov, "Wave-induced variations in noctilucent cloud brightness: Model and experimental studies," *J. Atmos. Sol.-Terr. Phys.*, vol. 203, 2020, Art. no. 105257, https://doi.org/10.1016/j.jastp.2020.105257
14. V. P. Hart et al., "Investigating gravity waves in polar mesospheric clouds using tomographic reconstructions of AIM satellite imagery," *J. Geophys. Res. Space Phys.*, vol. 123, pp. 955-973, 2018, https://doi.org/10.1002/2017JA024481
15. A. Solodovnik, A. Baibusinova, D. Kudabaeva, "Dynamics of the development of the field of noctilucent clouds in the northern Hemisphere in the period 2013-2020," *Bull. KazNTU*, no. 4(140), pp. 138-144, 2020.
16. P. Dalin et al., "Ground-based observations of noctilucent clouds with a Northern Hemisphere network of automatic digital cameras," *J. Atmos. Sol.-Terr. Phys.*, vol. 70, pp. 1460-1472, 2008. https://doi.org/10.1016/j.jastp.2008.04.018
17. A. Solodovnik, R. Zyryanov, P. Leontyev, B. Useinov, E. Gololobova, and P. Zhuravlev, "Experience of noctilucent clouds registering in the near infrared spectrum region," *Phys. Sci. Technol.*, vol. 11, no. 1-2, 2024. https://doi.org/10.26577/phst2024v11i1a10
18. A. A. Solodovnik, P. I. Leontyev, B. M. Useinov, A. D. Kadyrmin, and R. O. Zyryanov, "Application of electronic receivers for recording infrared images of celestial phenomena at the CAR of the NKU," *Phys. Sci. Technol.*, vol. 10, no. 1-2, 2023. https://doi.org/10.26577/phst.2023.v10.i1.07
19. A. Sheverdin, "Technological innovations of OmniVision CMOS cameras: An optimal choice for high-volume applications," (in Russian), *Komponenty i Tekhnologii*, no. 1, 2008.
20. Canon Inc., *Canon EOS 2000D User Manual*, (in Russian). Tokyo, Japan: Canon Inc., 2017.
21. S. Qiu et al., "Solar-induced 27-day modulation on polar mesospheric cloud (PMC), based on combined observations from SOFIE and MLS," *Front. Astron. Space Sci.*, vol. 10, 2023, Art. no. 1168841, https://doi.org/10.3389/fspas.2023.1168841
22. V. I. Perminov et al., "Response of the mesopause region airglow to short-period changes in solar activity," (in Russian), *Geomagn. Aeron.,* vol. 63, no. 1, pp. 63-72, 2023.
23. A. Sarsembayeva, L. Ryssaliyeva, F. Belissarova, and A. Sarsembay, "Solar magnetic activity and its terrestrial impact through correlations with drought indices," *Phys. Sci. Technol*., vol. 12, no. 1-2, pp. 38-44, 2025. https://doi.org/10.26577/phst20251214
24. Yu. I. Golub and F. V. Starovoitov, "Study of local contrast estimates of digital images in the absence of a reference," (in Russian), *Syst. Anal. Appl. Inform.*, no. 2, pp. 4-11, 2019, https://doi.org/10.21122/2309-4923-2019-2-4-11
25. S. A. Kadnichanskiy, "Contrast estimation of digital aerial photographs and satellite images," (in Russian), *Geod. Cartogr.,* no. 3, pp. 46-51, 2018, https://doi.org/10.22389/0016-7126-2018-933-3-46-51
26. "Numerical characteristics of the image. The tonal range," MyPresentation.ru. Accessed: Mar. 4, 2023. [Online]. Available: https://mypresentation.ru/presentation/chislovye-xarakteristiki-izobrazhenij

27. "Processing of images and video files. How to read, understand and recognize the histogram of an image," Rugraphics.ru. Accessed: Mar. 4, 2023. [Online]. Available: https://rugraphics.ru/photoshop/kak-chitat-ponimat-raspoznavat-gistogrammu

28. T. B. Kasenov, "Evaluation of image contrast when working with an infrared camera EOS Canon-1000D," (in Russian), in Proc. Int. Sci.-Pract. Conf. Youth and Science-2025: Modern Challenges and Scientific Approaches to Solving Them, Dedicated to the 100th Anniversary of Evnei Arstanovich Buketov, Petropavlovsk, Kazakhstan, Apr. 9, 2025, pp. 391–396, EDN: AIQXRA.

29. T. Ferreira and W. S. Rasband, "ImageJ User Guide—IJ 1.46," ImageJ.net, 2010-2012. [Online]. Available: https://imagej.net/ij/docs/guide/

30. A. V. Kislov and G. V. Surkova, *Climatology: Textbook.* Moscow, Russia: INFRA-M, 2022.

31. A. A. Solodovnik, R. A. Kleksin, P. I. Leontyev, B. M. Useinov, A. G. Markova, and S. A. Kassimova, "Revealing the noctilucent cloud fields structure by software processing of satellite images," *Phys. Sci. Technol*., vol. 12, no. 1-2, pp. 4-13, 2025. https://doi.org/10.26577/phst20251211

32. A. A. Solodovnik, B. M. Useinov, T. B. Kassenov, P. L. Zhuravlev, and E. A. Solodovnik, "Experience of using an infrared camera in the study of astronomical objects," *Recent Contrib. Phys.*, no. 1(96), pp. 14-22, 2026.

33. A. A. Solodovnik, P. I. Leontyev, S. A. Sartin, B. M. Useinov, D. V. Alyoshin, and P. Dalin, "Physical bases of meteor registration methods and the instrument complex of the NKU Observatory," *Int. J. Math. Phys.,* vol. 13, no. 2, 2022. https://doi.org/10.26577/ijmph.2022.v13.i2.04A

34. P. Razzhivalov, N. Korobova, and S. Shatalova, "Earth sensing capabilities yesterday and today," *Phys. Sci. Technol.,* vol. 8, no. 1-2, pp. 26-34, 2021. https://doi.org/10.26577/phst.2021.v8.i1.03

Information about the authors:

Andrey Solodovnik – Candidate of Physico-Mathematical Sciences, Professor at the M. Kozybayev North Kazakhstan University (Petropavlovsk, Kazakhstan, e-mail: asolodovnik@ku.edu.kz).

Timur Kassenov – Master's student at the M. Kozybayev North Kazakhstan University (Petropavlovsk, Kazakhstan, e-mail: timur.kasenov.2002@mail.ru).

Pavel Leontyev – Candidate of Physico-Mathematical Sciences, Associate professor at the M. Kozybayev North Kazakhstan University (Petropavlovsk, Kazakhstan, e-mail: pleontyev@mail.ru, pleontiev@ku.edu.kz).

Beibut Useinov (corresponding author) – Candidate of Physico-Mathematical Sciences, Professor at the M. Kozybayev North Kazakhstan University (Petropavlovsk, Kazakhstan, e-mail: buseinov@gmail.com).

Nadezhda Solodovnik – research associate at the M. Kozybayev North Kazakhstan University (Petropavlovsk, Kazakhstan, e-mail: npsolodovnik@mail.ru).

IRSTI 31.15.37 https://doi.org/10.26577/phst20261315

Synthesis of a montmorillonite-based nanocomposite with antibacterial properties

D.K. Bolatkan[1*], K. Akatan[1], S.K. Kabdrakhmanova[2*], V.V. Davydova[3] and Sh.A. Muzdybayeva[4]

[1]S.Amanzholov East Kazakhstan University, Ust-Kamenogorsk, Kazakhstan
[2]Satbayev University, Almaty, Kazakhstan
[3]International R&D Center for Advanced Functional Materials and their Composite, Almaty, Kazakhstan
[4]International Engineering Technological University, Almaty, Kazakhstan
*e-mail: chilibayeva35@gmail.com

(Received March 31, 2026; received in revised form May 18, 2026; accepted May 28, 2026)

This study investigates the intercalation of montmorillonite clays from the Tagan deposit with silver nanoparticles and evaluates their potential for biomedical applications. Purification of the raw material using the Salo method ensured the removal of coarse mineral impurities and enrichment of the montmorillonite fraction. The analyses revealed the predominance of montmorillonite and kaolinite in the purified samples, while SEM data confirmed increased porosity and effective distribution of silver nanoparticles within the interlayer space. Modification resulted in the formation of a hybrid structure with high surface reactivity, allowing the material to be considered a promising carrier for the immobilization and controlled release of pharmaceutical substances. In addition, the modified bentonite may be used in antimicrobial coatings, wound-healing materials, drug delivery systems, medicinal ointments, as well as in sorption and environmental protection technologies. The incorporation of silver nanoparticles also enhanced the antibacterial potential of the clay matrix, which is particularly important for the development of advanced biomedical and healthcare-related materials. Furthermore, the combination of natural clay minerals with nanoscale silver provides a cost-effective and environmentally friendly platform for creating multifunctional composites with improved physicochemical and biological properties. The results confirm that purification and functionalization with silver nanoparticles significantly improve the properties of these clays and expand their potential practical applications.

Keywords: montmorillonite, silver nanoparticles, green method, antibacterial properties, nanocomposite.

1. Introduction

The widespread application of montmorillonite clays is determined by their distinctive physicochemical properties, natural abundance, and environmental safety [1]. In recent years, the growing interest in the use of polymer–clay nanocomposites in drug delivery systems has made montmorillonite-based materials a relevant subject of biomedical research [2]. Montmorillonite is the principal mineralogical component of bentonite and, as a layered aluminosilicate belonging to the smectite group, is distinguished by its high sorption capacity, pronounced adsorption activity, and considerable swelling ability [3]. However, the presence of kaolinite, quartz, mica, calcite, and other mineral impurities in natural bentonites may reduce their degree of purity and functional performance. In addition, coarse dispersed impurities such as sand and stone disrupt the structural homogeneity of the clay matrix, thereby limiting the material's biomedical applicability[4]. Therefore, their preliminary removal is of critical importance [4]. For this reason, thorough purification and targeted pretreatment of the raw material play a decisive role in the production of bentonite-based materials intended for medical applications [5-6]. Purified bentonite exhibits high adsorption capacity, biocompatibility, and the ability to control the release of immobilized active components [7]. In this regard, it is regarded as an effective carrier material for the development of solid dosage forms, including tablets and capsules [8]. Studies [9-10] have reported that montmorillonites have increasingly been used as potential raw materials for the formulation of deep-cleansing facial

masks and skincare creams due to their safety, bioinertness, and environmental friendliness.

Recent studies have demonstrated that the effective functionalization of the interlayer space of bentonite with nanoparticles enables the targeted modification of its properties and the expansion of its application potential [11]. Although purified bentonite possesses a large specific surface area, high cation-exchange capacity, and good biocompatibility, its antibacterial activity remains limited. Studies [12–13] have shown that modification with silver and copper nanoparticles significantly enhances the functional characteristics of bentonite, including its antimicrobial activity. In this context, the interlayer space of bentonite serves as a favorable structural environment for the incorporation of metal nanoparticles. The incorporated metal atoms combine to form nanoparticles and establish stable interactions with the layers of the clay mineral. As a result of such interactions, silver nanoparticles become immobilized within the interlayer region, thereby preventing the formation of low-activity aggregates and conglomerates. This process is accomplished through a spontaneous cation-exchange mechanism. It has been concluded that this contributes to enhancing the stability and biological activity of nanocomposites based on modified bentonite.

In recent years, montmorillonite clay has been considered a promising inorganic matrix for the development of antibacterial nanocomposites due to its layered structure, high cation-exchange capacity, availability, and ability to stabilize metallic nanoparticles. Of particular interest are AgNP–MMT systems, in which silver nanoparticles can be intercalated into the interlayer space of montmorillonite. This may reduce AgNP aggregation, improve their dispersion, and contribute to prolonged antibacterial activity. According to recent literature data, silver-containing montmorillonite materials exhibit antibacterial activity against both Gram-positive and Gram-negative microorganisms, making them promising for biomedical, packaging, and environmental applications. In addition, the use of "green" synthesis methods involving plant extracts or mild reducing approaches can reduce the use of toxic reagents and improve the environmental safety of AgNP–MMT nanocomposite preparation. Recently, in accordance with the principles of green chemistry, priority has been given to the green synthesis of metal nanoparticles incorporated into antibacterial composites intended for biomedical applications [14]. Recent studies have demonstrated that nanostructured materials prepared by environmentally friendly approaches can exhibit promising properties for biomedical and bioimaging applications, highlighting the importance of particle size, surface chemistry, and biocompatibility for their practical use [15-17].This, in turn, has been found to ensure the environmentally safe use of synthesized metal nanoparticles and to maximize the safety of their application. The novelty of this study lies in the use of local bentonite clay from the Tagan deposit, with montmorillonite as the main mineral component, as a carrier matrix for silver nanoparticles. Unlike previously reported AgNP–montmorillonite systems, the present work focuses on the intercalation of green-synthesized silver nanoparticles into a local natural bentonite clay and the evaluation of the antibacterial properties of the obtained material. Thus, the study combines the use of regional mineral raw material, an environmentally friendly synthesis approach, and the development of a silver-containing bentonite material with potential antibacterial activity.

Accordingly, the present study aimed to investigate the possibility of obtaining an antibacterial nanocomposite by preliminary water activation of natural bentonite samples from the Tagan deposit and subsequent intercalation of green-synthesized silver nanoparticles into the bentonite matrix.

2. Experimental section

2.1 Pretreatment of bentonite clay

Bentonite samples obtained from the Tagan deposit were selected as the study material and prepared as a suspension in deionized water at a ratio of 1:20 g/mL, following the procedure reported in our previous study [4]. The obtained suspension was magnetically stirred at room temperature at 1000 rpm for 8 h, followed by treatment at 90 °C for 2 h. The resulting suspension was then lyophilized at −60 °C for 5 h.

2.2 Intercalation of silver nanoparticles synthesized via a green method into the montmorillonite matrix

Silver nanoparticles synthesized via the green method reported in study [18] were intercalated into the montmorillonite matrix. The required concentration was prepared using two different approaches. In the first method, 5 g of water-modified bentonite clay was added to silver nanoparticle suspensions with volumes of 25, 50, and 75 mL (samples 1-6), followed by continuous stirring on a magnetic stirrer. In the second method, silver nanoparticles were added to the aqueous swollen clay suspension at volume ratios of 1:3, 1:1, and 3:1 (mL/mL) and intercalated under continuous stirring (samples 7-12).

The bentonite samples investigated in this work were conventionally labeled as Mt_1 and Mt_2, while the nanocomposite clay samples intercalated with silver nanoparticles were designated as Mt_1-AgNPs and Mt_2-AgNPs. Depending on the nature of the analysis, either the suspension of modified montmorillonite clay or its lyophilized dry form was employed.

2.3 Determination of the microbiological purity of montmorillonite clay and the antibacterial properties of the obtained nanocomposite clay

The antibacterial properties and microbiological purity were determined by the inoculation method in accordance with the requirements of the State Pharmacopoeia of the Republic of Kazakhstan (pp. 176–180, Section 2.6.12). A suspension was prepared by adding 1 g of the nanocomposite to 9 mL of 0.9% sodium chloride solution containing peptone at pH 7, followed by intensive mixing. During the study, the suspension was subjected to a tenfold dilution.

A 1 mL aliquot of the tenfold diluted suspension was transferred into 90 mm Petri dishes, after which 15–20 mL of molten culture medium at a temperature not exceeding 45 °C was poured onto the sample. Meat-peptone agar was used for bacterial cultivation, whereas Sabouraud medium was employed for the cultivation of molds and yeasts. The bacterial strains were incubated at 30–35 °C for 48 h, while the molds were incubated at 20–25 °C for 5 days.

Colony counting was performed on plates containing 30–300 colonies for bacteria and 10–100 colonies for fungi. The number of viable microorganisms (CFU/mL) was calculated taking into account the dilution factor and the volume of the inoculated sample. The average value of two parallel analyses was used for the calculations.

The concentration of viable microorganisms was calculated using the following formula:

$$N = \frac{C}{V} * \frac{1}{d} \quad (1)$$

where N is the concentration of microorganisms in the initial sample (CFU/mL), C is the number of colonies on the plate, V is the volume of the inoculated sample (mL), and d is the dilution factor.

2.4 FTIR spectroscopy

The chemical structure of the samples was investigated using an FTIR FT-801 infrared spectrometer (Simex, Russia) in the 500–4000 cm^{-1} wavenumber range, with a resolution of 1 cm^{-1}, at 25 ± 2 °C, using 100 scans. During the analysis, the clay powders were mixed with potassium bromide at a 1:9 ratio and ground in an agate mortar until a completely homogeneous mixture was obtained. The resulting mixture was then placed in a pellet-forming ring and compressed using a press at 200 MPa for 5 min, while water vapor was removed by a vacuum pump, to obtain a pellet.

2.5 X-ray fluorescence analysis

The major elemental composition of bentonite clay was determined by energy-dispersive X-ray fluorescence (EDXRF) using an Epsilon 4 X-ray fluorescence spectrometer (Malvern Panalytical B.V., Almelo, The Netherlands). Measurements were carried out using an Ag-anode X-ray tube and an SDD detector, at an accelerating voltage range of 4.0–50 kV and a current of up to 3.0 mA. The samples were analyzed in powdered form as pressed pellets. The results were presented as elemental concentrations.

2.6 X-ray diffraction analysis

The structural and phase characteristics of the samples were investigated by X-ray diffraction using an X'PertPRO diffractometer (Malvern Panalytical Empyrean, The Netherlands) with monochromatized CuKα radiation (K-Alpha1 [Å] = 0.1542) at a scanning step size of 0.02°. During the analysis, the measurements were carried out over an angular range of 10–80°, with an X-ray tube voltage of 45 kV, a current of 30 mA, and a counting time of 0.5 s per step; a universal aluminum sample holder (PW1172/01) was used.

2.7 SEM analysis

The surface morphology of the samples was examined using a Quanta 200 3D scanning electron microscope (FEI™, Netherlands). The measurements were performed in high-vacuum mode at an accelerating voltage of 5 kV, using a secondary electron detector. To improve electron conductivity, the surface of the mineral clays was coated with gold nanoparticles.

2.8 Viscosity of the nanocomposite

The dynamic viscosity of the samples was determined using a rotational viscometer (BOYN, Hangzhou Boyn Instrument Co., Ltd., China). The analysis was performed at a temperature of 25 ± 2 °C and a relative humidity of 50 ± 5%. The sample was placed in the measuring vessel, and care was taken to prevent the formation of air bubbles. The spindle was immersed into the sample up to the working level, and the measurement was carried out at a rotational speed selected in accordance with the technical oper-

ating mode of the instrument. After the readings had stabilized, the viscosity value was recorded in mPa·s. To ensure measurement repeatability and comparability of the results, all analyses were performed under identical experimental conditions. Each sample was measured at least three times, and the results were processed as the mean ± standard deviation.

3. Results and discussion

3.1 Assessment of the microbiological purity of montmorillonite clay and the antibacterial activity of the obtained nanocomposite clay

According to the requirements of the State Pharmacopoeia of the Republic of Kazakhstan, the analysis of the microbiological purity of the purified clay samples Mt_1 and Mt_2 revealed a total aerobic microbial count of 0.92×10^4 CFU/g. This value did not exceed the permissible limit ($\leq 1 \times 10^4$ CFU/g). The yeast and mold count was 0.95×10^2 CFU/g, which also remained within the acceptable range ($\leq 1 \times 10^2$ CFU/g).

For the Mt_2 clay sample, the total aerobic microbial count was 0.89×10^4 CFU/g, while the yeast and mold count was 0.8×10^2 CFU/g. These values fully complied with the pharmacopoeial requirements. The obtained results demonstrated that the studied samples complied with the requirements of the State Pharmacopoeia of the Republic of Kazakhstan for non-sterile medicinal products of natural origin. In addition, these results were consistent with the data reported in study [4] regarding the microbiological purity of montmorillonite clay. Thus, it was confirmed that the samples used in the present study possessed the microbiological purity characteristic of montmorillonite clays.

Figure 1 presents the antibacterial properties of the initial montmorillonite clay samples, Mt_1 and Mt_2, as well as those of the nanocomposite samples obtained after intercalation. No inhibition zones were observed for either Mt_1 or Mt_2 clay against the tested microorganisms. For series 1–3 and 4–6 of the nanocomposite clay samples, a clear trend was observed toward an increase in the microbial growth inhibition zone with increasing volume of AgNPs in the solution. In sample No. 3 (Mt1 + 75 mL AgNPs), the inhibition zone reached 11 mm, whereas in sample No. 6 (Mt2 + 75 mL AgNPs), it was 11.2 mm. A similar relationship was also observed for the mixed compositions of samples 7–9 and 10–12. This indicates the dose-dependent nature of the antibacterial effect of AgNPs. Comparative analysis showed that the antibacterial activity of the studied compositions against Escherichia coli and Staphylococcus saprophyticus was generally comparable.

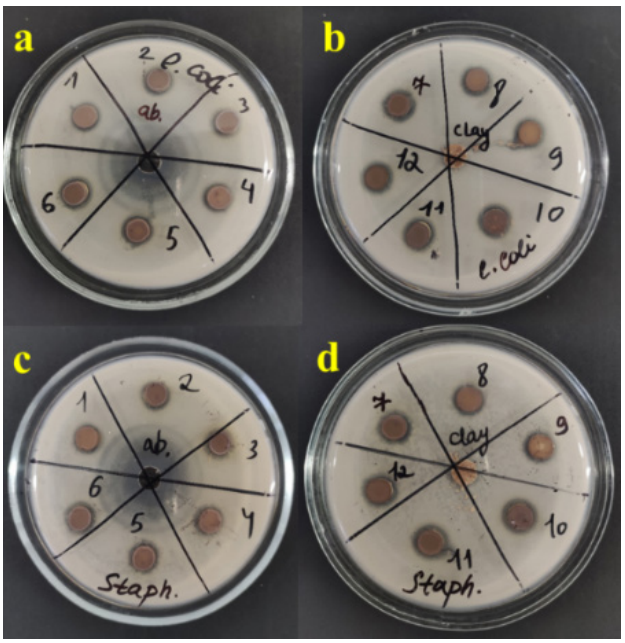

Figure 1. Results of the antibacterial activity assay. Inhibition zones against E. coli: (a) samples 1–6 and (b) samples 7–12; inhibition zones against S. saprophyticus: (c) samples 1–6 and (d) samples 7–12.

Table 1. Antibacterial activity of the nanocomposite clay.

Sample numbers	Sample designation	Average ± SEM (mm)	
		Escherichia coli	*Staphylococcus saprophyticus*
5 g of dry, purified montmorillonite clay and various concentrations of AgNPs			
1	Mt_1 + 25 ml AgNPs	10.00 ± 0.06^b	10.00 ± 0.07^b
2	Mt_1+ 50 ml AgNPs	10.40 ± 0.07^b	10.50 ± 0.06^b
3	Mt_1 + 75 ml AgNPs	11.00 ± 0.08^a	10.70 ± 0.07^{ab}
4	Mt_2 + 25 ml AgNPs	10.00 ± 0.06^b	10.30 ± 0.08^b

Continuation of the table

Sample numbers	Sample designation	Average ± SEM (mm)	
		Escherichia coli	*Staphylococcus saprophyticus*
5	Mt_2 + 50 ml AgNPs	10.30 ± 0.07[b]	10.20 ± 0.06[b]
6	Mt_2 + 75 ml AgNPs	11.20 ± 0.09[a]	11.40 ± 0.08[a]
Addition of AgNPs to the bentonite clay suspension in different volumes			
7	30 ml Mt_2 + 70 ml AgNPs	11.00 ± 0.07[a]	10.50 ± 0.06[b]
8	50 ml Mt_2 + 50 ml AgNPs	10.00 ± 0.06[b]	10.00 ± 0.07[b]
9	70 ml Mt_2 + 30 ml AgNPs	10.00 ± 0.07[b]	9.50 ± 0.08[c]
10	30 ml Mt_1 + 70 ml AgNPs	11.00 ± 0.08[a]	11.00 ± 0.07[a]
11	50 ml Mt_1 + 50 ml AgNPs	10.00 ± 0.06[b]	10.70 ± 0.08[ab]
12	70 ml Mt_1 + 30 ml AgNPs	9.70 ± 0.07[c]	10.50 ± 0.06[b]

The control samples consisting of the pristine clay did not exhibit any inhibitory activity. In contrast, the nanocomposite material intercalated with silver nanoparticles demonstrated pronounced antibacterial activity. These results indicate that silver nanoparticles play a decisive role in the development of antibacterial activity [18]. The results of the study revealed that the sample containing 5 g of montmorillonite clay intercalated with 75 mL of silver nanoparticles exhibited the highest antimicrobial activity. In addition, considering that the Mt_1 and Mt_2 samples met the requirements for microbiological purity, these two montmorillonite clay samples and this specific ratio with silver nanoparticles were selected as the basis for the subsequent synthesis of the nanocomposite material.

A clay–water system was used as a negative control to confirm that the pristine clay matrix itself did not exhibit antibacterial activity. No inhibition zone was observed for this control sample, indicating that the unmodified clay did not significantly suppress microbial growth. Erythromycin was used as a positive control to confirm the viability of the tested microorganisms and the correctness of the agar diffusion method. The inhibition zone of erythromycin was 22.1 mm, while the Mt_2-AgNPs sample obtained using 75 mL of AgNPs solution showed an inhibition zone of 11.2 mm.

For a more quantitative comparison, the relative antibacterial activity of Mt_2-AgNPs was calculated as follows:

$$\text{Relative antibacterial activity} = \\ = 11.2/22.1 \times 100 \approx 50.7\%$$

Thus, under the experimental conditions used in this study, the antibacterial activity of the Mt_2-AgNPs sample was approximately 50.7% of that of erythromycin. It should be noted that erythromycin was used not as a direct functional analogue of the studied material, but as a standard positive control to validate the test system.

In addition, our result is comparable with literature data [19] reported an inhibition zone of 10.74 mm for an AgNPs–MMT system, which is close to the value obtained in our study (11.2 mm). The difference is 0.46 mm, or approximately 4.3%, indicating that the antibacterial activity of our material is consistent with previously reported silver-containing montmorillonite systems.

3.2 FTIR analysis

Figure 2 shows the comparative FTIR spectra of the pristine Mt_1 and Mt_2 samples and the AgNP-modified samples, Mt_1-AgNPs and Mt_2-AgNPs. For all samples, the intense absorption band in the 1000-1002 cm^{-1} region is attributed to Si-O stretching vibrations characteristic of smectites, particularly montmorillonite. The peak near 920 cm^{-1} corresponds to the deformation vibrations of Al–Al–OH/Al–OH groups in the octahedral layer. The peaks in the region of 517 cm^{-1} are attributed to the lattice vibrations of Si–O–Al and Al–O–Si bonds. The peak at 1445 cm^{-1} is attributed to the presence of carbonate salts in the mineral clay composition. The band at 1632 cm^{-1} is associated with the H–O–H bending vibrations of adsorbed or interlayer water, while the broad absorption region at 3463–3632 cm^{-1} is explained by the O–H stretching vibrations of structural

hydroxyl groups and physically bound water. Such a set of peaks confirms the aluminosilicate nature of bentonite, more specifically its layered structure rich in montmorillonite, and this interpretation is consistent with studies in which clay minerals were investigated by FTIR spectroscopy [20]. The preservation of the main characteristic peaks after the incorporation of silver nanoparticles indicates that the silicate framework of bentonite remained intact. These results suggest that silver-containing species may interact with the montmorillonite structure, possibly through partial intercalation without causing destruction of the basic aluminosilicate framework [21]. Studies by Praus, P. and Turicová, M. have shown that the intercalation of AgNPs into the clay matrix occurs while preserving the structural framework [22]. From a biomedical perspective, such structural preservation and surface functionalization are of great importance, since silver-modified montmorillonite systems of this kind are considered promising components for antimicrobial materials, drug delivery platforms, and composite materials for external wound applications [23]. The preservation of the main Si–O, Al–OH, and O–H vibration bands after the incorporation of silver nanoparticles indicates that the basic layered aluminosilicate framework of bentonite remained intact. At the same time, slight changes in the intensityrelated to O–H stretching and H–O–H bending vibrations may reflect changes in the hydration state of the clay and possible interactions between silver-containing species, surface hydroxyl groups, and interlayer water molecules [24-25]. Therefore, the FTIR results suggest that AgNP incorporation is accompanied by interaction with active sites of the montmorillonite structure. These interactions may contribute to the stabilization and dispersion of silver nanoparticles in the clay matrix, which is important for maintaining antibacterial functionality [26-27].

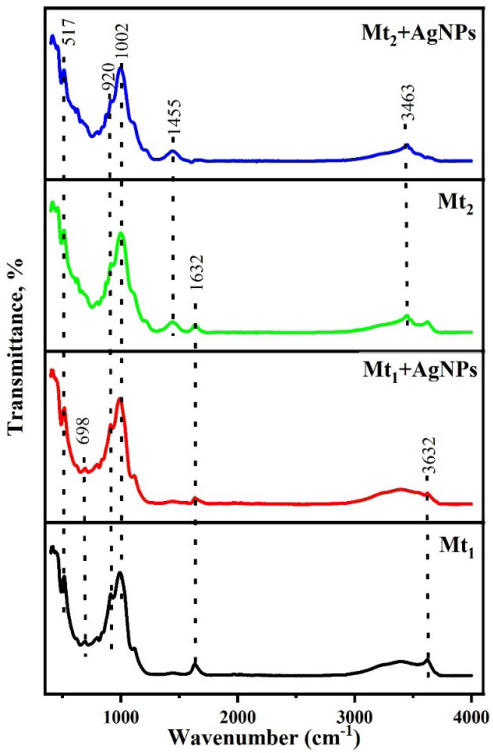

Figure 2. Comparative FTIR spectra of the initial Mt_1 and Mt_2 samples and the AgNP-modified samples, Mt_1-AgNPs and Mt_2-AgNPs.

3.3 XRF analysis

The comparative elemental composition of the pristine Mt_1 and Mt_2 samples, as well as the silver nanoparticle-modified Mt_1-AgNPs and Mt_2-AgNPs samples, is presented in the table. The obtained results indicate that the composition of the investigated samples is mainly represented by elements characteristic of aluminosilicate minerals. Si and Al were dominant in all samples, indicating that these elements constitute the main framework-forming com-

ponents. In particular, the pristine Mt_1 sample contained 25.021% Si, 8.315% Al, 2.119% Ca, 1.567% Fe, and 1.424% Mg, while the Mt_2 sample contained 26.989% Si, 9.017% Al, 4.991% Ca, 2.858% Fe, and 1.095% Mg. These values reflect the aluminosilicate nature of the studied samples and their elemental composition characteristic of clay minerals, including montmorillonitic materials. In addition, the presence of cation-exchangeable elements such as Ca, Mg, Fe, and K may positively contribute to the high sorption and ion-exchange properties of these materials [28].

After modification with silver nanoparticles, a slight decrease in the content of the major elements was observed in the Mt_1-AgNPs and Mt_2-AgNPs samples. For example, in the Mt_1-AgNPs sample, the Mg content decreased from 1.424% to 1.371%, Ca from 2.119% to 2.005%, Fe from 1.567% to 1.314%, and P from 0.444% to 0.412%. Similarly, in the Mt_2-AgNPs sample, the contents of Al, Si, Ca, and Fe were found to decrease from 9.017% to 8.099%, from 26.989% to 26.122%, from 4.991% to 4.361%, and from 2.858% to 2.658%, respectively. These changes can be explained by the partial substitution of weakly bound ions on the sample surface and in the interlayer space during the incorporation of silver nanoparticles, as well as by the restructuring of the surface layer [24].

In addition, the Ag content increased markedly after modification. Specifically, while the Ag content in the initial Mt_1 sample was only 0.003%, it increased to 0.312% in the Mt_1-AgNPs sample. A similar pattern was also observed in the Mt_2 system: the Ag content was 0.001% in the initial sample and increased to 0.297% in the Mt_2-AgNPs sample. These values confirm the successful immobilization of silver nanoparticles on the clay matrix surface and demonstrate the effectiveness of the modification process.

Table 2. Main elemental composition of the initial Mt_1 and Mt_2 samples and the AgNP-modified Mt_1-AgNPs and Mt_2-AgNPs samples.

Elements	Mt_1,%	Mt_1- AgNPs,%	Mt_2, %	Mt_2- AgNPs, %
Mg	1.424	1.371	1.095	1.071
Al	8.315	8.305	9.017	8.099
Si	25.021	25.001	26.989	26.122
P	0.444	0.412	0.412	0.365
K	0.078	0.052	0.132	0.06
Ca	2.119	2.005	4.991	4.361
Mn	0.119	0.105	0.157	0.147
Fe	1.567	1.314	2.858	2.658
Ag	0.003	0.312	0.001	0.297

3.4 X-ray diffraction analysis

Figure 3 shows the X-ray diffractograms of the initial Mt_1 and Mt_2 samples and the AgNP-modified samples, Mt_1-AgNPs and Mt_2-AgNPs. For the initial Mt_1 and Mt_2 samples, the intense reflection in the $2\theta = 26.5°$ (101) region is assigned to the quartz phase, while the peaks located at approximately 19.8° (110), 35.4° (200), and 62.3° (101) are characteristic of montmorillonite [20]. In the AgNP-modified Mt_1-AgNPs and Mt_2-AgNPs samples, the preservation of the main peaks of the aluminosilicate matrix indicates that the layered structure of bentonite remained intact during the modification process. Furthermore, the emergence of an additional peak in the $2\theta = 64–65°$ region is assigned to the (220) plane of the face-centered cubic (fcc) lattice of metallic silver. According to the studies of Shameli K. et al., in Ag/MMT-type systems the silver phase is typically characterized by peaks near 38.3° (111), 44.4° (200), 64.4° (220), and 77.7° (311) [24]; therefore, the observation of signals in these regions confirms the effective intercalation of AgNPs into the montmorillonite matrix.

The XRD results showed a shift of the basal reflection of montmorillonite toward lower 2θ values, accompanied by a slight increase in the interlayer distance d001 by approximately 0.0003–0.0006 nm. This change may indicate a partial expansion of the interlayer space and can be associated with the possible penetration of silver ions into the montmorillonite interlayer galleries.

Table 3. Changes in the interplane distance of the main peaks.

№	2 θ	d-spacing (Å)	2 θ	d-spacing (Å)	Δ d-spacing
	Main peaks of raw $Mt_{1,2}$		Main peaks of AgNP-$Mt_{1,2}$		
1	19.81	4.4715	19.79	4.48258	0.0110
2	35.03	2.55951	34.95	2.56519	0.0056
3	62.21	1.49107	62.05	1.49453	0.0034

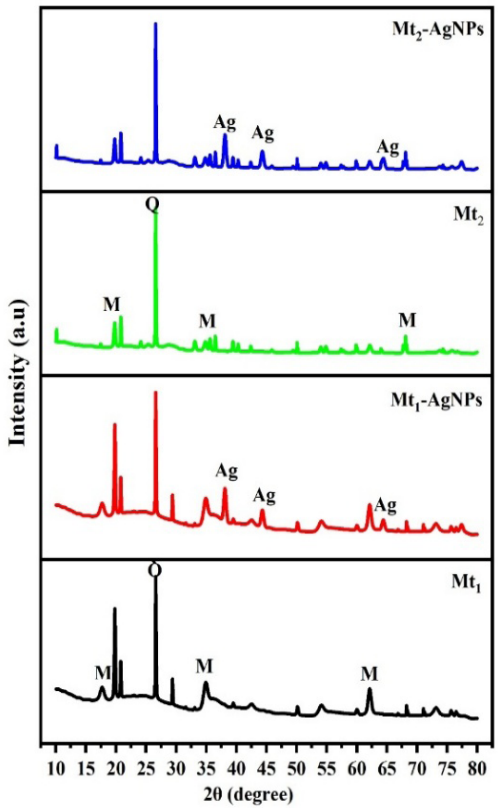

Figure 3. Comparative X-ray diffraction patterns of the initial Mt_1 a nd Mt_2 samples and the AgNP-modified Mt_1-AgNPs and Mt_2-AgNPs samples.

3.5 SEM images analysis

Figure 4 presents the SEM surface morphology of the initial Mt_1 and Mt_2 samples and the AgNP-modified Mt_1-AgNPs and Mt_2-AgNPs samples. The pristine Mt_1 and Mt_2 samples exhibited a morphology composed of agglomerated plate-like layers with a relatively irregular shape and a porous surface. In the present study, the particle size of the Mt_1 sample ranged from 805.4 nm to 1.540 μm, with an average of 1.22 μm, while that of the Mt_2 sample varied from 536.8 nm to 2.559 μm, with a mean value of 1.57 μm. These findings are in agreement with the submicron- and micron-sized ranges reported for montmorillonite particles in earlier studies [6,13,23], indicating that secondary agglomeration occurs in the pristine samples. After modification with silver nanoparticles, the overall layered morphology of the samples was preserved; however, the surface became denser, more compact, and more homogeneous. In particular, in the Mt_1-AgNPs sample, the shift in particle size to the range of 1.025–2.410 μm and the increase in the average value to 1.79 μm indicate that particle re-agglomeration and structural densification occurred after the introduction of AgNPs. Similar changes were also observed in the Mt_2-AgNPs sample, particularly surface smoothing and a closer packing of the layers. Such morphological transformations have likewise been reported for silver–montmorillonite composite systems [25].

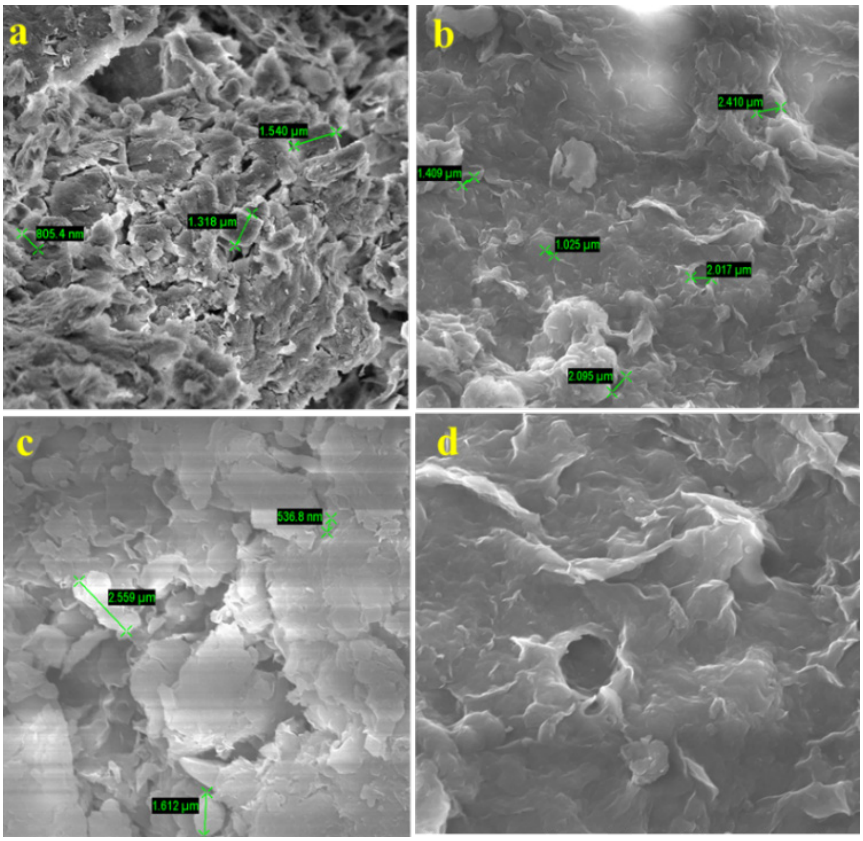

Figure 4. SEM images of the samples: (a) Mt_1, (b) Mt_1-AgNPs, (c) Mt_2, and (d) Mt_2-AgNPs.

3.6 Viscosity of the nanocomposite

The viscosity of the pristine Mt_1 and Mt_2 samples, as well as that of the AgNP-intercalated Mt_1-AgNPs and Mt_2-AgNPs samples, determined at room temperature, was 41.816, 39.994, 39.794, and 39.210 mPa·s, respectively. Following the incorporation of AgNPs, the viscosity decreased slightly, by 4.4% for Mt_1 and 1.5% for Mt_2. These findings suggest that the investigated systems retain a flowable dispersed state, which is favorable for facile application and uniform spreading on external wounds. For topical semisolid dosage forms, the rheological properties substantially affect the spreadability of the formulation, ease of application, release of the active component, and its penetration through the skin or wound surface. In this regard, the relatively low viscosity observed in the compositions studied in [28] may be regarded not as a drawback, but rather as a positive factor that contributes to improved spreadability of the composition, more effective contact of silver nanoparticles with the wound surface, and increased availability of the active phase. Therefore, montmorillonite material intercalated with silver nanoparticles may be regarded not as a classical high-viscosity ointment base, but rather as a promising matrix-forming agent for soft ointment or gel-ointment systems intended for external wound applications [29].

Table 4. Viscosity of the nanocomposite.

№	Mt_1	Mt_1-AgNPs	Mt_2	Mt_2-AgNPs
1	42.266 mPa·s	40.111 mPa·s	40.361 mPa·s	39.671 mPa·s
2	41.177 mPa·s	39.861 mPa·s	39.912 mPa·s	38.719 mPa·s
3	42.007 mPa·s	40.011 mPa·s	39.111 mPa·s	39.241 mPa·s
Average	41.816 mPa·s	39.994 mPa·s	39.794 mPa·s	39.210 mPa·s

Similar approaches to the evaluation of rheological properties of bentonite and clay-based systems have been reported in previous studies [30,31], where such materials were considered for topical drug delivery and semi-solid medical compositions.

Therefore, the viscosity analysis is relevant to the proposed application of the developed composite material.

4. Conclusion

The conducted studies made it possible to comprehensively evaluate the structural, morphological, and antibacterial properties of the Mt_1 and Mt_2 bentonite clays, as well as those of the silver nanoparticle-intercalated Mt_1-AgNPs and Mt_2-AgNPs samples. The FTIR, XRD, and SEM results showed that the main layered aluminosilicate framework of bentonite was preserved after modification, while the silver nanoparticles were distributed over the sample surface and within the interlayer space. According to the XRD data, the shift of the montmorillonite basal reflection and the slight increase in the interlayer distance may indicate the possible penetration of silver ions and/or silver-containing nanostructures into the interlayer space. The Mt_2-AgNPs sample obtained using 75 mL of AgNPs solution showed the highest antibacterial activity, with an inhibition zone of approximately 11–11.2 mm, under the experimental conditions used in this study, the antibacterial activity of the Mt_2-AgNPs sample was approximately 50.7% of that of erythromycin.This indicates its pronounced antibacterial effect. In addition, the microbiological purity of the investigated clay samples was found to comply with the requirements of the State Pharmacopoeia of the Republic of Kazakhstan. The viscosity of the modified samples, which remained within the range of 39–40 mPa·s, demonstrated their strong potential for rheological application as matrix materials in the development of soft dosage forms, including ointment compositions. The intercalation of silver nanoparticles promoted densification of the surface structure, morphological reorganization, and an increase in the functional activity of the samples. In general, the obtained findings suggest that silver nanoparticle-modified bentonite clays may be considered promising matrix materials for drug delivery systems, antimicrobial coatings, materials for external wound treatment, and the development of medicinal ointments.

Funding

This research has been funded by the Science Committee of the Ministry of Science and Higher Education of the Republic of Kazakhstan (Grant No. BR 24993105)

Conflicts of interest

The authors declare no conflict of interest.

Author contributions

Conceptualization: B.D.K. and K.A.; Methodology: K.A.; Software: B.D.K. and D.V.; Validation: K.A. and K.S.K.; Formal Analysis: B.D.K.; Investigation: M.Sh.A.; Resources. K.S.K. and A.K.; Data Curation: K.S.K. and A.K.; Writing – Original Draft Preparation: B.D.K. and K.A.; Writing – Review & Editing: K.S.K.; Visualization: B.D.K.; Supervision: K.A.; Project Administration: K.S.K.; Funding Acquisition.A.K. All authors have read and agreed to the published version of the manuscript.

References

1. D. Bolatkan, A. Kerimkulova, M. Beisebekov et al., "Quantitative assessment of the use of Kazakhstan montmorillonite clays as sorbent carriers for pharmaceutical substances," *Phys. Sci. Technol.*, vol. 12, no. 1–2, pp. 121–133, 2025. https://doi.org/10.26577/phst202512112

2. S. Saif, S. Mubeen, W. Abbass et al., "Exploring the feasibility of utilizing high plastic clays as an alternative material to bentonite clay in the production of ceramic tile: Advancing towards efficient life cycle cost," *Case Stud. Constr. Mater.*, vol. 20, 2024, Art. no. e03277. https://doi.org/10.1016/j.cscm.2024.e03277

3. W. A. Muslim, S. K. Al-Nasri, T. M. Albayati, and I. K. Salih, "Investigation of bentonite clay minerals as a natural adsorbents for Cs-137 real radioactive wastewater treatment," Desalin. Water Treat., vol. 317, 2024, Art. no. 100121. https://doi.org/10.1016/j.dwt.2024.100121

4. M. Skakov, "Highly efficient copper–palladium nanoalloy catalysts on modified carbon supports", *Phys. Sci. Technol.*, vol. 12, no. 3-4, pp. 10–27, Dec. 2025. https://doi.org/10.26577/phst202512

5. M. Bayandinova, A. . Kenesbekov, . A. Serikbaykyzy, . A. . Askhatov, Y. Batanov, and N. Bazarov, "Development of biocompatible coatings for orthopedic joint implants", *Phys. Sci. Technol.*, vol. 12, no. 1-2, pp. 84–94, Jun. 2025. https://doi.org/10.26577/phst20251218

6. M. Beisebekov, S. Kabdrakhmanova, N. Kantay et al., "Comparative study of a new sodium-bentonite clay for use in the pharmaceutical industry," *ES Mater. Manuf.*, vol. 30, 2025, Art. no. 1954. http://dx.doi.org/10.30919/mm1954

7. E. Srasra and I. Bekri-Abbes, "Bentonite clays for therapeutic purposes and biomaterial design," *Curr. Pharm. Des.*, vol. 26, 2020. https://doi.org/10.2174/1381612826666200203144034

8. M. S. Rana and S. Kim, "Bentonite in Korea: A resource and research focus for biomedical and cosmetic industries," *Materials*, vol. 17, no. 9, 2024, Art. no. 1982. https://doi.org/10.3390/ma17091982.

9. W. M. Alamier, M. Imran, S. K. Ali et al., "Synthesis of high-performance Fe_3O_4/graphene/bentonite clay nanocomposite for sustainable ciprofloxacin adsorption," *Inorg. Chem. Commun.*, vol. 174, pt. 1, 2025, Art. no. 113991. https://doi.org/10.1016/j.inoche.2025.113991

10. D. Luo and J. Wei, "Upgrading sodium montmorillonite into a reactive internal curing agent for sustainable cement composites through non-ionic functionalization," *Compos. Part B Eng.*, vol. 242, 2022, Art. no. 110076. https://doi.org/10.1016/j.compositesb.2022.110076

11. H. Tabasi, F. Oroojalian, and M. Darroudi, "Green clay ceramics as potential nanovehicles for drug delivery applications," *Ceram. Int.*, vol. 47, pp. 31042–31053, 2021. https://doi.org/10.1016/j.ceramint.2021.08.090

12. S. K. Kabdrakhmanova, A. Z. Kerimkulova, S. Z. Nauryzova et al., "Bentonite-based composites in medicine: Synthesis, characterization, and applications," *J. Compos. Sci.*, vol. 9, 2025, Art. no. 310. https://doi.org/10.3390/jcs9060310

13. T. Jamil, S. Yasin, N. Ramzan et al., "Bentonite-clay/CNT-based nano adsorbent for textile wastewater treatment: Optimization of process parameters," *Water*, vol. 15, no. 18, 2023, Art. no. 3197. https://doi.org/10.3390/w15183197

14. Y. Xing, X. Liao, X. Liu et al., "Characterization and antimicrobial activity of silver nanoparticles synthesized with the peel extract of mango," *Materials (Basel)*, vol. 14, no. 19, 2021, Art. no. 5878. https://doi.org/10.3390/ma14195878

15. A. Géloën, G. Mussabek, A. Kharin, T. Serdiuk, S. A. Alekseev, and V. Lysenko, "Impact of carbon fluoroxide nanoparticles on cell proliferation," *Nanomaterials*, vol. 11, no. 12, Art. no. 3168, Dec. 2021. https://doi.org/10.3390/nano11123168.

16. M. Isaiev, G. Mussabek, P. Lishchuk, K. Dubyk, N. Zhylkybayeva, G. Yar-Mukhmedova, D. Lacroix, and V. Lysenko, "Application of photoacoustic approach for characterization of nanostructured materials," *Nanomaterials*, vol. 12, no. 4, Art. no. 708, Feb. 2022. https://doi.org/10.3390/nano12040708.

17. N. Zhylkybayeva, K. Paliienko, A. Topchylo, A. Zaderko, A. Géloën, T. Borisova, L. Grishchenko, R. Mariychuk, V. Skryshevsky, G. Mussabek, and V. Lysenko, "Size dependent properties of Gd3+-free versus Gd3+-doped carbon dots for bioimaging application," *Sci. Rep.,* vol. 14, Art. no. 27812, Nov. 2024. https://doi.org/10.1038/s41598-024-76500-z.

18. J. Madejová, "FTIR techniques in clay mineral studies," *Vib. Spectrosc.*, vol. 31, no. 1, pp. 1–10, 2003. https://doi.org/10.1016/S0924-2031(02)00065-6

19. A. Mokhtar, A. B. Ahmed, B. Asli, B. Boukoussa, M. Hachemaoui, M. Sassi, and M. Abboud, "Recent advances in antibacterial metallic species supported on montmorillonite clay mineral: A review," *Minerals*, vol. 13, no. 10, 2023, Art. no. 1268. https://doi.org/10.3390/min13101268.

20. S. Z. Nauryzova, S. K. Kabdrakhmanova, A. K. Kabdrakhmanova et al., "Comprehensive study of silver nanoparticle functionalization of Kalzhat bentonite for medical application," *J. Compos. Sci.*, vol. 9, no. 12, 2025, Art. no. 702. https://doi.org/10.3390/jcs9120702

21. P. Praus, M. Turicová, V. Machovič, S. Študentová, and M. Klementová, "Characterization of silver nanoparticles deposited on montmorillonite," *Appl. Clay Sci.*, vol. 49, no. 3, pp. 341–345, 2010. https://doi.org/10.1016/j.clay.2010.06.009

22. S. Barakan, V. Aghazadeh, and M. Aghazadeh, "Separation and characterisation of montmorillonite from a low-grade natural bentonite using a non-destructive method," *Micro Nano Lett.*, 2019. https://doi.org/10.1049/mnl.2018.5364

23. M. Horue, M. L. Cacicedo, M. A. Fernandez et al., "Antimicrobial activities of bacterial cellulose–silver montmorillonite nanocomposites for wound healing," *Mater. Sci. Eng*. C, vol. 116, 2020, Art. no. 111152 https://doi.org/10.1016/j.msec.2020.111152

24. B. Tyagi, C. D. Chudasama, and R. V. Jasra, "Determination of structural modification in acid activated montmorillonite clay by FT-IR spectroscopy," *Spectrochim. Acta Part A Mol. Biomol. Spectrosc.*, vol. 64, no. 2, pp. 273–278, 2006. https://doi.org/10.1016/j.saa.2005.07.018.

25. K. Shameli et al., "Synthesis of silver nanoparticles in montmorillonite and their antibacterial behavior," *Int. J. Nanomedicine*, vol. 6, pp. 581–590, 2011. https://doi.org/10.2147/IJN.S17112.

26. K. Shameli, M. B. Ahmad, W. M. Z. W. Yunus et al., "Synthesis of silver/montmorillonite nanocomposites using γ-irradiation," *Int. J. Nanomedicine*, vol. 5, pp. 1067–1077, 2010. doi:10.2147/IJN.S15033

27. A. Agwu, A. Okorie, O. Akpanika, and A. Okon, "Activation of local bentonitic clays for use as viscosifiers in water-based drilling fluids," *J. Sci. Res. Rep*., vol. 12, pp. 1–11, 2016. https://doi.org/10.9734/JSRR/2016/28719.

28. A. Z. M. Badruddoza, M. I. Zahid, T. Walsh et al., "Topical drug delivery by Sepineo P600 emulgel: Relationship between rheology, physical stability, and formulation performance," *Int. J. Pharm.*, vol. 658, 2024, Art. no. 124210. https://doi.org/10.1016/j.ijpharm.2024.124210

29. Z. Rutkuniene, M. Balandyte, and G. Karbauskyte, "Formation of diamond like carbon films on materials for medical application", *Phys. Sci. Technol.*, vol. 8, no. 1-2, pp. 35–40, Jul. 2021. https://doi.org/10.26577/phst.2021.v8.i1.04

30. M. Ruggeri, R. Sánchez-Espejo, L. Casula, G. Sandri, L. Perioli, M. C. Cardia, et al., "Bentonite- and palygorskite-based gels for topical drug delivery applications," *Pharmaceutics*, vol. 15, 2023. https://doi.org/10.3390/pharmaceutics15041253.

31. M. N. Calienni, L. M. Martínez, M. C. Izquierdo, S. d. V. Alonso, and J. Montanari, "Rheological and viscoelastic analysis of hybrid formulations for topical application," *Pharmaceutics*, vol. 15, no. 10, p. 2392, 2023. https://doi.org/10.3390/pharmaceutics15102392.

Information about the authors:

Dana Bolatkan (corresponding author) – PhD student at S. Amanzholov East Kazakhstan University (Oskemen, Kazakhstan, email: chilibayeva35@gmail.com).

Kydyrmolla Akatan – PhD in chemistry, Head of the National Laboratory for Collective Use S. Amanzholov East Kazakhstan University (Oskemen, Kazakhstan, email: kidirmolla@gmail.com).

Kabdrakhmanova Sana Kanatbekovna – Candidate of Technical Sciences, Associate Professor, Director of the International R&D Center for Advanced Functional Materials and Their Composites, Satpaev University (Almaty, Kazakhstan, email: skabdrakhmanova@gmail.com).

Davydova Veronika – master student at Satpaev University, Junior researcher at International R&D Center for Advanced Functional Materials and Their Composites (Almaty, Kazakhstan, e-mail: veronikaspost17@gmail.com).

Muzdybayeva Sharbanu Akkazinovna – Candidate of Chemical Sciences and an Associate Professor at the Department of "Biochemical Engineering" of the International Engineering and Technology University (Almaty, Kazakhstan, e-mail: Sharbanu1958@mail.ru).

IRSTI 31.15.35 https://doi.org/10.26577/phst20261316

Photoelectrochemical reduction and electrochemical detection of Cr(VI) using TiO_2 nanosheet electrodes

N.Y. Akhanova[1], A.T. Tulegenova[1*], M.B. Aitzhanov[2], M.T. Gabdullin[1], A.Zh. Iskalieva[1], Zh. Ongaibergenov[2] and A.A. Markhabayeva[1]

[1]Kazakh-British Technical University Almaty, Kazakhstan
[2]Institute of Applied Science and Information Technologies, Almaty, Kazakhstan
*e-mail: tulegenova.aida@gmail.com

(*Received April 27, 2026; received in revised form May 30, 2026; accepted June 1, 2026*)

TiO_2 nanosheet electrodes were successfully fabricated on fluorine-doped tin oxide (FTO) substrates via a hydrothermal method using a $TiCl_4$–HCl–NH_4F system. The obtained hierarchical nanosheet morphology provides a high surface area and abundant active sites, which are favorable for electrochemical and photoelectrochemical processes. The electrochemical performance of the TiO_2 electrodes was investigated for both detection and reduction of hexavalent chromium (Cr (VI)), a highly toxic and hazardous pollutant in water systems. Cyclic voltammetry revealed enhanced cathodic currents and the appearance of a reduction peak in the presence of Cr (VI), confirming its electrochemical reduction. Chronoamperometric measurements demonstrated a rapid and concentration-dependent current response, with a linear detection range of 0.01–0.8 mM and a sensitivity of 0.213 $mA \cdot mM^{-1}$, and a limit of detection (LOD) of approximately 0.003 μM. Under UV illumination, a decrease in photocurrent was observed after the addition of Cr (VI), indicating the consumption of photogenerated electrons in the photoelectrochemical reduction process. This behavior confirms that Cr (VI) acts as an efficient electron acceptor, undergoing reduction to less toxic Cr (III). The combined electrochemical and photoelectrochemical results demonstrate that TiO_2 nanosheet electrodes can serve as multifunctional platforms for simultaneous detection and detoxification of Cr (VI). This work highlights the potential of TiO_2-based systems for sustainable water purification and environmental remediation, contributing to the development of clean water technologies.

Keywords: TiO_2 nanosheets, photoelectrochemical reduction, Cr (VI); electrochemical detection, water purification.

1. Introduction

Hexavalent chromium (Cr (VI)) is one of the most toxic and hazardous heavy metal pollutants, widely found in industrial wastewater from electroplating, leather processing, and textile industries. Due to its high solubility, mobility, and strong oxidizing nature, Cr (VI) poses severe risks to human health and the environment, including carcinogenic and mutagenic effects [1,2].

Among various approaches for chromium remediation, the reduction of Cr (VI) to trivalent chromium (Cr (III)) is considered an effective detoxification strategy, as Cr (III) is significantly less toxic and can be easily precipitated as hydroxides. Therefore, the development of efficient materials capable of both detection and reduction of Cr (VI) is of great importance [3,4].

Titanium dioxide (TiO_2) has been extensively studied as a photoactive material due to its excellent chemical stability, low cost, and strong photocatalytic properties. Under UV illumination, TiO_2 generates electron–hole pairs [5-7], enabling redox reactions at the surface. In particular, photogenerated electrons can participate in the reduction of Cr(VI), making TiO_2 a promising candidate for photoelectrochemical detoxification processes[6,7].

In addition to photocatalysis, TiO_2-based nanostructures have attracted attention for electrochemical sensing applications due to their large surface area and favorable charge transport properties. The combination of sensing and catalytic functionality in a single material offers a promising approach for

simultaneous detection and removal of toxic species [8-10].

Although various TiO_2-based nanostructures such as nanotubes, nanoparticles, thin films, and heterostructures have been previously investigated for Cr (VI) sensing and photoelectrochemical reduction, many reported systems require multistep fabrication procedures, noble metal modification, or complex multicomponent architectures to achieve enhanced performance. In contrast, the present work focuses on hydrothermally synthesized TiO_2 nanosheets with a hierarchical layered morphology providing a large exposed surface area, abundant active sites, and facilitated charge/electrolyte transport. In addition, the proposed TiO_2 nanosheet platform combines dual functionality, enabling both electrochemical detection and photoelectrochemical reduction of Cr (VI) within a single material system without the use of additional cocatalysts or noble metals.

In this work, TiO_2 nanosheet electrodes were synthesized via a hydrothermal method on FTO substrates and investigated for both electrochemical detection and photoelectrochemical reduction of Cr(VI). The electrochemical behavior, sensing performance, and reduction mechanism were systematically studied using cyclic voltammetry, chronoamperometry, and photoelectrochemical measurements.

2. Materials and methods

2.1 Synthesis of TiO_2

TiO_2 nanosheets were grown on FTO substrates via a hydrothermal method. Prior to synthesis, the FTO substrates (2 × 3 cm) were sequentially cleaned in acetone, isopropanol, and deionized water for 10 min each using ultrasonication. The substrates were then dried and optionally treated with UV-ozone to improve surface wettability. The growth solution was prepared by mixing 15 mL of deionized water and 15 mL of concentrated HCl (37%) under stirring. Subsequently, 0.10–0.20 g of NH_4F was added and fully dissolved. Finally, 0.5 mL of $TiCl_4$ was slowly introduced into the solution under continuous stirring. The resulting solution was transferred into a Teflon-lined stainless steel autoclave, filled to approximately 70–80% of its volume. The cleaned FTO substrate was placed inside the autoclave at an angle (~45°) with the conductive side facing downward. The hydrothermal reaction was carried out at 180 °C for 12 h. After cooling naturally to room temperature, the samples were removed, thoroughly rinsed with deionized water and ethanol, and dried at 60–80 °C. Finally, the samples were annealed in air at 450 °C for 2 h to improve crystallinity and adhesion.

The chemicals used in this work included potassium dichromate ($K_2Cr_2O_7$, ≥99% ACS reagent), sulfuric acid (H_2SO_4, ≥95% ACS reagent), acetone (≥95% Laborfarma), and 1,5-diphenylcarbazide (DPC ≥99% Sigma Aldrich). All aqueous solutions were prepared using deionized water. A 10 mM Cr(VI) stock solution was prepared by dissolving $K_2Cr_2O_7$ in 0.5 M H_2SO_4. For colorimetric analysis, a 0.5 wt.% DPC solution was prepared by dissolving 1,5-diphenylcarbazide in acetone. All chemicals were used as received without additional purification.

2.2 Electrochemical measurements

Electrochemical measurements were performed using a three-electrode configuration with the TiO_2/FTO sample as the working electrode, a platinum mesh as the counter electrode, and an Ag/AgCl (3 M KCl) electrode as the reference. The 0.5 M H_2SO_4 solution was used as electrolyte. All experiments were performed using a potentiostat (CorrTest CS310S) at room temperature. Chronoamperometric measurements were conducted at a fixed potential (0.2 V vs Ag/AgCl). After achieving a stable baseline current, successive aliquots of Cr (VI) stock solution (10 mM) were injected into the electrolyte under continuous stirring. The additions resulted in stepwise increases in Cr (VI) concentration, with cumulative concentrations of 0.01, 0.03, 0.08, 0.18, 0.28, 0.48, 0.78, and 1.18 mM. The steady-state current values were extracted from each step and used to construct a calibration curve of current response versus Cr (VI) concentration. A linear relationship was observed in the low concentration range (0.01–0.18 mM), and the sensitivity was calculated from the slope of the linear fit. After each addition, the current response was recorded until a steady-state value was reached.

Linear sweep voltammetry (LSV) measurements were performed under chopped UV illumination to evaluate the photoelectrochemical behavior of the TiO_2 electrode. The light source (Xe lamp) was periodically switched on and off during the potential scan. The scan rate was set to (10 mV s^{-1}). The photocurrent response was recorded in the absence and presence of Cr(VI) in 0.5 M H_2SO_4. The geometric area of the working electrode was approximately 1 cm^2.

3. Results and discussion

3.1 Morphology and structure

The surface morphology of the synthesized TiO_2 was examined by SEM (Figure 1). At low magnification (Figure 1a), the sample exhibits a relatively uniform coverage of the FTO substrate by micro- and nanoscale structures. The structures are randomly

oriented and densely distributed across the surface. At higher magnification (Figure 1b), the morphology reveals the presence of rod-like and plate-like structures with irregular orientations. These features appear to originate from nucleation and anisotropic growth during the hydrothermal process [11]. The high-magnification image (Figure 1c) clearly shows the formation of hierarchical TiO_2 nanosheets composed of stacked layers with well-defined edges. Such a layered architecture provides an increased surface area and abundant active sites, which are beneficial for electrochemical processes. The hierarchical nanosheet morphology is expected to facilitate charge transfer and electrolyte diffusion due to the presence of exposed edges and interconnected layered structures. Such architecture promotes efficient interaction between Cr(VI) species and the TiO_2 surface, contributing to the enhanced cathodic current response observed during electrochemical measurements. In addition, the large exposed surface area and reduced charge transport pathways can improve the separation and transfer of photogenerated charge carriers under UV illumination, thereby enhancing the photoelectrochemical reduction performance.

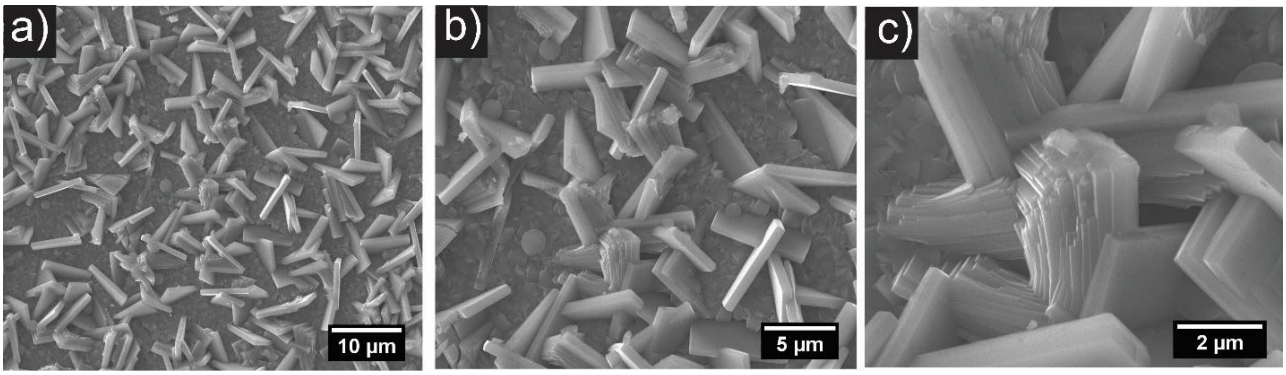

Figure 1. Scanning electron microscopy (SEM) images of TiO_2 structures grown on FTO substrate at different magnifications.

The crystalline structure of the synthesized TiO_2 nanosheets was investigated by X-ray diffraction (Figure 2). The diffraction pattern exhibits several well-defined peaks that can be indexed to TiO_2, in good agreement with the standard reference (JCPDS No. 00-001-0562). The presence of sharp and intense reflections indicates good crystallinity of the hydrothermally grown nanosheets. In addition to TiO_2 peaks, several diffraction signals corresponding to SnO_2 (JCPDS No. 01-080-6802) are observed, which originate from the FTO substrate. This confirms that the TiO_2 layer is relatively thin, allowing diffraction from the underlying conductive glass to be detected. No additional impurity phases were detected within the resolution of the measurement, indicating the phase purity of the synthesized TiO_2 nanosheets.

The structural properties of the synthesized TiO_2 nanosheets were further analyzed by Raman spectroscopy (Figure 3). The spectrum exhibits several characteristic peaks located at 140, 394, 514, and 636 cm^{-1}, which are attributed to the Eg, B1g, A1g, and Eg vibrational modes of anatase TiO_2, respectively. The strong and sharp Eg mode at ~140 cm^{-1} indicates good crystallinity and well-defined lattice structure [12,13]. The presence of all characteristic anatase modes confirms that the hydrothermal synthesis followed by annealing resulted in phase-pure anatase TiO_2.

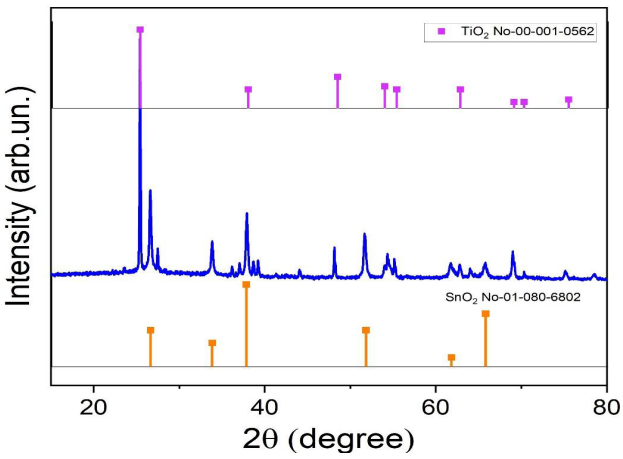

Figure 2. X-ray diffraction (XRD) pattern of TiO_2 nanosheets grown on FTO substrate.

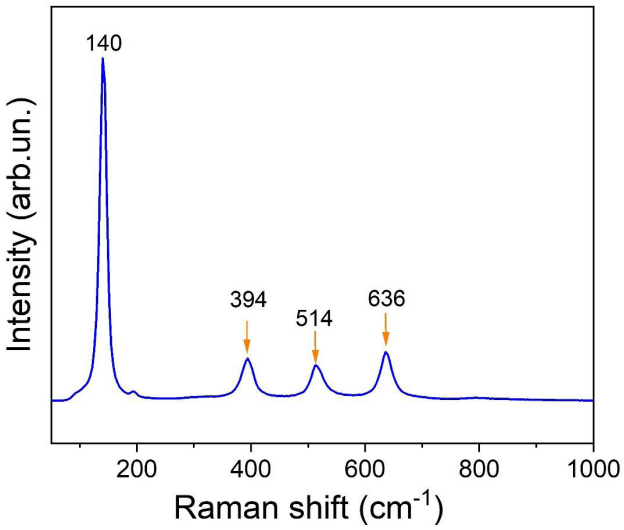

Figure 3. Raman spectrum of TiO_2 nanosheets grown on FTO substrate.

The characteristic vibrational modes are observed at 140, 394, 514, and 636 cm^{-1}, corresponding to the Eg, B1g, A1g, and Eg modes of anatase TiO_2, confirming the formation of the anatase phase.

3.2 Electrochemical performance

The electrochemical behavior of the TiO_2 electrode was investigated by cyclic voltammetry (Figure 4a). In the presence of Cr(VI), a significant increase in cathodic current is observed compared to the blank electrolyte [14]. Additionally, a reduction peak appears in the potential range of ~0.0–0.2 V vs. Ag/AgCl, indicating the electrochemical reduction of Cr (VI) to Cr (III). This confirms that the TiO_2 nanosheet electrode exhibits catalytic activity toward Cr (VI) reduction.

Figure 4b shows the chronoamperometric response of the TiO_2 electrode upon successive additions of Cr (VI). Each injection results in a sharp cathodic current drop followed by stabilization at a new steady-state level. The magnitude of the current response increases with increasing Cr (VI) concentration, indicating a concentration-dependent electrochemical response. The transient spikes are attributed to rapid mass transport and adsorption processes occurring at the electrode surface [15,16].

The steady-state current values were extracted from the chronoamperometric measurements to construct a calibration curve (Figure 4c). A linear relationship between current density and Cr (VI) concentration was observed, with a sensitivity of 0.213 $mA \cdot mM^{-1}$ and a correlation coefficient of $R^2 = 0.98$. This result demonstrates the good sensitivity of the TiO_2 electrode toward Cr (VI), making it suitable for electrochemical detection. The calibration plot exhibited a linear relationship between the current response and Cr (VI) concentration with a sensitivity of 0.213 mA mM^{-1}. The limit of detec $LOD = \frac{3\sigma}{S}$ was calculated according to the equation: , where σ is the standard deviation of the blank signal and S is the slope of the calibration curve. Based on the stable baseline region of the chronoamperometric response, the LOD was estimated to be approximately 0.01 μM.

The photoelectrochemical behavior of the TiO_2 electrode was further investigated under chopped UV illumination (Figure 4d). A clear photocurrent response is observed due to the generation of electron–hole pairs in TiO_2. After the addition of Cr (VI), a noticeable decrease in photocurrent is observed over the entire potential range. This behavior suggests that photogenerated electrons are consumed in the reduction of Cr (VI), confirming the photoelectrochemical reduction mechanism [17-19].

To further verify the reduction of Cr (VI), UV–Vis analysis using the diphenylcarbazide (DPC) method was performed before and after photoelectrochemical treatment (Figure 5). A pronounced decrease in the characteristic absorption band at ~540 nm was observed after PEC treatment, confirming the significant consumption of Cr (VI) during the reduction process.

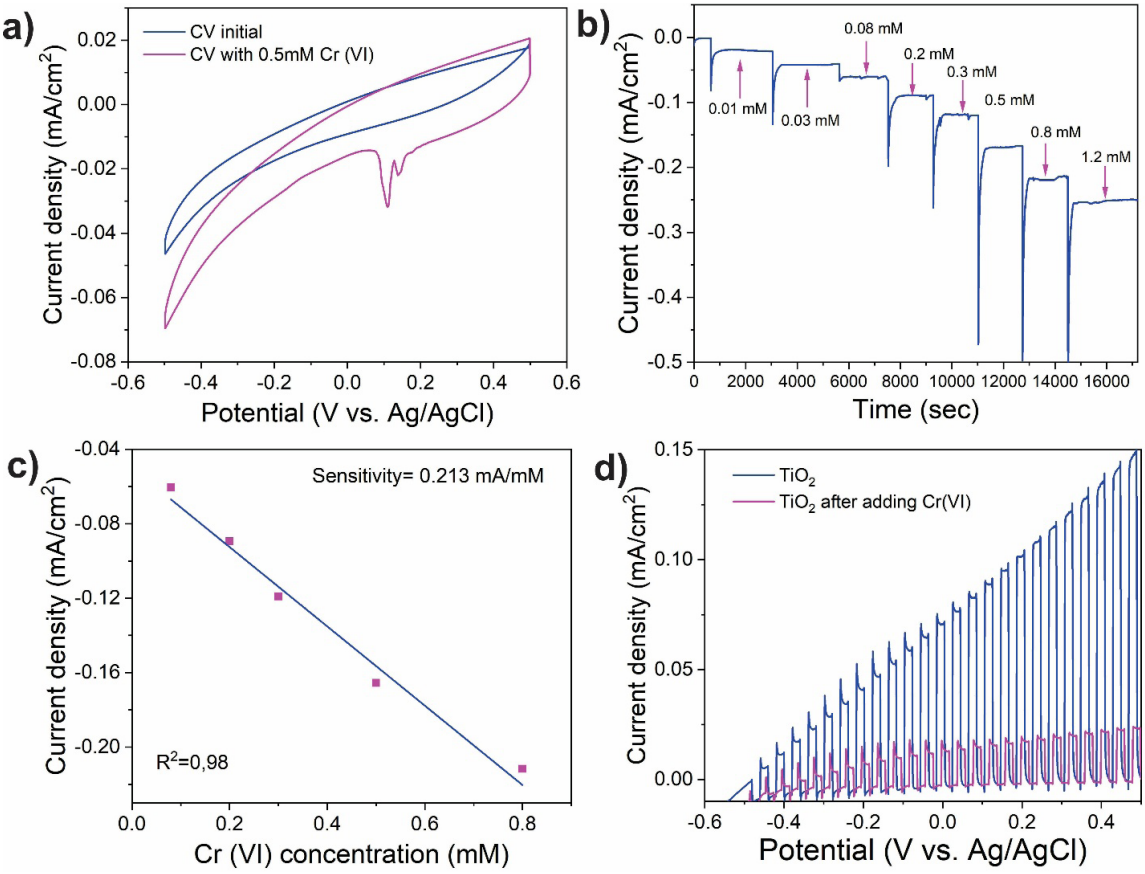

Figure 4. (a) Cyclic voltammetry (CV) curves of the TiO_2 nanosheet electrode recorded in the absence and presence of 0.5 mM Cr (VI) in 0.5 M H_2SO_4 electrolyte; (b) Chronoamperometric response of the TiO_2 nanosheet electrode upon successive additions of Cr (VI) solution at different concentrations (0.01–1.2 mM) under a constant applied potential. (c) Calibration curve of current response versus Cr (VI) concentration in the linear range of 0.01–0.18 mM; (d) Linear sweep voltammetry (LSV) curves under chopped UV illumination recorded before and after the addition of Cr (VI).

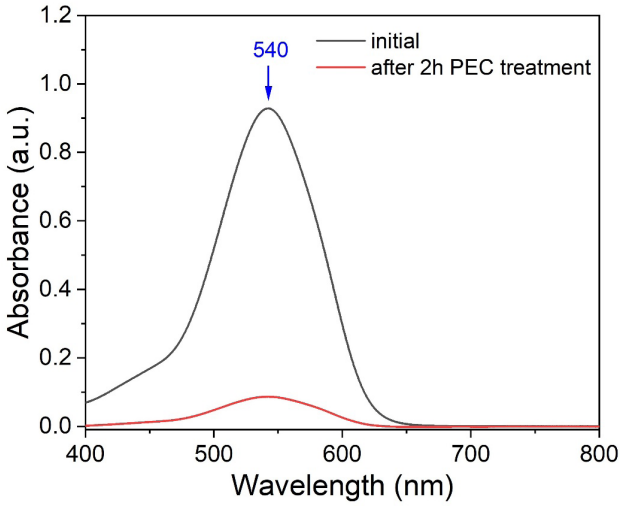

Figure 5. UV–Vis absorption spectra of the Cr(VI)–DPC complex before and after photoelectrochemical treatment under UV illumination.

The observed electrochemical and photoelectrochemical behavior can be explained by the role of Cr (VI) as a strong electron acceptor. Under applied potential and UV illumination, TiO_2 generates charge carriers (electrons and holes). The photogenerated electrons are readily transferred to Cr (VI), leading to its reduction to Cr (III) [20-26]. The schematic illustration of the proposed photoelectrochemical mechanism is presented in Figure 6. The overall process can be described as:

Cr (VI) → Cr (III)

$$TiO_2 + hv \rightarrow e^- + h^+$$

$$Cr_2O_7^{-2} + 14H^+ + 6e^- \rightarrow 2Cr^{3+} + 7H_2O$$

This electron transfer process enhances the cathodic current observed in CV and chronoampero-

metric measurements. The nanosheet architecture of TiO_2 further contributes to this behavior by providing improved electrode/electrolyte contact and facilitating interfacial electron transfer processes. The layered morphology also increases the accessibility of active sites for Cr(VI) adsorption and reduction. At the same time, the consumption of photogenerated electrons by Cr(VI) reduces their contribution to the external circuit, resulting in a decrease in photocurrent under UV illumination. Therefore, the presence of Cr (VI) simultaneously promotes electrochemical reduction while suppressing photocurrent, confirming its role as an efficient electron scavenger.

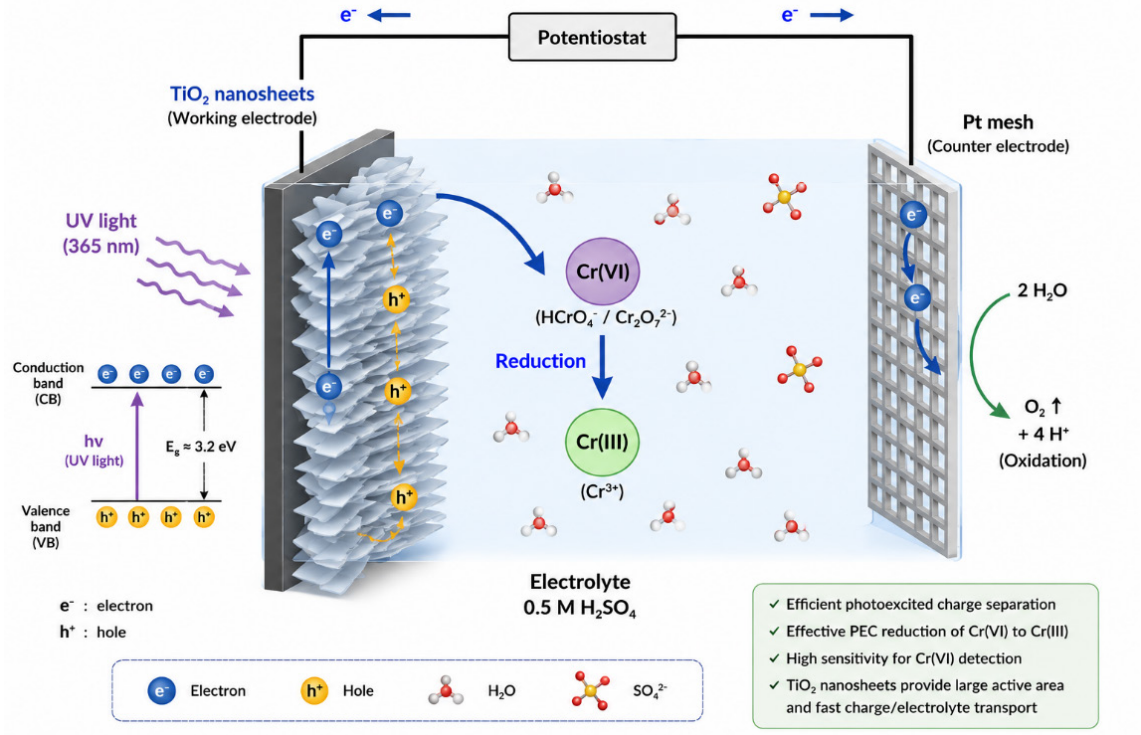

Figure 6. Schematic illustration of the photoelectrochemical reduction and detection mechanism of Cr (VI) on TiO_2 nanosheet electrodes under UV illumination.

Table 1. Comparison of Cr (VI) photoelectrochemical detection performance of various TiO_2-based and related photoelectrodes.

Material	Detection method	Linear range	LOD	Reference
TiO_2 nanosheets	PEC reduction and electrochemical detection	0.01–0.18 mM	0.003 μM	This work
Au-decorated TiO_2 nanorods	PEC sensing	0.01–50 μM	0.006 μM	21
Screen-printed TiO_2 electrode	PEC sensing	0.01–100 μM	0.004 μM	22
TiO_2 nanoparticles/GQDs/PCV	PEC sensing	0.08–100 μM	0.04 μM	23
NiCo-LDHs/TiO_2 nanotube arrays	PEC sensing	0.5–20, 20–400, 400–1800 μM	0.12 μM	24

4. Conclusion

Overall, the combined electrochemical and photoelectrochemical results demonstrate that TiO_2 nanosheet electrodes enable both the sensitive detection and efficient reduction of Cr(VI). The decrease in photocurrent under UV illumination, along with the enhanced cathodic response, confirms that Cr(VI) acts as an electron acceptor and undergoes reduction to Cr(III). The results highlight the potential of TiO_2

nanosheet electrodes as multifunctional platforms for environmental monitoring and detoxification. This work contributes to Sustainable Development Goal 6 (Clean Water and Sanitation) by addressing the removal and detection of toxic chromium species in aqueous systems.

Funding

This research was funded by the Committee of Science of the Ministry of Science and Higher Education of the Republic of Kazakhstan (Grant No. BR28712901).

Acknowledgements

The authors acknowledge the support of research facilities.

Conflicts of interest

The authors declare no conflict of interest.

Author contributions

Conceptualization: N.Y.A., A.T.T., A.Zh.I. and A.A.M.; Methodology: N.Y.A., A.A.M and M.B.A.; Software: M.B.A. and Zh.O.; Validation: N.Y.A., A.A.M., M.G.; Formal Analysis: A.T.T., A.Zh.I and A.A.M.; Data Curation: A.A.M., A.T.T.; Writing – Original Draft Preparation: A.A.M.; Writing – Review & Editing: N.Y.A., A.T.T and A.A.M.; Visualization: M.G.; Supervision: A.A.M.; Project Administration: A.A.M.; Funding Acquisition: N.Y.A. All authors have read and agreed to the published version of the manuscript.

References

1. P. Sharma, S. P. Singh, S. K. Parakh, and Y. W. Tong, "Health hazards of hexavalent chromium (Cr(VI)) and its microbial reduction," *Bioengineered*, vol. 13, no. 3, pp. 4923–4938, 2022. https://doi.org/10.1080/21655979.2022.2037273

2. S. Kerur, S. Bandekar, M. S. Hanagadakar, S. S. Nandi, G. Ratnamala, and P. G. Hegde, "Removal of hexavalent chromium: Industry treated water and wastewater—A review," *Mater. Today Proc.*, vol. 42, pp. 1112–1121, 2021. https://doi.org/10.1016/j.matpr.2020.12.492

3. S. Ambika et al., "Modified biochar as a green adsorbent for removal of hexavalent chromium from various environmental matrices: Mechanisms, methods, and prospects," *Chem. Eng. J.*, vol. 439, Art. no. 135716, 2022. https://doi.org/10.1016/j.cej.2022.135716

4. G Mussabek, S.A. Alekseev, A.I. Manilov, S. Tutashkonko, T. Nychyporuk, Y. Shabdan, G. Amirkhanova, S.V. Litvinenko, V.A. Skryshevsky, V. Lysenko, "Kinetics of Hydrogen Generation from Oxidation of Hydrogenated Silicon Nanocrystals in Aqueous Solutions," *Nanomaterials*. vol. 10, no.1413, 2020. https://doi.org/10.3390/nano10071413

5. R. Juturu, R. Selvaraj, and V. R. Murty, "Efficient removal of hexavalent chromium from wastewater using a novel magnetic biochar composite adsorbent," *J. Water Process Eng.*, vol. 66, Art. no. 105908, 2024. https://doi.org/10.1016/j.jwpe.2024.105908

6. L. Bertel, D. A. Miranda, and J. M. García-Martín, "Nanostructured titanium dioxide surfaces for electrochemical biosensing," *Sensors*, vol. 21, no. 18, Art. no. 6167, 2021. https://doi.org/10.3390/s21186167

7. G.Sh. Yar-Mukhamedova, D.M. Zellele, M. Rutkowska-Gorczyca, I. Makhambet, G. Mussabek, R. Atchibayev, A. Kemelzhanova, "Advancements in coating methods and properties of titanium based composite coatings: A review", *ES Materials and Manufacturing*, vol. 28, pp. 1669, 2025. https://dx.doi.org/10.30919/mm1569

8. J. Zhao et al., "The challenges and opportunities for TiO_2 nanostructures in gas sensing," *ACS Sens.*, vol. 9, no. 4, pp. 1644–1655, 2024. https://doi.org/10.1021/acssensors.4c00137

9. Y. Chen, B. Liu, Z. Chen, and X. Zuo, "Innovative electrochemical sensor using TiO_2 nanomaterials to detect phosphopeptides," *Anal. Chem.*, vol. 93, no. 30, pp. 10635–10643, 2021. https://doi.org/10.1021/acs.analchem.1c01973

10. G. Mussabek, N. Zhylkybayeva, S. Baktygerey, D. Yermukhamed, Ye Taurbayev, G. Sadykov, A.N. Zaderko, V.V. Lisnyak. "Preparation and characterization of hybrid nanopowder based on nanosilicon decorated with carbon nanostructures", *Applied Nanoscience*, vol.13, no.10, pp. 6709-6718. 2023. https://doi.org/10.1007/s13204-022-02681-6

11. J. M. Rzaij and A. M. Abass, "Review on TiO_2 thin film as a metal oxide gas sensor," *J. Chem. Rev.*, vol. 2, no. 2, pp. 114–121, 2020. https://doi.org/10.33945/SAMI/JCR.2020.2.4

12. A. Markhabayeva et al., "ZnO nanorods with GaSe nanoflakes form a heterojunction for solar water oxidation," *Appl. Surf. Sci.*, vol. 701, Art. no. 163275, 2025. https://doi.org/10.1016/j.apsusc.2025.163275

13. M. A. Ullah et al., "Facet-engineered {001} anatase TiO_2 nanoparticles for enhanced photocatalytic degradation of Congo Red," *J. Mol. Struct.*, 2025, Art. no. 144401. https://doi.org/10.1016/j.molstruc.2025.144401

14. B. Kuzmanović et al., "Understanding the role of interfacial PANI–TiO_2 interactions: A combined theoretical, spectroscopic, and electrochemical study," *J. Inorg. Organomet. Polym. Mater.*, 2026. https://doi.org/10.1007/s10904-026-04192-1

15. A. Markhabayeva, R. Dupre, R. Nemkayeva, and N. Nuraje, "Synthesis of hierarchical WO_3 microspheres for photoelectrochemical water splitting application," *Phys. Sci. Technol.*, vol. 10, no. 3–4, pp. 33–39, 2023. https://doi.org/10.26577/phst.2023.v10.i2.04

16. F. Bakhshandeh, S. Saha, S. Sakib, I. Zhitomirsky, and L. Soleymani, "TiO_2 nanoparticles co-sensitized with graphene quantum dots and pyrocatechol violet for photoelectrochemical detection of Cr(VI)," *J. Electrochem. Soc.*, vol. 169, no. 5, Art. no. 057520, 2022. https://doi.org/10.1149/1945-7111/ac6e90?urlappend=%3Futm_source%3Dresearchgate.net%26utm_medium%3Darticle

17. F. Eshaghzadeh, M. M. Momeni, and H. Farrokhpour, "Preparation of iron and chromium co-doped TiO_2 nanotubes and study of their photoelectrochemical properties," *J. Electron. Mater.*, vol. 52, no. 10, pp. 6977–6991, 2023.https://doi.org/10.1007/s11664-023-10596-3

18. C. Wang et al., "C-doped BiOCl/Bi_2S_3 heterojunction for highly efficient photoelectrochemical detection and photocatalytic reduction of Cr(VI)," *J. Mater. Sci. Technol.*, vol. 164, pp. 188–197, 2023. https://doi.org/10.1016/j.jmst.2023.03.066

19. C. V. Reddy et al., "Novel edge-capped ZrO_2 nanoparticles onto V_2O_5 nanowires for efficient photosensitized reduction of chromium (Cr(VI)), photoelectrochemical solar water splitting, and electrochemical energy storage applications," *Chem. Eng. J.*, vol. 430, Art. no. 132988, 2022. https://doi.org/10.1016/j.cej.2021.132988

20. B. Yuan et al., "Enhanced Cr(VI) stabilization by terrestrial-derived soil protein: Photoelectrochemical properties and reduction mechanisms," *J. Hazard. Mater.*, vol. 465, Art. no. 133153, 2024. https://doi.org/10.1016/j.jhazmat.2023.133153

21. R. Koutavarapu et al., "Novel Z-scheme binary zinc tungsten oxide/nickel ferrite nanohybrids for photocatalytic reduction of chromium (Cr(VI)), photoelectrochemical water splitting and degradation of toxic organic pollutants," *J. Hazard. Mater.*, vol. 423, Art. no. 127044, 2022. https://doi.org/10.1016/j.jhazmat.2021.127044

22. J. Qiao et al., "A photoelectrochemical sensor based on TiO_2 nanotube arrays decorated with nickel-cobalt layered double hydroxides for the effective and sensitive detection of chromium (VI)," *ACS Appl. Nano Mater.*, vol. 5, no. 4, pp. 5535–5543, 2022. https://doi.org/10.1021/acsanm.2c00521

23. H. Bahramian et al., "Enhanced Cr(VI) photoreduction in water using TiO_2/$CuWO_4$ photocatalytic coating," *Mater. Chem. Phys.*, vol. 354, Art. no. 132194, 2026. http://doi.org/10.1016/j.matchemphys.2026.132194

24. R. S. Moakhar, G. K. L. Goh, A. Dolati, and M. Ghorbani, "Sunlight-driven photoelectrochemical sensor for direct determination of hexavalent chromium based on Au-decorated rutile TiO_2 nanorods," *Appl. Catal. B Environ.*, vol. 201, pp. 411–418, 2017. https://doi.org/10.1016/j.apcatb.2016.08.026

25. R. S. Moakhar, G. K. L. Goh, A. Dolati, and M. Ghorbani, "A novel screen-printed TiO_2 photoelectrochemical sensor for direct determination and reduction of hexavalent chromium," *Electrochem. Commun.*, vol. 61, pp. 110–113, 2015. https://doi.org/10.1016/j.elecom.2015.10.011

26. J. Qiao, Y. Wang, Q. Liang, S. Dong, Z. Zeng, and S. Shao, "A photoelectrochemical sensor based on TiO_2 nanotube arrays decorated with nickel-cobalt layered double hydroxides for the effective and sensitive detection of chromium(VI)," *ACS Appl. Nano Mater.*, vol. 5, no. 4, pp. 5400–5409, 2022. https://doi.org/10.1021/acsanm.2c00521

Information about the authors:

Nazym Yerlanovna Akhanova (corresponding author) – PhD, Researcher, Kazakh-British Technical University (Almaty, Kazakhstan, e-mail: n.akhanova@kbtu.kz).

Aida Tulegenkyzy Tulegenova – PhD, Associate Professor, Researcher, Kazakh-British Technical University (Almaty, Kazakhstan, e-mail: tulegenova.aida@gmail.com).

Madi Bauirzhanovich Aitzhanov – Master's degree, Researcher, Institute of Applied Science and Information Technologies (Almaty, Kazakhstan, e-mail: madi.aitzhanov@outlook.com).

Maratbek Gabdullin – Candidate of Sciences, Professor, Rector of the Kazakh-British Technical University (Almaty, Kazakhstan, e-mail: m.gabdullin@kbtu.kz).

Asylzat Zh. Iskalieva – PhD, Assistant Professor, Researcher, Kazakh-British Technical University (Almaty, Kazakhstan, e-mail: a.iskalieva@kbtu.kz).

Zhanserik Ongaibergenov – Researcher, Institute of Applied Science and Information Technologies, Kazakhstan (Almaty, Kazakhstan, e-mail: onajbergenovz@gmail.com).

Aiymkul Alikhanovna Markhabayeva – PhD, Researcher, Kazakh-British Technical University (Almaty, Kazakhstan, e-mail: aiko.marx87@gmail.com).

IRSTI 29.19.22, 29.19.31 https://doi.org/10.26577/phst20261317

Optimization of the carbon ink printing process for the fabrication of flexible printed perovskite optoelectronic devices

Ye. Yerlanuly[1,2] and A.N. Jumabekov[1,2,*]

[1]National Laboratory Astana, Astana, Kazakhstan;
[2]Department of Physics, School of Sciences and Humanities, Nazarbayev University, Astana, Kazakhstan
*e-mail: askhat.jumabekov@nu.edu.kz

(Received February 26, 2026; received in revised form April 30, 2026; accepted May 8, 2026)

Carbon-based electrodes represent a promising alternative to noble metals for fully printed flexible perovskite solar cells (FPSCs) due to their low cost, chemical stability, and compatibility with scalable manufacturing. In this work, the printing and optimization of carbon ink electrodes using slot-die coating and screen-printing techniques are systematically investigated for application in fully printed FPSCs. The influence of printing parameters on the electrical and structural properties of carbon films is evaluated through sheet resistance measurements and Raman spectroscopy. Slot-die-coated carbon electrodes deposited at an optimized pump rate of 1 mL min^{-1} exhibit uniform films with a sheet resistance of approximately 80 Ω sq^{-1}, while screen-printed electrodes fabricated using a multi-point paste application strategy show improved uniformity with an average sheet resistance of ~125 Ω sq^{-1}. Using the optimized electrodes, fully printed FPSCs with a regular (n–i–p) architecture are fabricated on PET substrates. Devices incorporating slot-die-coated carbon electrodes achieve a power conversion efficiency (PCE) of ~0.6% over a large active area, whereas screen-printed carbon electrodes enable improved performance with a maximum PCE of 3.86%. These results demonstrate the feasibility of low-temperature, vacuum-free fabrication of flexible perovskite solar cells and provide practical guidelines for scalable roll-to-roll manufacturing.

Key words: printed perovskite solar cells; carbon electrodes; slot-die coating; screen printing; flexible electronics

1. Introduction

Perovskite photovoltaics have attracted extraordinary scientific and technological interest over the past decade, driven by rapid and unprecedented improvements in device performance [1, 2]. Since the first reports of perovskite-based solar cells [3-6], their power conversion efficiency (PCE) has increased at an exceptional pace, now exceeding 27% at the laboratory scale [3–5]. Beyond these record efficiencies, a defining advantage of perovskite photovoltaics lies in their solution-processable nature, which enables low-temperature fabrication and opens a clear pathway toward scalable, cost-effective manufacturing, particularly via roll-to-roll (R2R) coating technologies [1, 6–10].

In this context, fully printed perovskite photovoltaic (PV) devices are considered one of the most promising pathways toward industrial-scale production. Among various scalable deposition techniques, slot-die coating has emerged as a leading candidate for R2R fabrication of perovskite optoelectronic devices due to its high material utilization, excellent thickness control, and compatibility with continuous processing [11–13]. Using benchtop and pilot-scale slot-die systems, notable progress has been demonstrated for both regular (n–i–p) and inverted (p–i–n) device architectures. Reported PCEs have reached approximately 13% for slot-die-coated n–i–p devices and around 12% for inverted p–i–n configurations based on triple-cation mixed-halide perovskites, highlighting the strong potential of this approach for scalable manufacturing [14, 15].

Despite substantial progress in coating perovskite absorber layers and charge transport layers, the final electrode deposition step remains a major bottleneck for fully printed and flexible perovskite devices. High-efficiency laboratory devices still predominantly rely on vacuum deposition of noble metals such as gold or silver, which is inherently time-consuming, expensive, and incompatible with high-throughput R2R processing. Although PCE values exceeding 18% have been reported using alternative low-cost electrodes, including carbon-based contacts, the widespread adoption of such approaches remains limited [16–30]. Many exist-

ing carbon electrode strategies depend on high-temperature sintering, mesoporous scaffolds, or complex multilayer designs, which are unsuitable for flexible polymer substrates and continuous R2R fabrication.

In recent years, increasing attention has been directed toward the development of printable conductive inks based on organic and inorganic materials for flexible electronics. Among these, conductive carbon inks have emerged as particularly attractive candidates for use in fully printed perovskite solar cells (PSCs) and other optoelectronic devices [25, 31,32]. Carbon-based electrodes offer several key advantages over conventional metal contacts, including low cost, excellent chemical stability, intrinsic resistance to ion migration, and mechanical robustness under bending. Moreover, carbon inks can be deposited using scalable printing techniques such as slot-die coating, screen printing, and blade coating, significantly reducing fabrication complexity and overall production costs. These attributes are especially critical for printed flexible perovskite solar cells (FPSCs), where lightweight, mechanically compliant, and environmentally stable components are essential for reliable operation.

Nevertheless, the performance of carbon-based electrodes in printed flexible perovskite devices is highly sensitive to ink formulation, rheological properties, printing parameters, and post-deposition treatment. Inadequate control over these factors often leads to poor film uniformity, high sheet resistance, weak adhesion, and suboptimal interfacial contact with underlying layers, ultimately limiting device efficiency and reproducibility. Therefore, systematic optimization of the carbon ink printing process is a crucial step toward realizing high-performance, fully printed, and flexible perovskite optoelectronic devices compatible with industrial R2R manufacturing.

This paper investigates the optimization of carbon ink printing processes based on slot-die coating and screen-printing techniques for the fabrication of flexible electrodes. The electrical performance of the printed carbon layers was systematically evaluated through sheet resistance measurements as a function of printing parameters and ink formulation. Furthermore, fully printed FPSCs were successfully fabricated using the optimized carbon electrodes, demonstrating their suitability for scalable, low-temperature, and roll-to-roll–compatible perovskite optoelectronic device manufacturing.

2. Materials and methods

2.1 Materials

All the chemicals and reagents were used as received without any further purification. A flexible polyethylene terephthalate (PET, thickness 125 μm) with a layer of patterned transparent conducting indium-tin-oxide (ITO, thickness 150 nm, and sheet resistance – 45 Ω sq^{-1}) was purchased from Mekoprint. SnO_2 nanoparticle (NP) based colloid dispersion (15 wt.% colloidal dispersion in H_2O) is purchased from Alfa Aesar. Methylammonium iodide (MAI, 99.995%) is purchased from GreatCell solar. Lead iodide (PbI_2, 99%), methylamine solution (MA, in absolute ethanol 33 wt.%), acetonitrile (ACN, 99.8%), chlorobenzene (CB, 99.8%), acetone (99.9%), and 2-propanol (IPA, 99.5%) are purchased from Merck. PEDOT complex purchased from Ossila. Carbon ink (DM-CAP-4701S) was purchased from Dycotec.

2.2 Device fabrication

To fabricate fully printed FPSCs, PET/ITO substrates were sequentially cleaned in an ultrasonic bath for 10 minutes each in deionized (DI) water with detergent, DI water, acetone, and IPA, then dried using a nitrogen gun. The cleaned substrates were subsequently treated with UV-ozone for 15 minutes to enhance surface wettability. The fabrication of fully printed FPSCs was carried out using slot-die coating techniques. A VectorSC sheet-to-sheet slot-die coater (FOM technologies, Denmark) was employed to deposit the electron transport layer (ETL) made of SnO_2 NPs and the top carbon electrode. For the deposition of the perovskite ($MAPbI_3$) layer and PEDOT complex-based hole transport layer (HTL), a NanoRoll slot-die coater (FOM technologies, Denmark) was used, with the process conducted inside a glove box to ensure a controlled environment.

The tin oxide ETL was prepared from a commercial SnO_2 NP-based colloidal dispersion solution, which was diluted with DI water at a volume ratio of 1:3. The SnO_2 layer was printed on cleaned PET/ITO substrates at 150 μL min^{-1} pump rate and 80 cm min^{-1} chuck speed at temperature 50 °C, followed by annealing on a hot plate at 130 °C for 30 minutes. After annealing, the substrates underwent an additional UV-ozone treatment for 30 minutes to further improve film quality and interfacial properties.

Next, the $MAPbI_3$ layer was printed using a pump rate of 0.15 mL min^{-1} and the same coating speed, then annealed at 100 °C for 10 minutes. The perovskite ink was prepared by dissolving 1 mol of MAI (159.3 mg) and PbI_2 (461 mg) in 700 μL of MA, stirring at 460 rpm at 70°C for one hour. Afterward, 700 μL of ACN was added, and the solution was stirred at room temperature for 3 hours. The perovskite layer was coated at a pump rate of 70 μL min^{-1} and a chuck speed of 70 cm min^{-1} at a temperature of 130 °C. The films were then annealed on a hot plate at 100 °C for

10 minutes and allowed to cool to room temperature. Following the perovskite deposition, the PEDOT layer was applied under the same conditions as the perovskite layer. One sample was annealed at 100 °C for 10 minutes, while another was left unannealed.

The top carbon electrode was optimized and deposited using two methods: slot-die coating and screen-printing techniques.

2.3 Materials and device characterizations

The sheet resistance of electrodes was measured using a four-point system (RM3000, Jandel, UK). Raman Spectroscopy (Horiba LabRam Evolution) was used for structural characterization of carbon electrodes. A semiconductor device analyzer (B1500A, Keysight, USA) coupled with a 3A+ solar simulator (Oriel Sol3A, Newport, USA) providing an AM 1.5G illumination intensity of 100 mW cm^{-2} was used to measure the *J-V* characteristics of the devices.

3. Results and discussion

3.1 Optimization of carbon ink printing

First, experiments were carried out to evaluate the application of carbon ink (0.5 g in 1 mL of CB) and its electrical properties at varying pump rates (0.5-1 mL min^{-1}). The application speed was set at 0.8 m s^{-1}, and after the carbon film was deposited onto the PET substrate, the samples were annealed at 100 °C for 30 minutes to optimize film quality and ensure proper conductivity. Figure 1a shows a schematic sketch of the PET substrate used, displaying the numbering of the sections along the length of the substrate. Figure 1b displays a photographic image of the slot-die coating of a carbon film on top of a PET substrate. The carbon films were deposited at pump rates of 0.5, 0.75, and 1 mL min^{-1} (see Figures 1c and 1d). The results demonstrate that as the pump rate increases, sheet resistance decreases, which is attributed to the thicker carbon films produced with higher pump rates. Notably, at a pump rate of 1 mL min^{-1}, the carbon film exhibited a more uniform sheet resistance (~80 Ω sq^{-1}) compared to other pump rates, suggesting that this parameter offers a better consistency in film conductivity across the substrate (Figure 1c). This uniformity is crucial for improving the overall performance and reliability of devices.

The results indicate a clear inverse relationship between pump rate and sheet resistance. Although higher pump rates could potentially yield even lower resistance values, excessive ink supply may cause film inhomogeneity or ink overflow beyond the intended coating area. Based on these considerations, the optimized slot-die coating and annealing parameters for carbon electrode fabrication are summarized in Table 1.

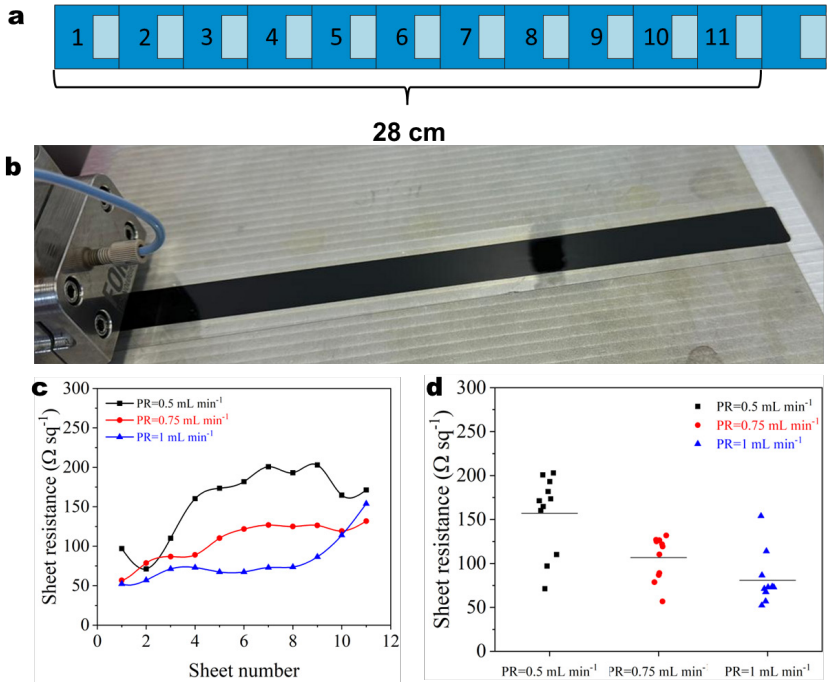

Figure 1. Sheet resistance of slot-die-coated carbon films on PET substrates at different pump rates (PR). a) Schematic of PET substrate section numbering for sheet resistance mapping. b) Photograph of a representative slot-die-coated carbon stripe on PET. c) Sheet resistance distribution along the substrate at PR = 0.5, 0.75, and 1.0 mL min^{-1}. d) Statistical comparison of sheet resistance at different PR.

Table 1. Optimal slot-die coating and annealing parameters for the carbon films on PET.

Coating parameters	Carbon
Chuck temperature (°C)	25
Coating speed (cm min^{-1})	80
Pump rate (mL min^{-1})	1
Coating window (μm)	221
Annealing temperature (°C)	100
Annealing time (min)	30

For the screen-printing process, a PET substrate was positioned beneath the patterned screen of the screen printer, which defined the electrode geometry. A controlled amount of carbon paste was then deposited onto the screen and transferred onto the PET substrate by sweeping a squeegee across the screen under uniform pressure, ensuring reproducible electrode formation. After printing, the screen was lifted, and the PET substrates with the printed carbon electrodes were annealed on a vacuum hot plate at 100 °C for 30 minutes to enhance film adhesion and electrical conductivity.

Two different electrode deposition strategies were investigated, as schematically illustrated in Figures 2a and 2b. In the first approach (Type 1), the carbon paste was applied at a single point along the screen (Figure 2a). In contrast, the second approach (Type 2) employed multi-point paste application along the printing direction to improve ink distribution (Figure 2b). As shown in Figure 2c, the single-point method resulted in non-uniform carbon electrode deposition, featuring thickness variations and incomplete coverage. In comparison, the multi-point method produced more homogeneous and continuous carbon films across the substrate.

The corresponding sheet resistance measurements are presented in Figures 2d and 2e. The electrodes fabricated using the multi-point printing strategy consistently exhibited lower sheet resistance values compared to those produced by the single-point method. The average sheet resistance of the optimized screen-printed carbon electrodes was approximately 125 Ω sq^{-1}. Owing to its superior film uniformity and electrical performance, the multi-point screen-printing method was selected for subsequent fabrication of fully printed FPSCs.

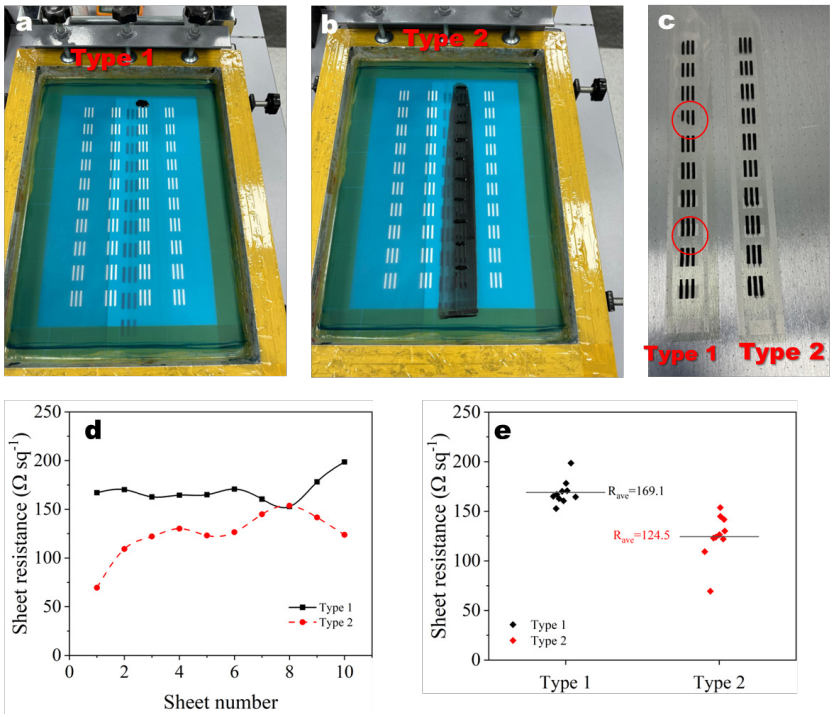

Figure 2. Comparison of carbon electrode deposition methods: single-point (Type 1) and multi-point (Type 2) screen printing. a) Screen-printing setup using single-point carbon paste application (Type 1). b) Screen-printing setup using multi-point carbon paste application (Type 2). c) Photograph of printed carbon electrode patterns obtained by Type 1 and Type 2. d) Sheet resistance distribution along the printed electrodes for Type 1 and Type 2. e) Statistical comparison of sheet resistance.

Figure 3 presents the Raman spectra of printed carbon films fabricated using two different coating techniques: slot-die coating and screen printing. The spectra exhibit characteristic features of carbon materials, including the D band (~1350 cm^{-1}), which is associated with structural disorder, and the G band (~1580 cm^{-1}), corresponding to graphitic sp^2-bonded carbon. Additional features, such as the D′ peak and the 2D band, provide further insight into the structural integrity and degree of graphitization of the films. The overall similarity of the Raman spectra indicates that the carbon films possess comparable structural properties, irrespective of the coating method employed.

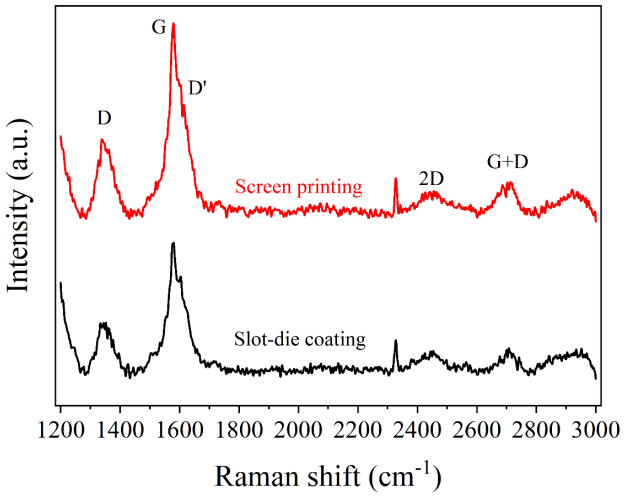

Figure 3. Raman spectra of printed carbon films on PET fabricated using different coating techniques.

Overall, both fabrication techniques – slot-die coating and screen printing – were effective to varying degrees, although the resulting electrodes exhibited different levels of conductivity. The lowest sheet resistance was obtained for the slot-die-coated electrodes, while the screen-printed electrodes exhibited higher sheet resistance. Nevertheless, screen printing offers a clear advantage in enabling the fabrication of small electrodes with well-defined and precise geometries required for device integration. Raman spectroscopy revealed comparable structural characteristics for the printed carbon electrodes, indicating that the coating method has a negligible impact on the intrinsic carbon structure.

3.2 Fabrication of fully printed flexible perovskite solar cells

Fully printed FPSCs incorporating printed carbon top electrodes were fabricated using optimized carbon printing parameters. All devices employed a regular (n–i–p) architecture, schematically illustrated in Figure 4a. The fabrication of fully printed FPSCs was carried out using slot-die coating techniques. The device architecture and corresponding layer thicknesses are as follows: PET (125 μm)/ITO (~150 nm)/SnO_2 ETL (~10 nm)/$MAPbI_3$ perovskite (~400 nm)/PEDOT HTL (~100 nm)/carbon electrode (~30–50 μm depending on deposition method). The thickness of the carbon electrode depends on the deposition technique, being ~40 μm for slot-die coating and ~30–50 μm for screen printing. Due to the inherent surface roughness and non-uniformity of printed carbon films, precise thickness determination is challenging, and profilometry measurements showed significant spatial variation.

Two types of fully printed FPSCs were prepared, distinguished by the carbon electrode deposition method. In the first configuration, a single-layer slot-die-coated carbon (C_{SDC}) electrode was employed as the top contact, yielding a PET/ITO/SnO_2/$MAPbI_3$/PEDOT/C_{SDC} device structure. In the second configuration, a single-layer screen-printed carbon (Indicate Type 2 C_{SP}) electrode served as the top contact, resulting in a similar PET/ITO/SnO_2/$MAPbI_3$/PEDOT/C_{SP} device structure.

Photographic images of the fabricated flexible devices are shown in Figures 4b and 4c. Figure 4b presents a representative fully printed FPSC with a continuous carbon top electrode, demonstrating good coverage and mechanical flexibility of the device. Figure 4c shows a flexible device with patterned printed carbon electrodes, highlighting the compatibility of the developed printing processes with electrode patterning and flexible substrate handling. These results demonstrate a successful integration of printed carbon electrodes into fully printed FPSCs.

Figure 5 displays the *J-V* curve of the best-performing fully printed FPSC with a C_{SDC} top electrode, along with statistical data for the photovoltaic parameters of ten devices. The active area of the devices was 1.95 cm^2. The results indicate that devices with C_{SDC} top electrodes demonstrate moderate performance, with the best-performing device achieving a PCE of approximately 0.6%. In addition, the

series resistance (Rs) of the devices was extracted and is presented in Figures 5f. The observed Rs values correlate well with the sheet resistance of the carbon electrodes, confirming that electrode conductivity plays a key role in charge transport and device performance. The main performance-limiting factors for these devices are attributed to low J_{SC} and FF, primarily due to the large active area and the low conductivity of the single-layer C_{SDC}. By reducing the active area and depositing multiple layers of C_{SDC}, it may be possible to achieve improved device performance.

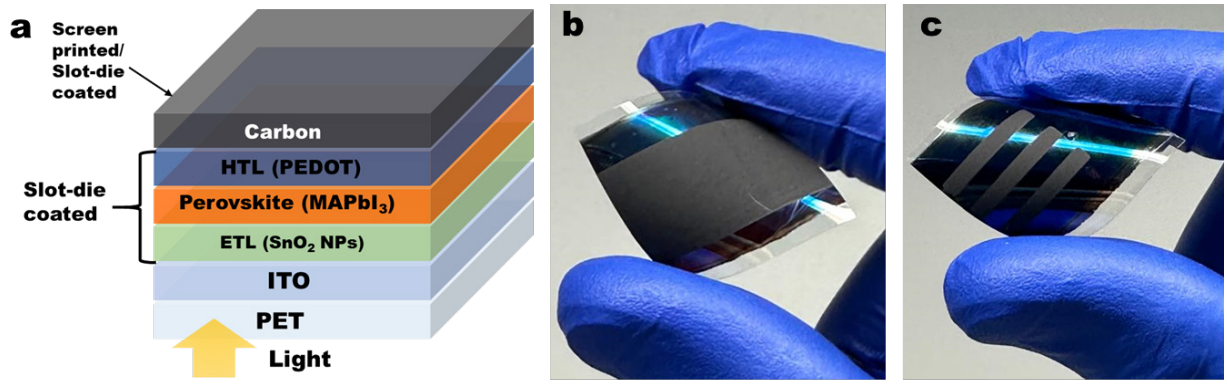

Figure 4. Schematic illustration of the FPSC device structure and photographic images of fully printed FPSCs fabricated with printed carbon electrodes. a) Schematic illustration of the n–i–p device structure. b) Photograph of a fully printed FPSC fabricated using the slot-die coating method. c) Photograph of a fully printed FPSC with screen-printed carbon electrodes.

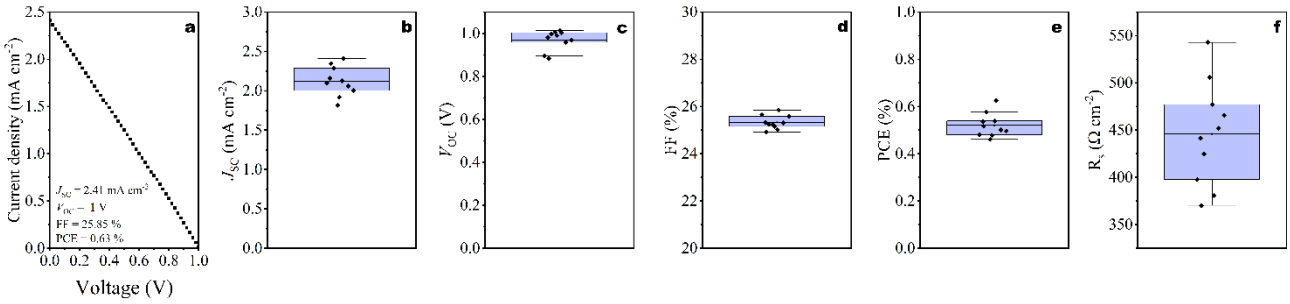

Figure 5. Solar cell performance results of fully printed FPSCs with C_{SDC} top electrodes. a) *J-V* curve of the best-performing device and statistical data for b) J_{SC}, c) V_{OC}, d) FF, e) PCE, and series resistance (Rs) of fully printed FPSCs with C_{SDC} top electrodes.

Figure 6 displays the *J-V* curve of the best-performing fully printed FPSC with a C_{SP} top electrode, along with statistical data for the photovoltaic parameters of twenty devices. The active area of the completed devices was 0.15 cm^2. The results indicate that devices with C_{SP} top electrodes exhibit improved performance, achieving a PCE of approximately 3.86%. In addition, the series resistance (Rs) of the devices was extracted and is presented in Figures 6f. The observed Rs values correlate well with the sheet resistance of the carbon electrodes, confirming that electrode conductivity plays a key role in charge transport and device performance. The main performance-limiting factor in this case is attributed to the low FF, which results from the low conductivity of the C_{SP}. Nevertheless, this represents a significant improvement compared to the devices with C_{SDC} (see Figure 5). Increasing the thickness of the C_{SP} holds promise for further enhancing device performance.

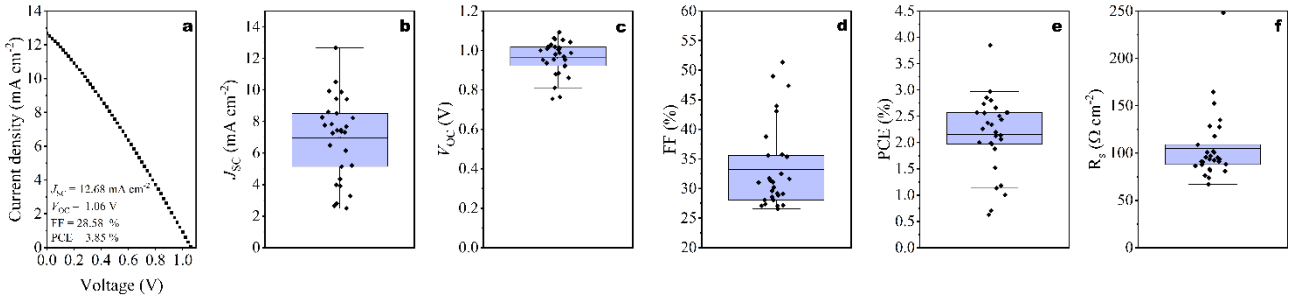

Figure 6. Solar cell performance results of fully printed FPSCs with C_{SP} top electrodes. a) *J-V* curve of the best-performing device and statistical data for b) J_{SC}, c) V_{OC}, d) FF, e) PCE, and series resistance (Rs) of fully printed FPSCs with C_{SP} top electrodes.

Overall, these results indicate that further performance enhancement of fully printed FPSCs with carbon top electrodes critically depends on optimizing the electrode morphology, electrical conductivity, and interfacial contact quality. This finding highlights the decisive role of carbon electrode deposition in governing the overall device performance of fully printed FPSCs.

In addition to the electrode-related limitations discussed above, the overall device performance is further constrained by interfacial and material-related factors. In particular, the HTL/carbon interface represents a critical bottleneck due to imperfect physical contact, surface roughness, and the absence of interfacial passivation, which can promote non-radiative recombination and hinder efficient charge extraction. These effects contribute to increased series resistance and reduced fill factor. Furthermore, the use of $MAPbI_3$ as the perovskite absorber introduces intrinsic limitations in terms of defect density and optoelectronic quality, resulting in lower achievable efficiencies compared to state-of-the-art multi-cation and mixed-halide perovskites.

To address these challenges, several strategies can be considered. The incorporation of interfacial passivation layers between the HTL and the carbon electrode could suppress recombination losses and improve energy level alignment. In addition, post-deposition treatments such as mechanical pressing or pulsed light annealing may enhance the physical contact and electrical connectivity at the interface. Finally, the implementation of more advanced perovskite compositions with improved crystallinity and reduced defect density is expected to significantly enhance device performance. These approaches provide a clear pathway toward improving the efficiency of fully printed FPSCs.

4. Conclusion

In this work, carbon-based electrodes for fully printed flexible perovskite solar cells were fabricated and optimized using two scalable printing techniques: slot-die coating and screen-printing. The influence of printing parameters on the electrical performance and uniformity of the carbon films was systematically investigated, followed by their integration into fully printed n–i–p perovskite device structure.

Slot-die-coated carbon electrodes exhibited a clear decrease in sheet resistance with increasing pump rate, with an optimized condition of 1 mL min^{-1} yielding uniform films with a sheet resistance of ~80 Ω sq^{-1} after low-temperature annealing. For screen-printed electrodes, a multi-point paste application strategy significantly improved film uniformity and reduced sheet resistance to ~125 Ω sq^{-1} compared to single-point deposition. Raman spectroscopy confirmed comparable structural properties of the carbon films produced by both methods, indicating that electrical differences mainly arise from film morphology and thickness.

Using the optimized electrodes, two types of fully printed FPSCs were fabricated. Devices with single-layer slot-die-coated carbon (C_{SDC}) top electrodes achieved a maximum PCE of ~0.6% over a large active area (1.95 cm^2), while devices employing screen-printed carbon (C_{SP}) electrodes reached a higher PCE of up to 3.86% for smaller-area devices (0.15 cm^2). The improved performance of CSP-based devices is attributed to enhanced charge collection resulting from thicker and more conductive carbon contacts.

Overall, this study demonstrates the feasibility of fully printed, flexible perovskite solar cells employing carbon-based top electrodes without vacuum processing. Further improvements are expected through

increasing carbon electrode thickness, enhancing conductivity, and optimizing interfacial contact, paving the way toward scalable, roll-to-roll fabrication of flexible perovskite optoelectronic devices.

Funding

Science Committee of the Ministry of Science and Higher Education of the Republic of Kazakhstan (grant numbers AP26194151).

Acknowledgements

We would like to thank the Core Facilities team of Nazarbayev University.

Conflicts of interest

The authors declare no conflict of interest.

Author contributions.

Conceptualization: Y.Y. and A.N.J.; Methodology Y.Y. and A.N.J.; Validation Y.Y.; Formal Analysis, Y.Y. and A.N.J.; Investigation, Y.Y. and A.N.J.; Resources, Y.Y. and A.N.J.; Data Curation, Y.Y.; Writing – Original Draft Preparation, Y.Y; Writing – Review & Editing, A.N.J..; Visualization, Y.Y.; Supervision, A.N.J.; Project Administration, Y.Y.; Funding Acquisition, Y.Y."

References

1. Y. Jung, K. Hwang, Y. Heo, J. Kim, D. Vak, D. Kim. "Progress in scalable cating and roll-to-roll compatible printing processes of perovskite solar cells toward realization of commercialization". *Adv. Opt. Mater*., vol.6, no. 11, Art. no. 1701182, 2018. https://doi.org/10.1002/adom.201701182.

2. T. Webb, S.J. Sweeney, W. Zhang, "Device architecture engineering: progress toward next generation perovskite solar cells", *Adv. Funct. Mater*., vol. 31, no 35, p. 2103121, 2021. https://doi.org/10.1002/adfm.202103121.

3. https://www.nrel.gov/pv/cell-efficiency.html .

4. A. Ghosh, A. Bakkar, Momina et al., "Enhancing solar cell efficiency beyond 27% through the implementation of an efficient charge transport layer utilizing an innovative inorganic perovskite Sr3PI3", *Journal of Physics and Chemistry of Solids,* vol.190, Art. no.112029, 2024. https://doi.org/10.1016/j.jpcs.2024.112029.

5. Z. Xiong, Q. Zhang, K. Cai et al., "Homogenized chlorine distribution for PCE;27% power conversion efficiency in perovskite solar cells", *Science*, vol. 390, no. 6773, pp.638–642, 2025. https://doi.org/10.1126/science.adw8780.

6. D. Beynon, E. Parvazian, K. Hooper et al., "All-printed roll-to-roll perovskite photovoltaics enabled by solution-processed carbon electrode", *Advanced Materials,* vol. 35, no. 16, Art. no.2208561, 2023. https://doi.org/10.1002/adma.202208561.

7. T.M. Schmidt, T.T. Larsen-Olsen, J.E. Carlé, D. Angmo, F.C. vKrebs, "Upscaling of perovskite solar cells: fully ambient roll processing of flexible perovskite solar cells with printed back electrodes", *Adv. Energy Mater.,* vol. 5, no. 15, Art. no. 1500569, 2015. https://doi.org/10.1002/aenm.201500569.

8. A.H. Ghahremani, T. Druffel, "Realizing perovskite solar cells on roll roll-to-roll compatible processes", in: 2019 IEEE 46th Photovoltaic Specialists Conference (PVSC), IEEE,: pp. 1–5, 2019. https://doi.org/10.1109/PVSC40753.2019.9198957.

9. A. Dyadenchuk, O. Roman, Y. Kuris, "Structural and electrical characteristics of the ZnO/porous-Si/Si heterostructure: from synthesis to analysis of photocell efficiency", *Int. J. of Math. and Phys.*, vol. 15, no. 2, pp. 34–41, 2024. https://doi.org/10.26577/ijmph.2024v15i2b4.

10. A.T. Sultanov, I. Zhirkov, A. Suleimenova, N. Beisenkhanov, "Computer simulation of planar bifacial TOPCon solar cells by using Quokka 3 software", *Physical Sciences and Technology*, vol. 12, no. 3-4, pp.93–105, 2025. https://doi.org/10.26577/phst20251229.

11. D. Burkitt, R. Patidar, P. Greenwood et al., "Roll-to-roll slot-die coated P–I–N perovskite solar cells using acetonitrile based single step perovskite solvent system", *Sustain. Energy Fuels*, vol.4, no. 7, pp. 3340–3351, 2020. https://doi.org/10.1039/D0SE00460J.

12. Y.Y. Kim, T.-Y. Yang, R. Suhonen, A. Kemppainen, K. Hwang, N.J. Jeon, J. Seo, "Roll-to-roll gravure-printed flexible perovskite solar cells using eco-friendly antisolvent bathing with wide processing window", *Nat. Commun.*, vol.11, Art. no. 5146, 2020. https://doi.org/10.1038/s41467-020-18940-5.

13. J. Kim, S. Kim, C. Zuo, M. Gao, D. Vak, D. Kim, "Humidity-tolerant roll-to-roll fabrication of perovskite solar cells via polymer-additive-assisted hot slot die deposition", *Adv. Funct. Mater.,* vol.29, no.29, Art. no.1809194, 2019. https://doi.org/10.1002/adfm.201809194.

14. H. Li, C. Zuo, D. Angmo, H. Weerasinghe, M. Gao, J. Yang, "Fully roll-to-roll processed efficient perovskite solar cells via precise control on the morphology of PbI_2:CsI layer", *Nanomicro Lett.,* vol.14, Art. no. 79, 2022. https://doi.org/10.1007/s40820-022-00815-7.

15. M. Othman, F. Zheng, A. Seeber et. al., "Millimeter-sized clusters of triple cation perovskite enables highly efficient and reproducible roll-to-roll fabricated inverted perovskite solar cells", *Adv. Funct. Mater.,* vol. 32, no. 12, Art. no. 2110700, 2022. https://doi.org/10.1002/adfm.202110700.

16. Z. Gu, L. Zuo, T.T. Larsen-Olsen, T. Ye, G. Wu, F.C. Krebs, H. Chen, "Interfacial engineering of self-assembled monolayer modified semi-roll-to-roll planar heterojunction perovskite solar cells on flexible substrates", *J. Mater. Chem. A Mater*., vol. 3, pp. 24254–24260, 2015. https://doi.org/10.1039/C5TA07008B.

17. F. Bisconti, A. Giuri, R. Suhonen et.al., "One-step polymer assisted roll-to-roll gravure-printed perovskite solar cells without using anti-solvent bathing", *Cell Rep. Phys. Sci*., vol. 2, no. 11, Art. no. 100639, 2021. https://doi.org/10.1016/j.xcrp.2021.100639.

18. L.J. Sutherland, D. Vak, M. Gao, T.A.N. Peiris, J. Jasieniak, G.P. Simon, H. Weerasinghe, "Vacuum-free and solvent-free deposition of electrodes for roll-to-roll fabricated perovskite solar cells", *Adv. Energy Mater.*, vol. 12, no. 40, Art. no. 2202142, 2022. https://doi.org/10.1002/aenm.202202142.

19. J.F. Benitez-Rodriguez, D. Chen, et.al., "Slot-die coating of a formamidinium-cesium mixed-cation perovskite for roll-to-roll fabrication of perovskite solar cells under ambient laboratory conditions", *Solar Energy Materials and Solar Cells*, vol. 246, Art. no. 111884, 2022. https://doi.org/10.1016/j.solmat.2022.111884.

20. A.G. Kakimov, Y. Yerlanuly, A. Akhanuly, et. al., "Passivation of perovskite layer surface states with pyridine in flexible and printed perovskite solar cells", *Flexible and Printed Electronics*, vol. 7, Art. no. 035012, 2022. https://doi.org/10.1088/2058-8585/ac8753.

21. M.S. Kiani, Z.T. Sadirkhanov, A.G. Kakimov, H.P. Parkhomenko, A. Ng, A.N. Jumabekov, "Solution-processed sno2 quantum dots for the electron transport layer of flexible and printed perovskite solar cells", *Nanomaterials*, vol. 12, no.15, Art. no. 2615, 2022. https://doi.org/10.3390/nano12152615.

22. M.S. Kiani, H.P. Parkhomenko, M. Mangrulkar, et. al., "Stepping toward portable optoelectronics with sno $_2$ quantum dot-based electron transport layers", *ACS Omega*, vol. 8, no. 23, pp.21212–21222, 2023. https://doi.org/10.1021/acsomega.3c02341.

23. H. Wang, F. Yang, X. Li, P. Zhang, "Fully printed high-performance quasi-two-dimensional perovskite solar cells via multifunctional interfacial engineering", *Adv. Funct. Mater*., vol. 34, no.10, Art. no. 2312250, 2024. https://doi.org/10.1002/adfm.202312250.

24. H.P. Parkhomenko, Y. Yerlanuly, V. V. Brus, A.N. Jumabekov, "Effect of mild mechanical stresses on device physics of slot-die coated flexible perovskite solar cells", *Org. Electron*., vol. 129, Art. no. 107049, 2024. https://doi.org/10.1016/j.orgel.2024.107049.

25. H.C. Weerasinghe, N. Macadam, J.-E. Kim, et al., "The first demonstration of entirely roll-to-roll fabricated perovskite solar cell modules under ambient room conditions", *Nat. Commun*., vol. 15, Art. no. 1656, 2024. https://doi.org/10.1038/s41467-024-46016-1.

26. L.J. Sutherland, J. Benitez-Rodriguez, D. Vak, et. al., "A high-pressure isostatic lamination technique to fabricate versatile carbon electrode-based perovskite solar cells", *Commun. Mater.,* vol. 5, Art. no. 90, 2024. https://doi.org/10.1038/s43246-024-00530-3.

27. V. Messerle, A. Ustimenko, "Plasmatron with renewable carbon nanostructured covering of electrodes", *Physical Sciences and Technology*, vol. 1, no.1, pp. 43–47, 2014. https://doi.org/10.26577/phst-2014-1-13.

28. A. Malgazhdarova, M. Kazankapova, B. Yermagambet, et. al., "Synthesis and characterization of carbon nanomaterials obtained using electric discharge", *Physical Sciences and Technology*, vol. 12, no. 1-2, pp. 68–83, 2025. https://doi.org/10.26577/phst20251217.

29. Sh.T. Nurbolat, M. Gabdullin, Zh. Kalkozova, M. Mirzaeian, Kh. Abdullin, "Capacitive electrodes based on a combination of activated carbon and graphene", *Physical Sciences and Technology*, vol. 9, no. 3-4, pp. 18–24, 2022. https://doi.org/10.26577/phst.2022.v9.i2.03.

30. Zh.A. Kudyshev, I.R. Gabitov, A. Kissan, Ye.S. Mukhametkarimov, "Hyperbolic metamaterials based on graphene sheets with different values of chemical potentials", *Physical Sciences and Technology*, vol. 3, no. 2, pp. 4–11, 2016. https://doi.org/10.26577/phst-2016-2-100.

31. N. Mussakhanuly, Y. Yerlanuly, H.P. Parkhomenko, A. Niyetullayeva, A.K. Azamat, A. Sultanov, Z. Kukhayeva, A. Ng, A.N. Jumabekov, "Laminated carbon based flexible printed perovskite solar cells passivated with tin(ii) phthalocyanine", *Adv. Mater. Interfaces*, vol. 12, no. 5, Art. no. 2400591, 2025. https://doi.org/10.1002/admi.202400591.

32. S.L. Mikhailova, O.Yu. Prikhodko, N.K. Manabaev, "Electrical properties of a-C:H films modified by Pt", *International Journal of Mathematics and Physics*, vol.5, no. 2, pp. 64–67, 2014. https://doi.org/10.26577/2218-7987-2014-5-2-64-67.

Information about authors:

Yerassyl Yerlanuly – PhD, Senior researcher, National Laboratory Astana, Department of Physics, School of Sciences and Humanities, Nazarbayev University (Astana, Kazakhstan, email: yerassyl.yerlanuly@nu.edu.kz);

Askhat N. Jumabekov (corresponding author) – Dr. rer. Nat. (PhD), Associate Professor of the Department of Physics, School of Sciences and Humanities, Nazarbayev University (Astana, Kazakhstan, email: askhat.jumabekov@nu.edu.kz).

IRSTI 47.45.00 https://doi.org/10.26577/phst20261318

The reduced size quasi-Yagi antenna with an ends-fed dipole-like driver

V. Atuchin[1,2,3*], D. Buhtiyarov[4], A. Gorbachev[3], V. Khrustalev[3] and N. Tarasenko[3]

[1]Kemerovo State University, Kemerovo, Russia
[2]Institute of Semiconductor Physics, SB RAS, Novosibirsk, Russia
[3]Novosibirsk State Technical University, Novosibirsk, Russia
[4]Institute of Cosmic and Aviation Materials (NIICAM Co. Ltd.), Pereslavl-Zalessky, Russia
*e-mail: atuchin@isp.nsc.ru

(Received April 4, 2026; received in revised form May 20, 2026; accepted May 29, 2026)

A modified version of the printed quasi-Yagi antenna by using the so-called ends-fed dipole-like radiator is presented. In this radiator, the excitation nodes are placed on the far ends of the dipole metallic halves rather than on the adjacent ones. As a result, the current distribution along each of the radiator cylindrical/printed wire significantly differs from that related to the ordinary center-fed dipole. That is why the frequency behavior of the proposed radiator input impedance guarantees the nontraditional radiation properties. Additionally, this approach to the choice of the excitation nodes leads to the simplification of the printed-circuit-board (PCB) implementation. A printed prototype operating at 2.8 GHz is developed and tested. Since the area around the radiating arms is fully free from any conductors and dielectrics (except for the substrate itself), the proposed quasi-Yagi antenna is a good candidate to emit radiation of high polarization purity. The measured results revealed that such an antenna is able to reach an effective area reduction to 40% with the enhanced up to 10 dB front-to-back ratio without decreasing the bandwidth.

Keywords: printed-circuit-board radiators, induced electromotive force method, quasi-Yagi antenna, radiation pattern, telecommunication.

1. Introduction

Modern wireless communication systems need wideband devices to transmit and receive simultaneously the signals with an acceptable isolation between transmitting and receiving channels [1]. To achieve this purpose, the development and improvement of printed directional antennas of various kinds remain topical [2]. A suppression of an unwanted radio frequency emission has led to an increasing demand for antennas, such as quasi-Yagi assemblies. There are many Yagi-Uda/quasi-Yagi antennas with a strip/coaxial feed and a dipole driver that have been presented for the last ten years [3-10]. Each of these antennas is a successful discovery in terms of its bandwidth, radiation patterns, size reduction and simple manufacturing. However, all the antennas contain a balance unit (balun) that is used to excite the center-fed dipole driver. Frequently, 180º out-of-phase balun nodes are displaced in the area substantially, and that increases the surroundings around the dipole nodes and affects the polarization purity of radiation. This also needs an accurate accomplishment of design, including the line length, as well as its meandering/turning. The difficulties mentioned bring some sort of motivation for a further investigation of quasi-Yagi antennas. Below, we describe a novel modification of the printed ones.

This approach is based on the utilization of the so-called “end-fed dipole radiator” (EFDR) patented in [11] and then successfully used in [12] to improve the one-band quasi-Yagi antenna. Lately, this EFDR was realized for the waveguide excitation [13] and was used in the printed dual-band quasi-Yagi antenna on the base of the broadband balun with microstrip-to-slotline transitions [14]. The architecture, which is described below, is the result of an attempt to alleviate the complication of a coaxial/strip feed with a regular wire antenna design principle by combining the nonstandard ends-fed dipole-like radiator and a

balun that is implemented on a base of the microstrip-slot and parallel stripline-microstrip transitions. A systematic study of the modified printed quasi-Yagi antenna is briefly presented, and the following numerical optimization of the proposed antenna by a proper 3D EM solver is described. As a result, all the key geometrical dimensions were established and then successfully used through the PCB fabrication on the standard Cu-clad dielectric substrate FAF-4D (Russia) with the 1.5 mm thickness. The simulation-derived and anechoic chamber-based experimental results are used to verify the described approach. The slight difference between the numerical and experimental values may be caused by the round corners of the strip-line topology as well as the discontinuity of the coaxial adapter, manufacturing imperfections and radio frequency interconnections by using a coaxial cable. These features were not taken into account through the full-wave simulation. The use of such a driver contributes to an increase in the degree of freedom in the design of printed quasi-Yagi antennas. At the same time, depending on the set of requirements of the tactical and technical specifications for the design, various optimization strategies can be constructed.

2. Current distribution along the stand-alone EFDR and its radiation resistance

As proposed in [11], an ends-fed dipole-like radiator contains two thin ($a \ll l$) collinear cylindrical wires 1 and 2, an energized coaxial cable 3 and the balance unit (balun) 4 having the input port 5 and 180º out-of-phase output ports 6 and 7 (Figure 1(a)). The adjacent ends 8 and 9 of both wires are placed in the immediate nearness ($b << l$), whereas the far ends of those play the role of the input terminals 10 and 11.

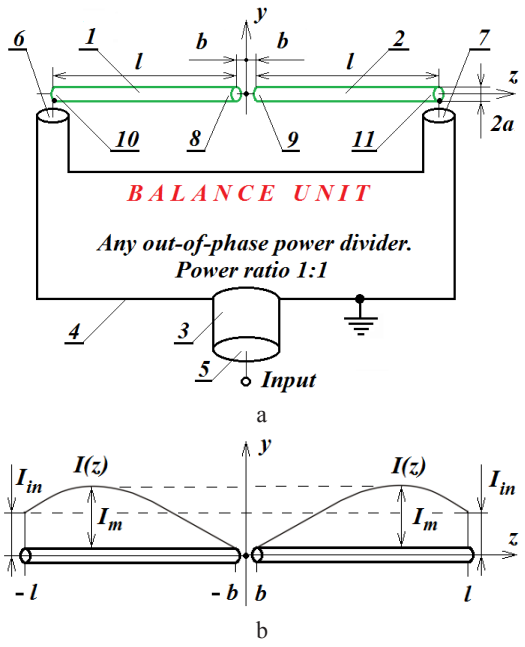

Figure 1. Stand-alone ends-fed dipole-like radiator: (a) functional scheme, (b) current distribution along the wires.

Now, the detailed analysis described in [15] leads to the following expressions for the current distribution $I(z)$ along the wires (Figure 1(b)) and for EFDR radiation resistance R_{rad}:

$$I(z)=\begin{cases} I_m \sin(+kz), 0 < z \le +l, \\ I_m \sin(-kz), -l \le z < 0. \end{cases}$$

$$R_{rad} = 2P_{rad} \Big/ |I_m|^2 = 60 \int_0^{\pi} \left[Q^2 \Big/ \sin\theta \right] d\theta$$

$$= 30 \left\{ 3\gamma + \ln\left[4(kl)^3 \right] + Ci(4kl) - 4Ci(2kl) + 2\sin\left[(kl)^2 \right] \left[\frac{\sin(2kl)}{2kl} - 1 \right] \right\}, \quad (1)$$

where P_{rad} represents the total power radiated from the EFDR through the closed sphere lying around a radiator in the far-field Fraunhofer region, I_m is the current maximum, k = 2π/λ, λ is the free space wavelength, γ = 0.5772157 (Euler constant), $Ci(x)$ is the cosine integral, and the quantity Q is determined as:

$$Q = 1 - \cos(kl\cos\theta)\cos(kl) - \sin(kl\cos\theta)\sin(kl)\cos\theta .$$

Now, according to [2, Chapter 8], the real part R_m of an input impedance $Z_m = R_m + jX_m$ referred to at the current maximum I_m can be expressed as $R_m = R_{rad}$, whereas the real part R_{in} of the input impedance $Z_{in} = R_{in} + jX_{in}$ referred to at the current I_{in} at the input terminals 10 and 11 (Figure 1(b)) can be obtained by a transfer relation $I_{in} = I_m \sin(kl)$, or:

$$R_{in} = R_m \Big/ \sin^2(kl) . \quad (2)$$

As may be seen, the current distribution $I(z)$ along the EFDR is significantly different from the distribution specific to a classical ordinary dipole radiator. Therefore, the frequency response of the input impedance of the EFDR considered will be significantly different from the similar frequency response of the classical dipole. This should be taken into account through the antenna design.

3. Self-impedance of the Stand-alone EFDR

As a result, the induced electromotive force (*emf*) method leads to closed-form solutions which provide such the design data that can be used directly as very good initial parameters in the full-wave 3D EM simulation. According to [15], both the real R_m [R_{in}] and the imaginary X_m [X_{in}] part of the self- [input] impedance $Z_m = R_m + jX_m$ referred to at the current maximum I_m [$Z_{in} = R_{in} + jX_{in}$ referred to at the current I_{in} at the input terminals 10 and 11] can be expressed for a free-space as (in Ohms):

$$R_m = 60 \left\{ \sin^2(kl) \left(\frac{\sin(kl\sqrt{4+(a/l)^2})}{kl\sqrt{4+(a/l)^2}} - \frac{\sin(ka)}{ka} \right) + 3Ci(ka) \right.$$

$$+0.5Ci[kl(\sqrt{4+(a/l)^2}+2)] + 0.5Ci[kl(\sqrt{4+(a/l)^2}-2)]$$

$$\left. -2Ci[kl(\sqrt{1+(a/l)^2}+1)] - 2Ci[kl(\sqrt{1+(a/l)^2}-1)] \right\} \quad (3)$$

$$X_m = 60 \left\{ \sin^2(kl) \left(\frac{\cos(kl\sqrt{4+(a/l)^2})}{kl\sqrt{4+(a/l)^2}} - \frac{\cos(ka)}{ka} \right) - 3Si(ka) \right.$$

$$-0.5Si[kl(\sqrt{4+(a/l)^2}+2)] - 0.5Si[kl(\sqrt{4+(a/l)^2}-2)]$$

$$\left. +2Si[kl(\sqrt{1+(a/l)^2}+1)] + 2Si[kl(\sqrt{1+(a/l)^2}-1)] \right\} \quad (4)$$

$$R_{in} = R_m \Big/ \left[\sin(kl)\right]^2 , \; X_{in} = X_m \Big/ \left[\sin(kl)\right]^2 . \quad (5)$$

The numerical analysis of the last relations indicates that the input impedance $Z_{in} = R_{in} + jX_{in}$ [quantities in (5)] is characterized by a significant capacitive component with a curvilinear change in l/λ within the range of $0.1 < l/\lambda < 0.6$. At the same time, the real part R_{in} [Ohm] changes in the range

of $15 < R_{in} < 180$. These results are used in the following considerations related to the EFDR vertically placed above the ground.

The presence of an obstacle (such as a rectangular waveguide), especially in the vicinity of a radiating element, will significantly alter the overall radiative properties of the antenna system. In practice, the most common always considered obstacle is the ground. The energy radiated by the radiating element and oriented in the direction of the earth is reflected. The amount of reflected energy and its direction are dependent on the ground metallic geometries and their dimensions.

To analyze the behavior of the antenna near a ground conductor, virtual sources (source images) must be introduced to take reflections and interference into account [2]. As it follows from the name, these are not real sources, but imaginary ones, which, when combined with real sources, form an equivalent system. For the purposes of analysis only, the equivalent system gives the same radiated field on and over the conductor as the real system itself. Under the conductor, the equivalent system is not able to give the correct field. However, in this region, the field is equal to zero and equivalence is not needed. When the height of the source above the plane h is equal to zero, primary and secondary horizontal fields of an electric vibrator and a vertical magnetic vibrator become equal in terms of amplitude and opposite in sign, the total field becomes zero and the radiation disappears. Conversely, in the case of a vertical electric vibrator and horizontal magnetic vibrator, the primary and secondary fields at $h = 0$ become equal in amplitude and sign, so that the total field is doubled relative to the field of the same source in free space. Concerning the resistance and conductivity of radiation sources, then, at $h = 0$ in the first case, they become equal to zero, and, in the second, – they double. The doubling resistance and conductivity of radiation is related to the fact that the radiated power density in each point in space is quadrupled, but the energy is radiated only into the upper half-space.

4. Printed quasi-Yagi antenna employing microstrip-slot and stripline-microstrip transitions

The results indicated in the previous section are used here to create the proposed antenna topology. Contrary to the version on the base of the printed rectangular-coaxial (recta-coax) transmission line described in [15], it is useful to modify both the driver and director in order to realize the more compact strip-line architecture. To do so, the quarter-wave directional coupler should be omitted from the architecture described in [15], and then the compact planar out-of-phase power divider proposed in [16] will be used. As a result, after the use of equations (1) – (5) for the recalculation of the strip widths, two proper dielectric substrates with copper clothes are used simultaneously to realize the printed ends-fed driver, as well as the printed director and power divider without any metallized via-holes (Figure 2, all dimensions are in mm).

After calculations, it is necessary to refine and optimize the pieces of the topology in a specialized program of electrodynamic modeling. The optimization in the program is divided into several stages, at each of which certain antenna components or fragments of complex elements are optimized. For example, in the case of a multi-component Yagi antenna having a dipole-like driver, several directors and a reflector, the optimization process is carried out in three steps. Before a brief description of the optimization steps, it is useful to note that, in printed versions of Yagi antennas, the edge of a metallized rectangle plays the role of a reflector. Such use of the grounded fragment foil edge as a reflector was previously described in printed Yagi antennas [3], and it was successfully applied as a reflector of other quasi-Yagi antennas, including the described novel printed quasi-Yagi antenna with an ends-fed dipole-like driver. In the authors' opinion, it is quite difficult to compact describe the optimization process with references to formulas (1) – (5). The optimization process itself is based on trial-and-error and depends heavily on the experience of the project implementers. Therefore, what follows is a description of the optimization process as the authors see it.

In the first optimization step, the distance between the driver and the nearest elements is optimized directly, i.e., usually the edge of the fragment located on the back of the dielectric substrate. Also, the distance between the driver and the first passive element (director) is optimized at the first step. Initially, the calculated dimensions of the driver itself are determined by the parameters of the terms of reference and correspond to the selected working frequency. In this case, the distances between passive elements and their dimensions are set in the program with a spread of parameters of

approximately 10-15%. This tolerance is quite enough to select the optimal dimensions of the antenna elements. At the first stage of optimization, it is desirable not to pay much attention to the shape of the radiation pattern, but to carry out the optimization itself in terms of the quality of antenna matching. Just this parameter, at the first stage, is the key and allows in the future, at the next steps, obtaining the necessary shape of the antenna pattern, as well as to reach the required gain.

At the second stage of optimization, distances between other directors are selected (if any). As the number of the directors increases, the antenna gain also increases, the beam pattern narrows, and the antenna becomes more directional. In other words, the optimization of a Yagi antenna with more than three directors is a long process involving many complex tasks, since it is necessary to control several parameters of the antenna (reflection coefficient, radiation pattern shape, gain) and at the same time ensure that the working frequency of the antenna remains unchanged. Additionally, with a large number of directors, in order to maintain the required characteristics, it is sometimes necessary to change the central location of passive elements, slightly shifting them from the central axis of the antenna in one direction or another. Also, the use of various types of drivers leads to a different distance between directors and to the width of passive elements.

At the third stage, the lengths and widths of the directors themselves are optimized. At this stage, the optimization is carried out on all necessary parameters and not only on the matching characteristic. At the same time, the center frequency of the antenna does not shift. And if the shape of the directional pattern does not meet the requirements of the terms of reference, in addition to changes in the third optimization step, it is necessary to make small changes in the director positions obtained in the previous step.

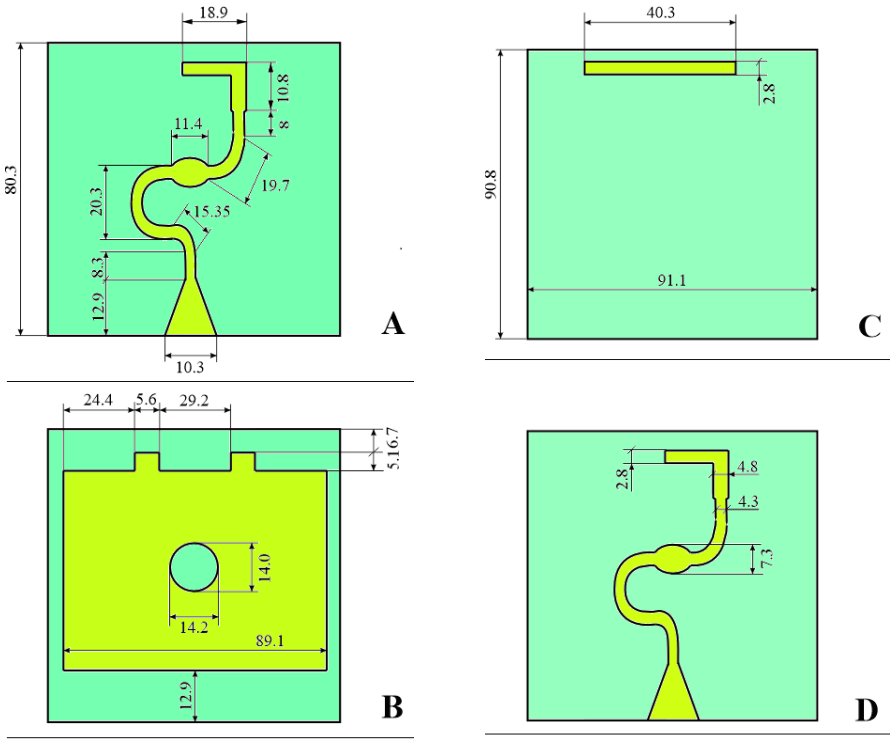

Figure 2. Three-layer printed-circuit-board implementation of the radiating domain and out-of-phase power splitter related to the modified version of the quasi-Yagi antenna employing only two dielectric substrates: (A) top side of the first substrate, (B) bottom one of that, (C) top side of the second substrate, and (D) bottom one of that.

In this modification, two Cu-clad dielectric sheets (Russia) are used. Namely, to realize the whole three-layer sandwich structure (Figure 2) related to both the radiating part of the quasi-Yagi antenna and the nonradiating domain containing the power divider itself, the 1.5 mm thick organic dielectric substrates FAF-4D (Russia) were used. This nomenclature was chosen because of its low loss tangent (tanδ = 0.002) and a small relative dielectric constant variation ($\varepsilon_r = 2.5 \pm 0.1$) [17]. The copper foil thickness is equal to 0.035 mm.

Without loss of generality, the center frequency of the proposed whole quasi-Yagi antenna was chosen to be 2.8 GHz. After the corresponding systemic design and nonlinear parametric optimization through the 3D full-wave solver "CST Studio Suite" [18], the final geometrical dimensions were found, as shown in Figure 2 (in mm). The printed-circuit-board implementation was performed using the conventional Russian photo-lithography procedure and wet etching.

As a result, the presented topology version of the planar quasi-Yagi antenna was measured on a base of the anechoic chamber by using an ordinary far-field measurement arrangement. The KRPG-434511.016 connector [19, Figure 3, Table 8] was used to connect the manufactured antenna (Fig. 3) with the measurement equipment. The impedance matching was investigated using an Agilent N5241A Performance Network Analyzer, whereas the antenna radiation patterns were established at the indoor far-field laboratory. The antenna-under-test was mounted on the rotating pedestal, and the standard linearly-polarized pyramidal horn was excited by an E8257D PSG microwave signal generator. Namely, the results related to the voltage standing wave ratio (VSWR) show the acceptable comparison (Figure 4). Some discrepancies are attributed to the impedance imperfections in the test equipment, including the soldering areas and attainable resolution of the wet etching.

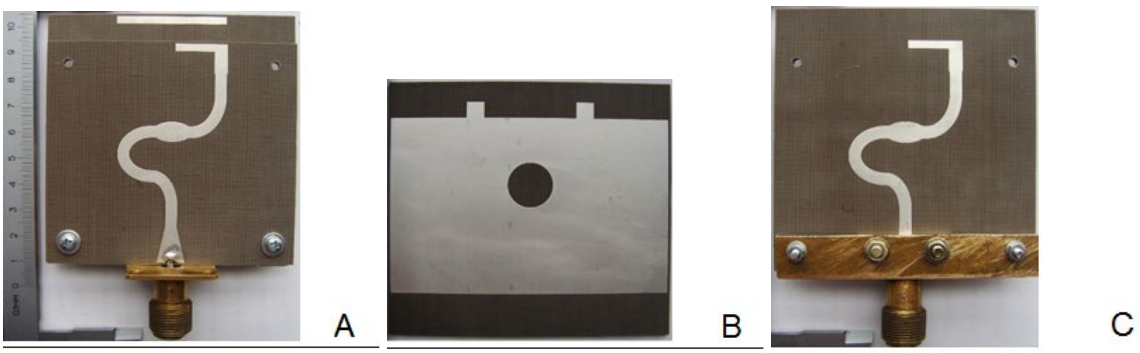

Figure 3. Photos of the proposed quasi-Yagi antenna: (A) face side, (B) the middle metallization realized on the bottom side of the first substrate, and (C) bottom side of the antenna.

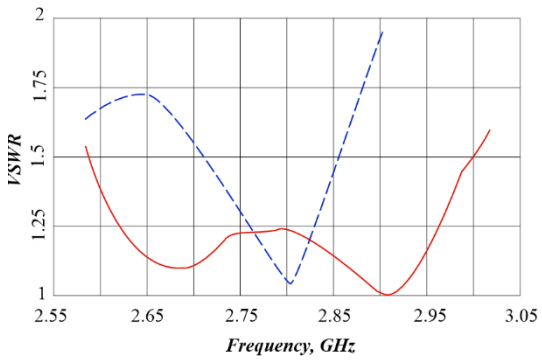

Figure 4. Simulated (- – -) and measured (—) VSWR of the proposed quasi-Yagi antenna.

As can be seen in Figure 4, the VSWR of the antenna at the 2.8 GHz center frequency is approximately 1.24. It can be noted that the experimentally obtained characteristic has its minima at frequencies 2.63 and 2.91 GHz, while the VSWR minimum value obtained from computer modeling is reached at the center frequency of the antenna 2.8 GHz. From the obtained data, it can be concluded that the change in the shape of the VSWR diagram after the implementation of the antenna is associated exclusively with the technological features of manufacture. Additionally, the parametric studies presented in Figs S10–S12 (please see the "Supporting information") show that the input VSWR is extremely sensitive to the vertical dimensions of the elliptical patch (Dy_cop) and the vacuum hole (Dy_vac). This explains also the discrepancy in the measured VSWR (Fig. 4). Apparently, the manufacturing tolerances of these specific elements are the likely cause of the dual-resonance behavior in the experimental prototype. So, for example, the modeling does not take into account the attachment screws connecting the two substrates. In addition, it is likely that the attachment of the feed connector, the presence and location of solder have a great influence. A detailed analysis of the VSWR diagram is not beyond the scope of this study. However, it is useful to note that the radiation pattern of the implemented sample at the center frequency of 2.8 GHz, practically, coincides with the radiation pattern obtained by computer modeling. At frequencies where the experimental VSWR diagram reaches minimum values, the antenna pattern has a slightly different, yet acceptable, shape. As a result, the technological inaccuracies have led to an increase in the antenna bandwidth. That is, the VSWR of the antenna is less than 1.25 in a frequency band of approximately 0.4 GHz. This fact can be used to study the possibility of expanding the antenna working frequency band while maintaining all the necessary characteristics, such as radiation pattern shape and antenna gain. In general, it can be concluded that, in order to improve the quality of antenna matching at the center frequency, it is necessary to make changes in the antenna manufacturing process, namely, in the power connector installation. At the same time, even the current VSWR value meets the requirements for antennas used in telecommunication systems. The corresponding simulated current distributions on the surfaces of the modeled quasi-Yagi antenna at the selected three frequencies are presented in "Supporting information". These figures confirm the proposed design based on the systematic parametric optimization. Additionally, the current distributions at the center frequency of 2.8 GHz are presented in Figure 5. This figure demonstrates the physical feasibility of the "ends-fed" concept. To improve the readability of the text, this figure is repeated in Figure S2 of the "Supporting information". It should be also noted that the differences between simulation and measurements are due to two main groups of influencing factors. Specifically, the first group is caused by the manufacturing process of nonradiative microstrip-slot and parallel stripline-microstrip transitions that contain a number of curved fragments proposed in [16]. The second one is driven by the optimization strategy and accuracy, related to the antenna's radiating part. This includes: lengths and widths of elongated linear conductors, as well as the distances between them and their arrangement on the antenna dielectric substrate. In this group, the manufacturing tolerances play a less prominent role due to the simplicity of implementing the elongated linear conductors.

Now, in Figure 6 are both the measured and simulation-derived E- and H-plane normalized radiation patterns at 2.8 GHz with a front-to-back ratio of approximately 9.8 dB. The simulated cross-polarization fields of the antenna exhibit almost omnidirectional patterns with the peak around -32 and -24 dB in the E– and H–planes, respectively, and they are not shown in the plots for brevity. The measured cross-polarization patterns are 7 dB larger than those produced through the simulation and they are also not shown here in the graphs for brevity. Thus, both the co-polarization patterns and the cross-polarization intensities have acceptable behaviors in the frequency range of interest. At the same time, the following parameters/indicators, related to the cross-polarization intensities, were implemented in previously published works [7], [9], [20], and [21], respectively:

- the maximum cross-polarization level in the E-plane is -15 dB [7], -20 dB [9], -18 dB [20], -19 dB [21];
- the maximum cross-polarization level in the H-plane is -12 dB [7], -15 dB [9], -14 dB [20], -15 dB [21].

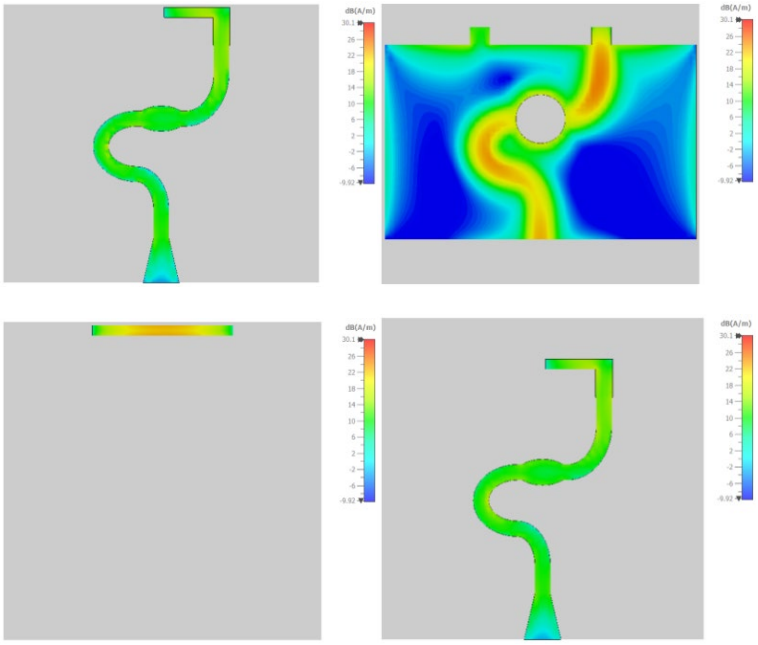

Figure 5. Simulated current distributions on the surfaces of all the layers at the frequency 2.8 GHz.

It is advisable to note that the use of two dielectric substrates noticeably complicates the antenna design. But on the other hand, this allows the implementation of an antenna with additional degrees of freedom through the design process. Additionally, the requirements of the structural and technological parameters are significantly weakened in the proposed antenna, and it is possible to assign bigger allowances to the geometric dimensions of printed strip conductors.

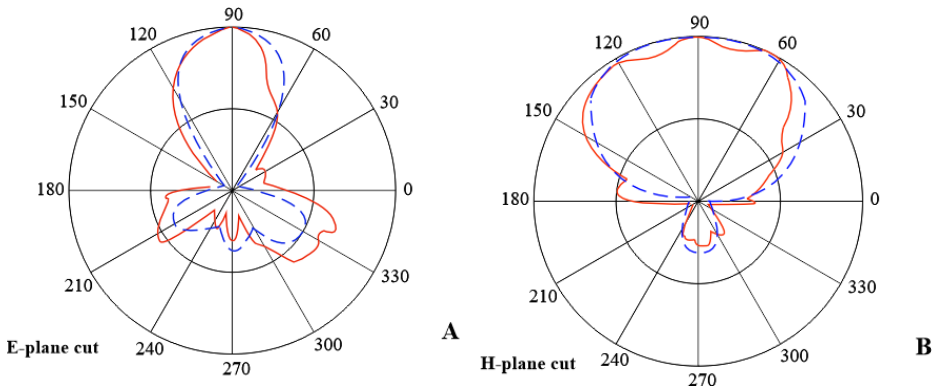

Figure 6. Simulated (- – -) and measured (—) radiation patterns: (A) E–plane, (B) H–plane.

As can be seen in Figure 6, the antenna beam width in the half power level in the E-plane cut is approximately 45 °, which is the optimal value required in the design of radio engineering systems. However, this beam width is slightly less than that obtained as a result of computer modeling, and also it turns out to be insignificantly shifted towards the left hemisphere. It is also worth noting that the radiation level in the lower hemisphere in this plane reaches sufficiently high values. It is possible to reduce the side lobes by including an additional number of directors in the antenna, as well as by implementing the antenna on one dielectric sheet, without using a second fragment on which the director is located in the antenna described above. One of the factors affecting the diagram is the

presence of attachment screws connecting the two substrates. Thus, the implementation of an antenna on a single dielectric sheet will help to improve the shape of the radiation pattern and will probably lead to an improvement in the quality of antenna matching at the center frequency. Aligning the direction and shape of the main lobe of the antenna is likely to allow the director to move some distance in one or another direction relative to the central axis of the antenna. This goal was not set in the current work, and so it is not considered. The beam width in the H-plane cut is approximately 110°. At the same time, in the lower hemisphere, the maximum radiation level is characterized by acceptable values and turns out to be lower than the values obtained as a result of computer optimization, which is an acceptable indicator for most technical applications.

In general, the shape of the radiation pattern of the described antenna is acceptable for the use in various telecommunications systems. To the author knowledge and comprehension, contrary to the latest contributions [20], [21], [22], the proposed quasi-Yagi antenna is characterized by the acceptable radiation properties, as well as by the more compact architecture. This offers an additional degree of freedom through the PCB implementation. To be used in the systems that require a more narrow oriented diagram, as well as higher noise immunity and, as a result, a lower level of side lobes, it is necessary to modify the antenna by increasing the number of directors, changing the technical implementation (using one dielectric substrate instead of two), as well as more detailed optimization in the computer program.

The efficiency of the proposed antenna can be discussed as an analysis of the curves shown in Figures 4 and 6. As can be seen in Figure 4, the VSWR of the antenna at the 2.8 GHz center frequency is approximately 1.24. The VSWR of the antenna that was obtained after the 3D simulation is much better, and it is close to 1.05. It means that the antenna matching can be much better and can be improved by not using, for example, the attachment screws connecting the two substrates. As can be seen in Figure 6, the antenna beam width in the half power level in the E-plane cut is approximately 45°, which is the optimal value required in the design of radio engineering systems. The side lobes level is worse than the same one of the 3D simulation model. The efficiency can be increased, if this side lobe level is decreased. As it was pointed, one of the factors affecting the diagram is the presence of attachment screws connecting the two substrates. Thus, the implementation of an antenna on a single dielectric sheet would help to improve the radiation pattern shape and will also, probably, lead to an improvement in the quality of antenna matching at the center frequency. The parametric studies of the proposed antenna are of great significance, and the results are presented in Figures S1-S14 (Supporting materials). For example, Figure S7 shows that the E-plane pattern is rather sensitive to the director length. This confirms that the antenna's performance is tied to a very specific optimized state, reinforcing the need for high-precision PCB manufacturing in case of mass production. The obtained dependences indicate that the proposed quasi-Yagi antenna is characterized by appropriate properties and, accordingly, it can be used in compact printed antenna systems with linearly polarized radiation properties. It is worth noting that a more rigorous comparison between simulation and measurement results can be performed based, for example, on the approach presented in [24]. However, the referenced study utilized curved radiating sector-like antenna fragments. In contrast, the radiating fragments in the authors' study are simpler – elongated and linear – allowing for the application of more straightforward system-oriented optimization approaches.

5. Conclusion

A novel implementation of the printed quasi-Yagi antenna with end fire-like radiation and good polarization purity was proposed. To realize the necessary pattern, an ends-fed dipole-like radiator was briefly described for completeness. According to this description and by addition the corresponding mathematical expressions in closed forms established in [12], [13], the novel architecture of the quasi-Yagi antenna was proposed. Through this improvement, the systematic parametric optimization was successfully used in order to include the classical out-of-phase power divider in the design process [16]. This divider is very compact in the PCB implementation and acts as the necessary balance unit. The above-mentioned radiation properties make the antenna a qualitative standalone module or a suitable candidate for phased arrays. The antenna can be used as a single unit or as a part of phased array. Also it can be used as a radiator or as a driver element of the Yagi antenna with more than one director element. It should be noted once again that the proposed antenna employs an innovative dipole-like driver with ends-fed excitation [11]. Although it does not deliver breakthrough radiation performances compared to recent quasi-Yagi antenna designs [3 – 9], the use of this driver

still increases the number of degrees of freedom when designing similar antennas. If any antenna system (e.g., phased array) needs an antenna beam width of about 30°, the antenna must contain more than two directors. If it is used in telecommunication systems, the antenna beam width can stand the same as that obtained in this work. An attractive feature of the described quasi-Yagi antenna is its compact size for microwave frequency band that paves a way for new applications in wireless communication systems. Apparently, the authors of other similar studies pursued the same goals. Works [23] and [24] can be cited as examples.

Funding

The research was carried out with financial support from the Russian Science Foundation within the framework of scientific project No. 24-29-20048, https://rscf.ru/project/24-29-20048/, as well as by the financial support from the Government of Novosibirsk region, agreement No. p-77.

Conflicts of interest

The authors declare no conflict of interest.

Author contributions

Conceptualization, A.G.; Data curation, V.K. and N.T.; Formal analysis, D.B. and N..T.; Investigation, V.A. and N.T.; Methodology, A.G.; Software, D.B.; Supervision, V.A.; Validation, V.A. and D.B.; Writing – original draft, A.G.; Writing – review & editing, N.T; Funding Acquisition, A.G.

References

1. Z. N. Chen, Editor. *Handbook of Antenna Technologies*, Singapore: Springer, 2016, Volume 3, Chapter VI.
2. C. A. Balanis, *Antenna Theory. Analysis and Design,* Hoboken, NJ: John Wiley & Sons, 2016, Chapters 2, and 5.
3. S.-J. Wu et al., "A multiband quasi-Yagi type antenna," *IEEE Trans. Antennas Propag*., vol. 58, no. 2, 2010, pp. 593–596.
4. P.-Y. Qin et al., "Frequency reconfigurable quasi-Yagi folded dipole antenna," *IEEE Trans. Antennas Propag*., vol. 58, no. 8, 2010, pp.2742–2747. https://doi.org/10.1109/TAP.2010.2050455
5. Y. Ding et al., "Design of a multiband quasi-Yagi-type antenna with CPW-to-CPS transition", *IEEE Antennas Wireless Propag. Lett*., vol. 10, 2011, pp. 1120–1123. https://doi.org/10.1109/LAWP.2011.2170950
6. P.-Y. Qin et al., "A beam switching quasi-Yagi dipole antenna", *IEEE Trans. Antennas Propag*., vol. 61, no. 10, 2013, pp. 4891–4899. https://doi.org/10.1109/TAP.2013.2274635
7. J. Wu et al., "Bandwidth enhancement of a planar printed quasi-Yagi antenna with size reduction", *IEEE Trans. Antennas Propag*., vol. 62, no. 1, 2014, pp. 463–467. https://doi.org/10.1109/TAP.2013.2287286
8. Z. Liang et al., "A novel microstrip quasi Yagi array antenna with annular sector directors", *IEEE Trans. Antennas Propag*., vol. 63, no. 10, 2015, pp. 4524–4529. https://doi.org/10.1109/TAP.2015.2456875
9. M.-C. Tang et al., "Flexible efficient quasi-Yagi printed uniplanar antenna", *IEEE Trans. Antennas Propag*., vol. 63, no. 12, 2015, pp. 5343–5350. https://doi.org/10.1109/TAP.2015.2486807
10. A. P. Gorbachev et al., "Planar dual-frequency quasi-Yagi antenna", *Electromagnetics*, vol. 36, no. 5, 2016, pp. 328–339.
11. D. A. Bukhtijarov et al., "Dipole emitter", Russian Patent 2 472 261, Date of filing: 10.08.2011, Date of publication: 10.01.2013.
12. D. A. Buhtiyarov et al., "Improvement of the quasi-Yagi antenna performances by using an ends-fed dipole driver", *Universal J. Electr. Electron. Eng*., vol. 2, no. 1, 2014, pp. 6–17.
13. D. A. Buhtiyarov et al., "The linearly polarized waveguide-fed dipole-like antenna", *J. Electromagn. Waves Appl*., vol. 29, no. 13, 2015, pp. 1720–1727. https://doi.org/10.1080/09205071.2015.1059293
14. S. A. Alekseytsev, A. P. Gorbachev, "The novel printed dual-band quasi-Yagi antenna with end-fed dipole-like driver", *IEEE Trans. Antennas Propag*. vol. 68, no. 5, 2020, pp. 4088–4090.
15. M. Rafatullah, Editor. *Newest Updates in Physical Science Research*. London, Tarakeswar: BP Int, 2021, Volume 6, Chapter 8, https://doi.org/10.9734/bpi/nupsr/v6/2339F
16. A. M. Abbosh et al., "An UWB planar out-of-phase power divider employing microstrip-slot and parallel stripline-microstrip transitions", *Proc. Asia-Pacific Microwave Conf*., 2006, vol. 1, pp. 905-908.
17. Price-list of the Company "SIBPROMISOLIT", Kotelnikov's Street, House no. 10, Room no. 41, Site Omsk, Omsk region, 644121, Russian Federation.
18. CST Studio Suite. Accessed: January 14, 2026, online. Available: http://www.cst.com/academia/student-edition.
19. K. Dzurinskyi, "Foreign and Russian radiofrequency connectors", *Components and Technologies,* no. 2, 2011, pp. 38-43 (in Russian; available at www.kit-e.ru).
20. Z. Zhang et al., "Low-profile shared-structure dual-polarized Yagi-Uda antennas", *IEEE Antennas and Wireless Propag. Lett*., vol. 21, no. 4, 2022, pp. 843–847. https://doi.org/10.1109/LAWP.2022.3150846
21. J. Lu et al., "Pattern reconfigurable Yagi antenna based on active corrugated stripline", *IEEE Trans. Antennas Propag*., vol. 71, no. 1, 2023, pp. 1011–1016. https://doi.org/10.1109/TAP.2022.3215813
22. Y. Yin, K. Wu, "Endfire circularly polarized planar antennas: a review of their development", *IEEE Antennas Propag. Mag*., vol. 65, no. 2, 2022, pp. 63–75. https://doi.org/10.1109/MAP.2022.3154977

23. A. K. Ospanova et al., “All-dielectric nanoantenna for efficient reflectors irradiation”, *Physical Sciences and Technology*, vol. 7, no. 1-2, 2020, pp. 25- 30. https://doi.org/10.26577/phst.2020.v7.i1.04

24. Q. Wang, et al., “Machine learning-assisted bandwidth optimization of quasi-Yagi antenna with adaptive dynamic parameter search range”, *IEEE Antennas and Wireless Propagation Letters*, vol. 25, no. 3, 2026, pp. 949 – 953.

Information about the authors:

Victor Atuchin (corresponding author) – Candidate of Physical and Mathematical Sciences, Professor, Research and Development Department, Kemerovo State University, Kemerovo, Russia; Laboratory of Optical Materials and Structures, Institute of Semiconductor Physics, SB RAS, Novosibirsk, Russia; Department of Industrial Machinery Design, Novosibirsk State Technical University (Novosibirsk 630073, Russia, e-mail: atuchin@isp.nsc.ru).

Dmitriy Buhtiyarov – Candidate of Technical Sciences, Researcher, Institute of Cosmic and Aviation Materials (NIICAM Co. Ltd.) Pereslavl-Zalessky, Russia, e-mail: ghostandfound@mail.ru;

Anatoly Gorbachev – Doctor of Technical Sciences, Professor, Radio Received and Transmitted Device Department, Novosibirsk State Technical University (Novosibirsk, Russia, e-mail: apgor1904@yandex.ru).

Vladimir Khrustalev – Doctor of Technical Sciences, Professor, General Physics Department, Novosibirsk State Technical University (Novosibirsk, Russia, e-mail: khrustalev@corp.nstu.ru).

Natalya Tarasenko – Candidate of Technical Sciences, Acting Associate Professor, General Physics Department, Novosibirsk State Technical University (Novosibirsk, Russia, e-mail: natalyavtarasenko@gmail.com).

Supporting materials

THE REDUCED SIZE QUASI-YAGI ANTENNA WITH AN ENDS-FED DIPOLE-LIKE DRIVER

First of all, the corresponding simulated current distributions on the surfaces of the modeled quasi-Yagi antenna at the selected three frequencies are presented in Figures S1-S3. These patterns confirm the proposed design based on the systematic parametric optimization.

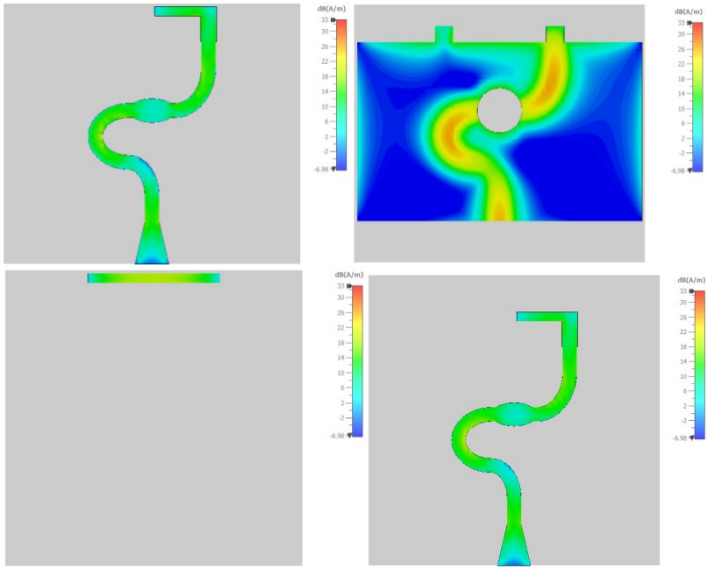

Figure S1. Simulated current distributions on the surfaces of all the layers at the frequency 2.55 GHz.

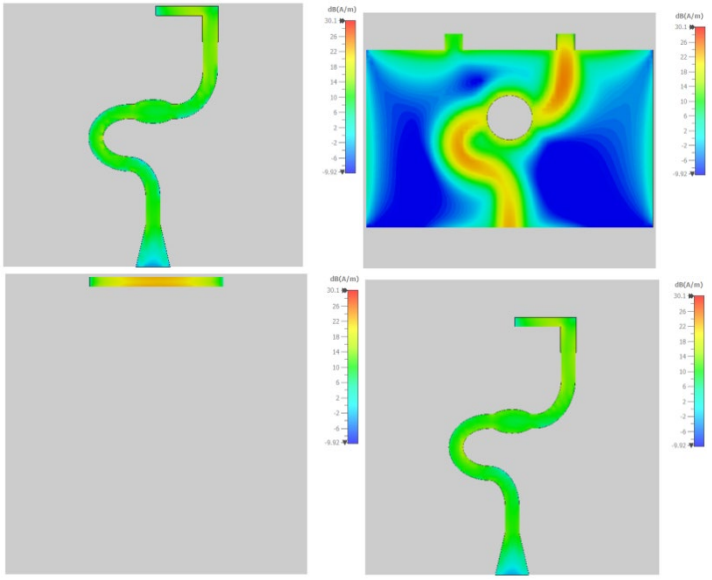

Figure S2. Simulated current distributions on the surfaces of all the layers at the frequency 2.8 GHz.

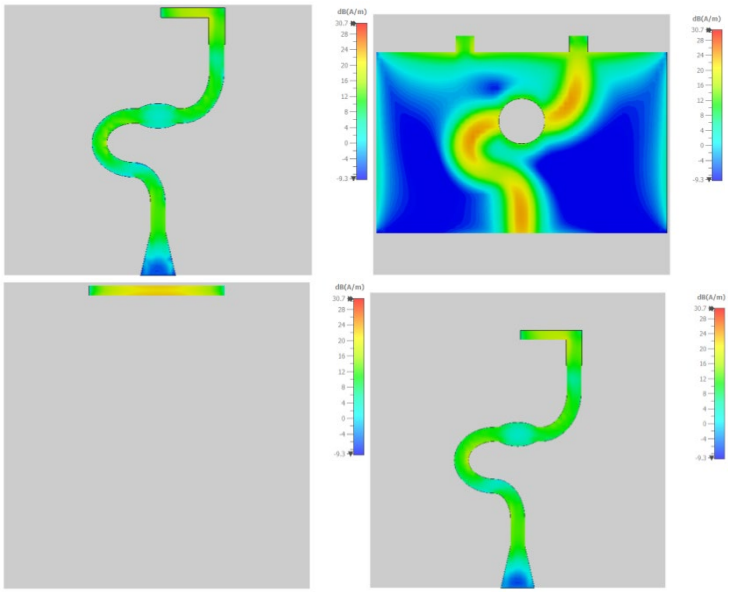

Figure S3. Simulated current distributions on the surfaces of all the layers at the frequency 3.05 GHz.

Secondly, to continue the analysis, the parametric studies are useful. Namely, Figure S4 displays the axis directions of the CST-model related to the proposed antenna whereas the little fragments inside Figure S5 represent the antenna topologies with additional designations by the letters related to following parametric studies.

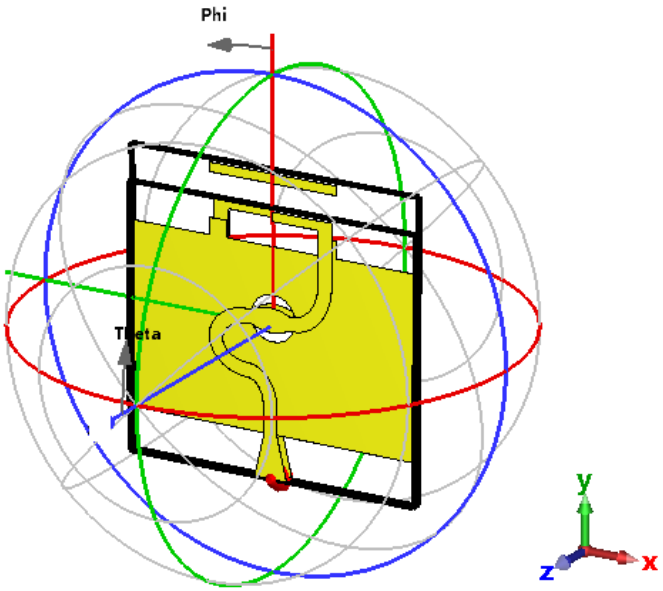

Figure S4. The axis directions of the antenna proposed.

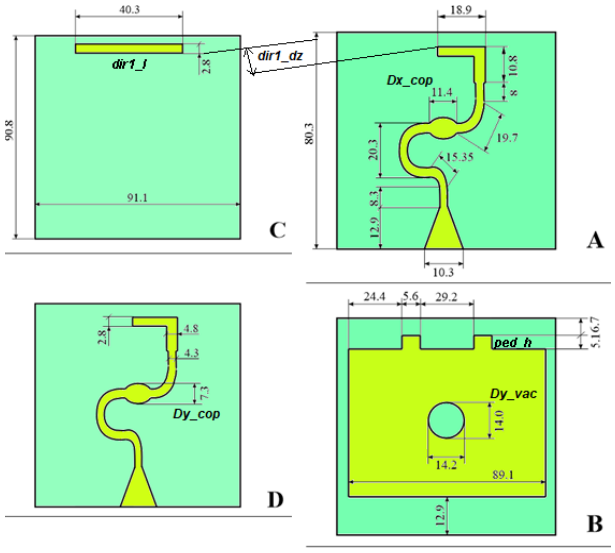

Figure S5. The antenna topologies with additional designations by the letters in order to display these values in the following Figures.

Now, Figures S6-S7 display the influences of the director length (dir1_l) on the input VSWR (Figure S6) and on the 2D co-polarized gain patterns in the E(xoy)-plane cut and in the H(zoy)-plane one (Figure S7).

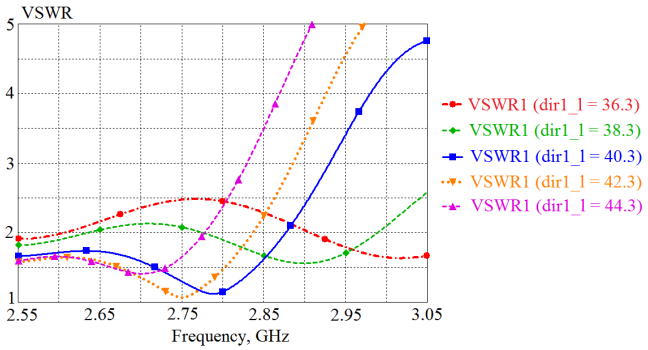

Figure S6. Input VSWR versus frequency with various director lengths (dir1_l).

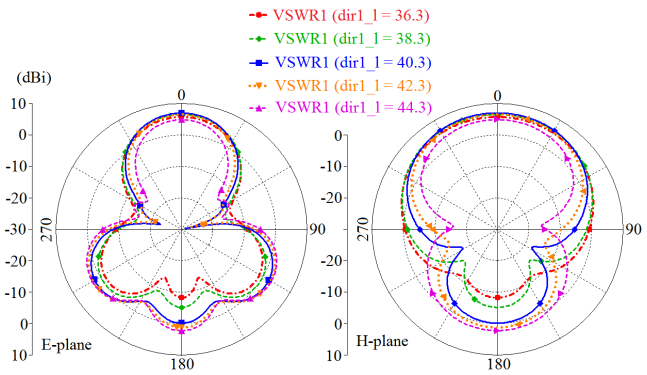

Figure S7. E- and H-plane co-polarized patterns versus the director length (dir1_l).

The following Figures S8-S9 present the influences of the distance (dir1_dz) between the director and the driver on the corresponding antenna performances when the value of the director length dir1_l is equal to 40.3 mm (blue curves in Figures S6-S7).

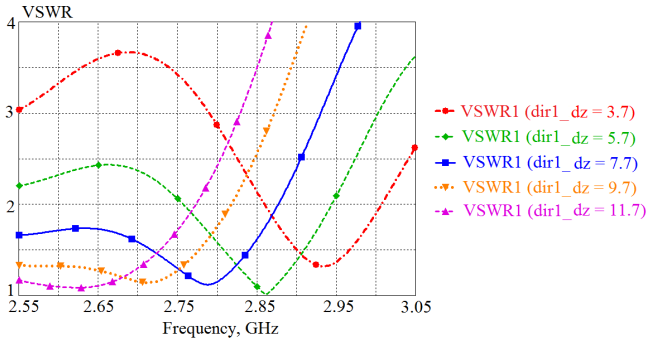

Figure S8. The input VSWR versus frequency for various driver-to-director distances (dir1_dz).

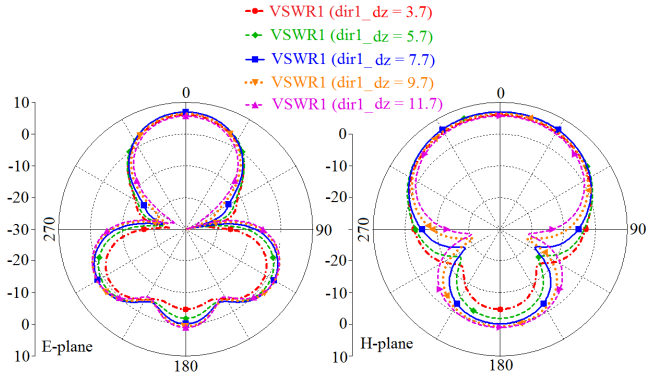

Figure S9. E- and H-plane co-polarized patterns for various driver-to-director distances (dir1_dz).

Figures S10-S12 display the influences of the pedestal height (ped_h), of the vertical diameter (Dy_vac) of the hole, and of the vertical dimension (Dy_cop) of the elliptical patch on the input VSWR.

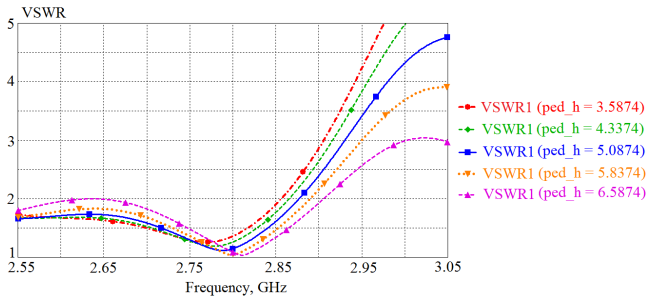

Figure S10. Input VSWR versus frequency for various pedestal heights (ped_h).

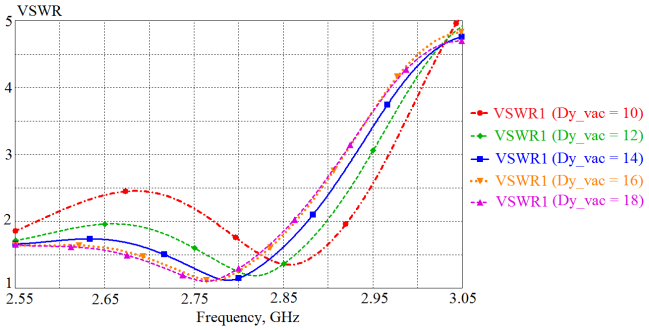

Figure S11. Input VSWR versus frequency
for various vertical diameters of the hole (Dy_vac).

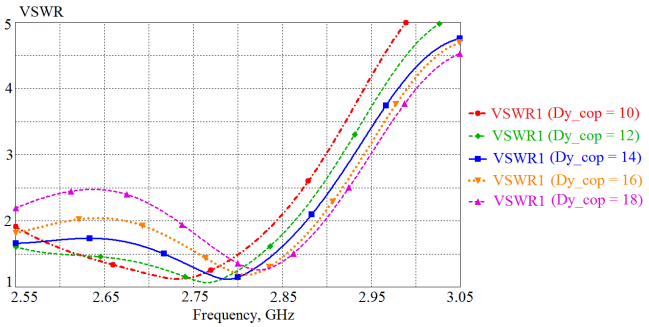

Figure S12. Input VSWR versus frequency
for various vertical dimensions of the elliptical patch (Dy_cop).

Thus, the parametric study confirms the proposed approach. Additionally, all the blue curves correspond to the optimum quantities of the quasi-Yagi antenna proposed.

IRSTI 41.23.39; 41.23.21 https://doi.org/10.26577/phst20261319

Correlation analysis of the wind acceleration parameter in high-mass X-ray binaries

Z. Muratkhan[1,2*], S. Toktarbay[1], A. Muratkhan[1], A. Taukenova[1] and N. Azhar[3]

[1]Al-Farabi Kazakh National University, Almaty, Kazakhstan
[2]Kazakh National Women's Teacher Training University, Almaty, Kazakhstan
[3]National University of Modern Languages (NUML), Lahore, Pakistan
*e-mail: muratkhan_zhantay1@live.kaznu.kz

(Received January 20, 2026; received in revised form April 30, 2026; accepted May 5, 2026)

This work presents a correlation analysis of the wind acceleration parameter β in high-mass X-ray binaries (HMXBs). The aim of the study is to determine how β depends on the geometric and dynamical characteristics of the system, primarily on the ratio of the orbital radius to the stellar radius, a/R_* and on the terminal wind velocity v_∞. For this purpose, published values of R_*, a and v_∞ together with measured wind velocities in the vicinity of the neutron star, were used. Based on these data, the parameters of the β-velocity law were determined numerically. The resulting β values were then approximated using a linear regression, $\beta \approx k\,a/R_* + c$, yielding a simple empirical relation. The results show that the linear correlation between β and the orbital-to-stellar radius ratio is weak (with a Pearson correlation coefficient $r \approx 0.22$) and is accompanied by substantial scatter, indicating the influence of additional physical factors. The linear regression yields a small positive slope ($k \approx 0.14$), which suggests only a weak tendency for β to increase with the orbital ratio. Because of the small sample size, this trend should be regarded as tentative. The proposed linear model allows β to be estimated without detailed spectroscopic analysis and may be useful as a rough empirical indicator of wind-accretion properties in HMXBs. The originality of this study lies in providing a simple empirical first-order assessment of the β parameter in HMXBs based on observed orbital and wind properties in systems where detailed spectroscopic constraints are limited.

Keywords: high-mass X-ray binaries (HMXBs), β-law (β-velocity profile), wind velocity profile, terminal wind velocity, orbital ratio a/R_*, correlation analysis.

1. Introduction

High-mass X-ray binaries (HMXBs) are close binary systems in which a neutron star accretes matter from the radiatively driven stellar wind of a massive early-type companion (O–B/Oe–Be). Since the density and velocity of the stellar wind at the neutron-star orbit determine the efficiency of mass capture, these parameters directly affect the accretion regime, the X-ray luminosity, and the spin evolution of the compact object [1, 2]. Despite the large number of observational studies of HMXBs, the detailed shape of the wind acceleration profile (i.e. the parameters of the β-law) remains poorly constrained. This uncertainty complicates reliable modelling of wind accretion and hampers predictions of neutron-star spin evolution.

The wind velocity as a function of distance from the surface of the donor star is commonly described by the so-called β-law (or CAK-type law):

$$v(r) = v_\infty \left(1 - b\frac{R_*}{r}\right)^\beta,$$

where v_∞ is the terminal wind velocity, R_* is the radius of the donor star, b is a parameter that determines the initial wind speed at the stellar surface, and β characterizes the smoothness of the acceleration. Physically, the parameter β controls how rapidly the outflow reaches v_∞ larger β values correspond to slower, more gradual acceleration, leading to higher wind densities near the neutron star and, consequently, to subsonic (settling) accretion and neutron-star spin-up. In contrast, smaller β values (steeper acceleration) reduce the gas density at the orbital radius and may trigger a transition to the propeller regime, accompanied by neutron-star spin-down. Thus, even relatively small variations in β can significantly alter the accretion regime and the long-term spin evolution of the neutron star [3, 4].

The terminal wind velocity v_∞ is usually determined from ultraviolet spectral lines; however, the parameters b and β are much more difficult to constrain observationally, especially under conditions of strong X-ray irradiation and wind clumping. Moreover, recent studies indicate that the winds of donor stars in HMXBs differ substantially from those of isolated OB stars due to photoionization effects, wind inhomogeneities, and interactions with the orbiting neutron star. Consequently, standard wind parameters derived for single stars cannot be applied directly to HMXBs, and empirical estimates of wind acceleration in individual systems are required to properly understand the accretion processes [5, 6]. This need for empirical constraints is reinforced by recent system-by-system reconstructions of β-law wind profiles in HMXBs, where the parameters b and β were inferred directly from observed terminal and local wind velocities, showing that slowly accelerating, denser winds tend to correspond to larger β values under strong X-ray photoionization [7].

The aim of the present work is to investigate the correlation between the wind acceleration parameter β and the geometric and dynamical properties of high-mass X-ray binaries. In particular, we examine how β depends on the orbital-to-stellar radius ratio a/R_* and on the terminal wind velocity v_∞. To this end, we use published measurements of R_*, a and v_∞ together with estimates of the local wind velocity at the neutron-star orbit, and numerically determine the parameters b and β. We then construct a linear regression of β as a function of a/R_* and evaluate the correlation between β and v_∞. This approach yields a simple empirical estimate of β that does not require detailed spectral analysis, thereby providing a practical tool for the rough classification of accretion regimes and for qualitative predictions of neutron-star spin evolution.

The relevance of this study is supported by recent review works. Recent studies have emphasized the combined roles of radiative driving, photoionization, hydrodynamics, wind clumping, and neutron-star feedback in HMXB winds [2, 6, 8]. The systematic empirical determination of the parameter β presented in this work, based on a correlation analysis, helps to bridge the gap between observations and theory and provides new constraints for future studies.

2. Materials and methods

2.1 Determination of the parameters b and β.

For each HMXB considered in this study, published values of the donor-star radius R_*, the orbital semi-major axis a, the terminal wind velocity v_∞ and the measured wind velocity $\upsilon(a)$ in the vicinity of the neutron star are used. The SED-fitting method for determining the parameters of hot supergiants can serve as an independent source of donor-star parameters (T_{eff}, $\log g$, A_V), which may be used as input data for constructing relationships between wind properties [9]. The parameters b and β of the wind velocity law given by Eq. (1).

$$v(r) = v_\infty \left(1 - b\frac{R_*}{r}\right)^{\beta} \quad (1)$$

are determined such that, for given v_∞, R_* and a the model wind velocity $\upsilon(a)$ reproduces the observed value.

The approach observational data → model fitting → parameter extraction in X-ray binary systems is methodologically consistent with the reconstruction of the β-parameter based on published HMXB data [10,11]. The calculation procedure is as follows:

• The stellar radius R_* and the orbital separation a are converted from solar radii to astronomical units (AU). We adopt the relation $1\ R_\odot$=0.00465 AU; thus, a/R_* = (a/AU)/($R_*/R_\odot$) · $0{,}00465^{-1}$.

• An initial estimate of the photospheric wind velocity v_0 is adopted, typically v_0=10–20 km/s.

• From the boundary condition $\upsilon(R_*) = v_0$, applied to Eq. (1) the parameter b is expressed as:

$$b = 1 - \left(\frac{v_0}{v_\infty}\right)^{1/\beta} \quad (2)$$

• For a trial value of β, the corresponding b is computed using the above expression and substituted into $v(a) = v_\infty \left(1 - b\frac{R_*}{a}\right)^{\beta}$. The value of β is then determined numerically by requiring the model velocity $\upsilon(a)$ to match the observed value. This is achieved using a root-finding procedure (the root scalar function from the *SciPy* library). Once β is

obtained, the parameter b is recalculated accordingly. This procedure is repeated for all systems in the sample. In addition, the input parameters are varied within their observational uncertainties in order to assess the sensitivity of the derived values of b and β.

2.2 Correlation Analysis.

Pearson correlation analysis is a standard statistical tool widely used in astrophysical studies. In this work, it is employed to investigate the dependence of the wind acceleration parameter β on the system geometry and wind velocity in HMXBs [12]. To search for a statistical relationship between the wind acceleration parameter β and the orbital ratio a/R_*, the Pearson correlation coefficient is calculated using Eq. (3):

$$r_{xy} = \frac{\sum_i (x_i - \bar{x})(y_i - \bar{y})}{\sqrt{\sum_i (x_i - \bar{x})^2 \sum_i (y_i - \bar{y})^2}}, \quad (3)$$

where $x_i = a/R_{*,i}$, $y_i = \beta_i$, $\bar{x}$ and $\bar{y}$ — denote the mean values of x and y over the sample. To approximate the dependence of β on the orbital-to-stellar radius ratio, a linear regression of the form

$$b \approx k\frac{a}{R_*} + c$$

is constructed, where the coefficients are determined as:

$$k = \frac{\sum (x_i - \bar{x})(y_i - \bar{y})}{\sum (x_i - \bar{x})^2}, \qquad c = \bar{y} - k\bar{x}.$$

The obtained coefficients k and c characterize the slope and intercept of the regression line. In the present study, the sign and magnitude of k are used only to describe the direction and strength of the empirical trend.

2.3 Error Estimation.

Uncertainties in the input parameters (R_*, a, v_∞, $v(a)$) propagate into the derived results. To assess the sensitivity of the method, the input parameters are repeatedly varied at random within their observational uncertainties. For each realization of the input data, the corresponding values of b and β are computed. The resulting distributions are then used to estimate the mean values and variances of b and β. This approach makes it possible to evaluate the robustness of the results against measurement errors and to identify which parameters most strongly contribute to the uncertainty in β.

2.4 The systems considered.

CenX-3

Cen X-3 was discovered in 1967 by the *Uhuru* space observatory as a point-like X-ray source. Subsequent observations revealed regular X-ray pulsations with a period of $P_s = 4.876 \pm 0.0154$ s, which allowed the source to be identified as an X-ray pulsar [1]. The detection of sinusoidal intensity variations with a period of ∼2.087 days further demonstrated that Cen X-3 is an eclipsing binary system with a massive companion. Optical observations of the Cen X-3 field performed with telescopes at the ESO and Las Campanas observatories during 1973–1974 led to the identification of the optical counterpart as an early-type star with a spectral classification of O9–O9.5 V or B0 I–III. As a result, Cen X-3 became the first object firmly identified as an X-ray pulsar in a massive binary system. Subsequent optical studies refined the spectral type of the donor [13] star to O6.5 II–III, with a mass of approximately $\sim 20{,}2\, M_\odot$ located at a distance of $d_0 \simeq 5{,}7 \pm 1{,}5$ kpc [14]. The orbital eccentricity of the compact object is extremely small, $e \simeq 0{,}00021$, indicating an orbit that is nearly circular. The terminal wind velocity is $v_\infty \sim 2000$ km/s [15].

OAO1657-415

OAO 1657–415 was initially discovered in 1978 as an eclipsing X-ray source and was identified one year later as an accreting X-ray pulsar with a spin period of 38,22 *s* at that time. The X-ray luminosity of the source in the 18–50 keV energy band during the 2002–2016 observations varied smoothly within the range $L_x \simeq 0.1 - 2 \times 10^{37}\,(d/d_0)^2$ erg/s [16]. OAO 1657–415 is located at a distance of $d_0 = 6{,}4 \pm 1{,}5$ kpc and is identified as a high-mass X-ray binary system with an orbital period of $P_{orb} \simeq 10{,}44$ days [17]. The orbital eccentricity is $e \simeq 0.104$. The system consists of a neutron star and a massive supergiant companion of spectral type Ofpe [18]. The neutron star currently rotates with a spin period of $P_s \simeq 37.024\, s$ and possesses a surface magnetic field strength of $B_{NS} = (3{,}1 \pm 0{,}2) \times 10^{12}$ G, as inferred from the analysis of a cyclotron resonance scattering feature detected in the X-ray spectrum of the source. The terminal wind velocity is $v_\infty \sim 500$ km/s [19].

VelaX-1

Vela X-1, like Cen X-3, was originally discovered by the *Uhuru* space observatory during the early years of X-ray astronomy in 1967 and was subsequently identified as an X-ray pulsar in a massive binary system. The spin period of the compact object is $P_s \sim 283{,}43$ s [20]. The orbit has a relatively small eccentricity, close to circular, e~0,088, which is characteristic of quasi-stationary wind-fed pulsars. The orbital period is $P_{orb} \sim 8{,}96$ days [17]. The neutron star is accompanied by the supergiant star HD~77581, located at a distance of d_0=1,9±0,2 kpc and classified as a B0.5~Ia star with an estimated mass of M_*~26 $M_\odot$ [17]. Based on optical and ultraviolet spectroscopic studies, terminal wind velocity is v_∞=1100 km/s and a mass-loss rate of $\dot{M} \sim 4 \times 10^{-6}\, M_\odot$/yr. have been reported [21].

4U1538-52

4U~1538–52 was discovered in 1976 by the *OSO-8* space observatory as an eclipsing X-ray source in a binary system. Subsequent observations carried out during the *Ariel-5* mission revealed X-ray pulsations with a period of~528,93 s, associated with the axial rotation of the neutron star. At the present epoch, the spin period of 4U~1538–52 is $P_s \simeq 526{,}23\, s$ [22], while the orbital period is $P_{orb} \simeq 3{,}728$ days [17]. Optical spectroscopic observations performed with the 3,9-m telescope at the Siding Spring Observatory (Australia) allowed the identification of the normal companion (QV~Nor) as an early-type supergiant of spectral class B0.2~Ia, with an estimated mass-loss rate of~10^{-6} $M_\odot$/yr. [23]. The distance to the source is estimated to be d≃5±0,5 kpc. The terminal wind velocity is v_∞~1450 km/s [24].

GX301-2

GX~301–2 is a unique object among the population of quasi-persistent X-ray pulsars in high-mass binary systems, as it possesses an orbit with a relatively large eccentricity e≃0,46 [25], which is more typical of transient X-ray pulsars. In the vast majority of quasi-persistent systems, the orbital eccentricity does not exceed 0,2. The distance to the source is estimated to be 3,5±0,5 kpc. The normal component of the system is the supergiant star BP~Cru [5], classified as an early-type B1.5~Ia star with an estimated mass of M_*~48 $M_\odot$ [16], making it one of the most massive donor stars among the Galactic population of X-ray pulsars in high-mass X-ray binaries. Optical spectroscopic studies of the donor star performed with the ESO 3,6-m telescope (Chile) revealed prominent P~Cygni profiles, which allowed estimates of the mass-loss rate in the range $\dot{M} \sim 5 \times 10^{-6} - 10^{-5}\, M_\odot$/yr. with a terminal wind velocity of v_∞~400 km/s [5].

2S0114+650

2S~0114+650 was discovered in 1977 during an all-sky survey carried out by the *SAS-3* X-ray observatory. Several months after its identification, it was established that the compact source is a member of a binary system with a massive companion, the star LS~I~+65~010 (V662~Cas). Based on its observational properties, 2S~0114+650 is classified as a quasi-persistent X-ray pulsar with an exceptionally long spin period of $P_s \sim 9475$ s. making it the second slowest-spinning pulsar among the Galactic population of HMXBs. Since its discovery, 2S~0114+650 has exhibited a long-term spin-up trend at a rate of ~10^{-6} s/s, although the physical origin of its extremely long spin period remains unclear. The current orbital period of the system is $P_{orb} \simeq 11{,}591$ days. The massive companion of the neutron star is the supergiant V662~Cas, classified as a B1~Ia star [17]. Detailed optical spectroscopic studies of V662~Cas conducted with the 2,5-m Isaac Newton Telescope at the La Palma Observatory yielded estimates of the terminal wind velocity v_∞≃1200±300 km/s and a mass-loss rate of $\dot{M} \sim 3 \times 10^{-6}$ $M_\odot$/yr. [26].

3. Results

3.1 Input data and derived parameters.

Table 1 lists the input parameters (R_*, a, v_∞, $v(a)$) for each HMXB considered, together with the derived parameters b, β and the orbital ratio a/R_*. The values of the local wind velocity $v(a)$ were taken from published X-ray observations [27], while the terminal wind velocities v_∞ were adopted from ultraviolet spectroscopy. The stellar radii R_* and orbital separations a were obtained from optical and dynamical measurements. The parameter b was calculated using $b = 1 - (v_0/v_\infty)^{1/\beta}$ assuming a photospheric wind velocity v_0 = 20 km/s, whereas the parameter β was determined numerically by solving the equation $v(a) = v_\infty \left(1 - b\frac{R_*}{a}\right)^\beta$.

Table 1. Input data and derived parameters for the HMXB system.

Systems	$R_*(R_\odot)$	$a(AU)$	$v_\infty(km/s)$	$v(a)(km/s)$	a/R_*	b	β
Cen X−3	12.1	0.08	2000	1010	1.42	0.999	0.5625
OAO 1657–415	25.0	0.21	500	210	1.81	0.933	1.1948
Vela X-1	30.4	0.23	700	610	1.63	1.000	0.1443
4U 1538–52	13.0	0.11	1450	810	1.82	0.997	0.7333
GX 301–2	62.0	0.83	400	290	2.88	0.979	0.7735
2S 0114+650	37.0	0.26	1200	510	1.51	0.994	0.7978

3.2 Plot of β as a function of a/R_*.

Figure 1 presents the β versus a/R_* diagram for the systems considered in this study. The points correspond to the values listed in Table 1 and indicate only a weak correlation between the orbital-to-stellar radius ratio and the wind acceleration parameter β. The Pearson correlation coefficient between β and a/R_* is $r \approx 0{,}22$, indicating a weak positive correlation accompanied by a substantial scatter in the data. Uncertainty bars are not shown in Figures because the available input uncertainties are heterogeneous across the selected systems; the plot is therefore intended only for qualitative visualization of the trend.

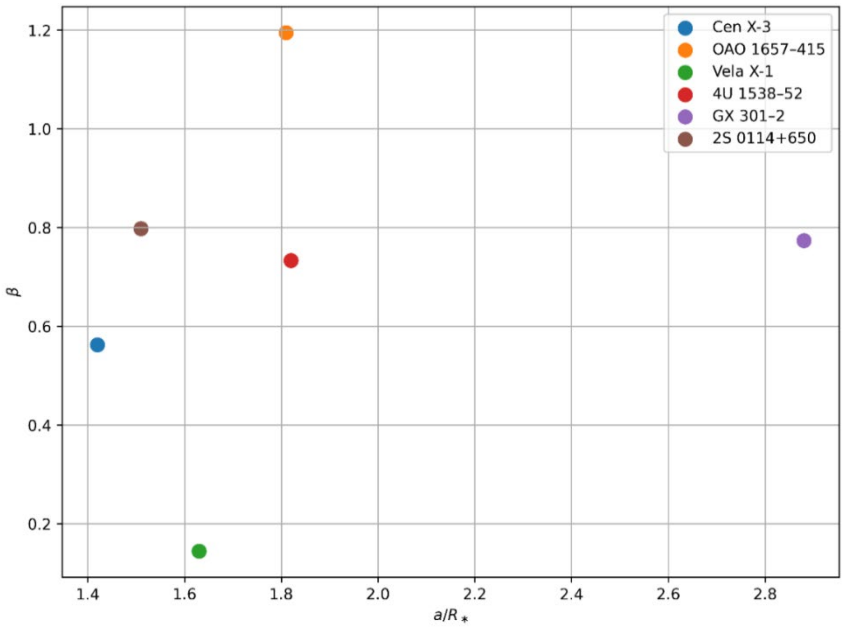

Figure 1. Dependence of the parameter β on a/R_* for HMXBs.

3.3 Plot of β as a function of terminal wind velocity v_∞.

Figure 2 shows the dependence of the wind acceleration parameter β on the terminal wind velocity v_∞. Overall, the diagram does not reveal a clear linear relationship between β and v_∞ and the data exhibit substantial scatter. Nevertheless, systems with relatively low v_∞ may show higher β, corresponding to a more gradual wind acceleration, whereas faster winds tend to be associated with smaller β values. This behavior is physically plausible, although the small sample size and the presence of outliers indicate that additional physical factors (e.g. X-ray photoionization, clumping, and binary interaction effects) likely play an important role.

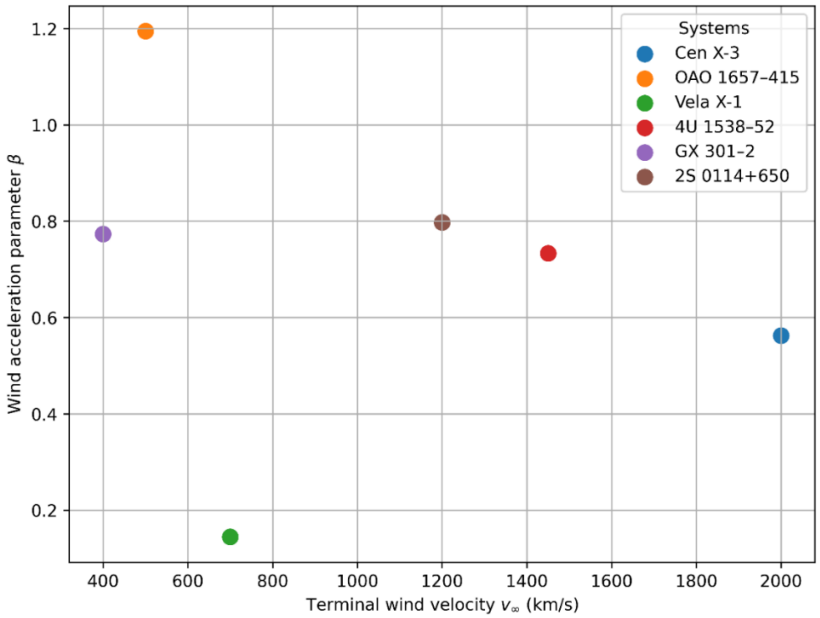

Figure 2. Dependence of the parameter β on the terminal wind velocity v_∞. The color of each point corresponds to a specific system; see the legend inside the figure.

3.4 Discussion of correlation parameters

A numerical approximation in the form of a linear relation $\beta(a/R_*)$ yields coefficients $k \approx 0.14$ and $c \approx 0.44$. The positive but small value of k indicates a very weak tendency for β to increase with the orbital-to-stellar radius ratio a/R_*. The Pearson correlation coefficient $r \approx 0.22$ confirms that the linear dependence between β and this geometric orbital parameter is weak and not statistically significant. This suggests that, in addition to the system geometry, the wind acceleration parameter β is strongly influenced by other physical factors, such as the donor star's spectral type, the level of X-ray photoionization, the neutron star's magnetic field, and wind inhomogeneity. Nevertheless, the linear model may be considered only as a preliminary empirical approximation. Higher β values are generally associated with slower wind acceleration and higher wind density near the neutron star, whereas lower β values correspond to faster acceleration. However, given the weak correlation and the limited sample size, the present analysis does not allow firm conclusions about specific accretion regimes or spin evolution pathways.

4. Discussion

4.1 Physical interpretation of the β correlation

Given the small sample size and the exploratory nature of the present study, a linear regression was adopted only as a first-order empirical approximation. More complex nonlinear dependencies may exist, but their assessment requires a larger sample and is beyond the scope of this work. The analysis of the dependence of the wind acceleration parameter β on the orbital ratio suggests at most a weak positive tendency for β to increase with increasing orbital-to-stellar radius ratio. However, this trend is accompanied by substantial scatter and is not statistically significant. Therefore, the observed relation should be interpreted with caution. A possible interpretation is that the wind acceleration parameter is influenced not only by orbital geometry, but also by several additional factors, including X-ray photoionization, wind clumping, donor spectral type, and magnetic interaction effects. For this reason, the orbital ratio alone cannot be considered a reliable predictor of β. The present result should be treated as a preliminary empirical trend that requires confirmation with a larger sample.

4.2 Connection between β and accretion regimes

It is well known that large values of β (of order unity and above) correspond to smooth, slow wind acceleration. Physical effects affecting X-ray emission in the vicinity of a neutron star are discussed; this context is important for interpreting wind accretion and potential regime transitions in HMXBs [28]. In this case, the wind velocity at the neutron-star orbit remains significantly below the terminal

value, leading to a larger effective capture radius and favoring subsonic (settling) accretion. Such accretion is associated with a relatively stable transfer of angular momentum, resulting in neutron-star spin-up. This interpretation is also consistent with recent statistical comparisons of persistent and transient HMXBs, which show that differences in X-ray luminosity behaviour and variability are closely related to the underlying accretion conditions and wind-feeding properties of the systems [29]. The theoretical framework for modeling the rotation of compact objects provides a basis for discussing the spin evolution of an accreting neutron star in HMXBs [30, 31]. In the present sample, the derived β values suggest possible differences in wind acceleration among the analyzed systems. The relatively high value obtained for OAO~1657–415 ($\beta \approx 1.2$) is broadly consistent with slower wind acceleration, whereas the very low value found for Vela~X-1 ($\beta \approx 0.14$) may indicate more rapid acceleration. Intermediate β values (~0.6–0.8) obtained for Cen~X-3, 4U~1538–52, GX~301–2, and 2S~0114+650 are compatible with moderately accelerating winds. Nevertheless, these associations should be treated as qualitative rather than predictive, because the present sample is small and the inferred correlation remains weak and statistically insignificant.

4.3 Limitations of the study

It should be emphasized that our sample is small (six systems) and does not include Be/X-ray binaries. Therefore, the statistical significance of the inferred correlations is low (with a Pearson correlation coefficient $r \approx 0.22$). In addition, the model is based on the simplified β-law and does not account for the effects of photoionization, magnetohydrodynamic processes, or wind clustering (clumping). These factors can significantly modify the actual wind acceleration, particularly in systems subject to strong X-ray irradiation. It should also be noted that the derived values of β and b are sensitive to uncertainties in the input parameters (R_*, a, v_∞, $v(a)$); more accurate observations may change the shape of the inferred dependence.

4.4 Comparison with theory and observations.

Our results are generally consistent with theoretical expectations: classical models of radiatively driven winds in single OB stars predict $\beta \sim 0.5{-}1.0$ whereas in HMXBs higher β values may arise due to X-ray irradiation and orbital interaction effects. Recent analytical work on generalized β-velocity laws in X-ray-illuminated HMXBs has shown that the allowed parameter space of b and β is physically constrained by the requirement of a smooth monotonic CAK-type outflow, with a robust lower bound $\beta \geq 1/2$, while strong X-ray irradiation may favor larger β values [32]. In the present sample, the fitted linear relation yields only a small positive slope, and the correlation remains weak and statistically insignificant. Therefore, the current data do not support a firm monotonic dependence of β on orbital geometry alone. A comparison with previous studies shows that our estimated β values (0.14–1.19) lie within the broad range reported for donor-star winds and wind-fed accretion systems. In particular, systems with relatively low v_∞ and high β, such as OAO 1657–415, are broadly consistent with denser and more slowly accelerating winds, whereas systems with higher v_∞ and lower β may be associated with more rapidly accelerating and less dense outflows. However, these interpretations should be regarded as qualitative, since the present sample is limited and the inferred trend is not statistically strong.

Future work based on an expanded sample, including Be/X-ray binaries, will be necessary to clarify whether any systematic dependence of β on orbital parameters is physically meaningful. Investigating orbital-phase variations of β and incorporating photoionization effects may also help to develop more accurate models capable of reproducing the observed behavior of X-ray luminosity and neutron-star spin evolution.

5. Conclusion

In this work, we proposed and implemented a simple linear model relating the wind acceleration parameter β to the orbital-to-stellar radius ratio a/R_*. The correlation analysis shows that the relationship between a/R_* and β is weak ($r \approx 0.22$) and accompanied by substantial scatter, indicating that the dependence is not statistically significant. The fitted empirical relation, $\beta \approx 0.14\ (a/R_*) + 0.44$, therefore represents only a preliminary approximation rather than a robust physical law.

The proposed model may be useful for obtaining rough first-order estimates of β in systems where detailed spectroscopic constraints are not available. However, due to the limited sample size and the weak correlation, the relation should be applied with caution and should not be used for quantitative predictions of accretion regimes or neutron-star spin evolution without additional supporting evidence.

The results suggest that the wind acceleration parameter β is influenced not only by orbital geometry but also by other physical factors, such as X-ray photoionization, wind clumping, and magnetic interactions. Therefore, the orbital-to-stellar radius ratio alone cannot serve as a reliable predictor of wind acceleration properties in high-mass X-ray binaries.

Future work should focus on expanding the sample of sources, including systems with Be-type companions, in order to improve the statistical significance of the analysis. It is also important to incorporate additional physical processes into the modeling and to investigate possible orbital-phase and long-term variations of β and related parameters. Such studies will help to clarify the role of wind structure in accretion processes and to develop more accurate models of mass transfer and spin evolution in high-mass X-ray binaries.

Funding

This research was supported by the Ministry of Science and Higher Education of the Republic of Kazakhstan (grant No. AP25795219).

Acknowledgements

The authors acknowledge the institutional support provided by the Institute for Experimental and Theoretical Physics, Al-Farabi Kazakh National University, and the Department of Physics, Kazakh National Women's Teacher Training University. The authors are also grateful for the research environment and academic support that contributed to the completion of this study.

Conflicts of interest

The authors declare no conflict of interest.

Author contributions

Conceptualization, Z.M. and S.T.; Methodology, Z.M., S.T. and N.A.; Formal Analysis, Z.M. and N.A.; Investigation, Z.M., A.M. and N.A.; Data Curation, Z.M. and A.M.; Visualization, A.T. and Z.M.; Writing – Original Draft Preparation, Z.M.; Writing – Review \& Editing, S.T., A.M., A.T. and N.A.; Validation, S.T., A.T. and N.A.; Supervision, S.T. All authors have read and agreed to the published version of the manuscript.

References

1. R. Giacconi, H. Gursky, E. Kellogg, E. Schreier, and H. Tananbaum, "Discovery of periodic X-ray pulsations in Centaurus X-3 from UHURU," *Astrophys. J.*, vol. 167, pp. L67–L71, 1971, https://doi.org/10.1086/180765

2. H. J. G. L. M. Lamers and J. P. Cassinelli, Introduction to Stellar Winds. Cambridge, U.K.: Cambridge Univ. Press, 1999.

3. J. I. Castor, D. C. Abbott, and R. I. Klein, "Radiation-driven winds in hot stars," *Astrophys. J.*, vol. 195, pp. 157–174, 1975, https://doi.org/10.1086/153315

4. N. I. Shakura, K. A. Postnov, A. Y. Kochetkova, and L. Hjalmarsdotter, "Quasi-spherical subsonic accretion in X-ray pulsars," *Phys.-Uspekhi,* vol. 56, pp. 321–346, 2013, https://doi.org/10.3367/UFNe.0183.201304a.0337

5. L. Kaper, H. J. G. L. M. Lamers, E. Ruymaekers, E. P. J. van den Heuvel, and E. J. Zuiderwijk, "Wray 977 (GX 301–2): A hypergiant with a pulsar companion," *Astron. Astrophys.*, vol. 300, pp. 446–456, 1995.

6. L. M. Oskinova, A. Feldmeier, and P. Kretschmar, "Clumped stellar winds in supergiant high-mass X-ray binaries," *Mon. Not. R. Astron. Soc.*, vol. 421, pp. 2820–2831, 2012, https://doi.org/10.1111/j.1365-2966.2012.20420.x

7. Z. Muratkhan, M. Khassanov, A. Taukenova, and S. Toktarbay, "Empirical Determination of β-Law Wind Acceleration Profiles in High-Mass X-Ray Binaries," *Universe*, vol. 12, no. 3, Art. no. 67, 2026, https://doi.org/10.3390/universe12030067

8. S. Martínez-Núñez, P. Kretschmar, V. Sguera, et al., "Unified view of wind accretion in high-mass X-ray binaries," *Space Sci. Rev.,* vol. 212, pp. 59–150, 2017, https://doi.org/10.1007/s11214-017-0340-1

9. A. Gyuchtash, S. Nurmakhametova, N. Vaidman, S. Khokhlov, A. Agishev, and A. Bakhytkyzy, "A method for determining the physical parameters of hot supergiants based on spectral energy distribution analysis," *Phys. Sci. Technol.*, vol. 12, no. 1–2, pp. 45–56, 2025, https://doi.org/10.26577/phst20251215

10. K. Boshkayev, M. Muccino, J. Rueda, and G. Zhumakhanova, "Fundamental frequencies in the Schwarzschild spacetime," *Phys. Sci. Technol.*, vol. 3, no. 2, pp. 25–31, 2018, https://doi.org/10.26577/phst-2016-2-103

11. L. Maftunzada, "Definition of physical parameters of 8 X-class solar flares," *International Journal of Mathematics and Physics,* vol. 12, no. 1, pp. 52–56, 2021, https://doi.org/10.26577/ijmph.2021.v12.i1.08

12. A. Sarsembayeva, L. Ryssaliyeva, F. Belissarova, and A. Sarsembay, "Solar magnetic activity and its terrestrial impact," *Phys. Sci. Technol.*, vol. 12, no. 1–2, pp. 38–44, 2025, https://doi.org/10.26577/phst20251214

13. J. Hutchings, D. Crampton, J. van Paradijs, and N. White, "Centaurus X-3," *Astrophys. J.,* vol. 229, pp. 1079–1084, 1979, https://doi.org/10.1086/157027

14. T. D. C. Ash, A. P. Reynolds, P. Roche, A. J. Norton, M. D. Still, and L. Morales-Rueda, "The mass of the neutron star in Centaurus X-3," *Mon. Not. R. Astron. Soc.*, vol. 307, pp. 357–364, 1999, https://doi.org/10.1046/j.1365-8711.1999.02616.x

15. C. S. R. Day and I. R. Stevens, "An X-ray excited wind in Centaurus X-3," *Astrophys. J.*, vol. 403, pp. 322–332, 1993, https://doi.org/10.1086/172206

16. L. Sidoli and A. Paizis, “INTEGRAL overview of high-mass X-ray binaries,” *Mon. Not. R. Astron. Soc*., vol. 481, pp. 2779–2803, 2018, https://doi.org/10.1093/mnras/sty2480

17. F. Fortin, F. García, A. Simaz Bunzel, and S. Chaty, “A catalogue of high-mass X-ray binaries,” *Astron. Astrophys.,* vol. 671, Art. no. A149, 2023, https://doi.org/10.1051/0004-6361/202244415

18. D. Chakrabarty, Z. Wang, J. Lee, and P. Roche, “X-ray position and infrared counterpart of OAO 1657–415,” *Astrophys. J.,* vol. 573, pp. 789–793, 2002, https://doi.org/10.1086/340789

19. A. Pasquali, W. Schmutz, C. Leitherer, et al., “Fundamental properties of Ofpe/WN9 stars,” in Science with the HST, pp. 386–390, 1996.

20. F. Fürst, K. Pottschmidt, J. Wilms, et al., “NuSTAR discovery in Vela X-1,” *Astrophys. J.,* vol. 780, Art. no. 133, 2014, https://doi.org/10.1088/0004-637X/780/2/133

21. A. A. C. Sander, F. Fürst, P. Kretschmar, et al., “Stellar wind stratification in Vela X-1,” *Astron. Astrophys*., vol. 610, Art. no. A60, 2018, https://doi.org/10.1051/0004-6361/201731823

22. R. Tamang, M. Ghising, M. Tobrej, B. Rai, and B. C. Paul, “Evolution of cyclotron line energy in 4U 1538–52,” *Mon. Not. R. Astron. Soc.,* vol. 527, pp. 3164–3173, 2024, https://doi.org/10.1093/mnras/stad3394

23. G. E. Parkes, P. G. Murdin, and K. O. Mason, “Optical counterpart of 4U 1538–52,” *Mon. Not. R. Astron. Soc*., vol. 184, pp. 73P–77P, 1978.

24. R. P. Kudritzki and J. Puls, “Winds from hot stars,” *Annu. Rev. Astron. Astrophys.*, vol. 38, pp. 613–666, 2000, https://doi.org/10.1146/annurev.astro.38.1.613

25. N. Sato, F. Nagase, N. Kawai, et al., “Orbital elements of GX 301–2,” *Astrophys. J.,* vol. 304, pp. 241–248, 1986, https://doi.org/10.1086/164160

26. P. Reig, D. Chakrabarty, M. J. Coe, et al., “Parameters of 2S 0114+650,” *Astron. Astrophys.*, vol. 311, pp. 879–888, 1996.

27. N. Beskrovnaya, N. Ikhsanov, and V. Kim, “Stellar wind parameters in HMXBs,” *Galaxies*, vol. 13, Art. no. 37, 2025, https://doi.org/10.3390/galaxies13010037

28. M. Abishev, N. Beissen, Zh. Brisheva, and F. Belissarova, “Propagation of X-ray and gamma-ray emissions,” *Phys. Sci. Technol.,* vol. 2, no. 2, pp. 70–74, 2016, https://doi.org/10.26577/2409-6121-2015-2-2-70-74

29. Zh. Muratkhan, M. Khassanov, A. Muratkhan, A. Taukenova, and A. Sadu, “Comparative Analysis of X-Ray Luminosity of Persistent and Transient High-Mass X-Ray Binaries,” *Her. Kazakh-Brit. Tech. Univ.*, vol. 23, no. 1, pp. 305–315, 2026, https://doi.org/10.55452/1998-6688-2026-23-1-305-315

30. K. Boshkayev, J. Rueda, R. Ruffini, et al., “Non-rotating and slowly rotating white dwarfs in classical physics,” *Phys. Sci. Technol.*, vol. 2, no. 1, pp. 66–71, 2016, https://doi.org/10.26577/2409-6121-2015-2-1-66-71

31. K. Boshkayev, O. Luongo, M. Muccino, and H. Quevedo, “Static and rotating white dwarf stars at finite temperatures,” *International Journal of Mathematics and Physics*, vol. 12, no. 2, pp. 61–69, 2021, https://doi.org/10.26577/ijmph.2021.v12.i2.07

32. S. Toktarbay, Z. Muratkhan, et al., “Analytical constraints on generalized β-velocity laws in X-ray-illuminated HMXBs,” *Mon. Not. R. Astron. Soc.,* vol. 547, no. 4, 2026, https://doi.org/10.1093/mnras/stag271

Information about the authors:

Zhantay Muratkhan (corresponding author) – PhD doctoral student, Faculty of Physics and Technology, Al-Farabi Kazakh National University, Almaty, Kazakhstan, e-mail: muratkhan_zhantay1@live.kaznu.kz; Department of Physics, Kazakh National Women’s Teacher Training University (Almaty, Kazakhstan).

Saken Toktarbay – PhD, Senior Lecturer, Department of Theoretical and Nuclear Physics, Al-Farabi Kazakh National University (Almaty, Kazakhstan, e-mail: saken.toktarbay@kaznu.edu.kz).

Aray Muratkhan – PhD, Senior Lecturer, Department of Theoretical and Nuclear Physics, Al-Farabi Kazakh National University (Almaty, Kazakhstan, e-mail: Muratkhan.Aray@kaznu.kz).

Aliya S. Taukenova – PhD, Associate Professor, Department of Theoretical and Nuclear Physics, Al-Farabi Kazakh National University (Almaty, Kazakhstan, e-mail: alyiya.taukenova@kaznu.edu.kz).

Nadeem Azhar – PhD, Associate Professor, Department of Mathematics, National University of Modern Languages (NUML), Lahore Campus (Lahore, Pakistan, e-mail: nadeemazharsaeed@gmail.com).

IRSTI 41.25.31; 41.25.19; 41.25.29 https://doi.org/10.26577/phst202613110

Identification of young star objects in the serpens south star-forming region of the aquila molecular cloud

N.Sh. Alimgazinova [1,2], A.B. Manapbayeva [2,3], A.Zh. Omar [1,2*], K.M. Turekhanova [1,2], N.E. Abildayev [4], A. Demessinova [1, 2], A.A. Alibek [3] and N.B. Shaimoldin [5]

[1]Faculty of Physics and Technology, Farabi University, Almaty, Kazakhstan
[2]Institute of Experimental and Theoretical Physics, Farabi University, Almaty, Kazakhstan
[3]Kazakh National Women's Teacher Training University, Almaty, Kazakhstan
[4]Faculty of Mechanics and Mathematics, Farabi University, Almaty, Kazakhstan
[5]State Key Laboratory of Radio Astronomy and Technology,
Xinjiang Astronomical Observatory, CAS, Urumqi, Xinjiang, P. R. China
*e-mail: omar.aruzhan@kaznu.kz
(Received November 6, 2025; received in revised form May 20, 2026; accepted May 25, 2026)

We present the results of a search and identification of young stellar objects (YSOs) in the Serpens South star-forming region, which is part of the Aquila Rift complex. Using AllWISE catalog data within a radius of 7′ from the center of the region, a multi-stage filtering procedure was applied to remove contaminating sources, including galaxies, active galactic nuclei, shock emission sources and PAH emission. Photometric criteria were then used to classify the sources according to their evolutionary stages. As a result, a sample of 145 YSO candidates was identified, including 1 protostar, 37 Class I objects, 48 Class II objects, 47 Class III objects and 12 transition disks. A quantitative analysis of the spatial distribution of the sources was performed using cumulative distribution functions, the Kolmogorov–Smirnov test and bootstrap resampling. The results show that early-stage objects (Class I) exhibit pronounced clustering in the central region (R_{50} = 0.26 pc) and are associated with dense filamentary structures, whereas Class II and III objects display a more extended distribution. A Jeans analysis combined with Monte Carlo simulations yielded a median gas density of $n \approx 1.6 \times 10^5$ cm^{-3}, consistent with dense prestellar cores. Multiwavelength verification using infrared, X-ray, optical and radio catalogs showed that 78.6% of the objects possess independent infrared confirmation, while 70.3% have X-ray detections. In addition, 11 new YSO candidates not previously reported in published catalogs were identified. The obtained results demonstrate the high efficiency of WISE data for detecting heavily obscured sources and provide new insights into the early stages of star formation in dense filamentary environments.

Keywords: Young stellar objects, Serpens South, Aquila Rift, WISE, star formation.

1. Introduction

The study of star formation and stellar evolution remains one of the central problems of modern astrophysics, since stars play a fundamental role in the formation and dynamical evolution of galaxies. In this context, star-forming regions are of particular importance, as they provide an opportunity to investigate the early stages of stellar evolution and the spatial distribution of young stellar objects (YSOs).

Observations of young stars embedded in molecular clouds are significantly hindered at optical wavelengths because of strong extinction caused by interstellar dust [1]. Infrared observations provide an effective way to overcome this limitation by revealing sources with infrared excess emission associated with circumstellar disks and envelopes. Major advances in this field have been enabled by the Spitzer Space Telescope [2] and the Wide-field Infrared Survey Explorer (WISE) mission [3], which provided extensive infrared photometric surveys that form the basis of modern YSO identification techniques.

The classification of YSOs [4–10] is commonly performed using two principal approaches: infrared color diagnostics and the spectral index α, which characterizes the slope of the spectral energy distribution. Infrared color criteria are widely used in the analysis of large infrared surveys, allowing efficient identification of YSO candidates while simultaneously removing a significant fraction of background

contaminants [11–14]. At the same time, classification based on the spectral index provides a physically motivated separation of sources into evolutionary classes (Class I, II and III) [15]. In the present work, we primarily focus on photometric classification based on infrared colors using modern criteria for contaminant rejection and sample purification.

The Serpens South star-forming region, which is part of the Aquila Rift complex, is an active environment characterized by a high concentration of young stellar objects and a pronounced filamentary structure [16–19]. Despite the availability of high-angular-resolution observations obtained with facilities such as *Spitzer* and *Herschel*, the WISE catalog remains an important resource because of its full-sky coverage and the uniformity of its photometric data, which are particularly valuable for statistical analyses and cross-matching studies.

In contrast to studies aimed at constructing large-scale YSO catalogs across extended sky regions using uniform selection criteria [20], this work focuses on a detailed investigation of the local Serpens South star-forming region. Such a localized analysis makes it possible to examine how environmental factors, including extinction, gas density and the evolutionary state of the molecular cloud, influence the observed properties of the YSO population [21].

A comprehensive source-selection procedure was implemented, combining successive contaminant removal with multi-stage verification of YSO candidates using data from 19 astrophysical catalogs covering the infrared, X-ray, radio and optical wavelength ranges. In addition, statistical techniques and numerical simulations were employed to study the spatial distribution of YSOs belonging to different evolutionary classes, enabling an assessment of their clustering behavior and its relation to the physical characteristics of the surrounding medium.

The adopted methodology resulted in the identification of previously uncataloged YSO candidates and allowed us to investigate the connection between their spatial distribution and evolutionary properties. These results provide additional constraints on the physical conditions and dynamical state of the star-forming environment in the Serpens South region.

2. Observations

The Aquila molecular cloud complex, also known as the Aquila Rift, is a prominent dark-cloud structure located in the constellations Aquila, Serpens Cauda and Ophiuchus. It consists of extended interstellar dust and molecular clouds distributed along a large northeast–southwest elongated feature. The Aquila Rift forms part of the Great Rift, a nearby system of dark clouds whose dust obscures the central regions of the Galactic plane and the inner sectors of the Milky Way.

Several active star-forming regions are located within the western part of the Aquila Rift, including Serpens Main, Serpens South, W40 and MWC297. CO and HI observations [22, 23] show that the complex extends along the Galactic plane over Galactic longitudes from approximately 20° to 40° and Galactic latitudes from about −1° to 10°. However, the relative distances between the embedded protoclusters Serpens South and W40 remain uncertain. Whether the Aquila Rift and the main Serpens cloud belong to the same molecular complex and therefore share a common distance is still under discussion [24, 25].

Previous studies have suggested that Serpens Main and the Aquila Rift may represent physically distinct structures, which could explain the discrepancy between their estimated distances [26, 27]. In particular, distance estimates of approximately 200–280 pc have been reported for the Aquila Rift complex, whereas Serpens Main is commonly placed at a distance of about 415 pc, implying that Serpens Main is located farther away than Serpens South. More recent studies focused on the Serpens South protocluster [28] adopted a distance of approximately 260 pc for this star-forming region.

Based on extinction measurements [29] and radio spectral-line observations [30, 31], the nearby H II region W40 has generally been placed at distances ranging from about 300 to 700 pc. A more recent Chandra X-ray study [32], based on X-ray luminosity function arguments, suggested that the most probable distance to the W40 cluster is approximately 600 pc, although a smaller distance of about 300 pc could not be excluded.

Among the star-forming regions associated with the Aquila Rift cloud complex, Serpens South is of particular interest. Serpens South is a young embedded cluster discovered through infrared observations with *Spitzer*. The cluster is embedded within a dense filamentary molecular cloud containing a large population of protostars. Owing to the high concentration of protostars and prestellar cores in this region, Serpens South is considered one of the most active sites of star formation within the Aquila Rift complex (Figure 1). Large-scale magnetic fields have been detected in the region, oriented predominantly perpendicular to the main cloud filament, whereas several sub-filaments tend to align parallel to the primary filamentary structure. Such magnetic fields may play an important role in slowing the gravitational collapse of dense molecular condensations within the complex.

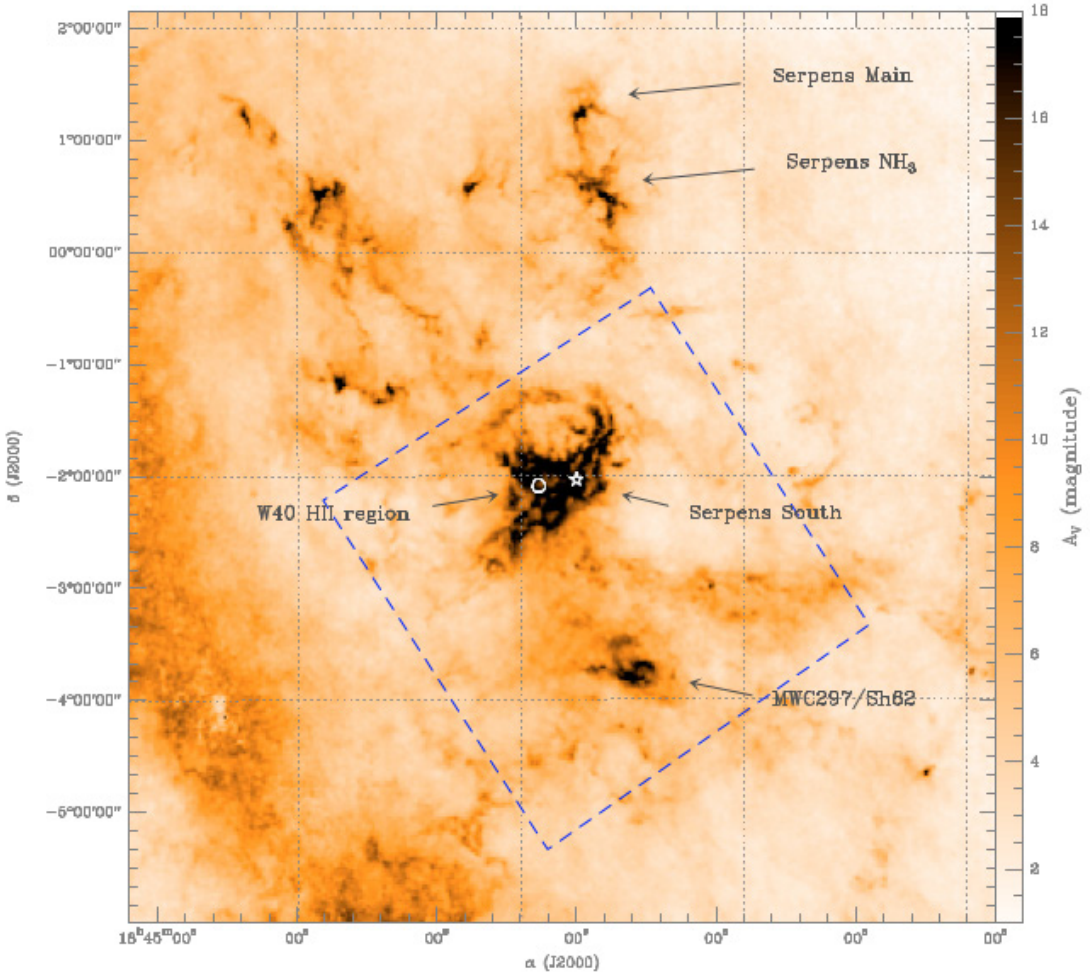

Figure 1. Aquila Rift/Serpens region based on 2MASS observations [16].

Spitzer observations show that W40 and the embedded Serpens South cluster are located close to each other on the plane of the sky, suggesting that Serpens South may be physically associated with the more evolved W40 region. Recent distance measurements for Serpens Main and W40 yielded values of approximately 436 pc, implying that Serpens South may be located at a similar distance because the two regions appear to be kinematically connected. Studies by [33, 34] estimated the mass of the giant molecular cloud associated with W40 to be approximately ~1.4×10^5 $M_\odot$ and derived a characteristic distance of about 474 pc. Similarly, it has been suggested that Serpens South may interact with the expanding shell of the W40 H II region, further supporting the possibility that the two regions are located at nearly the same distance. However, large-scale observations of the ^{12}CO (2–1) and ^{13}CO (2–1) emission toward the Aquila Rift revealed two spatially extended components associated with Serpens South and W40 that exhibit different radial velocities. These results suggest that large-scale expanding shells, bubbles and/or gas flows influence the observed velocity fields and may play an important role in the formation and evolution of these molecular clouds [35].

As part of the Herschel Gould Belt Survey [36], a 3.3° × 3.3° region toward the Aquila complex was mapped in the far-infrared wavelength range. The resulting maps provide high spatial resolution and sensitivity across five bands between 70 and 500 μm. A large population of previously unidentified protostars and prestellar cores was detected, primarily concentrated within three active star-forming regions: the filamentary molecular cloud hosting Serpens South, the eastern H II region W40/Sh2-64 and the southern MWC 297/Sh2-62 region.

Therefore, the Aquila Rift complex, which contains star-forming regions at different evolutionary stages and physical conditions, represents an important laboratory for investigating the early stages of

star formation over a wide range of wavelengths and observational techniques.

3. Source Selection and Initial Data Processing

A literature review of nearby star-forming regions was carried out in order to determine their central coordinates, angular sizes and the corresponding search radius required for the identification of young stellar objects (YSOs). The Serpens South region, centered at RA(J2000) = $18^h30^m03^s$ and Dec(J2000) = −02°01′58.2″, has an apparent size of approximately 14.4 × 20.3 arcmin.

The search for YSO candidates was performed using the SIMBAD Astronomical Database (CDS, Strasbourg) and the AllWISE Data Release catalog [37]. For the Serpens South region, a search radius of 7 arcmin was adopted within the coordinate range $277.39° \leq \alpha \leq 277.62°$ and $-2.031° \leq \delta \leq -2.036°$. A total of 682 infrared sources were identified within this area. The detected source density is consistent with the expected infrared source population toward this portion of the Galactic plane and includes both potential YSO candidates and a significant number of background and extragalactic contaminants.

An initial photometric quality filtering was applied to the Serpens South dataset in order to exclude sources with unreliable flux measurements. Only objects with photometric uncertainties smaller than 0.2 mag were retained. This threshold provides a balance between sample completeness and photometric reliability by removing low signal-to-noise detections, consistent with approaches commonly adopted in similar studies. At the same time, it should be noted that this criterion may exclude a fraction of faint but physically real sources.

For the subsequent analysis, only sources with non-zero magnitudes in all four WISE bands (W1, W2, W3 and W4) were considered. For convenience, the following color-index notation was adopted throughout this work: W1-W2 by W_{12}; W2-W3 by W_{23}; W1-W3 by W_{13}, W2-W4 by W_{24} и W3-W4 by W_{34}.

The next stage of the analysis involved the removal of contaminating sources that may exhibit infrared colors similar to those of YSOs. The first class of contaminants consists of star-forming galaxies. Galaxies undergoing active star formation typically show enhanced polycyclic aromatic hydrocarbon (PAH) emission produced through interactions between interstellar dust and ultraviolet radiation fields.

Star-forming galaxies dominated by polycyclic aromatic hydrocarbon (PAH) emission typically exhibit very red infrared colors, characterized by large values of W23 and are generally fainter than typical young stellar objects. In this study, we adopted the same approach based on established color-selection criteria. The criteria used to identify and remove probable star-forming galaxies were: $W_{23}>1$; $W_{12}<1$; $W_{12}<0.46 \cdot W_{23}-0.466$ and W1>12 (or W2>11). All criteria were required to be satisfied simultaneously in order to reliably identify contaminating sources. Applying these conditions to the Serpens South region resulted in the identification of 5 infrared sources associated with star-forming galaxies. The adopted selection criteria are based on characteristic infrared colors related to PAH emission and are widely used in similar studies, confirming their effectiveness for separating extragalactic contaminants from YSO candidates.

Another important class of contaminants consists of active galactic nuclei (AGNs), whose mid-infrared fluxes may closely resemble those of young stellar objects. AGN emission is generally fainter than that of typical YSOs in regions located within approximately 5 kpc. Since the studied region is located at a distance of less than 1 kpc, these selection criteria are particularly important for the present sample. The criteria adopted to identify and remove probable AGNs were: $W1>1.8 \cdot W_{13}+4.1$ and W1>13 (or W2>12, or $W1> W_{13}+11$). Applying these criteria to the Serpens South region resulted in the identification of 211 infrared sources consistent with AGN contamination. It should be noted that, despite the application of strict selection criteria, some AGNs may still remain within the sample because of the overlap between their photometric properties and those of young stellar objects, representing one of the main sources of uncertainty in the classification process.

In addition to star-forming galaxies and AGNs, infrared emission may also arise from shocked gas structures and polycyclic aromatic hydrocarbon (PAH) emission associated with the interstellar medium. The criteria adopted for removing these Galactic contaminants were based on their characteristic infrared colors. Shock-emission sources were identified using the color criteria $W_{12}>1$ and $W_{23}<2$. Applying these conditions to the Serpens South region resulted in the identification of 40 shock-emission sources. The relatively large number of such sources supports previous evidence for active motions of interstellar material within the region. To exclude PAH-emission sources, two sets of color criteria were applied: first, $W_{12} < 1$ and $W_{23} > 4.9$ and second, $W_{12} < 0.25$ and $W_{23} > 4.75$. Using these conditions, 17 PAH-emission sources were identified in the Serpens South region. The removal of these types of contaminants represents an important step

in the analysis, since diffuse interstellar emission and shocked structures may mimic the infrared characteristics of young stellar objects, particularly in active star-forming environments.

For the investigated Serpens South region, the application of all photometric quality and color-selection criteria resulted in the exclusion of 273 out of 496 infrared sources as potential contaminants, including galaxies, active galactic nuclei, PAH-emission sources and shock-related structures. Such a high contamination fraction is a common characteristic of wide-field infrared surveys such as WISE, where extragalactic sources and diffuse interstellar structures may reproduce the photometric properties of young stellar objects.

To improve the reliability of the results, an additional assessment of photometric quality was performed using the AllWISE catalog flags [38]. Only sources with quality flags A and B, corresponding to signal-to-noise ratios of $w_{SNR} > 3$, were included in the analysis, ensuring sufficient photometric accuracy in the infrared bands. Nevertheless, even sources satisfying these criteria may still be associated with diffuse interstellar emission, particularly in the W3 (12 μm) band, where the background contribution becomes significant. Therefore, all candidates were additionally inspected visually using W3 images and combined W1–W3 maps, following approaches commonly adopted in studies of star-forming regions. Sources that did not exhibit a clear point-like morphology in the W3 band or were associated with diffuse structures were excluded from further analysis [39].

After all stages of filtering, the final sample consisted of 148 sources, corresponding to approximately 29.8% of the initial sample. Although photometric classification based on infrared criteria inevitably retains some degree of uncertainty because of the limited spatial resolution of WISE data and the partial overlap between the color properties of different source populations, the applied filtering procedure substantially reduces contamination and provides a statistically reliable sample of probable young stellar object candidates suitable for further analysis.

4. Results and discussion

4.1 Identification of young stellar objects

In this study, the identification of YSOs was performed using WISE photometric criteria combined with a classification scheme supplemented by 2MASS data. The inclusion of near-infrared measurements makes it possible to refine the classification boundaries and reduce the overlap between the color distributions of different source populations, thereby improving the robustness of the method and reducing the probability of false classifications.

Additional selection criteria involving fluxes in all four WISE bands (W1–W4) were applied for the identification of protostars, allowing a more reliable separation from extragalactic contaminants, including active galactic nuclei (AGNs). As a result, 2 protostar candidates were identified in the Serpens South region. Their presence is supported by previous infrared observations, particularly *Spitzer* Gould Belt Survey data, which revealed a dense embedded cluster of protostars in this region, as well as by far-infrared *Herschel* observations indicating a large population of protostellar and prestellar cores.

The identification of Class I and Class II objects was carried out using WISE color criteria with additional constraints based on 2MASS data. In total, 37 Class I objects and 48 Class II objects were identified. In addition, 12 sources were classified as transition-disk objects, while 49 sources were assigned to Class III.

Based on the resulting classification, a color–color diagram (W_{12} versus W_{23}) was constructed for all identified YSO candidates (Figure 2). The dashed lines indicate the classification boundaries separating different evolutionary stages of YSOs. The horizontal boundary at $W_{12} = 0.25$ defines the lower limit of infrared excess, whereas the vertical boundary at $W_{23} = 2.0$ separates more deeply embedded sources with enhanced mid-infrared emission.

The distribution of sources on the diagram demonstrates a clear evolutionary sequence. Class I objects are concentrated in the region of large color indices, consistent with the presence of dense dusty envelopes. Class II objects occupy an intermediate region associated with protoplanetary disks, while Class III objects and transition disks are located closer to the photospheric region, reflecting the reduced infrared excess at later evolutionary stages. One protostar is located in the region of high W12 values, indicating the presence of a dense cocoon-like envelope of gas and dust. Although its color index is lower than that of some Class I objects, it remains significantly separated from the photospheric and Class II regions, supporting its classification as one of the youngest and most deeply embedded objects in the sample.

During the analysis, several sources with anomalous color indices were identified, including objects with negative values of W23 or W12. Such values are inconsistent with the expected infrared properties of dusty envelopes and are most likely associ-

ated with the sensitivity limitations of the WISE telescope, particularly in the W3 band, as well as with contamination from diffuse background emission. In total, 3 anomalous sources out of 148 (≈2.0%) were identified. The complete list of anomalous objects is provided in Appendix A.

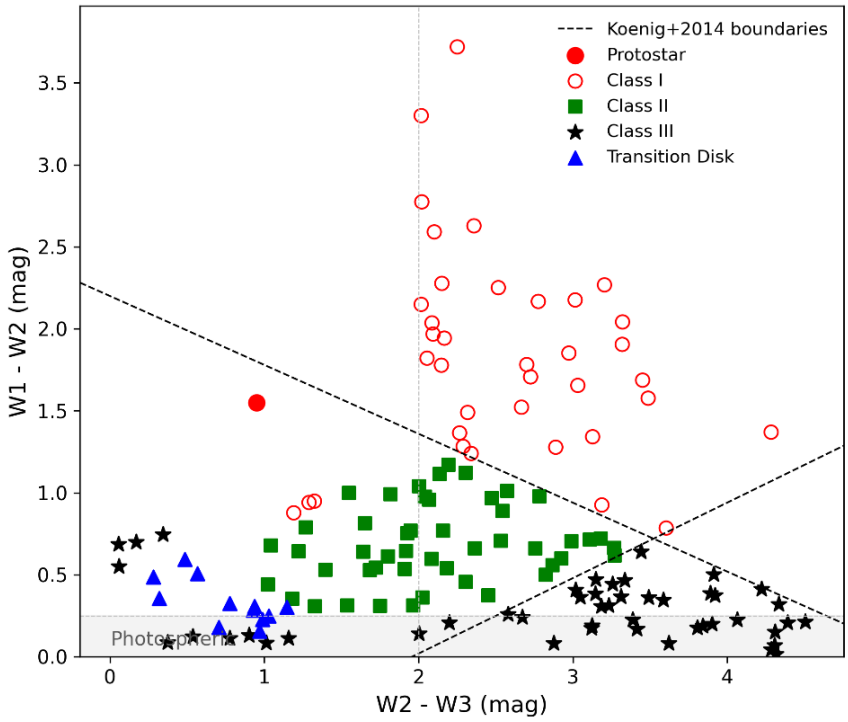

Figure 2. WISE color–color diagram (W1−W2) vs. (W2−W3) for young stellar object candidates in the Serpens South region.

The presence of these anomalous sources reflects residual photometric uncertainties and does not significantly affect the overall distribution of the sample. The relatively low fraction of anomalous objects (~2%) indicates the high purity of the final sample and confirms the effectiveness of the adopted filtering procedure.

Thus, the constructed color–color diagram reflects the distribution of reliably identified sources and confirms the validity of the adopted classification criteria, while also demonstrating the evolutionary structure of the young stellar object population in the Serpens South region.

4.2 Spatial distribution of young stellar objects

a) Spatial distribution map of young stellar objects

To investigate the structural relationship between YSOs at different evolutionary stages and the surrounding interstellar medium, a spatial distribution map of YSOs in the Serpens South region was constructed. Figure 3 presents the identified YSO candidates overlaid on a WISE 12 μm infrared image. Such a visualization makes it possible to examine the degree of concentration of the youngest objects, including protostars and Class I sources, along the dense gas-and-dust filaments of the nebula, as well as to trace the evolutionary segregation process, in which stars gradually disperse as they evolve from deeply embedded protostellar cores into more evolved Class III systems.

Figure 3a shows the spatial distribution of Class I objects, Class II objects, transition disks and protostars. Sources at the earliest evolutionary stages, including protostars and Class I objects, exhibit a pronounced concentration toward the central region, spatially coinciding with the densest and most highly obscured structures visible in the infrared map. Such a distribution is characteristic of young protostellar populations closely associated with dense molecular filaments [40]. Class II objects display a more extended distribution, occupying both the central and

peripheral regions, indicating a more advanced evolutionary stage and partial dynamical relaxation [41]. Transition-disk objects do not exhibit a strong central concentration and are predominantly distributed at intermediate and larger distances from the cluster center, consistent with their interpretation as more evolved systems. It should be noted that the protostar sample in the present study is limited (N = 1), preventing statistically significant conclusions regarding their spatial distribution.

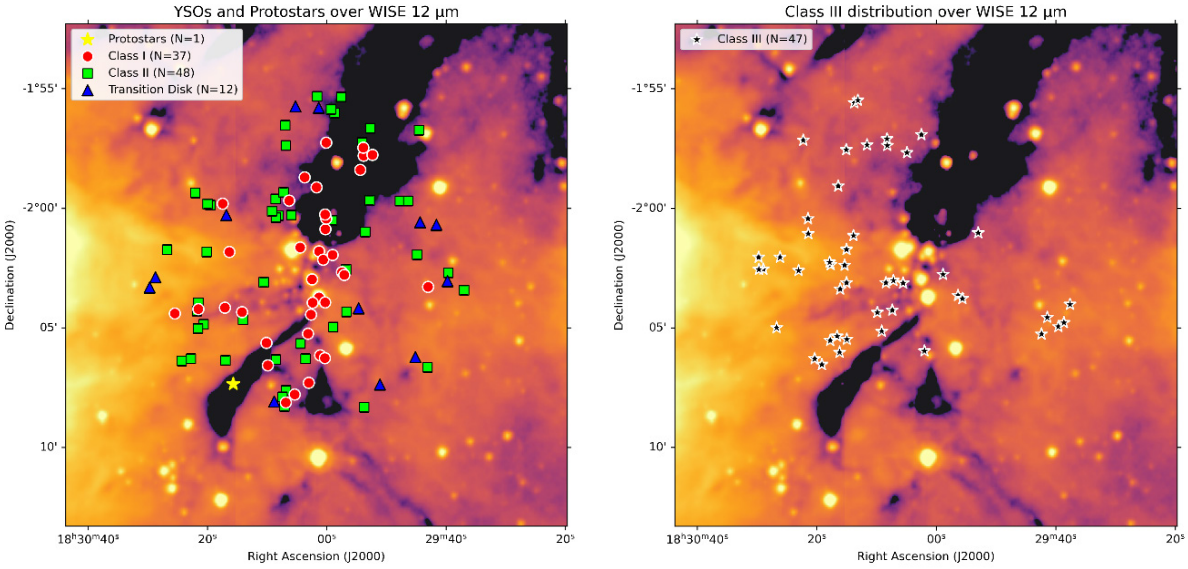

(a) YSO candidates: protostar, Class I and Class II objects and transition disks

(b) Class III YSO candidates

Figure 3. Spatial distribution of YSO candidates of different evolutionary classes in the Serpens South region overlaid on the WISE 12 μm map.

The observed spatial distribution of different YSO classes reflects an evolutionary sequence in which younger objects remain closely associated with dense molecular-cloud structures, whereas more evolved sources gradually disperse as a result of cluster dynamical evolution and interactions with the surrounding environment. Similar behavior has previously been reported in several star-forming regions, including Serpens South and Orion.

Figure 3b shows the spatial distribution of Class III YSO candidates in the Serpens South region. In contrast to younger objects, Class III sources exhibit a significantly more uniform and extended spatial distribution, without a pronounced concentration toward the central part of the region. Such a distribution is consistent with the expected dynamical evolution of stellar clusters, in which Class III objects, having lost their protoplanetary disks, represent a more evolved population that has had sufficient time to migrate away from their formation sites. The absence of a clear correlation with dense infrared structures further indicates that these objects are no longer directly associated with active star-forming regions, in agreement with observations of other star-forming environments.

b) Radial properties of YSO candidates of different evolutionary classes

To quantitatively investigate the spatial distribution of YSO candidates in the Serpens South region, radial distances relative to the cluster center were analyzed. Source coordinates were obtained from the AllWISE catalog and converted into equatorial coordinates (J2000) expressed in degrees. The cluster center was defined using the median coordinates of the Class I objects. This choice is motivated by the fact that Class I sources correspond to the earliest evolutionary stages and are therefore expected to remain spatially associated with ongoing star formation. The use of median values instead of mean coordinates reduces the influence of asymmetries and outliers in the spatial distribution.

Radial distances were calculated under the small-angle approximation with a cosine correction applied to declination $r = \sqrt{(\Delta cos\delta)^2 + (\Delta\delta)^2}$, where Δα and

Δδ represent the offsets in right ascension and declination relative to the cluster center and r is expressed in arcminutes [42].

To compare the spatial distributions of different evolutionary classes (Class I, II, III and transition-disk YSO candidates), cumulative distribution functions (CDFs) were used, thereby avoiding dependence on binning and enabling robust comparisons between samples of different sizes [43]. For each class, an empirical cumulative distribution function of radial distances was constructed. The statistical significance of the differences between distributions was evaluated using the Kolmogorov–Smirnov test, which measures the maximum deviation between two empirical cumulative distributions and estimates the probability that the samples originate from the same parent distribution. In addition, mean and median radial distances were calculated for each class and used as independent indicators of spatial concentration.

To evaluate the robustness of the median values, a bootstrap resampling procedure was applied [44]. For each sample, 5000 bootstrap realizations with replacement were generated, allowing the distribution of median radii and the corresponding 68% confidence intervals to be determined. This procedure is particularly important for the relatively small sample of transition disks (N = 12), for which standard statistical estimates may be unstable.

Figure 4 presents the cumulative radial distributions (CDFs) for Class I, II, III and transition-disk YSO candidates relative to the cluster center. The distribution corresponding to Class I objects is systematically shifted toward smaller radii, indicating a high degree of spatial concentration. The median radius for this class is r_{med} = 3.50 arcmin.

The distributions of Class II and III objects are nearly identical and are characterized by median radii of approximately 5.2 arcmin, indicating a more spatially extended structure. This result is supported by the Kolmogorov–Smirnov test, which reveals no statistically significant difference between these classes ($p \approx 0.91$).

Transition disks exhibit a systematic shift toward larger radii, with a median value of r_{med} = 5.46 arcmin. The confidence interval derived from bootstrap resampling (5.38–6.09 arcmin) does not overlap with that of the Class I population, indicating the absence of strong central concentration for transition-disk objects. At the same time, partial overlap with the distributions of Class II and III sources suggests statistical consistency with more evolved populations.

Overall, the obtained results are consistent with the standard evolutionary picture of YSOs, in which younger objects remain concentrated in the central star-forming regions, whereas more evolved sources become distributed over a larger spatial volume.

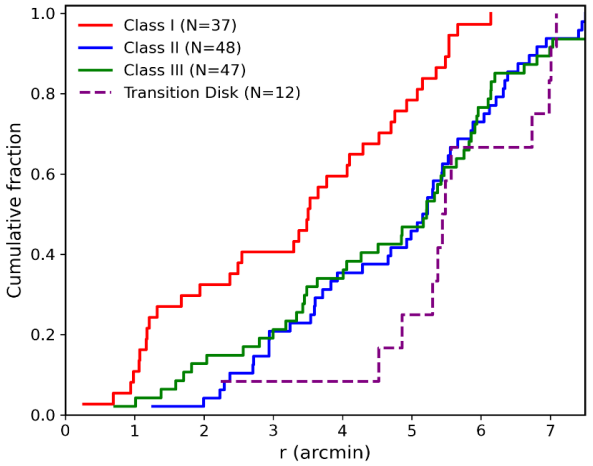

Figure 4. Cumulative distribution functions of radial distances for young stellar object candidates of different evolutionary classes in the Serpens South region.

Table 1. Radial properties of YSO candidates belonging to different evolutionary classes.

Class of objects	N	⟨r⟩ (arcmin)	r_{med} (arcmin)	68% CI (arcmin)
Class I	37	3.27	3.50	3.30–3.77
Class II	48	4.81	5.19	4.93–5.31
Class III	47	4.66	5.22	4.85–5.37
Transition Disk	12	5.55	5.46	5.38–6.09

c) Quantitative analysis of the spatial distribution of YSOs

A quantitative analysis of the spatial distribution of young stellar objects at early evolutionary stages in the Serpens South region was further performed, revealing systematic differences between evolutionary classes.

Figure 5 presents the spatial distribution of YSO candidates in the Serpens South region overlaid on the WISE 12 μm infrared emission map together with contour lines corresponding to the kernel density estimation (KDE) of the source distribution [45]. The color map represents the infrared intensity on a logarithmic scale (MJy/sr^{-1}). The left panel (Figure 5a) shows the distribution of protostars (yellow stars) and Class I objects (red circles). Regions of enhanced source density, indicated by white contours, demon-

strate pronounced clustering, with the sources concentrated along an elongated structure associated with a dense molecular filament. The right panel (Figure 5b) presents the distribution of Class II objects (green squares). Their spatial distribution appears more diffuse, while the density contours (green) indicate significantly weaker clustering compared with the Class I population.

For the early evolutionary classes of YSO candidates, several quantitative spatial parameters were calculated, including R50, the characteristic radius containing 50% of the objects of a given class; NN (Nearest Neighbor), defined as the mean distance to the nearest neighboring source; and KDE (Kernel Density Estimation), corresponding to the peak value of the kernel density distribution. The first parameter characterizes the local concentration of objects, the second describes the compactness of the population and the third reflects the maximum projected surface density of sources within the cluster.

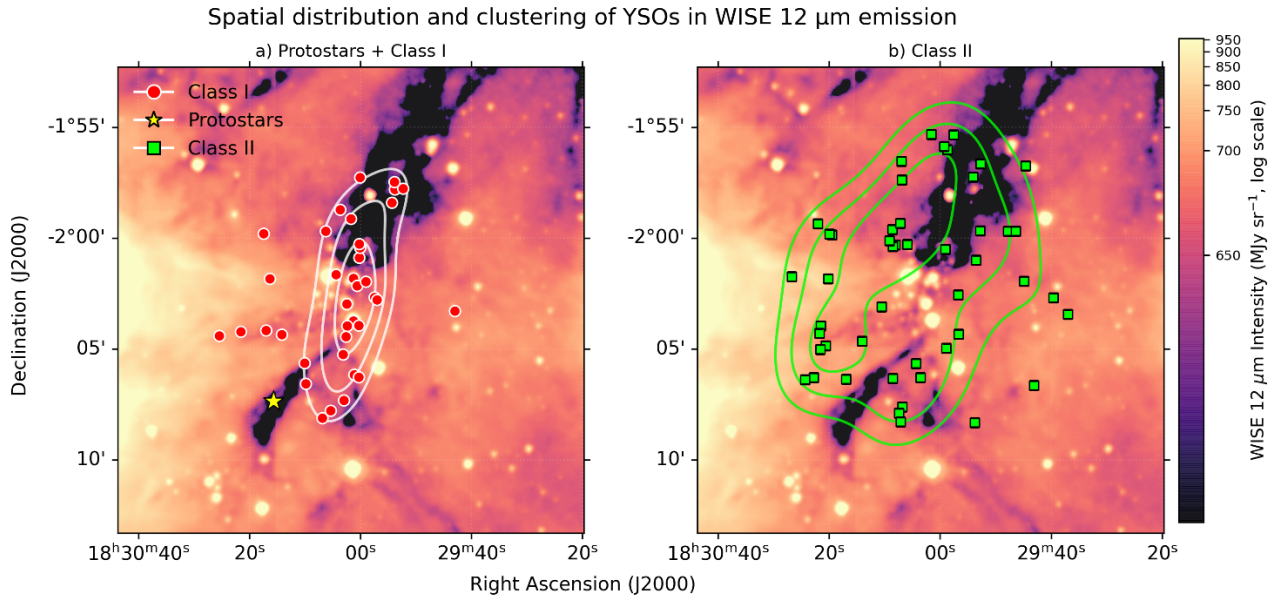

Figure 5. Spatial distribution and clustering of YSO candidates based on WISE infrared emission at 12 μm.

Class I objects exhibit a more compact spatial distribution, characterized by a radius of R_{50} = 0.26 ± 0.03 pc, whereas Class II objects show a larger characteristic radius of R_{50} = 0.37 ± 0.02 pc. Thus, the characteristic spatial scale increases by approximately 40% from Class I to Class II sources. The mean nearest-neighbor distance also increases from 0.055 pc for Class I objects to 0.066 pc for Class II objects, indicating a decrease in the local source density. The KDE analysis further shows that the peak density of the Class I population is approximately three times higher than that of the Class II population, implying significantly stronger clustering at earlier evolutionary stages.

Protostars in the present sample are represented by a limited number of objects (N = 1), preventing a statistically meaningful quantitative analysis of their spatial distribution. Nevertheless, their localization within the region of maximum source density is consistent with the expected location of the youngest objects near the centers of active star formation.

The obtained results are consistent with the established evolutionary picture of stellar clusters, in which the youngest objects, including protostars and Class I sources, remain concentrated within dense filamentary structures, whereas more evolved objects, such as Class II and Class III sources, exhibit a more extended spatial distribution.

Table 2. Spatial distribution parameters.

Parameter	Class I	Class II
Number of objects (N)	37	48
(R_{50}) (pc)	0.26 ± 0.03	0.37 ± 0.02
NN (pc)	0.055	0.066
KDE peak	$2.95 \cdot 10^{-5}$	$1.05 \cdot 10^{-5}$

d) Estimation of the Physical Parameters of the Serpens South Region Using the Monte Carlo Method

To quantitatively interpret the observed clustering scale of the identified young stellar objects, a Jeans analysis was performed taking into account the uncertainties of the input parameters. The mean nearest-neighbor separation, $L_{obs} \approx 0.06$ pc, was adopted as the characteristic fragmentation scale. The gas temperature was assumed to lie within the range of 10–15 K, corresponding to typical conditions in dense molecular clouds [46]. Since the Jeans length depends nonlinearly on both temperature and density, Monte Carlo simulations were applied in order to obtain a statistically robust estimate of the physical parameters of the environment. Within 10^4 realizations, the gas temperature and the observed spatial scale were randomly varied and for each realization the gas density satisfying the condition $\lambda_J \approx L_{obs}$ was determined.

The simulation results are presented in Figure 6, which shows the resulting gas-density distribution. The histogram represents the Monte Carlo sample, while the solid curve corresponds to the smoothed kernel density estimation (KDE). The vertical dashed line marks the median value, whereas the dotted lines indicate the 68% confidence interval. The resulting distribution is close to log-normal in shape, with a moderate asymmetry toward higher densities.

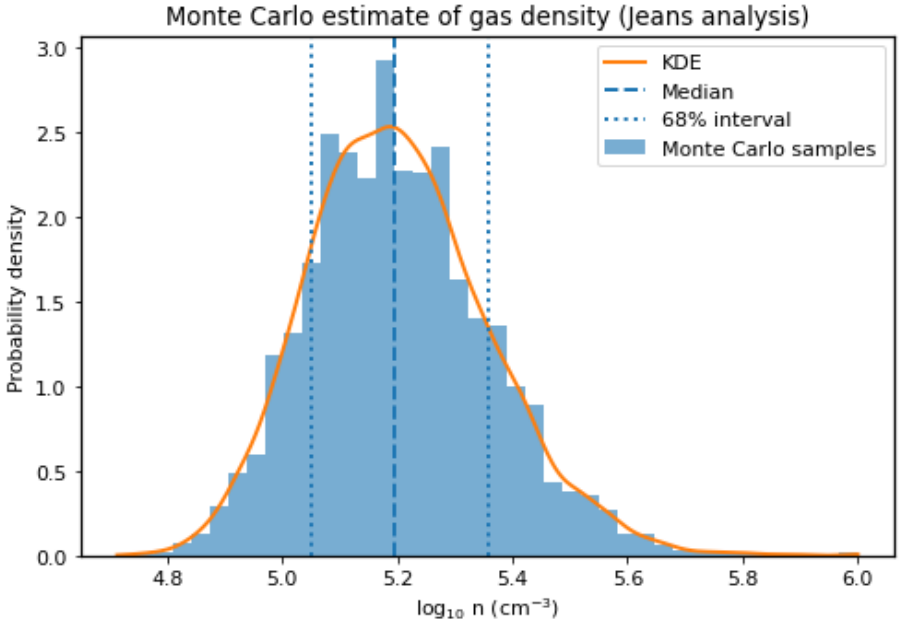

Figure 6. Monte Carlo estimation of gas density from Jeans analysis in Serpens South.

The numerical estimates are summarized in Table 3. The median gas density is found to be $n \approx 1.6 \times 10^5$ cm^{-3}, with a 68% confidence interval of $n \approx (1.1–2.2) \times 10^5$ cm^{-3}. These values significantly exceed the average density of typical molecular clouds ($\sim 10^3–10^4$ cm^{-3}) and are consistent with dense filamentary structures and prestellar cores [47]. Previous studies of the Serpens South region have shown that star formation occurs within a dense filamentary structure characterized by a high concentration of protostars [48].

Thus, the obtained results are consistent with the current paradigm of filamentary star formation, in which gravitational fragmentation of dense filaments plays a key role [49]. The observed clustering scale of the YSO candidates corresponds to the Jeans scale within the densest regions of the filaments, confirming the connection between the spatial distribution of the sources and the physical conditions of the surrounding medium.

It is important to note that the contribution of temperature uncertainty to the final result is secondary compared to the effect of gas density, in agreement with theoretical estimates of the Jeans-length sensitivity [50]. This indicates that gas density plays the dominant role in determining the fragmentation scale.

Table 3. Estimated gas density parameters.

Parameter	Value
Median (n)	(1.56×10^5) cm^{-3}
Mean (n)	(1.71×10^5) cm^{-3}
Lower limit (16%)	(1.12×10^5) cm^{-3}
Upper limit (84%)	(2.24×10^5) cm^{-3}
Confidence interval (68%)	$((1.12–2.24)\times10^5)$ cm^{-3}

4.3 Multiwavelength verification and comparative analysis of YSO candidates

To independently verify the adopted classification and evaluate the novelty of the resulting YSO candidate sample in the Serpens South region (1 protostar, 37 Class I objects, 48 Class II objects, 47 Class III objects and 12 transition disks), a multiwavelength cross-identification analysis was performed using 19 astrophysical catalogs and published studies. The analysis included infrared catalogs (7 catalogs, including 2MASS, WISE/NEOWISE, *Spitzer*, as well as the general source catalog and YSO sample presented in [20]), X-ray catalogs (3 catalogs: SFiNCs [51], *Chandra* and MORX [52]), radio [40] and submillimeter catalogs (4 catalogs: VLA GBS [53-55]), as well as combined and optical datasets [56–59]. The results of the cross-identification analysis are presented in Appendices B and C.

a) Cross-identification with infrared catalogs

To independently validate our classification and assess the novelty of the resulting sample, we performed a cross-identification of all 145 YSO candidates with the infrared catalogs presented in [20], where deep near-infrared (NIR) mapping of the W40–Serpens South region was carried out using CFHT observations combined with data from the 2MASS, UKIDSS and *Spitzer* surveys, resulting in a cleaned catalog containing 901,910 point sources. It is important to emphasize that the data presented in [20] were obtained using an independent methodology based on deep NIR and *Spitzer* observations and do not include WISE photometry, which forms the basis of the classification adopted in the present work. This makes the cross-comparison particularly valuable for an objective assessment of the reliability of our sample. The positional cross-identification shows that 137 out of 145 YSO candidates (94.5%) have counterparts in the general catalog presented in [20]. The highest completeness is achieved for the more evolved populations (Class II, Class III and transition disks), which is expected because of their enhanced brightness in the near-infrared wavelength range. A key result, however, is that comparison with the final sample of 832 verified YSOs identified in [20] shows that 124 out of our 145 candidates (85.5%) are absent from their final YSO catalog. Particularly notable are the results for the later evolutionary classes: 97.9% of the Class III objects and 100% of the transition-disk objects were not classified as YSOs in [20], indicating a substantial degree of novelty within the resulting sample. At the same time, it should be noted that a significant fraction of these sources had previously been identified in other studies of the Serpens South region based on X-ray, infrared and submillimeter observations. As an additional verification step, the 2MASS photometry of our objects was compared with the catalog data reported in [20], confirming the reliability of the source identifications (see Appendix B for details).

Since the infrared wavelength range provides the dominant contribution to the identification of young stellar objects in the studied region, additional data from several independent infrared surveys and specialized YSO catalogs were incorporated into the analysis

First, data from the *Spitzer*, WISE and NEOWISE space missions were used. The *Spitzer* survey (IRAC and MIPS) provides deep mid-infrared coverage in the 3.6–24 μm range, which is critically important for detecting circumstellar disks and protostellar objects, whereas WISE and its extension NEOWISE (3.4–22 μm) provide complete coverage of the entire region over a wider field of view, although with lower sensitivity compared to *Spitzer*. The combination of these surveys enables reliable identification of sources exhibiting infrared excess emission associated with accretion disks and dusty envelopes.

Second, several specialized YSO catalogs were employed. The MIRES (*Mid-InfraRed Excess Sources*) catalog presented in [60] was developed for the identification of massive young stellar objects and protostars using *Spitzer*/IRAC observations. In addition, the *Spitzer* YSO SED catalog provides a systematic classification of sources based on spectral energy distribution (SED) modeling in 22 star-forming regions, including Serpens South and represents one of the most widely used resources for identifying circumstellar disk systems.

Third, results from several independent studies were incorporated into the analysis. A combined analysis of infrared and X-ray observations in the Serpens South region revealed a significant number of YSO candidates. A machine-learning approach for YSO classification based on WISE data was developed in [61], while an updated catalog of young stel-

lar objects was presented in [62]. In addition, YSO candidates in the Serpens–Aquila Rift complex were identified using a combination of WISE, 2MASS and Gaia observations.

Taken together, the combined use of these datasets showed that 114 out of 145 objects (78.6% of the sample) possess independent infrared confirmation of their YSO nature. Such a high fraction is expected because infrared wavelengths, particularly in the mid- and far-infrared ranges, penetrate the parental molecular clouds that strongly absorb optical and ultraviolet radiation. Moreover, infrared excess emission is a direct indicator of circumstellar disks and dusty envelopes, making infrared observations the primary and in many cases the only, method for identifying young stellar objects at early evolutionary stages. The obtained results confirm that the infrared wavelength range remains the principal tool for identifying protostellar and disk-bearing systems in the Serpens South region and further demonstrate the high reliability of the present sample, since the overwhelming majority of the candidates possess independent infrared confirmation from multiple datasets.

b) ross-identification with radio and X-ray catalogs

To independently verify the young nature of the sample of 145 YSO candidates, a cross-identification analysis was performed using radio and X-ray catalogs, as well as independent source catalogs associated with star-forming regions (the results are presented in Appendices B and C).

A comparison with the VLA Gould's Belt Survey (GBS) radio catalog, containing 146 sources detected at 4.5 GHz with a sensitivity of 10–15 μJy, revealed no positional matches within a search radius of 30″.

Despite the absence of direct matches with the VLA catalog, three objects in our sample possess independent confirmation in the radio and submillimeter wavelength ranges based on specialized studies of the Serpens South region. Previous molecular and radio investigations of the Aquila Rift complex have revealed dense molecular condensations, selective CO dissociation regions and complex gas kinematics associated with active star formation [63-65]. A catalog of millimeter and submillimeter sources in the W40–Serpens South region obtained with the JCMT telescope using the SCUBA-2 instrument (450 and 850 μm) revealed dense cold cores, many of which are associated with protostellar objects at early evolutionary stages. High-angular-resolution SMA observations further identified several compact millimeter sources corresponding to individual protostars and compact multiple systems in Serpens South. Recent interferometric studies of massive star-forming regions obtained with ALMA have additionally demonstrated the importance of molecular and ionized gas diagnostics for investigating the physical and dynamical properties of embedded young stellar environments [66-70]. Additional confirmation is provided by complementary catalogs of submillimeter and infrared-selected YSOs, as previously reported in [40, 62]. The catalog presented in [71] includes submillimeter and millimeter continuum sources identified in the Serpens South region using JCMT and IRAM 30m observations. The *Spitzer* YSO SED catalog additionally includes millimeter and radio detections for part of the sample, allowing these sources to be classified as protostellar objects with confirmed cold dust components. Based on these studies, three objects in our sample were identified as having radio or submillimeter confirmation: the first source was detected in the submillimeter range, as previously reported in [58, 62]; the second object was classified as a millimeter/radio source in [40]; and the third object was identified in the submillimeter range [71].

All three objects belong to the early evolutionary stages (Class I), which is expected because such sources possess the most massive and cold dusty envelopes emitting strongly in the submillimeter and millimeter wavelength ranges. The absence of matches with the VLA GBS catalog even for these three objects can be explained by differences in sensitivity and observing frequencies. The survey presented in [53] was carried out at 4.5 GHz (6 cm) and was optimized for the detection of free–free emission from ionized gas, whereas submillimeter observations in the 450–850 μm range are primarily sensitive to cold dust emission. Thus, these two observational regimes trace different physical components of protostellar systems (ionized winds/jets versus cold dusty envelopes) and are not necessarily expected to correlate directly.

The very small number of radio detections (≈2.1% of the total sample) is consistent with the results previously reported in [53], where only ~30% of YSOs in the Gould Belt were found to be detectable at radio wavelengths. Under the extreme conditions of the Serpens South region, this fraction may be even lower because of free–free absorption and the high optical depth of the surrounding medium.

Additional cross-identification with the MORX (*Million Optical Radio/X-ray Associations*) catalog did not reveal statistically significant matches within the investigated area (≈0.05 deg^2), which is likely explained by the high extinction and incomplete coverage by deep surveys.

In contrast, X-ray observations provide strong independent confirmation of the young nature of the sources, since high-energy emission is a direct indicator of magnetic activity characteristic of stars at early evolutionary stages. The principal contribution comes from two major catalogs. The first is the SFiNCs (*Star Formation in Nearby Clouds*) catalog, derived from a homogeneous analysis of archival *Chandra* X-ray and *Spitzer* infrared observations covering 22 star-forming regions [51]. This project identified more than 15,300 X-ray sources, nearly 8,500 of which were classified as probable young stellar members, increasing the known YSO populations in some regions by factors of 6%–200%.

The second dataset is a dedicated X-ray study of the Serpens South region, as previously reported in [52]. Using *Chandra* ACIS-I observations, that study identified 152 X-ray sources, of which 66 obtained reliable infrared counterparts based on *Spitzer* and 2MASS data, while 95 were classified as new YSO candidates.

Within our sample, 102 objects (70.3%) possess independent X-ray confirmation. This fraction demonstrates not merely a significant but rather a dominant overlap between the infrared- and X-ray-selected populations. The obtained value is fully consistent with the fundamental observational trends established for star-forming regions. Previous studies [63] have shown that the X-ray detection fraction of YSOs reaches approximately 70%–75% for more evolved objects, particularly Class II and Class III sources. Our results are therefore fully consistent with this established statistical behavior and confirm that the observed population represents a typical sample of young stars, for which X-ray activity serves as a reliable indicator of youth independent of the effects of dusty envelopes and circumstellar disks. The optical depth for soft X-ray emission (~0.5–8 keV) is substantially lower than at optical wavelengths, allowing the detection of sources deeply embedded within their parental molecular clouds.

Thus, the X-ray data not only complement but also independently validate the infrared classification. The high fraction of joint detections (infrared + X-ray) serves as a robust indicator that the identified sources represent a real and physically young stellar population rather than artifacts or erroneous identifications.

c) Cross-identification with multiwavelength data

An integrated assessment of the multiwavelength confirmations was performed in order to quantitatively evaluate the contribution of each wavelength range to the verification of the sample. Based on comparisons with infrared (*Spitzer*, WISE, NEOWISE and 2MASS), X-ray (SFiNCs and *Chandra*, as previously reported in [52]) and optical datasets, all 145 candidates were classified according to the type of observational confirmation.

Objects possessing exclusively infrared confirmation, without detections in the X-ray or optical wavelength ranges, account for 61 sources (42.1% of the sample). This category mainly includes highly obscured objects for which the X-ray emission may be significantly attenuated, as well as intrinsically faint X-ray sources lying below the sensitivity limits of the adopted surveys.

A total of 13 objects (9.0% of the sample) are detected only in X-rays without independent infrared confirmation. The presence of X-ray emission in the absence of detectable infrared excess may indicate several possible scenarios: (a) very low-mass objects such as ultracool dwarfs, (b) sources so strongly obscured in the infrared range that they are absent from the adopted catalogs, or (c) possible artifacts related to X-ray data processing. Additional spectral energy distribution (SED) analysis is required for the final classification of these objects.

Joint infrared and X-ray confirmation is observed for 28 objects (19.3% of the sample). Such sources represent highly reliable YSO candidates because two independent physical mechanisms – thermal emission from circumstellar dust and X-ray emission from magnetically active coronae – simultaneously indicate a young stellar nature. This category may therefore be considered the "gold standard" for cross-validation of YSO samples.

Optical data play a secondary role, providing confirmation for only 21 objects (14.5% of the sample). Such a low fraction is expected because of the extreme conditions in the Serpens South region: the high level of interstellar extinction typical of dense molecular clouds strongly suppresses optical emission, even in the I band (~800–900 nm). Consequently, optical detections are generally limited to the outermost and least obscured members of the association or to foreground objects.

Complete three-wavelength confirmation (infrared + X-ray + optical) is achieved for 21 objects (14.5% of the sample). These represent the most reliable YSO candidates, for which not only high-energy and dust-related emission but also optical radiation has been detected, primarily in red optical filters. This suggests comparatively low extinction along the line of sight or a location outside the densest regions of the molecular cloud.

Particular attention should be given to 11 objects (7.6% of the sample) that do not possess confirmation in any of the considered wavelength ranges (infrared, X-ray, or optical) (Table 4). A key result of the present study is the demonstration that all of these sources are present in the general point-source catalog presented in [20], which contains 901,910 reliable astronomical sources in the Serpens South region. Therefore, these objects represent real astrophysical sources rather than artifacts related to WISE data processing. Moreover, although these sources are included in the deep multiwavelength catalog reported in [20], they were not included in the final sample of 832 verified YSOs identified in that study. This discrepancy is likely explained by two factors. First, the methodology adopted in [20] relied primarily on deep NIR (CFHT) and *Spitzer* observations together with more restrictive selection criteria designed to minimize false identifications, potentially excluding fainter or more heavily obscured sources. Second, the present work makes extensive use of WISE photometry, which was not incorporated into the methodology of [20]. In particular, the W3 (12 μm) and W4 (22 μm) bands provide unique sensitivity to warm dust emission associated with circumstellar disks and dusty envelopes, enabling the identification of YSOs that may remain undetected in shorter-wavelength NIR observations. Thus, the WISE-based criteria adopted in the present study made it possible to identify a population of young objects that was not recovered using the more restrictive selection procedure of [20]. Collectively, these results emphasize the substantial novelty of the present study, in which these sources are identified for the first time as YSO candidates.

The absence of X-ray, optical and radio detections for these 11 objects, including Class I, II and III sources, does not contradict their young stellar nature. For Class II and III objects, this may be explained by several factors: (a) the large intrinsic spread in YSO X-ray luminosities, which may vary by up to two orders of magnitude within a single evolutionary class [72, 73], allowing weak sources to fall below the sensitivity limit of *Chandra* observations; (b) variability of magnetic activity analogous to solar flares; and (c) residual extinction attenuating soft X-ray emission. For Class I objects, an additional factor is the strong shielding produced by dense dusty envelopes.

The absence of optical detections is also expected. Even for Class III sources in Serpens South, the typical extinction reaches several magnitudes, rendering optical emission inaccessible to most ground-based surveys. Likewise, the absence of radio detections is not unusual, since only approximately 30% of YSOs in the Gould Belt are detectable at 4.5 GHz, as previously reported in [53].

Therefore, the absence of multiwavelength confirmations can be explained by a combination of factors, including low luminosity, variability, extinction and survey sensitivity limitations, rather than by the absence of a young stellar nature. These 11 objects represent valuable candidates for future deep observations. Additional observations with facilities such as ALMA, JCMT and NOEMA, together with detailed Herschel-based spectral energy distribution analysis are required for the final verification and classification of these sources.

Overall, the combined analysis presented here demonstrates the varying levels of reliability in YSO identification across the studied region and emphasizes the essential role of a multiwavelength approach, particularly for heavily obscured star-forming environments.

Table 4. New YSO candidates in the Serpens south region.

№	*AllWISE*	*RA(J2000), deg*	*DE(J2000), deg*	*W1, mag*	*W2, mag*	*W3, mag*	*W4, mag*	*YSO Candidate (class)*
SS_YSO_01	J183003.69-015842.5	277.52	-01.98	15.877	13.835	10.513	8.120	I
SS_YSO_02	J183016.33-020149.3	277.57	-02.03	15.210	13.840	9.555	7.049	I
SS_YSO_03	J183017.04-020409.5	277.57	-02.07	15.548	13.280	10.075	7.338	I
SS_YSO_04	J183000.31-020616.0	277.50	-02.10	14.222	12.732	10.414	4.829	I
SS_YSO_05	J183006.84-020806.8	277.53	-02.14	14.243	12.207	10.120	8.193	I
SS_YSO_06	J183004.38-020539.0	277.52	-02.09	14.050	12.936	10.799	8.580	II
SS_YSO_07	J182947.76-015941.6	277.45	-01.99	13.132	12.588	10.866	8.631	II
SS_YSO_08	J183022.05-015921.5	277.59	-01.99	13.266	12.547	9.367	6.740	II

Continuation of the table

№	AllWISE	RA(J2000), deg	DE(J2000), deg	W1, mag	W2, mag	W3, mag	W4, mag	YSO Candidate (class)
SS_YSO_09	J183017.84-020215.3	277.57	-02.04	14.179	13.792	9.900	7.986	III
SS_YSO_10	J182942.40-020515.0	277.423	-02.09	12.044	11.902	9.898	6.883	III
SS_YSO_11	J182937.64-020401.0	277.41	-02.07	13.242	13.067	9.947	6.579	III

4.4 Comparison with other star-forming regions and interpretation

The results obtained in the present study allow a comparison between the Serpens South region and other well-studied star-forming environments, including NGC 1333, Ophiuchus, Serpens Core and IC 348.

1. A systematic comparison of five star-forming regions – Serpens South, Serpens Core, Ophiuchus, NGC 1333 and IC 348 — was previously presented in [74]. That study showed that, for most regions, the distribution of young stellar objects on scales larger than 0.15 pc is well described by the gas column density distribution, while the spatial distribution of YSOs at a given column density remains statistically random. However, Serpens South and NGC 1333 exhibit significant deviations from this behavior on smaller spatial scales (~0.15 pc), indicating that star formation in these two regions cannot be explained solely by gas column density. Instead, additional local processes, such as turbulence, magnetic fields, or dynamical interactions, likely play an important role.

Our analysis of the spatial distribution (Figures 3–5) fully supports this interpretation. Figure 3a shows that the youngest objects, including protostars and Class I sources, are concentrated toward the central region and coincide with the densest structures visible in the WISE 12 μm infrared map, whereas Figure 3b demonstrates that Class III objects exhibit a substantially more uniform distribution. Figure 4 presents the cumulative distribution functions (CDFs) of radial distances for different evolutionary classes, showing a systematic shift of the Class I distribution toward smaller radii compared with the Class II and III populations. In addition, Figure 5 shows the kernel density estimation (KDE) of the source distribution, where the contours associated with Class I objects demonstrate pronounced clustering, while the Class II population exhibits a significantly weaker concentration.

The quantitative estimates summarized in Table 2 show that the characteristic radius for Class I objects is $R_{50} = 0.26 \pm 0.03$ pc, whereas for Class II objects $R_{50} = 0.37 \pm 0.02$ pc. The median gas density derived from our Jeans analysis ($n \approx 1.6\times10^5$ см$^{-3}$; see Figure 6 and Table 3 in Section 3.3d) significantly exceeds the average density of typical molecular clouds (~10^3–10^4 см$^{-3}$) and corresponds to dense filamentary structures and prestellar cores detected with *Herschel*, as previously reported in [28, 36].

2. Comparison with the nearby W40 region provides important evolutionary information. According to the deep near-infrared survey presented in [20], the central region of W40 is dominated by Class II YSOs, corresponding to a more evolved stellar population, whereas approximately half of the YSOs in Serpens South belong to the younger Class I stage. This suggests that Serpens South is in an earlier stage of cluster evolution despite its spatial proximity and kinematic association with W40.

Our results are fully consistent with this interpretation. In the present sample, the fraction of Class I objects and protostars reaches approximately 26% (38 out of 145 objects). Furthermore, 124 out of 145 YSO candidates (85.5%) are absent from the final YSO catalog presented in [20], demonstrating the high efficiency of WISE data for identifying heavily obscured sources at early evolutionary stages.

3. The density estimates and clustering scales derived in this work can also be compared with those observed in other young embedded clusters. For example, in the NGC 1333 cluster, which also exhibits deviations from the model of on small spatial scales, the average gas density is approximately ~10^5 см$^{-3}$, nearly identical to our estimate for Serpens South ($n \approx 1.6\times10^5$ см$^{-3}$; see Table 3). By contrast, in more diffuse star-forming regions such as IC 348 and Taurus, the gas density is significantly lower and the spatial distribution of YSOs is more accurately described by the gas column density distribution without requiring additional local interactions.

The characteristic clustering scale obtained for Serpens South in the present study ($R_{50} = 0.26 \pm 0.03$ pc for Class I objects; see Table 2) is also consistent with the typical sizes of dense cores embedded within filamentary structures observed by *Herschel* as part of the Gould Belt Survey, as previously reported in [28, 36]. The mean nearest-neighbor distance for

Class I objects is 0.055 pc (Table 2), corresponding to typical fragmentation scales of dense molecular filaments.

4. A recent study [75] investigated the hierarchical structure of YSOs in the W40–Serpens South region using the minimum spanning tree (MST) method. The authors showed that the fractal dimensions in the central regions are approximately 1.6 for W40 and 1.4 for Serpens South. The lower fractal dimension derived for Serpens South indicates a higher degree of clustering, implying that the YSOs in Serpens South are concentrated into more compact groups.

Our analysis (see Figure 5 with KDE contours and Table 2 with the quantitative parameters) yields results fully consistent with this interpretation. Figure 3 shows that the youngest objects (Class I sources) exhibit the highest degree of spatial concentration, whereas Class II and III objects are distributed more uniformly throughout the region. The peak KDE density for the Class I population (2.95×10^{-5}) is approximately three times higher than that of the Class II population (1.05×10^{-5}), confirming a substantially stronger degree of clustering at earlier evolutionary stages. As previously reported in [20], four MST branches overlap with the main filament of Serpens South and molecular gas "hubs" together with an enhanced concentration of Class I YSOs are observed at their intersection points.

Thus, the comparison presented here, based on the quantitative results of our study (Figures 3–6 and Tables 1–3), allows the following conclusions to be drawn.

Serpens South, together with NGC 1333, belongs to the class of star-forming regions in which small-scale processes, including local interactions, turbulence and magnetic fields, play a key role in regulating star formation, distinguishing these environments from more diffuse regions such as IC 348 [76]. Our CDF distributions (Figure 4) and radial parameters (Table 1) quantitatively support this conclusion.

From an evolutionary perspective, Serpens South appears to be at an earlier stage of cluster evolution than the neighboring W40 region, as indicated by the high fraction of Class I objects identified both in our sample and in the catalog presented in [20].

The higher degree of clustering (corresponding to a lower fractal dimension) observed for the young population in Serpens South relative to other star-forming regions reflects the hierarchical structure of the dense filamentary cloud in which the stars are forming. Our KDE maps (Figure 5) and clustering parameters (Table 2) provide a quantitative basis for this interpretation.

5. Conclusion

In the present work, a comprehensive study of the young stellar object (YSO) population in the active star-forming region Serpens South, located within the Aquila Rift complex, has been carried out. Using multiwavelength data from the AllWISE catalog together with modern photometric selection criteria, a set of results was obtained that provides insight into the physical processes occurring within the region.

A representative sample of 145 YSO candidates was identified and classified according to their probable evolutionary stages. Protostellar candidates together with Class I objects account for approximately 26% of the sample, which, combined with the detected Class II population, suggests a high level of ongoing star formation activity. The presence of Class III candidates and transition disks further indicates a possible evolutionary sequence within the region, supporting the interpretation of Serpens South as one of the youngest nearby star-forming environments in the Galaxy.

The analysis of the spatial distribution of the sources indicates a likely correlation between evolutionary stage and the morphology of the surrounding gas. Early-stage objects exhibit clear spatial segregation and are preferentially concentrated along dense dusty filaments. In contrast, the more diffuse distribution of Class II and III objects may reflect dynamical relaxation processes and the gradual dispersal of the stellar population from the parental molecular structures.

A Jeans analysis combined with statistical modeling was used to estimate the local physical conditions within the fragmentation regions. The derived gas volume density, $n \approx 1.6 \times 10^5$ cm^{-3}, is consistent with theoretical models of star formation occurring within filamentary hubs and may support the important role of gravitational instability in this region.

The performed cross-identification with independent astrophysical catalogs, including *Chandra*/SFiNCs and *Spitzer* datasets, provides additional confirmation of the reliability of the adopted methodology. A substantial fraction of the sample exhibits both infrared excess emission and X-ray activity, characteristic of magnetically active young stellar objects.

During the course of this study, 11 new YSO candidates not previously reported in the literature were identified, including one potentially deeply embedded Class I source. These results suggest that WISE observations provide an efficient method for detecting objects located in regions of strong interstellar

extinction that may remain inaccessible to near-infrared surveys.

Overall, the obtained results expand the current understanding of the star-forming architecture of the Serpens South region. The identified spatial structure together with the newly detected YSO candidates demonstrates the importance of further observational studies aimed at determining the detailed physical properties of individual members of this association.

Funding

This research was funded by the Science Committee of the Ministry of science and Higher Education of the Republic of Kazakhstan (Grant No. AP23489575).

Conflicts of interest

The authors declare no conflict of interest.

Author contributions

Conceptualization, N.Sh. and A.B.; Methodology, A.Zh.; Formal Analysis, N.Sh.; Investigation, N.E.; Data Curation, A.B. and N.B.; Visualization, K.M. and N.E.; Writing–Original Draft Preparation, A.Zh. and N.Sh.; Writing–Review and Editing, A.M., N.B., N.Sh., and A.Zh.; Validation, A.A., K.M., and A.B.; Supervision, N.Sh. and A.Zh. All authors have read and agreed to the published version of the manuscript.

References

1. G. Saral *et al.*, "Young Stellar Objects in the Massive Star-forming Regions W51 and W43," *The Astrophysical Journal*, vol. 839, no. 2, pp. 108–108, Apr. 2017, https://doi.org/10.3847/1538-4357/aa6575

2. M. W. Werner *et al.*, "The *Spitzer Space Telescope* Mission," *The Astrophysical Journal Supplement Series*, vol. 154, no. 1, pp. 1–9, Sep. 2004, doi: https://doi.org/10.1086/422992

3. E. L. Wright *et al.*, "The wide-field infrared survey explorer (wise): mission description and initial on-orbit performance," *The Astronomical Journal*, vol. 140, no. 6, pp. 1868–1881, Nov. 2010, doi: https://doi.org/10.1088/0004-6256/140/6/1868

4. M. Sewiło *et al.*, "Identifying Young Stellar Objects in the Outer Galaxy: $l = 224°$ Region in Canis Major," *The Astrophysical Journal Supplement Series*, vol. 240, no. 2, pp. 26–26, Feb. 2019, https://doi.org/10.3847/1538-4365/aaf86f

5. A.B. Manapbayeva, J. Esimbek, N.Sh. Alimgazinova, M.T. Kyzgarina, A.B. Atamurat, "Identification of Young Star Objects Near the Dust Bubble N22," *Academic Scientific Journal of Computer Science*, no. 3, pp. 96–105, 2021, https://doi.org/10.32014/2020.2518-1726.51

6. A. B. Nazar, N. Sh. Alimgazinova, M. T. Kyzgarina, A. M. Demessinova and A. B. Manapbayeva, "Identification of young star objects near dust bubble N10," *Recent Contributions to Physics*, vol. 83, no. 4, Dec. 2022, doi: https://doi.org/10.26577/rcph.2022.v83.i4.02

7. A. M. Alisher, "Search and identification of young stellar objects in infrared dust bubbles N19," *Recent Contributions to Physics*, vol. 86, no. 3, Sep. 2023, https://doi.org/10.26577/rcph.2023.v86.i3.02

8. N. Alimgazinova *et al.*, "Study of the N126 dust bubble in the infrared wavelength range," *Recent Contributions to Physics*, vol. 89, no. 2, pp. 19–26, 2024,https://doi.org/10.26577/rcph.2024v89i2-03

9. N. Sh. Alimgazinova, A. B. Manapbayeva, A. Z. Omar, A. M. Demessinova, K. Turekhanova and N. E. Abildayev, "Study of the W40 Star-Forming Region Based on Observations by the WISE Infrared Space Telescope," *Herald of the Kazakh-British Technical University*, vol. 23, no. 1, pp. 346–357, Mar. 2026, https://doi.org/10.55452/1998-6688-2026-23-1-346-357

10. S.-J. Kang, C. R. Kerton, M. Choi and M. Kang, "A Comparative Observational Study of YSO Classification in Four Small Star-forming H ii Regions," *The Astrophysical Journal*,vol.845,no.1,p.21,Aug.2017, https://doi.org/10.3847/1538-4357/aa7da3

11. S. T. Megeath *et al.*, "Initial Results from the Spitzer Young Stellar Cluster Survey," vol. 154, no. 1, pp. 367–373, Sep. 2004, https://doi.org/10.1086/422823

12. R. A. Gutermuth *et al.*, "The *Spitzer* Gould Belt Survey of Large Nearby Interstellar Clouds: Discovery of a Dense Embedded Cluster in the Serpens-Aquila Rift," *The Astrophysical Journal*, vol. 673, no. 2, pp. L151–L154, Jan. 2008, https://doi.org/10.1086/528710

13. X. Koenig, D. Leisawitz, D. J. Benford, L. M. Rebull, D. Padgett and R. J. Assef, "*Wide-Field Infrared Survey Explorer Observations of the Evolution of Massive Star-Forming Regions*," *The Astrophysical Journal*, vol. 744, no. 2, pp. 130–130, Dec. 2011, https://doi.org/10.1088/0004-637x/744/2/130

14. X. P. Koenig and D. T. Leisawitz, "A Classification Scheme for Young Stellar Objects Using the Wide-Field Infrared Survey Explorer AllWISE Catalog: Revealing Low-Density Star Formation in the Outer Galaxy", *The Astrophysical Journal*, vol. 791, no. 2, p. 131, Aug. 2014, https://doi.org/10.1088/0004-637x/791/2/131

15. C. J. Lada, "Star Formation: From OB Associations to Protostars," *Symposium - International Astronomical Union*, vol. 115, pp. 1–18, 1987, https://doi.org/10.1017/S0074180900094766

16. T. P. Robitaille, "A modular set of synthetic spectral energy distributions for young stellar objects," *Astronomy & Astrophysics*, vol. 600, p. A11, Mar. 2017, https://doi.org/10.1051/0004-6361/201425486

17. S. Bontemps *et al.*, "The*Herschel*first look at protostars in the Aquila rift," *Astronomy and Astrophysics*, vol. 518, pp. L85–L85, Jul. 2010, doi: https://doi.org/10.1051/0004-6361/201014661.

18. "VizieR," *Unistra.fr*, 2021. https://vizier.cds.unistra.fr/viz-bin/VizieR-3?-source=II/368&-out.max=50&-out.form=HTML%20Table&-out.add=_ut.add=_RAJ (accessed May 06, 2026).

19. "VizieR," *Unistra.fr*, 2017. https://vizier.cds.unistra.fr/viz-bin/VizieR-3?-source=VIII/106/hppsc070&-out.max=50&-out.form=HTML%20Table&-out.add=_r&-out.add=_RAJ (accessed May 06, 2026).

20. J. Sun *et al.*, "Deep near-infrared survey towards the W40 and Serpens South region in the Aquila Rift: A comprehensive catalogue of young stellar objects," *Monthly Notices of the Royal Astronomical Society*, vol. 516, no. 4, pp. 5244–5257, Sep. 2022, doi: https://doi.org/10.1093/mnras/stac2191

21. F. Jansen *et al.*, "XMM-Newton observatory," *Astronomy & Astrophysics*, vol. 365, no. 1, pp. L1–L6, Jan. 2001, doi: https://doi.org/10.1051/0004-6361:20000036

22. T. M. Dame, D. Hartmann and P. Thaddeus, "The Milky Way in Molecular Clouds: A New Complete CO Survey," *The Astrophysical Journal*, vol. 547, no. 2, pp. 792–813, Feb. 2001, doi: https://doi.org/10.1086/318388

23. L. Prato, E. L. Rice and V. M. Dame, "Where are all the Young Stars in Aquila?," arXiv e-prints, p. arXiv:0811.2842

24. S. Dzib, L. Loinard, A. J. Mioduszewski, A. F. Boden, L. F. Rodríguez and R. M. Torres, "Vlba determination of the distance to nearby star-forming regions. iv. a preliminary distance to the proto-herbig aebe star ec 95 in the serpens core," *The Astrophysical Journal*, vol. 718, no. 2, pp. 610–619, Jul. 2010, https://doi.org/10.1088/0004-637x/718/2/610

25. G. N. Ortiz-León *et al.*, "The Gould's Belt Distances Survey (GOBELINS). V. Distances and Kinematics of the Perseus Molecular Cloud," vol. 865, no. 1, pp. 73–73, Aug. 2018, https://doi.org/10.3847/1538-4357/aada49

26. V. Straižys, K. Černis and S. Bartašiūtė, "Interstellar extinction in the area of the Serpens Cauda molecular cloud," *Open Astronomy*, vol. 5, no. 1, Jan. 1996, https://doi.org/10.1515/astro-1996-0106

27. J. Knude and C. Fabricius, "Luminosity and Intrinsic Color Calibration of Main-Sequence Stars With 2Mass Photometry: All Sky Local Extinction," *Open Astronomy*, vol. 12, no. 4, Dec. 2003, https://doi.org/10.1515/astro-2017-0073

28. A. Men'shchikov *et al.*, "Filamentary structures and compact objects in the Aquila and Polaris clouds observed by*Herschel,*" vol. 518, pp. L103–L103, Jul. 2010, doi: https://doi.org/10.1051/0004-6361/201014668.

29. J. Smith, A. Bentley, M. Castelaz, R. D. Gehrz, G. L. Grasdalen and J. A. Hackwell, "Infrared sources and excitation of the W40 complex," *The Astrophysical Journal*, vol. 291, p. 571, Apr. 1985, https://doi.org/10.1086/163097

30. J. P. Vallee, "Behind the H II region Sharpless 217 - The envelope of the diffuse molecular cloud at G159.1 + 3.3," *The Astronomical Journal*, vol. 94, p. 679, Sep. 1987, https://doi.org/10.1086/114505

31. Vallee, J. P., Guilloteau, S. and MacLeod, J. M., "The edge of a molecular cloud : obseravtions of millimetric 13CO and C18O transitions in W 40.", Astronomy and Astrophysics, vol. 266, EDP, pp. 520–531, 1992.

32. M. A. Kuhn, E. D. Feigelson, B. Reipurth, S. A. Rodney and G. P. Garmire, "A*chandra*observation of the obscured star-forming complex W40," *The Astrophysical journal*, vol. 725, no. 2, pp. 2485–2506, Dec. 2010, https://doi.org/10.1088/0004-637x/725/2/2485

33. G. N. Ortiz-León *et al.*, "The gould's belt distances survey (gobelins). iii. the distance to the serpens/aquila molecular complex," *The Astrophysical Journal*, vol. 834, no. 2, pp. 143–143, Jan. 2017, doi: https://doi.org/10.3847/1538-4357/834/2/143

34. Y. Su *et al.*, "Local Molecular Gas toward the Aquila Rift Region," *The Astrophysical Journal*, vol. 893, no. 2, p. 91, Apr. 2020, https://doi.org/10.3847/1538-4357/ab7fff

35. F. Nakamura, K. Dobashi, T. Shimoikura, T. Tanaka and T. Onishi, "Wide-field ^{12}CO ( ) and ^{13}CO ( ) Observations toward the Aquila Rift and Serpens Molecular Cloud Complexes. I. Molecular Clouds and Their Physical Properties," *The Astrophysical Journal*, vol. 837, no. 2, p. 154, Mar. 2017, https://doi.org/10.3847/1538-4357/aa5ea6

36. Ph. André *et al.*, "From filamentary clouds to prestellar cores to the stellar IMF: Initial highlights from the*Herschel*Gould Belt Survey," *Astronomy and Astrophysics*, vol. 518, p. L102, Jul. 2010, https://doi.org/10.1051/0004-6361/201014666

37. "SIMBAD Astronomical Database - CDS (Strasbourg)," *simbad.cds.unistra.fr*. https://simbad.cds.unistra.fr/simbad/

38. R. M. Cutri et al., "2MASS All Sky Catalog of Point Sources," NASA/IPAC Infrared Science Archive, 2003. Available: http://irsa.ipac.caltech.edu/applications/Gator/

39. S. T. Megeath *et al.*, "The *spitzer space telescope*survey of the orion a and b molecular clouds. II. The spatial distribution and demographics of dusty young stellar objects," *The Astronomical Journal*, vol. 151, no. 1, p. 5, Dec. 2015, https://doi.org/10.3847/0004-6256/151/1/5

40. M. M. Dunham *et al.*, "Young stellar objects in the gould belt," *The Astrophysical Journal Supplement Series*, vol. 220, no. 1, p. 11, Sep. 2015, https://doi.org/10.1088/0067-0049/220/1/11

41. N. J. Evans II *et al.*, "The Spitzer c2d Legacy Results: Star-Formation Rates and Efficiencies; Evolution and Lifetimes," *The Astrophysical Journal Supplement Series*, vol. 181, pp. 321–350, Apr. 2009, https://doi.org/10.1088/0067-0049/181/2/321

42. W. M. Smart, "Textbook on Spherical Astronomy," 6th ed., Cambridge University Press, 1977, https://doi.org/10.1017/CBO9780511628791

43. E. D. Feigelson and L. Sivakumar, "Modern Statistical Methods for Astronomy," Jul. 2012, https://doi.org/10.1017/cbo9781139015653

44. B. Efron, "Bootstrap Methods: Another Look at the Jackknife," *The Annals of Statistics*, vol. 7, no. 1, pp. 1–26, Jan. 1979, doi: https://doi.org/10.1214/aos/1176344552

45. B. W. Silverman, *Density Estimation for Statistics and Data Analysis*. Boston, MA: Springer US, 1986. https://doi.org/10.1007/978-1-4899-3324-9

46. V. Könyves *et al.*, "A census of dense cores in the Aquila cloud complex: SPIRE/PACS observations from theHerschelGould Belt survey," *Astronomy & Astrophysics*, vol. 584, p. A91, Nov. 2015, https://doi.org/10.1051/0004-6361/201525861

47. D. Arzoumanian *et al.*, "Characterizing interstellar filaments with*Herschel*in IC 5146," *Astronomy and Astrophysics*, vol. 529, pp. L6–L6, May 2011, doi: https://doi.org/10.1051/0004-6361/201116596

48. H. Kirk, P. C. Myers, T. L. Bourke, R. A. Gutermuth, A. Hedden and G. W. Wilson, "Filamentary accretion flows in the embedded serpens south protocluster," *The Astrophysical Journal*, vol. 766, no. 2, pp. 115–115, Mar. 2013, doi: https://doi.org/10.1088/0004-637x/766/2/115

49. P. André et al., "From filamentary networks to dense cores in molecular clouds: Toward a new paradigm for star formation," in Protostars and Planets VI, H. Beuther et al., Eds., University of Arizona Press, Tucson, 2014, pp. 27–51.

50. R. B. Larson, "Cloud fragmentation and stellar masses," *Monthly Notices of the Royal Astronomical Society*, vol. 214, no. 3, pp. 379–398, Jun. 1985, https://doi.org/10.1093/mnras/214.3.379

51. K. V. Getman *et al.*, "Star Formation In Nearby Clouds (SFiNCs): X-Ray and Infrared Source Catalogs and Membership," *The Astrophysical Journal Supplement Series*, vol. 229, no. 2, pp. 28–28, Mar. 2017, https://doi.org/10.3847/1538-4365/229/2/28

52. E. Winston, S. J. Wolk, R. Gutermuth and T. L. Bourke, "Chandra Detection of an Evolved Population of Young Stars in Serpens South," *The Astronomical Journal*, vol. 155, no. 6, p. 241, May 2018, doi: https://doi.org/10.3847/1538-3881/aabe82

53. G. N. Ortiz-León *et al.*, "The gould's belt very large array survey. ii. the serpens region," *The Astrophysical Journal*, vol. 805, no. 1, p. 9, May 2015, https://doi.org/10.1088/0004-637x/805/1/9

54. C. P. Gutiérrez *et al.*, "Supernova 2010ev: A reddened high velocity gradient type Ia supernova," *Astronomy & Astrophysics*, vol. 590, p. A5, Apr. 2016, https://doi.org/10.1051/0004-6361/201527228

55. J. S. Urquhart *et al.*, "The Red MSX Source survey: distribution and properties of a sample of massive young stars," *Monthly Notices of the Royal Astronomical Society*, vol. 410, no. 2, pp. 1237–1250, Sep. 2010, https://doi.org/10.1111/j.1365-2966.2010.17514.x

56. S. J. Wolk *et al.*, "YSOVAR: Mid-infrared Variability among YSOs in the Star Formation Region Serpens South," *The Astronomical Journal*, vol. 155, no. 2, p. 99, Feb. 2018, https://doi.org/10.3847/1538-3881/aaa6c4

57. C. Ricci *et al.*, "BASS XXXVII: The Role of Radiative Feedback in the Growth and Obscuration Properties of Nearby Supermassive Black Holes," *The Astrophysical Journal*, vol. 938, no. 1, pp. 67–67, Oct. 2022, https://doi.org/10.3847/1538-4357/ac8e67

58. M. Zhang *et al.*, "A deep near-infrared survey toward the aquila molecular cloud. i. molecular hydrogen outflows," *The Astrophysical Journal Supplement Series*, vol. 219, no. 2, p. 21, Aug. 2015, https://doi.org/10.1088/0067-0049/219/2/21

59. W. Park *et al.*, "Quantifying Variability of Young Stellar Objects in the Mid-infrared Over 6 Years with the Near-Earth Object Wide-field Infrared Survey Explorer," *The Astrophysical Journal*, vol. 920, no. 2, p. 132, Oct. 2021, https://doi.org/10.3847/1538-4357/ac1745

60. M. S. Povich *et al.*, "THE MYStIX INFRARED-EXCESS SOURCE CATALOG," *The Astrophysical Journal Supplement Series*, vol. 209, no. 2, pp. 31–31, Nov. 2013, https://doi.org/10.1088/0067-0049/209/2/31

61. M. Juvela and D. Tharakkal, "Fast fitting of spectral lines with Gaussian and hyperfine structure models," *Astronomy & Astrophysics*, vol. 685, p. A164, May 2024, https://doi.org/10.1051/0004-6361/202349044

62. A. Pietarila and J. W. Harvey, "Ca II 854.2 nm BISECTORS AND CIRCUMFACULAR REGIONS," *The Astrophysical Journal*, vol. 764, no. 2, p. 153, Feb. 2013, https://doi.org/10.1088/0004-637x/764/2/153

63. K. Tursun *et al.*, "Ammonia observations towards the Aquila Rift cloud complex," *Astronomy & Astrophysics*, vol. 643, p. A178, Nov. 2020, https://doi.org/10.1051/0004-6361/202037659

64. T. Komesh *et al.*, "Studies of the distinct regions due to CO selective dissociation in the Aquila molecular cloud," *Astronomy & Astrophysics*, vol. 644, p. A46, Dec. 2020, https://doi.org/10.1051/0004-6361/202038632

65. T. Komesh *et al.*, "H_2CO and H110α Observations toward the Aquila Molecular Cloud," *The Astrophysical Journal*, vol. 874, no. 2, p. 172, Apr. 2019, https://doi.org/10.3847/1538-4357/ab0ae3

66. T. Komesh *et al.*, "ALMA observations of the environments of G333.0162+00.7615," *Proceedings of the International Astronomical Union*, vol. 17, no. S373, pp. 35–38, Aug. 2021, https://doi.org/10.1017/s1743921323000121

67. A. A. Abdirakhman, A. Zh. Omar, N. Sh. Alimgazinova, D. R. Tuiakbayeva and D. Y. Baitursyn, "Identification of complex organic molecules in the hot molecular core G335.79+0.17," *Eurasian Physical Technical Journal*, vol. 23, no. 1 (55), pp. 130–137, Mar. 2026, https://doi.org/10.31489/2025n2/130-137

68. A. Abdirakhman *et al.*, "Kinematics and structure of the massive star-forming region G350.29+0.12," *Herald of the Kazakh-British Technical University*, vol. 23, no. 1, pp. 334–345, Mar. 2026, https://doi.org/10.55452/1998-6688-2026-23-1-334-345

69. Zh. Assembay *et al.*, "ALMA observations of the environments of G301.1364-00.2249A," *Proceedings of the International Astronomical Union*, vol. 18, no. S380, pp. 204–206, Dec. 2022, https://doi.org/10.1017/s1743921323002624

70. A. Omar *et al.*, "ALMA Observations of G333.6-0.2: Molecular and Ionized Gas Environment," *Galaxies*, vol. 13, no. 4, p. 73, Jun. 2025, https://doi.org/10.3390/galaxies13040073

71. S. Casanova, T. Montmerle, E. D. Feigelson and P. André, "ROSAT X-ray sources in the ρ Ophiuchi cloud core," The Astrophysical Journal, vol. 439, p. 752, 1995, https://doi.org/10.1086/175211.

72. T. Preibisch *et al.*, "The Origin of T Tauri X-Ray Emission: New Insights from the *Chandra* Orion Ultradeep Project," *The Astrophysical Journal Supplement Series*, vol. 160, no. 2, pp. 401–422, Oct. 2005, https://doi.org/10.1086/432891

73. E. D. Feigelson and T. Montmerle, "High-Energy Processes in Young Stellar Objects," *Annual Review of Astronomy and Astrophysics*, vol. 37, no. 1, pp. 363–408, Sep. 1999, https://doi.org/10.1146/annurev.astro.37.1.363

74. J. Schaye and C. Dalla Vecchia, "On the relation between the Schmidt and Kennicutt-Schmidt star formation laws and its implications for numerical simulations," *Monthly Notices of the Royal Astronomical Society*, vol. 383, no. 3, pp. 1210–1222, Dec. 2007, https://doi.org/10.1111/j.1365-2966.2007.12639.x

75. K. V. Getman, E. D. Feigelson, L. Townsley, J. Bally, C. J. Lada and B. Reipurth, "*Chandra*Study of Young Stellar Objects in the NGC 1333 Star-forming Cloud," *The Astrophysical Journal*, vol. 575, no. 1, pp. 354–377, Aug. 2002, https://doi.org/10.1086/341219

76. J. Sun, R. A. Gutermuth, H. Wang, S. Zhang and M. Long, "Hierarchical structure of YSO clusters in the W40 and Serpens South region: group extraction and comparison with fractal clusters," *Monthly Notices of the Royal Astronomical Society*, vol. 516, no. 4, pp. 5258–5269, Sep. 2022, https://doi.org/10.1093/mnras/stac2362

77. Plunkett, S., Arce, H. G., Corder, S. A., Dunham, M. M., Garay, G., Mardones, D., & Bourke, T. L., The distribution of protostars in the Serpens South filamentary cluster. *Astronomy & Astrophysics*, 615, A9., 2018, https://doi.org/10.1051/0004-6361/201731945

78. Marton, G., Tóth, L. V., Zahorecz, S., & Molinari, S., The Herschel/PACS Point Source Catalogue. *Astronomy & Astrophysics,* 688, A203.,2024, https://doi.org/10.1051/0004-6361/202349044

79. van der Marel, N., Verhaar, B. W., van Terwisga, S., Merín, B., Herczeg, G. J., van Dishoeck, E. F., & Bouwman, J., A survey of transition disks in nearby star-forming regions. *Astronomy & Astrophysics,* 592, A126. 2016, https://doi.org/10.1051/0004-6361/201628073

80. Anderson, B., Dunham, M. M., Arce, H. G., Plunkett, S., & Mardones, D., ALMA observations of CO emission toward young stellar objects in the Serpens region. The Astrophysical Journal, 938, 55. 2022, https://doi.org/10.3847/1538-4357/ac8c2f

Information about the authors:

Alimgazinova Nazgul – Candidate of Physical and Mathematical Sciences, Associate Professor, Department of Electronics and Astrophysics, Farabi University (Almaty, Kazakhstan, e-mail: nazgul.alimgazinova@kaznu.edu.kz).

Manapbayeva Arailym – PhD, Senior Lecturer, Department of Physics, Kazakh National Women's Teacher Training University (Almaty, Kazakhstan, e-mail: manapbayeva.arailym@gmail.com).

Omar Aruzhan (corresponding author) – PhD, Associate Professor-Researcher, Department of Electronics and Astrophysics, Farabi University (Almaty, Kazakhstan, e-mail: omar.aruzhan@kaznu.kz).

Turekhanova Kunduz – Candidate of Physical and Mathematical Sciences, Associate Professor-Researcher, Department of Plasma Physics, Nanotechnology and Computer Physics, Farabi University (Almaty, Kazakhstan, e-mail: kunduz@physics.kz).

Abildayev Nurlan – student, Department of Mathematics, Farabi University (Almaty, Kazakhstan, e-mail: nurlanabildaev833@gmail.com).

Demessinova Aizat – PhD, Senior Lecturer, Department of Electronics and Astrophysics, Farabi University (Almaty, Kazakhstan, e-mail: aizat.dem@gmail.com).

Alibek Akmaral – Senior Lecturer, Department of Physics, Kazakh National Women's Teacher Training University (Almaty, Kazakhstan, e-mail: alibek.akmaral@list.ru).

Shaimoldin Nurzhan – PhD student, State Key Laboratory of Radio Astronomy and Technology, Xinjiang Astronomical Observatory (Urumqi, China, e-mail: nurzhan@xao.ac.cn).

APPENDIX A
Complete list of anomalous sources.

Table A1. Candidate YSOs with anomalous color indices.

AllWISE ID	RA (deg)	Dec (deg)	W1, mag	W2, mag	W3, mag	W1−W2, mag	W2−W3, mag	YSO
J183003.51−015647.0	18.500978	−1.946338	12.561	9.569	11.027	2.992	−1.458	Protostar
J183010.76−015813.1	18.502991	−1.970293	11.385	10.394	10.632	0.991	−0.238	Class III
J182936.66−015548.3	18.493519	−1.930082	13.666	13.692	10.151	−0.026	3.541	Class III

APPENDIX B
Cross-identification with the infrared catalog.

Cross-identification with the infrared catalog previously reported in [20] was performed to independently verify our classification and assess the novelty of the obtained sample. The authors of [20] carried out deep near-infrared (NIR) mapping of the W40–Serpens South region using the CFHT (Canada–France–Hawaii Telescope) and combined these observations with data from the 2MASS, UKIDSS and *Spitzer* surveys. As a result, they produced a cleaned point-source catalog containing 901,910 reliable objects after applying strict artifact rejection procedures, including the removal of halos, false detections and lateral stripes. From this catalog, a sample of 832 verified young stellar objects (YSOs) of different evolutionary classes was identified.

It is important to emphasize that the data presented in [20] were obtained using an independent approach based on deep NIR and *Spitzer* observations and do not include WISE photometry, which forms the basis of our classification scheme. This makes the cross-comparison particularly valuable for an objective assessment of the reliability of our sample.

For each of the 145 YSO candidates identified in this work, we searched for positional counterparts in the catalog reported in [20]. A matching radius of 2″ was adopted, corresponding to the typical astrometric accuracy of the surveys considered. For every source in our sample, the angular distances to all objects in the comparison catalog were calculated and the closest source within the adopted radius was considered a counterpart.

The cross-identification with the full catalog of 901 910 sources demonstrated a high degree of positional agreement. Detailed statistics for the different object classes are presented in Table B1.

Table B1. Results of the cross-identification of YSO candidates with the full catalog.

YSO Class	Total Number of Objects Identified in This Study	Found in the Catalog of [20]	Agreement (%)
Class I	37	31	83.8
Class II	48	47	97.9
Class III	47	46	97.9
Transition Disk	12	12	100.0
Protostars	1	1	100.0
Total	145	137	94.5

n average, 94.5% of our candidates have positional counterparts in the independent deep NIR catalog previously reported in [20]. This strongly demonstrates that our sample consists of real astrophysical sources rather than artifacts or noise associated with WISE data processing. The highest matching completeness is achieved for the more evolved classes (Class II, Class III and Transition Disk), which is expected because these objects are brighter in the near-infrared wavelength range forming the basis of the catalog presented in [20].

Among the eight YSO candidates in our sample (5.5% of the total 145 sources) that were not found in the cleaned catalog of [20], seven objects possess independent confirmations in other astrophysical databases and published studies, indicating their genuine astrophysical nature despite the absence of cross-identification with the catalog of [20]. In particular, several objects have independent cross-identifications confirming their nature: J183000.62−020208.8 (Class I) is classified as a “confirmed Young Stellar Object” based on the 2MASS survey [39]; J183002.38−020356.9 (Class I) is identified as a “confirmed millimetric source (protostar)” [56]; the objects J183000.27−020356.1, J182952.35−015745.9 (Class I) and J183010.50−020307.6 (Class II) are confirmed as “Young Stellar Objects” in *Spitzer* surveys, whereas J183005.37−020746.5 (Class I) and J183008.32−015705.7 (Class III) are classified as “Young Stellar Object candidates” based on the same data [54]. All of these sources therefore possess independent cross-identifications in published catalogs, confirming their astrophysical reality.

The only object that was not found either in the catalog of [20] or in any other available published studies is WISE J183000.32−020616.0 (Class I) with coordinates $\alpha(J2000) = 18^h30^m00.316^s$ and $\delta(J2000) = -02°06'16.04''$. Since it has not previously been reported either as a confirmed YSO or as a YSO candidate, we classify it as a new Class I young stellar object candidate, corresponding to the most deeply embedded and earliest evolutionary stage of star formation. This makes the source particularly valuable for future spectroscopic and multiwavelength investigations. Thus, our study not only confirms the existence of previously known sources omitted from the catalog of [20], but also reveals one genuinely new candidate, highlighting the advantage of the WISE-based classification method for identifying highly obscured protostellar objects.

For additional verification, we compared the 2MASS photometry of our objects with the measurements reported in the catalog of [20]. A match was considered confirmed when the photometric difference satisfied $\Delta m \leq 0.05$ mag in all three bands (J, H and K). The adopted threshold corresponds to a flux ratio of $F_1/F_2 \approx 0.955$ (a relative difference of 4.5%) and exceeds the typical photometric uncertainties ($\sigma \approx 0.01$–0.03 mag) by a factor of 2–5, corresponding to a significance level of approximately 1.7–5σ [39, 24]. Overall, 74.5% (102 out of 137) of the positionally matched sources passed the photometric consistency test. A clear dependence on evolutionary class is observed, ranging from 32.3% for heavily embedded Class I objects to 100% for Transition Disk sources with optically thin disks, further supporting the reliability of our classification scheme.

Table B2. 2MASS photometric confirmation for matched objects.

YSO Class	Found in the Full Catalog of [20]	Good 2MASS Agreement	Fraction (%)
Class I	31	10	32.3
Class II	47	38	80.9
Class III	46	42	91.3
Transition Disk	12	12	100.0
Protostars	1	0	0
Total	137	102	74.5

A key result of our study is the comparison with the sample of 832 YSOs previously reported in [20]. As shown in Table B3, 124 out of 145 of our candidates (85.5%) are not included in their final YSO list.

The results are particularly significant for the later evolutionary classes: 97.9% of the Class III objects and 100% of the Transition Disk sources were not classified as YSOs in the study of [20]. At the same time, it should be emphasized that, despite the absence of identification in that work, a substantial fraction of these sources has been independently detected and classified as young stellar objects in other catalogs and studies of the Serpens South region based on X-ray, infrared and submillimeter observations.

Table B3. Comparison of our sample with the verified YSOs of [20].

YSO Class	Total Number of Objects Identified in This Study	Found in the YSO Sample	Unmatched Objects	Fraction of Unmatched Objects (%)
Class I	37	14	23	62.2
Class II	48	5	43	89.6
Class III	47	1	46	97.9
Transition Disk	12	0	12	100.0
Protostars	1	1	0	0
Total	145	21	124	85.5

APPENDIX C

Table C1. Identified YSOs in the Serpens south region.

AllWISE	RA(J2000), deg	DE(J2000), deg	W1, mag	W2, mag	W3, mag	W4, mag	Observations	Reference	Catalog class
J183015.69-020720.5	277.57	-02.12	13.589	12.040	11.091	4.335	Sub-mm; IR	[53]; [58]; [20]	Protostar; YSO
J183001.27-020148.3	277.51	-02.03	10.375	7.075	5.058	1.815	IR; Sub-mm; X-ray	[80]; [58]; [79]; [20]	
J183004.44-020138.4	277.52	-02.03	9.948	8.293	5.261	2.294	IR; X-ray	[80]; [78]; [58]; [20]	
J183000.61-020208.8	277.50	-02.04	11.289	9.346	7.179	3.195	IR	[39]; [58]	YSO
J182959.03-020157.4	277.50	-02.03	12.950	11.243	8.517	5.898	IR; X-ray	[80]; [78]; [58]; [20]	Protostar; YSO
J183002.46-020258.0	277.51	-02.05	8.532	6.383	4.366	1.443		[58]; [20]	
J183000.24-020052.5	277.50	-02.02	14.877	12.286	10.184	5.866	Sub-mm; X-ray; IR	[54]; [58];[20]	YSO
J182957.46-020240.3	277.49	-02.05	14.917	13.639	10.750	8.562	X-ray; IR	[78]; [58];	
J183000.11-020026.3	277.50	-02.00	14.378	13.036	9.908	6.905	IR	[58]	YSO Cand.
J182957.05-020246.8	277.49	-02.05	15.950	14.045	10.725	8.764			YSO
J183001.30-020343.2	277.51	-02.06	8.089	5.922	3.146	0.758	IR; Sub-mm; X-ray	[60]; [54]; [58]; [64]; [20]	Protostar; YSO
J183000.26-020015.5	277.50	-02.00	14.143	12.175	10.081	6.977	IR; X-ray	[58]; [20]	YSO
J183002.37-020356.9	277.51	-02.07	14.195	11.944	9.427	3.921	IR; Radio	[77]; [40]	Protostar; Millimetric Radio Source
J183000.27-020356.1	277.50	-02.07	14.471	12.295	9.280	4.061	IR	[54] ; [58]	YSO
J183006.29-015941.1	277.53	-01.99	14.300	13.060	10.719	8.106	X-ray	[78]; [58]	
J183002.64-020426.4	277.51	-02.07	15.820	13.192	10.833	8.433	IR; X-ray	[58]	?
J183001.72-015907.7	277.51	-01.99	15.037	13.515	10.848	8.200	X-ray		
J183014.20-020420.4	277.56	-02.07	15.785	14.098	10.646	7.930	IR	[58]	YSO
J183010.09-020537.4	277.54	-02.09	15.286	13.434	10.460	7.760	X-ray		?
J182954.36-015823.5	277.48	-01.97	14.580	11.806	9.785	6.930	IR; X-ray	[58]; [20]	YSO

Continuation of the table

AllWISE	RA(J2000), deg	DE(J2000), deg	W1, mag	W2, mag	W3, mag	W4, mag	Observations	Reference	Catalog class
J183001.09-020608.9	277.50	-02.10	11.143	9.365	7.217	3.304	IR; Sub-mm; X-ray	[40]; [58];[20]	Protostar; YSO
J183017.43-015948.2	277.57	-01.99	15.352	14.567	10.962	8.218	X-ray	[58]	?
J182953.81-015748.3	277.47	-01.96	11.899	10.078	8.023	5.580	IR	[20]	YSO
J183000.08-015715.7	277.50	-01.95	12.301	10.519	7.818	5.033	IR; Sub-mm; X-ray	[78]; [20] [54]; [58]	Protostar; YSO
J183009.87-020633.7	277.54	-02.11	14.770	13.844	10.656	8.055	X-ray	[78]; [58]	YSO
J182952.34-015745.9	277.47	-01.96	16.256	12.537	10.286	6.066	IR; X-ray	[54]; [58]; [20]	
J182953.87-015727.9	277.47	-01.96	13.774	12.409	10.143	7.295	IR	[54]; [58]	
J183021.54-020412.7	277.59	-02.07	13.871	12.588	10.299	7.317	X-ray		?
J183005.37-020746.5	277.52	-02.13	14.724	12.447	10.296	8.378	IR		YSO Cand.
J183025.45-020423.9	277.61	-02.07	14.382	12.805	9.317	6.774	X-ray		?
J183003.14-020514.8	277.51	-02.09	11.421	10.472	9.147	6.491	Sub-mm; X-ray	[78]; [58]; [20]	YSO
J182943.00-020317.1	277.43	-02.05	10.437	9.496	8.206	6.984	IR; X-ray	[58]; [20]	
J183002.99-020717.9	277.51	-02.12	12.770	11.892	10.701	8.453	X-ray	[78]; [58]	
J182956.75-020233.1	277.49	-02.04	14.467	13.761	10.771	8.743	X-ray; IR	[53]; [58]	
J182959.07-020030.0	277.49	-02.00	12.929	11.918	9.345	6.760			
J183005.93-020017.3	277.52	-02.00	13.232	12.192	10.190	7.759	IR	[58]	
J183008.06-020018.1	277.53	-02.01	14.104	13.443	10.686	8.348	X-ray; IR	[53]; [58]	
J183008.55-020023.0	277.54	-02.01	13.384	12.631	10.704	8.182			
J183010.56-020305.3	277.54	-02.05	13.375	12.560	10.909	7.628	IR	[54]; [58]	
J183009.16-020007.3	277.54	-02.00	12.133	11.454	10.411	8.370	X-ray; IR	[53]; [58]	YSO Cand.
J182953.54-020059.4	277.47	-02.02	13.888	13.389	10.565	7.932			
J183008.57-015936.6	277.54	-01.99	12.459	11.927	10.530	8.557			
J182956.68-020419.6	277.49	-02.07	10.864	10.510	9.328	7.298			

Continuation of the table

AllWISE	RA(J2000), deg	DE(J2000), deg	W1, mag	W2, mag	W3, mag	W4, mag	Observations	Reference	Catalog class
J183007.22-015919.7	277.53	-01.99	10.218	9.429	8.160	6.107	IR; Sub-mm; X-ray	[53]; [54]; [58]; [20]	YSO
J182958.90-020458.0	277.49	-02.08	13.253	12.613	10.971	8.394	X-ray; IR	[53]; [58]	
J182952.80-015939.9	277.47	-01.99	13.838	12.863	10.823	7.679	X-ray	[53]	?
J183014.03-020438.8	277.56	-02.08	13.079	12.765	10.801	8.393			
J183020.13-020149.5	277.58	-02.03	11.345	10.970	8.518	6.011			
J183003.55-020617.4	277.51	-02.10	12.547	11.548	9.998	7.393			
J182944.88-020156.5	277.44	-02.03	13.051	12.524	10.838	8.443			
J183019.50-015951.6	277.58	-01.99	14.563	13.898	10.630	8.018			
J183006.87-015722.6	277.53	-01.96	11.791	11.478	9.940	7.702	IR	[58]	YSO Cand.
J182946.36-015941.5	277.44	-01.99	13.157	12.700	10.395	8.199	X-ray	[53]	?
J183019.97-015948.9	277.58	-01.99	13.703	13.104	10.179	7.520			
J183021.51-020356.8	277.59	-02.07	13.477	12.770	10.237	8.003			
J182954.05-015714.8	277.48	-01.95	14.128	13.149	10.364	8.240	X-ray; IR	[53]; [58]	YSO
J183021.76-020417.7	277.59	-02.07	13.099	12.107	10.290	7.331	X-ray	[53]	?
J183020.65-020450.8	277.59	-02.08	13.062	12.292	10.135	7.716			
J183006.93-015631.7	277.53	-01.94	11.967	11.354	9.553	7.236	X-ray; IR	[53]; [54]; [20]	YSO
J183021.58-020501.1	277.59	-02.08	13.585	13.026	10.159	7.563	X-ray	[53]	?
J183016.98-020621.4	277.57	-02.11	11.718	11.183	9.272	6.180	X-ray; IR	[53]; [58]	YSO
J183006.79-020736.6	277.53	-02.13	13.919	12.748	10.555	8.412	IR	[58]	
J182939.61-020241.7	277.42	-02.04	11.620	10.975	9.055	6.534	X-ray; IR; Sub-mm	[53]; [78]; [54]; [79]; [20]	Disk; YSO
J182952.69-015639.0	277.47	-01.94	13.396	12.734	10.368	8.168	X-ray; IR	[53]; [58]	YSO Cand.
J183026.76-020143.5	277.61	-02.03	11.274	10.963	9.213	6.762	X-ray	[53]	?

Continuation of the table

AllWISE	RA(J2000), deg	DE(J2000), deg	W1, mag	W2, mag	W3, mag	W4, mag	Observations	Reference	Catalog class
J183007.39-020753.3	277.53	-02.13	14.040	12.919	10.615	8.226	X-ray; IR	[53]; [58]	YSO Cand.
J182958.68-015600.9	277.49	-01.93	13.942	12.983	10.914	8.695			
J182959.28-015552.0	277.49	-01.93	13.921	13.033	10.488	8.525			YSO
J183007.11-020816.9	277.53	-02.14	13.597	12.629	10.155	8.200	IR	[58]	
J183022.78-020616.9	277.59	-02.10	13.652	13.112	10.930	8.402	X-ray	[53]	?
J183001.60-015519.3	277.51	-01.92	13.365	13.003	10.978	8.881	X-ray; IR	[53]; [58]	YSO
J182936.98-020325.6	277.40	-02.06	10.914	10.270	9.049	6.735		[53]; [54]; [20]	
J182953.74-020819.0	277.47	-02.14	13.017	12.420	10.336	7.944	X-ray	[53]	?
J182957.56-015520.6	277.49	-01.92	13.257	12.489	10.540	8.459	X-ray; IR	[53]; [58]	YSO
J182943.12-020638.7	277.43	-02.11	11.975	11.668	10.340	7.200	X-ray	[53]	?
J183024.31-020623.0	277.60	-02.11	13.527	12.812	9.701	6.960	X-ray; IR	[53]; [58];[20]	YSO
J182944.56-015644.5	277.44	-01.95	13.267	12.650	9.380	5.291	X-ray	[53]	?
J183008.55-020619.0	277.54	-02.11	11.278	10.838	9.815	7.433	X-ray; IR	[53]; [58]	YSO Cand.
J182954.67-020410.4	277.48	-02.07	10.404	9.918	9.638	7.730			
J183016.81-020017.0	277.57	-02.00	11.484	10.977	10.411	8.018	X-ray	[53];	?
J182944.37-020035.0	277.44	-02.01	11.026	10.669	10.350	8.014			
J182941.61-020041.4	277.42	-02.01	11.074	10.918	9.950	7.120			
J182939.79-020302.3	277.42	-02.05	12.242	11.939	10.793	8.499		[53]; [54];	YSO
J182945.16-020612.8	277.44	-02.10	10.709	10.423	9.494	7.286		[53];	?
J182951.06-020722.0	277.46	-02.12	11.704	11.110	10.625	8.435			
J183001.34-015547.7	277.51	-01.93	11.606	11.281	10.506	8.558	X-ray; IR	[53]; [58]	YSO Cand.
J183005.22-015544.5	277.52	-01.93	11.982	11.754	10.765	8.588			
J183008.79-020804.0	277.54	-02.13	10.676	10.368	9.431	6.968			
J183028.69-020253.0	277.62	-02.05	10.583	10.335	9.307	7.340	X-ray	[53];	?
J183029.70-020318.2	277.62	-02.06	10.981	10.801	10.096	7.660			

Continuation of the table

AllWISE	RA(J2000), deg	DE(J2000), deg	W1, mag	W2, mag	W3, mag	W4, mag	Observations	Reference	Catalog class
J182958.86-020245.7	277.49	-02.05	11.345	11.257	10.884	8.593	X-ray; IR	[53]; [58]	YSO
J183005.54-020307.6	277.52	-02.05	12.113	11.999	10.843	7.156	IR	[58]	
J183007.17-020301.0	277.53	-02.05	8.330	7.779	7.721	6.854	X-ray; IR	[53]; [58]	YSO Cand.
J183008.43-020306.4	277.54	-02.05	8.797	8.096	7.927	7.472			
J182956.36-020338.9	277.48	-02.06	13.965	13.894	9.588	7.204			YSO
J183007.35-020415.5	277.53	-02.07	13.999	13.811	9.969	7.434			
J182955.61-020346.3	277.48	-02.06	14.197	14.113	10.491	8.283			YSO Cand.
J182952.99-020101.5	277.47	-02.02	13.744	13.430	10.197	7.531			
J183013.86-020108.1	277.56	-02.02	13.689	13.218	10.069	7.279			
J183009.86-020420.8	277.54	-02.07	9.687	8.942	8.599	7.652			
J183015.01-020143.2	277.56	-02.03	13.576	13.531	9.245	7.005	X-ray	[53]	?
J183015.34-020222.9	277.56	-02.04	13.723	13.464	10.884	8.141			
J183015.01-020306.9	277.56	-02.05	13.493	13.322	9.908	7.343			
J183009.14-020508.2	277.54	-02.09	13.692	13.190	9.278	7.014			
J183016.08-020322.6	277.57	-02.06	13.891	13.506	10.360	7.336			
J183017.68-020221.7	277.57	-02.04	13.901	13.592	10.409	8.233			
J183001.97-020557.8	277.51	-02.10	11.367	11.243	10.706	5.584			
J183004.89-015740.4	277.52	-01.96	13.872	13.427	10.171	8.206	X-ray; IR	[53]; [58]	YSO Cand.
J183016.42-015904.1	277.57	-01.98	14.044	13.577	10.242	7.824		[54]; [20]	YSO
J183014.96-020528.6	277.56	-02.09	13.650	13.473	9.667	7.044	X-ray	[53]	?
J183021.42-020103.4	277.59	-02.02	13.878	13.503	9.582	6.674			
J183008.21-015722.5	277.53	-01.96	14.272	13.905	10.593	8.384	IR	[58]	YSO Cand.
J183016.60-020520.6	277.57	-02.09	13.685	13.534	9.225	7.051	X-ray	[53]	?
J183021.48-020025.8	277.59	-02.01	14.001	13.592	10.575	8.337			
J183023.03-020235.8	277.59	-02.04	14.217	13.805	9.581	7.227			

Continuation of the table

AllWISE	RA(J2000), deg	DE(J2000), deg	W1, mag	W2, mag	W3, mag	W4, mag	Observations	Reference	Catalog class
J183002.50-015655.5	277.51	-01.95	13.760	13.559	9.658	7.690	X-ray; IR	[53]; [58]	YSO Cand.
J183008.22-015705.7	277.53	-01.95	13.243	13.002	10.329	8.235	IR	[54] ; [58]	
J183011.59-015721.4	277.55	-01.96	14.244	13.879	10.832	8.306	X-ray; IR	[53]; [58]	
J183017.77-020531.6	277.57	-02.09	14.312	14.103	9.712	6.861	X-ray	[53]	?
J183016.18-020601.1	277.57	-02.10	13.289	12.943	9.357	6.379	X-ray; IR	[53]; [58]	YSO Cand.
J183015.06-015732.9	277.56	-01.96	13.951	13.760	10.636	7.760	X-ray	[53]	?
J183026.15-020202.4	277.61	-02.03	14.243	13.923	9.589	7.091			
J182941.43-020433.7	277.42	-02.08	11.705	11.592	10.815	8.267			
J183019.17-020632.0	277.58	-02.11	13.805	13.579	9.515	6.772	X-ray; IR	[53]; [58]	YSO
J183020.37-020617.0	277.58	-02.10	13.466	13.105	9.613	6.871	X-ray	[53]	?
J183028.95-020232.3	277.62	-02.04	13.250	13.023	9.636	7.158			
J182939.58-020456.3	277.41	-02.08	11.651	11.520	10.620	8.557			
J183026.72-020459.0	277.61	-02.08	13.689	13.049	9.606	7.654			
J183029.72-020202.4	277.62	-02.03	13.742	13.726	9.412	7.414			
J183029.70-020233.5	277.62	-02.04	14.078	13.864	9.358	7.145			
J182938.64-020446.7	277.41	-02.08	10.963	10.877	9.864	7.682			
J183022.25-015709.4	277.59	-01.95	8.342	7.655	7.599	7.368	X-ray; IR	[53]; [78];[40]	YSO Cand.
J183013.74-015535.6	277.56	-01.93	13.527	13.444	10.567	8.066	X-ray	[53]	?
J183013.11-015529.1	277.55	-01.92	13.115	12.907	10.708	8.417			

IRSTI 29.17.15 https://doi.org/10.26577/phst202613111

Peculiarities of diffusive and convective mixing in gas mixtures with fine dust in isobaric-isothermal conditions

V. Mukamedenkyzy[1], H. Altenbach[2], A. Tolepbergen[1*] and V. Kossov[3]

[1]Al Farabi Kazakh National University, Almaty, Kazakhstan
[2]Otto von Guericke University, Magdeburg, Germany
[3]Abai Kazak National Pedagogical University, Almaty, Kazakhstan
*e-mail: arsen4236@gmail.com

(Received January 12, 2026; received in revised form May 9, 2026; accepted May 16, 2026)

This paper presents a numerical study of diffusive–convective mixing in gas–solid systems under isothermal and isobaric conditions. Two model systems, CO_2 + Si – N_2 and H_2O + C – Air, were investigated to analyze the transport of gas components and dispersed solid particles. Simulations were performed in the ANSYS Fluent environment using the Species Transport and Eulerian Multiphase Flow models, enabling the coupled description of gas-phase diffusion and particle motion. Calculations were carried out for a two-dimensional vertical channel geometry previously employed in studies of gas–gas mixing, where instability of mechanical equilibrium in the diffusion layer was observed. The results show that the dispersed solid phase forms localized regions of increased density that subsequently undergo gravitational displacement, leading to the development of convective structures and intensive mixing. At later stages, the system evolves toward a quasi-stationary concentration distribution. The study extends a previously validated numerical approach for gas mixtures to gas–solid media with different physicochemical properties and demonstrates the formation of Rayleigh–Taylor-type structures in the absence of thermal and chemical effects. The proposed methodology provides an effective tool for modeling diffusion–convective processes in multiphase systems and may be applied to the analysis of aerosol transport and dust particle dynamics in both atmospheric and technological environments.

Keywords: diffusion, convection, instability, Eulerian model, numerical modeling, ANSYS fluent, Rayleigh-Taylor instability.

1. Introduction

Diffusion and convective mass transfer in gas–solid systems play a critical role in a wide range of natural and industrial processes, including atmospheric aerosol transport, dust emission from thermal power plants, and mixing in chemical reactors. In many practically relevant scenarios, these processes occur under isothermal and isobaric conditions, yet their dynamics remain poorly understood due to the complex interplay between concentration-driven instabilities and gravitational settling of the dispersed phase.

In isothermal multicomponent gas mixtures, a substantial difference in the diffusion coefficients of the components can disrupt the mechanical equilibrium of the system [1–3]. Depending on the relationship between the partial concentration gradients and the thermophysical parameters of the mixture, regions of elevated or reduced density may form [4, 5], triggering concentration-driven gravitational convection. The threshold conditions for this instability can be determined experimentally [6], analytically within the framework of Rayleigh stability theory [1, 7], or numerically [8, 9]. A comprehensive review of this phenomenon for gas mixtures is given in [10].

Previous studies [1, 10] addressed the case in which the mixture density decreases with height – a configuration that suppresses gravitational instability. The present work focuses on the opposite situation: a density gradient directed upward, which

gives rise to Rayleigh–Taylor convection. Identifying the thermophysical parameter ranges in which convective contributions to mass transfer are negligible is of direct practical importance, as it defines the experimental conditions under which mutual diffusion coefficients can be reliably determined.

When the density gradient is directed such that the heavier phase is positioned above the lighter one, the system becomes susceptible to Rayleigh–Taylor instability [11]. In gas–solid mixtures, this instability takes a distinctive form: the dispersed solid phase generates local density inversions that drive the formation of descending particle jets, clump structures, and vortex cells. While Rayleigh–Taylor dynamics have been extensively studied in gas–liquid and gas–gas configurations [12–14], the corresponding behavior in gas–solid systems – where interphase momentum exchange, buoyancy, and particle inertia act simultaneously – has received considerably less attention.

Experimental investigation of such processes is hindered by the optical opacity of particle-laden media, micro-scale interfacial effects, and the inherently non-stationary character of the phase boundary [15–18]. Computational fluid dynamics (CFD) methods provide a viable alternative, enabling detailed resolution of multicomponent and multiphase flows. However, existing numerical models frequently rely on simplified approximations or empirical closures that limit predictive accuracy for stratified gas–solid flows [19–23].

The present work addresses this gap by proposing a physically consistent numerical model for diffusion-convective mixing in binary gas mixtures containing a dispersed solid phase. The approach combines the Species Transport formulation – previously validated for ternary gas systems [24, 25] – with the Eulerian Multiphase Flow method, which accounts for interphase momentum exchange without the need for empirical corrections. Two representative systems are examined: CO_2 + Si – N_2 at T = 300 K and H_2O + C – Air at T = 393 K, both modelled under isobaric conditions at p = 0.1 MPa with initial solid-phase volume fractions of 1%, 2.5%, and 5%. The objective is to characterize the universal stages of flow evolution, quantify the influence of particle loading on gas-phase transport, and establish the conditions under which Rayleigh–Taylor-like convective structures emerge in gas–solid media.

2. Mathematical model and numerical methods

The system under study consists of two cylindrical vessels arranged vertically and connected by a thin cylindrical channel. At the initial moment of time, the upper vessel is filled with a mixture of gases (CO_2 or H_2O) and solid microparticles (Si or C), and the lower vessel contains pure N_2 or air. After the partition between the vessels is opened, the components interpenetrate under the action of concentration gradients and gravitational forces.

The process proceeds under isothermal and isobaric conditions. The interaction between phases is described by volume fractions and momentum exchange. The solid phase is modelled as a dispersed medium with spherical particles with a diameter of d_p=10^{-5} m. The initial volume fractions of solid particles in the upper vessel are 1%, 2.5%, and 5%. The selected initial particle volume fractions (1%, 2.5% and 5%) correspond to a dilute and moderately loaded dispersed phase regime. This range was chosen to evaluate the influence of particle loading on the evolution of diffusion-convective structures while remaining within the applicability limits of the adopted Eulerian multiphase approach without introducing additional submodels for agglomeration, hindered settling, or dense granular interactions. At these concentrations, the solid phase already produces a noticeable contribution to the local density stratification and interphase momentum exchange, but the system does not yet transition to a densely packed regime. At particle concentrations exceeding approximately 10%, one may expect stronger interparticle effects, partial suppression or restructuring of convective cells, and a substantial increase in the role of collective settling and nonlinearity of momentum exchange. Detailed thermophysical properties of gases and solid particles can be found in Table 1.

Table 1. Physicochemical properties of gases and particulate matter for the systems CO_2 + Si – N_2 and H_2O + C – Air.

Component	Phase type	Molar mass, g/mol	Density, kg/m³	Viscosity, Pa·s	Thermal conductivity, W/(m·K)	c_p, J/(kg·K)
CO_2	gas	44.01	1.977	1.48×10^{-5}	0.0166	844
Si	solid	28.09	2330	–	148	700
N_2	gas	28.02	1.165	1.76×10^{-5}	0.0259	1040
H_2O (steam)	gas	18.02	0.804	2.00×10^{-5}	0.025	1995
C	solid	12.01	2000	–	6	710
Air	gas	28.97	1.161	1.85×10^{-5}	0.026	1005

Based on the thermophysical parameters presented in Table 1, a computational model of diffusion-convective mixing was developed. The spatial configuration of the system, reproducing the mutual arrangement of the flasks and the connecting channel, is shown in Figure 1.

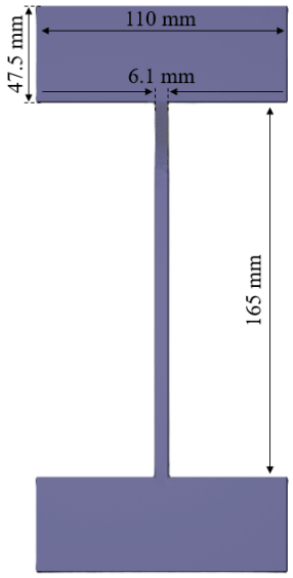

Figure 1. Geometric model of the study area.

The geometry of the area (Fig. 1) is two-dimensional and axisymmetric: the height of each vessel is 47.5 mm, the height of the connecting channel is 70 mm, and the diameter of the channel is 6.1 mm. The walls are considered impermeable and adhesive to particles, without slippage or heat exchange.

3. Basic equations of the model

The calculation method is based on a previously verified gas diffusion model [24, 25], extended in the present work to account for the solid dispersed phase. The gas-phase transport of species is described by the Species Transport equations under isothermal and isobaric conditions, with turbulence modelled using the *k–ω SST* approach. To incorporate the solid phase, the Eulerian Multiphase Flow framework is adopted, in which each phase – gas and solid – is treated as an interpenetrating continuum with its own velocity, pressure, and volume fraction fields.

Mass conservation for phase q is expressed by the continuity equation:

$$\frac{\partial}{\partial t}(\alpha_q\rho_q)+\nabla\cdot(\alpha_q\rho_q\vec{v}_q)= =\sum_{p=1}^{n}(\dot{m}_{pq}-\dot{m}_{qp})+S_q \quad (1)$$

where $\vec{v}_q$ – phase transition rate and $\dot{m}_{pq}$ characterizes mass transfer from phase p to phase q, and $\dot{m}_{qp}$ characterizes mass transfer from phase q to phase p and these mechanisms can be specified separately [26]. In the present configuration, no phase transition or chemical reaction occurs, so these terms vanish identically.

The momentum balance for phase q takes the form:

$$\frac{\partial}{\partial t}(\alpha_q\rho_q\vec{v}_q)+\nabla\cdot(\alpha_q\rho_q\vec{v}_q\vec{v}_q)= =-\alpha\nabla p+\nabla\cdot\bar{\bar{\tau}}_q+\alpha_q\rho_q\vec{g}+ +\sum_{p=1}^{n}(\vec{R}_{pq}+\dot{m}_{pq}\vec{v}_{pq}-\dot{m}_{qp}\vec{v}_{qp})+ +(\vec{F}_q+\vec{F}_{lift,q}+\vec{F}_{wl,q}+\vec{F}_{vm,q}+\vec{F}_{td,q}) \quad (2)$$

where the stress–strain tensor, effective phase density, and standard body-force contributions are defined according to the Eulerian multiphase formulation [26]. The gravitational term plays a central role in the present problem, as the density inversion between the particle-laden upper region and the pure gas in the lower flask drives the Rayleigh–Taylor-like instability observed in the results.

Interphase momentum exchange between the gas and solid phases is described by:

$$\sum_{p=1}^{n} \vec{R}_{pq} = \sum_{p=1}^{n} K_{pq}(\vec{v}_p - \vec{v}_q) \tag{3}$$

where K_{pq} is the interphase momentum exchange coefficient, determined from the Schiller–Naumann drag correlation for spherical particles of diameter d_p=10^{-5} m. This term is the primary coupling mechanism between the two phases and governs the rate of gravitational particle settling and the feedback of particle drag on the gas velocity field.

The volume fraction of each phase is obtained by solving the transport equation:

$$\frac{1}{\rho_{rq}}\left(\frac{\partial}{\partial t}(\alpha_q \rho_q) + \nabla \cdot (\alpha_q \rho_q \vec{v}_q) = \sum_{p=1}^{n} (\dot{m}_{pq} - \dot{m}_{qp})\right) \tag{4}$$

subject to the constraint that volume fractions sum to unity across all phases. This equation is solved for each secondary phase; the primary phase fraction is then determined algebraically.

The momentum balance for the solid phase s, accounting for particle pressure and granular stresses, is given by:

$$\begin{aligned} &\frac{\partial}{\partial t}(\alpha_s \rho_s \vec{v}_s) + \nabla \cdot (\alpha_s \rho_s \vec{v}_s \vec{v}_s) = \\ &= -\alpha_s \nabla p - \nabla p_s + \nabla \cdot \bar{\bar{\tau}}_s + \alpha_s \rho_s \vec{g} + \\ &+ \sum_{l=1}^{N} (K_{ls}(\vec{v}_l - \vec{v}_s) + \dot{m}_{ls}\vec{v}_{ls} - \dot{m}_{sl}\vec{v}_{sl}) + \\ &+ (\vec{F}_s + \vec{F}_{lift,s} + \vec{F}_{wl,s} + \vec{F}_{vm,s} + \vec{F}_{td,s}) \end{aligned} \tag{5}$$

where p_s – solid particle pressure s, $K_{ls} = K_{sl}$ – momentum exchange coefficient between liquid or solid phase l and solid phase s, N – total number of phases.

The rheological behaviour of the solid phase is described within the kinetic theory of granular flows. By analogy with molecular motion in a gas, the random translational velocity of particles arising from inter-particle collisions is characterised by a granular temperature Θ_s, defined as one third of the mean square of the particle velocity fluctuation. This quantity governs the effective pressure, viscosity, and normal stresses of the solid phase, and accounts for the partially inelastic nature of inter-particle collisions. The granular temperature is solved as an additional transport equation coupled to the momentum balance (5).

4. Boundary and initial conditions

At the initial moment:

- upper region: mixture of gas (CO_2 or H_2O) and dust from solid particles (Si or C);
- lower region and channel: pure gas (N_2 or Air);

On the walls:

$$u_q = 0, \ \frac{\partial Y_i}{\partial n} = 0 \tag{6}$$

For particles – no-slip boundary condition. Pressure and temperature are assumed to be constant: p=0.1 MPa, T=300 K (CO_2+Si–N_2) and T=393 K (H_2O+C–Air).

5. Numerical implementation

The calculation was performed in a non-stationary setting, which made it possible to track the dynamics of mixing and phase transfer over time. The time step was 1 s, and the total number of integration steps in time was 1200, which corresponds to 20 minutes of real time of the process. This time interval was chosen to make it possible to track the transition of the system from the initial unstable state to a quasi-steady-state distribution of concentrations.

The calculations used a pressure-based coupled solver with full coupling between the pressure and velocity fields. The Second Order Upwind scheme

was used to approximate convective terms, and the PRESTO! scheme was used for pressure, providing increased accuracy in the presence of gravitational effects. Time discretization was implemented using the Second Order Implicit scheme, which ensured the stability of the solution at the selected time step.

The computational grid had a structured topology and contained 164 120 cells and 165 974 nodes. The minimum cell size in the channel area was 0.25 mm, which ensured correct resolution of local concentration and velocity gradients at interphase boundaries. Convergence criteria for all equations were set at no higher than 10^{-6} for velocity and pressure fields, and 10^{-8} for concentrations and volume fractions of phases.

6. Results and discussion

The mixing process in both systems considered – CO_2 + Si – N_2 and H_2O + C – Air – is characterized by pronounced non-stationarity and multi-stage evolution. Almost immediately after the start of the calculation, a contact zone with contrasting densities forms, causing a disturbance in mechanical equilibrium and the formation of downward and upward flows. In the first seconds of the calculation, gas from the upper flask begins to penetrate the lower flask, while the solid phase settles under the action of gravity.

The spatial evolution of both phases is illustrated in Figs. 2 and 3 for the CO_2 + Si – N_2 and H_2O + C – Air systems, respectively, at four time instants: t = 30, 60, 90, and 120 s.

For the gas phase (Figs. 2a and 3a), the concentration front descends progressively through the connecting channel. At t = 30 s, the CO_2 (or H_2O) distribution is already non-uniform along the channel axis, with a distinct concentration gradient visible between the upper and lower regions. By t = 60–90 s, the front reaches the lower flask and begins to spread laterally, driven by the combined action of diffusion and the developing convective flow. The H_2O + C – Air system (Fig. 3a) shows a visibly more advanced penetration front at equivalent time steps, consistent with the higher gas-phase transfer rates reported in Table 2 and attributable to the lower molar mass and higher diffusion mobility of water vapor.

The solid phase dynamics (Figs. 2b and 3b) present a qualitatively different picture. At t = 30 s, the particles have already concentrated into a narrow elongated region within the channel, indicating rapid gravitational settling from the upper flask. At t = 60 s, a compact high-concentration cluster is clearly visible at the channel exit – this structure corresponds to the moment of maximum local solid-phase density prior to its entry into the lower flask. By t = 90 s, the cluster detaches and enters the lower flask, adopting the characteristic teardrop morphology discussed in relation to Fig. 5. For the C particles in the H_2O system (Fig. 3b), this sequence occurs approximately 7–10 s earlier compared to Si in the CO_2 system, reflecting the influence of gas viscosity and density on particle settling dynamics. At t = 120 s, the solid phase in both systems has largely accumulated at the bottom of the lower flask, with only a residual thread remaining in the channel.

In general, the behavior of the systems is consistent with diffusion-convection processes in a gravitational field, where concentration and density gradients act simultaneously. Already in the early stages of the calculation, Rayleigh–Taylor instabilities form, manifesting themselves in the form of local wave-like deformations of the gas interface, which then transition into elongated convective jets.

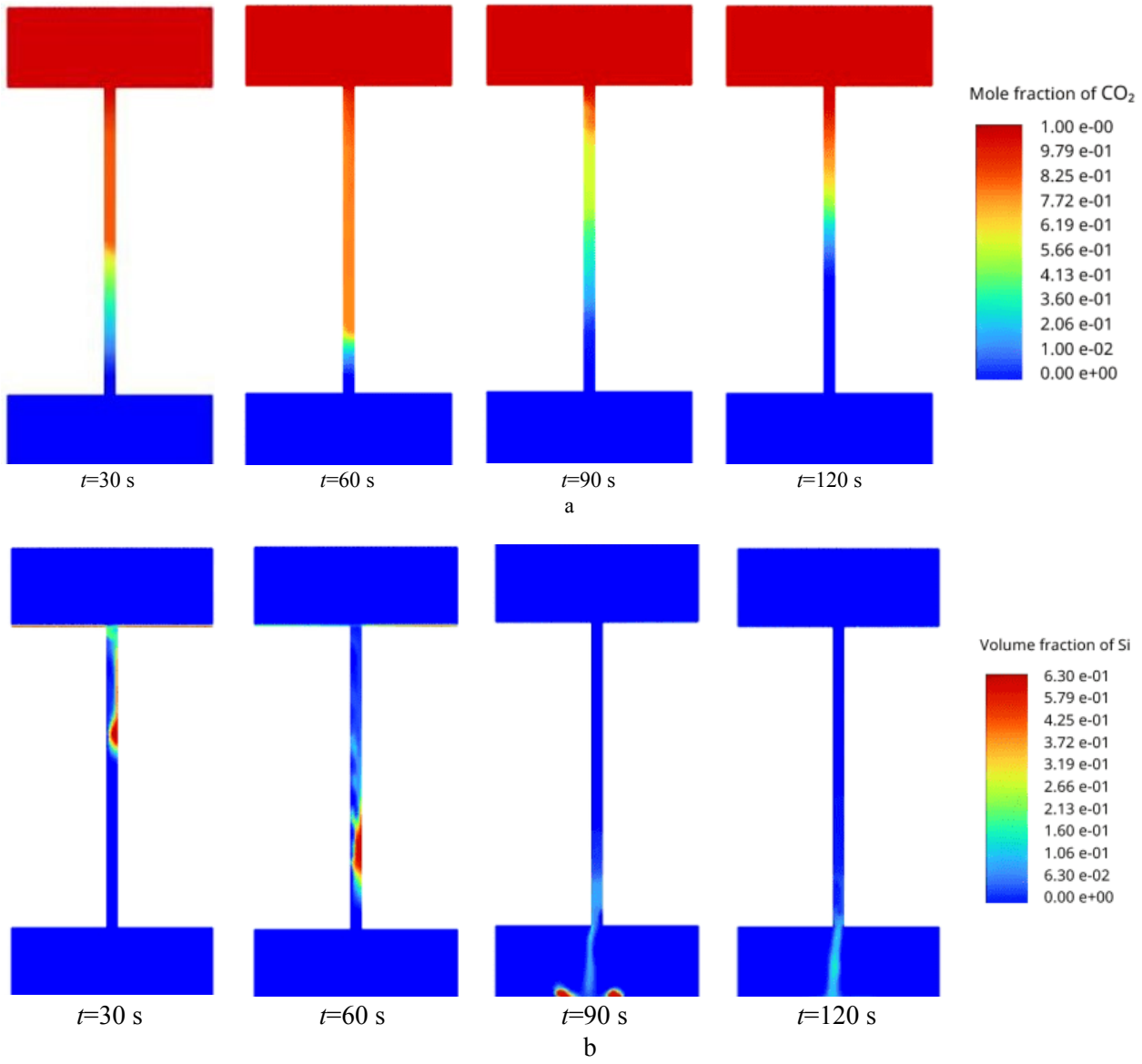

Figure 2. Gas/solid particle movement for the system CO_2 + 0.025 Si – N_2 at p=0.1 MPa, T=300 K depending on the time:
a) concentration change of CO_2; b) concentration change of Si.

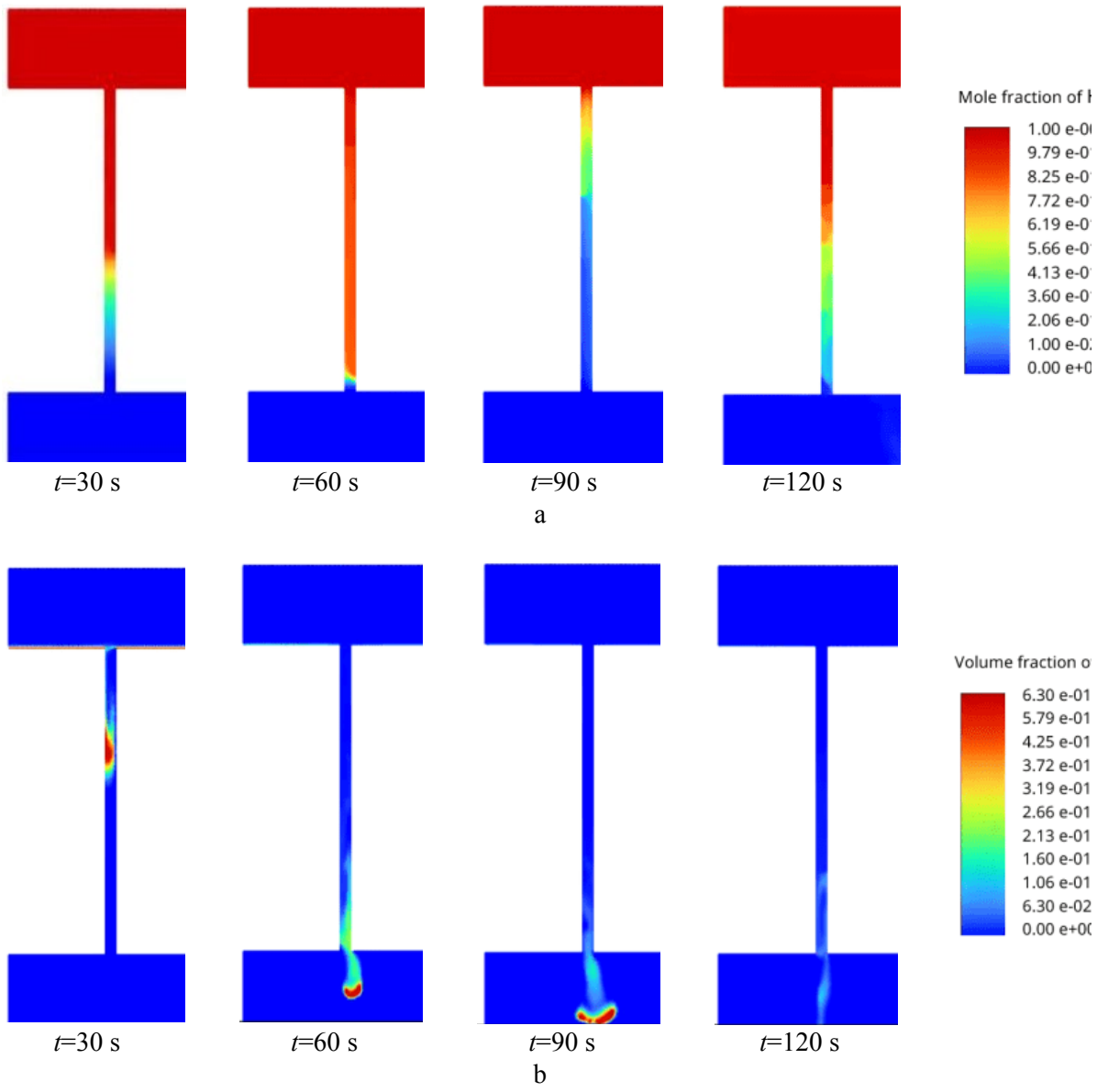

Figure 3. Gas/solid particle movement for the system H_2O + 0.025 C – Air at p=0.1 MPa, T=393 K depending on the time:
a) concentration change of H_2O; b) concentration change of C.

Upon opening of the partition, CO_2 (or H_2O) undergoes immediate penetration into the lower flask, driven by the concentration gradient across the channel. Within the first seconds, the volume-averaged mole fraction of CO_2 in the lower flask reaches approximately 0.035 – a value established quasi-instantaneously relative to the total process duration. This rapid onset reflects the dominant role of molecular diffusion prior to the development of convective structures. The solid phase remains largely confined to the upper flask during this interval, exhibiting negligible transfer to the lower volume.

The redistribution of the dispersed phase within the upper flask generates local regions of elevated density near the bottom wall. The resulting density inversion triggers Rayleigh–Taylor-type instability, manifesting as elongated convective jets visible in Figs. 2–3. For the gas phase (Fig. 4a, 4c), this stage appears as a sustained and monotonic concentration increase. The solid phase (Fig. 4b, 4d), by contrast, exhibits strongly oscillatory behavior with

characteristic fluctuations in the range 200–500 s, peak amplitude reaching ~0.025–0.026 for Si and ~0.023–0.025 for C. This contrast in kinetic behavior – smooth for the gas, impulsive for the particles – reflects a fundamental difference in the transfer mechanisms: gas transport is governed by diffusion-enhanced convection, whereas particle transfer occurs intermittently through gravitational avalanches associated with the evolving instability structures.

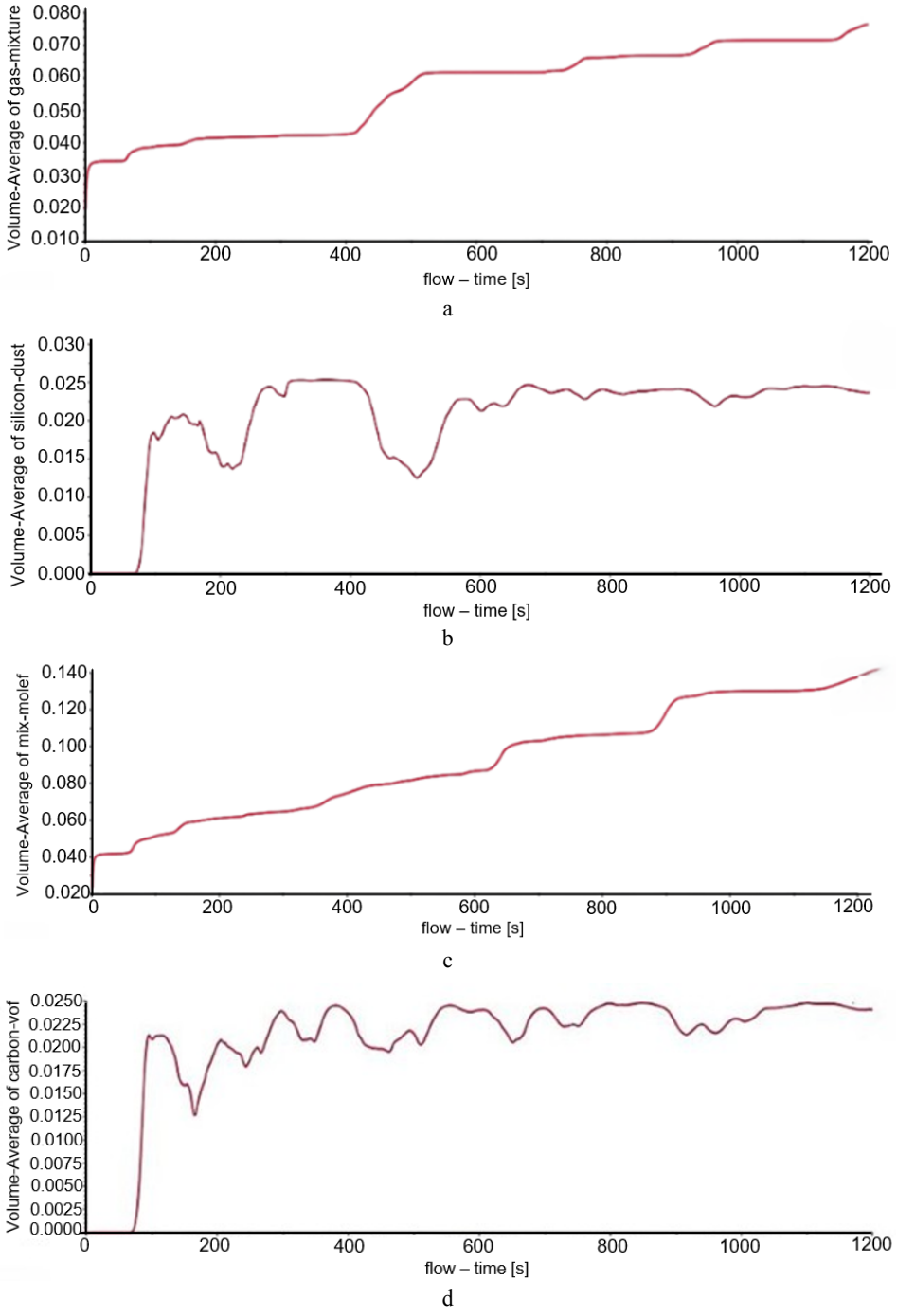

Figure 4. Dynamics of changes in the amount of gas/solid particles for systems CO_2 + 0.025 Si – N_2 at p=0.1 MPa, T=300 K and H_2O + 0.025 C – Air at p=0.1 MPa, T=393 K depending on the time in the lower flask: a) plot for CO_2; b) plot for Si; c) plot for H_2O; d) plot for C.

Both phases approach stable concentration distributions. The gas fraction in the lower flask continues to grow slowly, while solid phase oscillations decay and converge to a near-constant value. At t = 1200 s, the volume fraction of particles in the lower flask reaches 95–99% of the total injected particle mass, confirming near-complete gravitational settling.

Table 2 reveals a clear and quantitatively significant inverse relationship between initial solid-phase volume fraction and the extent of gas-phase transfer. For the CO_2 + Si – N_2 system, the mole fraction of CO_2 in the lower flask at t = 1200 s decreases from 0.1179 at φ = 1% to 0.0764 at φ = 2.5% and 0.0439 at φ = 5% – a reduction by a factor of 2.7 across the studied range. This trend indicates that higher particle loading progressively suppresses convective gas transport, likely through increased momentum dissipation in the dispersed-phase continuum and partial disruption of coherent convective structures. A symmetric but less pronounced effect is observed for the H_2O + C – Air system (Table 2).

Table 2. The amount of gas/solid particle diffusing from one chamber to another.

System	CO_2	Si	N_2	System	H_2O	C	Air
CO_2 + 0.050 Si – N_2	0.0439	0.04980	0.8990	H_2O + 0.050 C – Air	0.0425	0.0396	0.8102
CO_2 + 0.025 Si – N_2	0.0764	0.02364	0.8812	H_2O + 0.025 C – Air	0.1377	0.0240	0.7944
CO_2 + 0.010 Si – N_2	0.1179	0.00998	0.7813	H_2O + 0.010 C – Air	0.2496	0.0101	0.6997

Under identical geometric and boundary conditions, the H_2O + C – Air system consistently exhibits higher gas-phase transfer relative to CO_2 + Si – N_2. At φ = 1%, the mole fraction of H_2O in the lower flask (0.2496) is approximately 2.1 times higher than that of CO_2 (0.1179). This difference is attributable to the lower molar mass and higher diffusion mobility of water vapor compared to CO_2, which leads to a larger diffusion-driven contribution at early stages and faster convective onset. The qualitative flow structure, however, remains identical between the two systems, confirming the universality of the observed instability mechanism.

A particularly notable finding concerns the timing of teardrop-shaped particle cluster formation in the lower flask (Fig. 5). For both systems and both φ = 1% and φ = 2.5%, the cluster appears at t ≈ 82.5 s, while at φ = 5% it forms marginally earlier at t ≈ 75.0 s – a difference of only 9%. This near-independence of cluster formation time from initial solid-phase concentration suggests that the onset of Rayleigh–Taylor-like instability is governed primarily by hydrodynamic factors – the density inversion threshold and gravitational acceleration – rather than by the quantity of dispersed material. The consistent timing across both chemical systems further supports the interpretation of this phenomenon as a universal structural feature of gas–solid convective instability under the given geometric and thermodynamic constraints.

The results obtained are consistent with general ideas about the behavior of dispersed phases in gravitational flows and demonstrate the possibility of using the *ANSYS Fluent* numerical model based on a combination of Species Transport and Eulerian Multiphase Flow to describe such processes without the use of experimental data.

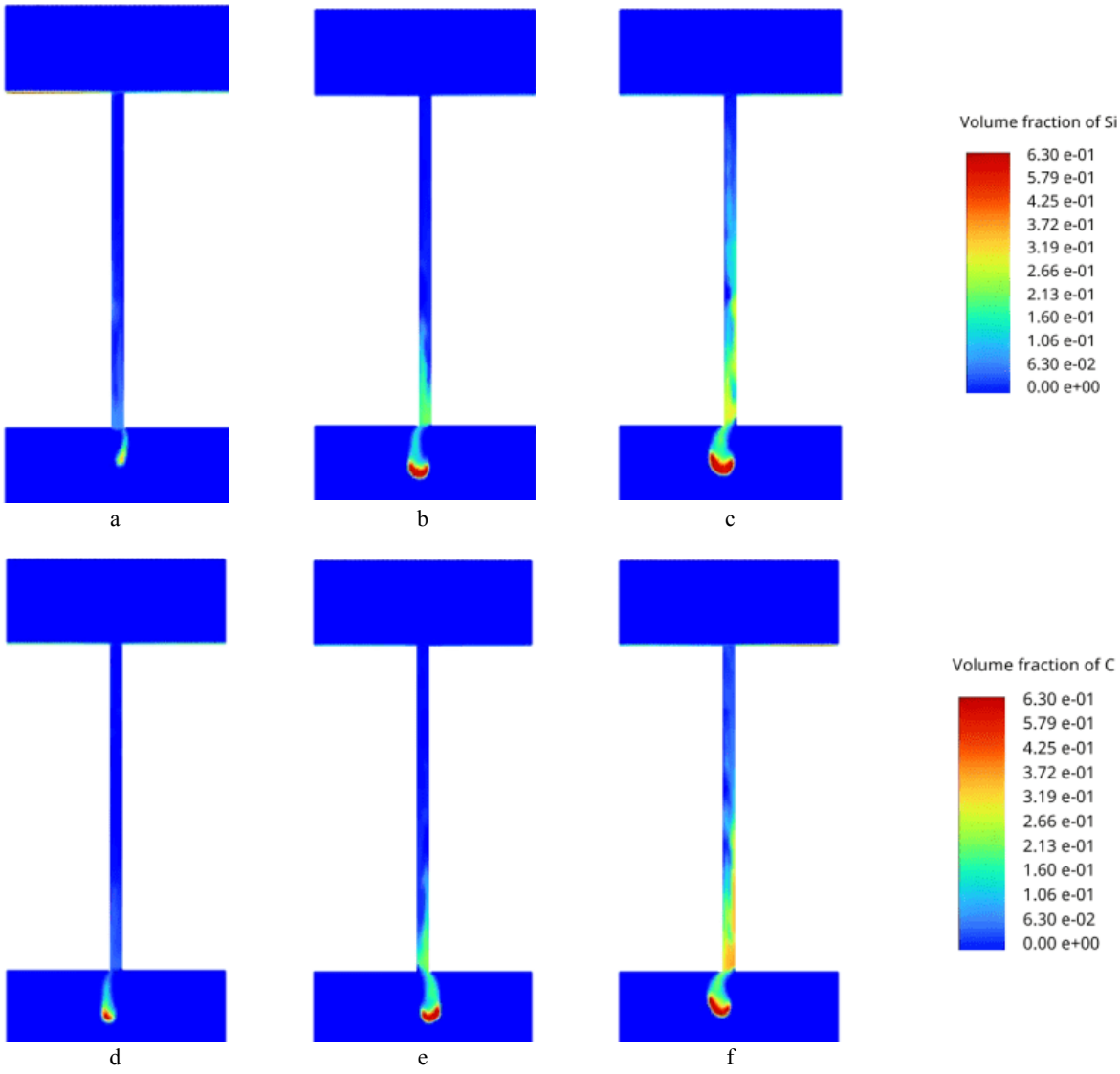

Figure 5. The moment of formation of a teardrop-shaped solid phase structure in the lower flask: a) CO_2 + 0.010 Si – N_2 (t=82.5 s); b) CO_2 + 0.025 Si – N_2 (t=82.5 s); c) CO_2 + 0.050 Si – N_2 (t=75.0 s); d) H_2O + 0.010 C – Air (t=82.5 s); e) H_2O + 0.025 C – Air (t=82.5 s); f) H_2O + 0.050 C – Air (t=75.0 s).

7. Conclusion

This paper presents a numerical study of diffusion-convective mixing in multiphase systems containing gas and solid dispersed components. Modeling was performed under isothermal and isobaric conditions using a combined approach based on the integration of Species Transport and Eulerian Multiphase Flow models in the *ANSYS Fluent 2025 R1* environment.

Two systems are considered: CO_2 + Si – N_2 and H_2O + C – Air, which differ in terms of the temperature and physical properties of the gas phase. The same qualitative patterns of flow evolution have been established for both systems. At the initial stage, gas diffusion into the lower flask and sedimentation of solid particles under the action of gravity are observed. At subsequent stages, convective structures typical of Rayleigh–Taylor instability are formed, which is confirmed by the formation of droplet-like solid phase formations in the channel. It is shown that the moment of formation of structural aerosol formations practically coincides for both systems and does not

depend on the initial concentration of solid particles (1%, 2.5%, 5%), which indicates the dominant role of hydrodynamic factors and density inversion of the mixture in the development of the flow structure.

A comparison with a previously verified model showed a qualitative match in the dynamics and time scales of mixing, confirming the correctness of the numerical approach used [21].

The results obtained are of fundamental importance, as they allow determining the ranges of thermophysical parameters in which reliable determination of mutual diffusion coefficients is possible. These coefficients are key transport constants that affect the accuracy of calculations when modeling various multiphase and multicomponent systems. Thus, this study contributes to the refinement of diffusion transport parameters and expands our understanding of the laws of mass transfer in gas-solid media.

The developed methodology can be used to analyze gas-solid diffusion processes of various nature–from laboratory experiments to problems related to aerosol mixture emissions from thermal power plants. A promising direction for further research is the inclusion of heat exchange, reaction effects, and the transition to three-dimensional geometry for a more complete description of the dynamics of mixing and sedimentation of solid particles.

Acknowledgements

The work was supported by the Committee of Science of the Ministry of Science and Higher Education of the Republic of Kazakhstan, project AP23488139.

Conflicts of interest

The authors declare no conflict of interest.

Author contributions

Conceptualization, V.N.K.; Methodology, A.T.; Software, A.T.; Validation, A.T.; Formal Analysis, A.T., V.N.K., V.M. and H.A.; Investigation, A.T.; Resources, V.N.K., V.M.; Data Curation, A.T.; Writing – Original Draft Preparation, A.T. and H.A.; Writing – Review & Editing, V.N.K. and V.M.; Visualization, A.T.; Supervision, V.N.K., V.M. and H.A.; Project Administration, V.N.K.; Funding Acquisition, V.N.K.

References

1. V. N. Kosov and V. D. Seleznev, *Anomalous Occurrence of Free Gravitational Convection in Isothermal Ternary Gas Mixtures*. Ekaterinburg, Russia: Ural Branch of the Russian Academy of Sciences, 2004.

2. V. V. Dil'man, D. A. Lipatov, V. A. Lotkhov, et al., "Instability in unsteady-state evaporation of binary solutions into an inert gas," *Theor. Found. Chem. Eng*., vol. 39, no. 6, pp. 566–572, 2005, https://doi.org/10.1007/s11236-005-0118-0

3. S. Bolegenova, A. Askarova, N. Slavinskaya, S. Ospanova, A. Maxutkhanova, A. Aldiyarova, and D. Yerbosynov, "Statistical modeling of spray formation, combustion, and evaporation of liquid fuel droplets," *Phys. Sci. Technol*., vol. 9, no. 3–4, pp. 69–82, 2022, https://doi.org/10.26577/phst.2022.v9.i2.09

4. V. A. Kaminskii, "Special modes of three-component diffusion in gases," *Russ. J. Phys. Chem. A,* vol. 85, no. 12, pp. 2203–2208, 2011, https://doi.org/10.1134/S0036024411120156

5. V. N. Kosov, Yu. I. Zhavrin, and V. D. Seleznev, "Inversion of the density gradient and the 'gate' in isothermal mixing of gases," *Tech. Phys., vol*. 43, no. 5, pp. 488–492, 1998.

6. V. N. Kosov, Yu. I. Zhavrin, D. U. Kul'zhanov, and K. K. Karataeva, "Effect of pressure on the type of mixing in a three-component gas mixture containing a real gas component," *Tech. Phys. Lett.*, vol. 26, no. 12, pp. 1108–1109, 2000.

7. V. N. Kosov, O. V. Fedorenko, Yu. I. Zhavrin, and V. Mukamedenkyzy, "Instability of mechanical equilibrium during diffusion in a three-component gas mixture in a vertical cylinder," *Tech. Phys.*, vol. 59, no. 4, pp. 482–486, 2014, https://doi.org/10.1134/S1063784214040161

8. A. Zhussanbayeva, V. N. Kossov, O. V. Fedorenko, and M. Zhaneli, "Instability of mechanical equilibrium and concentration convection in isothermal ternary gaseous systems," *Phys. Sci. Technol.*, vol. 9, no. 1–2, pp. 55–61, 2022, https://doi.org/10.26577/phst.2022.v9.i1.07

9. M. Moldabekova, V. Mukamedenkyzy, M. Asembayeva and A. Tolepbergen, "Investigation of the diffusion of two gases equally diluted with different ballast gases," *Recent Contrib. Phys*., vol. 89, no. 2, pp. 57–61, 2024, https://doi.org/10.26577/RCPh.2024v89i2-08

10. V. N. Kossov and H. Altenbach, "Diffusion mechanisms of convective instability in liquid and gas mixtures," *J. Appl. Math. Mech*., vol. 103, no. 11, Art. no. e202300801, 2023, https://doi.org/10.1002/zamm.20230080

11. A. Banerjee, "Rayleigh–Taylor instability: A status review of experimental designs and diagnostics," *J. Fluids Eng*., vol. 142, no. 12, Art. no. 120801, 2020, https://doi.org/10.1115/1.4048349

12. S. A. Bazarbekov, "Application of high-speed gas-flame technology for surface hardening," *Phys. Sci. Technol*., vol. 8, no. 1–2, pp. 47–52, 2021, https://doi.org/10.26577/phst.2021.v8.i1.06

13. S. Balachandar and J. K. Eaton, “Turbulent dispersed multiphase flow,” *Annu. Rev. Fluid Mech*., vol. 42, pp. 111–133, 2010, https://doi.org/10.1146/annurev.fluid.010908.165243

14. J. Capecelatro et al., “Gas–particle dynamics in high-speed flows: A review,” *Annu. Rev. Fluid Mech*., vol. 56, pp. 379–403, 2024, https://doi.org/10.1146/annurev-fluid-121021-015818

15. L. Villafañe, A. Aliseda, S. Ceccio, P. Di Marco, N. Machicoane, and T. J. Heindel, “Experimental methods for dispersed multiphase flows,” *Int. J. Multiphase Flow*, vol. 189, Art. no. 105239, 2025, https://doi.org/10.1016/j.ijmultiphaseflow.2025.105239

16. Y. Yan, K. Mohanarangam, W. Yang, and J. Tu, “Experimental measuring techniques for industrial-scale multiphase flow problems,” *Exp. Comput. Multiph. Flow*, vol. 6, pp. 1–13, 2024, https://doi.org/10.1007/s42757-023-0172-z

17. S. Bolegenova, A. Askarova, S. Ospanova, et al., “Technology of reducing greenhouse gas emissions,” *Phys. Sci. Technol*., vol. 11, no. 1–2, pp. 64–75, 2024, https://doi.org/10.26577/phst2024v11i1a8

18. S. Tas-Koehler et al., “A critical analysis of drag force modelling for disperse gas–solid flows,” *Chem. Eng. Sci*., Art. no. 117007, 2021, https://doi.org/10.1016/j.ces.2021.117007

19. B. Akula and D. Ranjan, “Dynamics of buoyancy-driven flows at moderately high Atwood numbers,” *J. Fluid Mech*., vol. 795, pp. 313–355, 2016, https://doi.org/10.1017/jfm.2016.199

20. Y. Liang, A. Alkindi, K. Alzeyoudi, L. Liu, M. Ali, and N. Masmoudi, “Experimental investigation of three-dimensional Rayleigh–Taylor instability,” *J. Fluid Mech*., vol. 994, Art. no. A7, 2024, https://doi.org/10.1017/jfm.2024.754

21. C. Liu, Y. Zhang, and Z. Xiao, “Unified model for Rayleigh–Taylor and Richtmyer–Meshkov fingers,” *J. Fluid Mech*., vol. 954, Art. no. A13, 2023, https://doi.org/10.1017/jfm.2022.1000

22. M. L. R. Peixoto, M. S. C. A. Brito, R. J. Santos, and V. J. P. Vilar, “Kinetic model implementation in raceway pond reactors,” *Chem. Eng. Res. Des*., vol. 210, pp. 150–162, 2024, https://doi.org/10.1016/j.cherd.2024.08.030

23. P. M. Pancorbo, J. M. Ortiz de Zárate, H. Bataller, and F. Croccolo, “Gravity effects on Soret-induced fluctuations,” *Eur. Phys. J. E*, vol. 40, no. 2, Art. no. 22, 2017, https://doi.org/10.1140/epje/i2017-11513-9

24. V. N. Kossov, V. Mukamedenkyzy, A. Tolepbergen, and H. Altenbach, “Peculiarities of combined mixing caused by instability of mechanical equilibrium,” *Int. J. Chem. Eng*., Art. no. 9643371, 2025, https://doi.org/10.1155/ijce/9643371

25. V. Mukamedenkyzy and A. Tolepbergen, “Some features of Rayleigh–Taylor convection in the mixing of ideal gas mixtures,” *Recent Contrib. Phys*., vol. 92, no. 1, pp. 110–119, 2025, https://doi.org/10.26577/RCPh202592112

26. ANSYS, Inc. "*ANSYS Fluent Theory Guide 2025 R1*." ANSYS Documentation. Accessed: November 2025. [Online]. Available: https://ansyshelp.ansys.com

Information about the authors:

Venera Mukamedenkyzy – Candidate of Physical and Mathematical Sciences, Associate Professor, Al Farabi Kazakh National University (Almaty, Kazakhstan, e-mail: mukameden@inbox.ru).

Holm Altenbach – Dr.-Ing. habil., Professor, Otto von Guericke University Magdeburg (Magdeburg, Germany, e-mail: holm.altenbach@ovgu.de).

Arsen Tolepbergen (corresponding author) – 3rd year PhD student, Al-Farabi Kazakh National University (Almaty, Kazakhstan, e-mail: arsen4236@gmail.com).

Vladimir Kossov – Doctor of Physical and Mathematical Sciences, Professor, Abai Kazakh National Pedagogical University (Almaty, Kazakhstan, e-mail: kosov_vlad_nik@list.ru).

CONTENTS